Study of high energy particles in extensive air showers

H. Nejabat

Nejabat, H. (1980) Study of high energy particles in extensive air showers. Doctoral thesis, Durham University.

STUDY OF HIGH ENERGY PARTICLES
IN EXTENSIVE AIR SHOWERS

by

H. Nejabat, B.Sc.(Shiraz)

A Thesis submitted to the

University of Durham

for the degree of Doctor of Philosophy

May, 1980.

CONTENTS

ABSTRACT

Using a large volume flash tube chamber ($\sim$ 11,000 tubes) and a relatively small air shower array (Durham EAS array), major components of air showers of size $1.5.10^4$-4.10^6 particles within 75m of the shower axis have been studied.

A detailed description of the apparatus used in the experiment and also different methods of analysing air showers are given.

The differential and integral number spectrum at sea level for showers of size $1.5.10^4$-4.10^6 particles are measured and compared with other work. The results indicate a change of slope around 8.10^5 particles.

Measurements of the lateral distribution of low energy muons (E_μ > 0.5 GeV) have been obtained and similar to most of other experiments, the present measured distribution is flatter than expected. The reasons for this discrepancy are thought to be a combination of (a) large transverse momenta for pions produced in high energy interactions, (b) the height of origin of muon production being higher in the atmosphere than expected and (c) errors in core location.

The spatial separation of distribution of neighbouring muons in groups of muons traversing the flash tube chamber are measured. These are compared with spatial distributions based on a random spatial distribution between muons in groups of muons in EAS.

The hadronic component of EAS is investigated. Energy spectra and lateral distribution of hadrons with energy greater than 13 GeV for showers of mean size 3.10^5 particles have been measured and compared with other measurements as well as theoretical predictions based on established models such as the standard CKP and isobar-fireball models.

Using data from the flash tube chamber, an attempt has been made to estimate the ratio of charged to neutral hadrons in EAS.

PREFACE

This thesis contains an account of the work carried out in the period 1976-1979 while the author was a research student under the supervision of Dr. F Ashton in the Cosmic Ray Group of the Physics department of the University of Durham. When the author joined the group in January 1976, the flash tube chamber was in an early stage of modification to allow an experiment for faster than light particles (tachyons), as well as EAS studies to be performed. The author helped in the general running and maintenance of the apparatus and also shared, with his colleagues, the collection of data from the flash tube chamber. The author is solely responsible for calculations, analysis and interpretation of experimental data described in this thesis.

Preliminary results of this work have been presented at the 15th and 16th International Cosmic Ray Conferences held in Plovdiv and Kyoto respectively.

ACKNOWLEDGEMENTS

I wish to thank Professors B.H.Bransden and A.W. Wolfendale for the provision of the facilities for this work and for their interest and support.

I am deeply indebted to my supervisor, Dr.F.Ashton for his advice, guidance and invaluable help throughout this work. I would like to thank Dr. M.G.Thompson, Dr.A.C.Smith, Mr. T.Stewart and Mr.M. Treasure for providing extensive air shower data.

Many members of the Cosmic Ray Research Group, staff and research students, are thanked for helpful assistance, and especially Mr. I.A.Ward and S.J.Fatemi for helping to operate the flash tube chamber.

The technical staff of the Physics department, in particular Mr. W.Leslie and Mr. K.Tindale, are thanked for their willing help and Mrs. P.A.Russell and Miss K.Gittins for the excellent preparation of the diagrams in this thesis.

I wish to extend special thanks to Mrs. S.Mellanby for her careful and rapid typing of this thesis.

I am extremely grateful to my parents for their moral and financial support.

Lastly, but by no means least, I would like to thank my wife for her continuous encouragement, endurance and patience.

CHAPTER ONE

HISTORICAL BACKGROUND

1.1 INTRODUCTION

For many centuries man has known and studied the effects and information from the space surrounding the earth, but this information has almost entirely been conveyed by visual light. It was only by the beginning of this century that the first indication of a penetrating extraterrestial radiation came from studies of residual conductivity of enclosed and shielded samples of air. Wilson (1901), in his studies with an ionization chamber, suspected the presence of an ionizing radiation that could penetrate thick layers of the earth and he speculated a possible extraterrestial source for it. It was left to Hess (1912) to demonstrate in a balloon flight that after an initial reduction with altitude in ionization, an increase occurred and continued up to the greatest height of about 5 km that he reached. At first it was assumed that the radiation was γ-rays due to the high penetrating power of it. This doubtful idea was clarified after the discovery of the latitude effect which indicates a lower intensity of cosmic rays near the equator where the horizontal component of the earth's geomagnetic field is stronger, and hence Clay (1927), concluded that the primary of cosmic rays must be charged particles. The East-West effect which shows that more particles arrive from the west than the east led Johnson and Street (1933) to the conclusion that the majority of primary cosmic rays were positively charged. It became clear that the primary cosmic radiation interacted with the earth's atmosphere to produce further radiation and experiments continued to determine the nature of the primary and secondary radiation and speculation arose about the origin of primary cosmic rays.

Progress of cosmic ray studies over the next two decades led to the discovery of many new particles such as positron (Anderson, 1932), which had been predicted by Dirac and the pion (Lattes et al, 1947) which proved to be the particle proposed by Yukowa to be responsible for the nuclear glue which binds together nucleons in nuclei. Particle discoveries continued when in 1947 Rochester and Butler identified in a cloud chamber a neutral particle (Λ^0) so called strange particle and led to the introduction of the quantum number of strangeness.

1.2 SIGNIFICANCE OF COSMIC RAY STUDIES

Over the past 60 years the study of cosmic radiations has led to major advances in our understanding of the fundamental processes of nature. The enormous energy carried by individual particles had enabled some insight of both the smallest and largest part of the universe. The interest of cosmic rays to the physicist lies in their astrophysical and in nuclear physics of their interactions with the earth's atmosphere. The astrophysicists are concerned with the origin of primary cosmic rays, the processes required in possible sources and the interstellar medium, to explain the energy spectrum, mass composition and the variation of primary cosmic rays incident on the earth. Perhaps the most interesting problem is the study of mechanism by which primary particles are generated and accelerated to such energies seen in cosmic rays.

As far as nuclear physics is concerned, cosmic rays have provided the nuclear physicist with a beam of very energetic particles and the possibility of studying the primary as well as secondary particles.

With the advent of particle accelerators, controlled experiments with high particle densities have become possible and the considerable knowledge gained from cosmic ray studies has been greatly extended. However, even the latest generation of accelerators will only enable nuclear interactions to be studied up to laboratory energies of 5.10^3 Gev and so cosmic rays are expected to remain an important field of study for some years to come.

1.3 INTENSITY OF PRIMARY COSMIC RAYS

One of the most interesting features of cosmic radiation is the wide range of energy which it covers. The energy spectrum of the primary particles is strongly dependent on the particle energy. Griesen (1966) quotes an integral spectrum varying with the particle energy E, measured in eV as :

$$\begin{aligned} I(>E) &= 2.5 \times 10^{18}\, E^{-1.6} & & 10^{10}\text{eV} < E < 10^{15}\ \text{eV} \\ &= 5.0 \times 10^{27}\, E^{-2.2} & m^{-2}\sec^{-1}\text{st}^{-1} \quad & 10^{15}\text{eV} < E < 10^{18}\ \text{eV} \\ &= 4.0 \times 10^{16}\, E^{-1.6} & & 10^{18}\text{eV} < E \end{aligned}$$

Broadly speaking there are four different regions of the spectrum to be considered. Below 10^{10} eV where the information comes mainly from the experiments carried out in satellites and ballons (Figure 1). In this region, the interplanetary magnetic field reduces the primary intensity and imposes an asymmetry in the arrival direction of these pre-

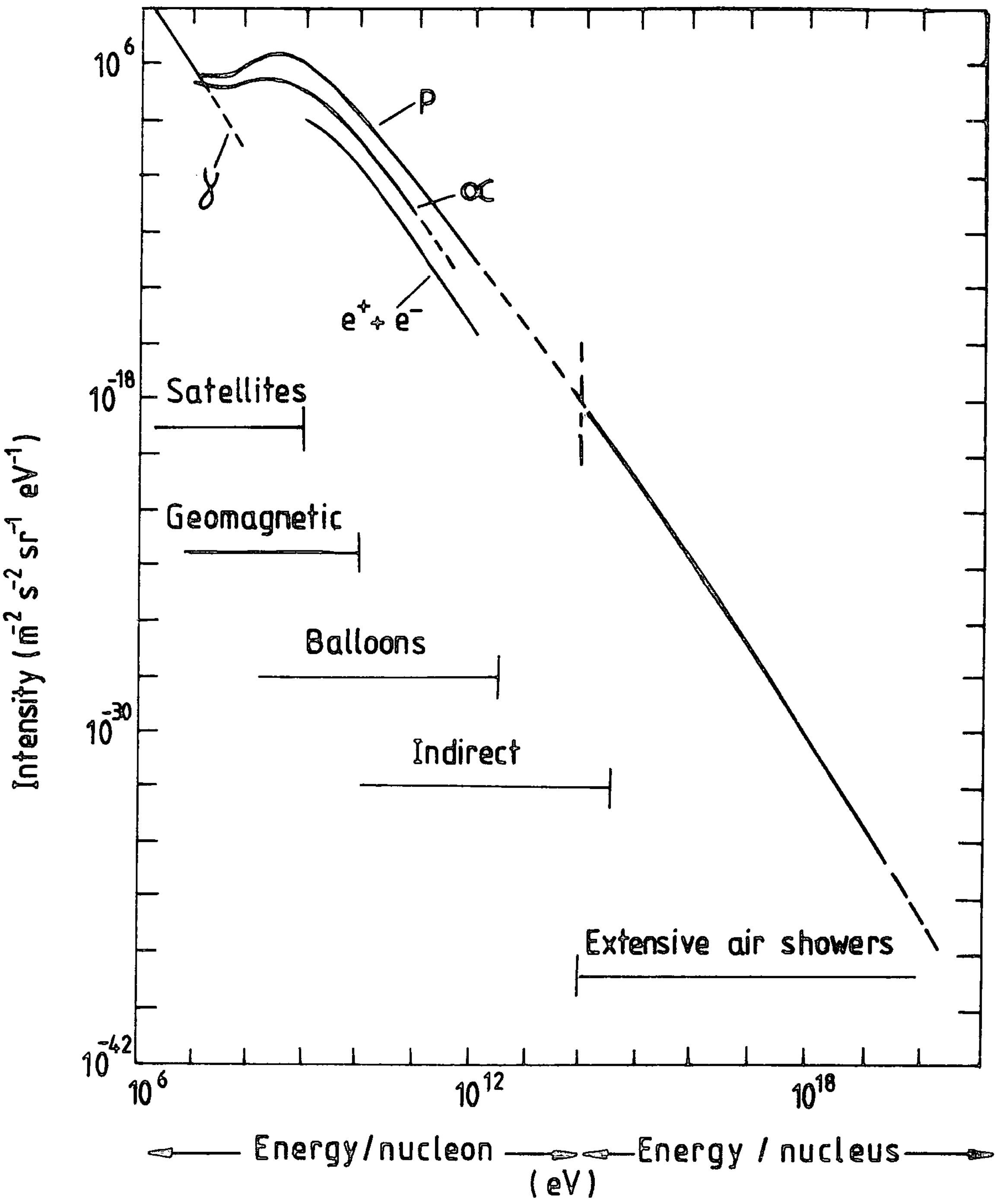

Figure 1.1 : The energy spectrum of primary cosmic rays (after Wolfendale 1973).

dominantly positively charged particles.

Above 10^{10} eV up to 10^{15} eV the slope to the integral spectrum is -1.6. In this region, the highest energy at which direct measurements have been made are reported by Gregorov et al (1971), but have not met with universal acceptance, because of steeper slope to the spectrum and also a lower flux of protons detected by their proton Satellite compared to the spectrum suggested by less direct measurements. An obvious feature of spectrum appears around 3.10^{15} eV where a sudden change in spectral slope from -1.6 to -2.2 takes place. This change of slope is generally believed to be due to the inability of the galactic magnetic fields to contain various types of particles as their rigidities are exceeded. At around 3.10^{18} eV the slope reverts back to -1.6 and this change was initially attributed to the extragalactic sources of radiation but more recently a re-analysis of the data in this region, which comes exclusively from air showers, has raised doubts as to the existence of this 'kink' in spectrum. At high energies around 6.10^{19} eV, Greisen (1966) suggested a cut-off due to energy loss by high energy primary protons because of the interactions between protons and background microwaves, ($p + \gamma \rightarrow p + \pi$'s) At present there is not enough evidence for confirmation or otherwise of such discontinuity in the spectrum. Hillas, in his summary (1975) points out that the data from large air shower arrays shows no interruption in the cosmic ray spectrum up to approximately 10^{20} eV.

1.4 COMPOSITION AND ABUNDANCE OF ELEMENTS IN PRIMARY COSMIC RAYS

The composition of primary cosmic rays for energies $\leq 10^{13}$ eV has been measured and presented in Table 1.1 (after

Julliussen, 1975). The data is normalized to a percentage of the total.

Z Elements	Kinetic Energy per Nucleus(eV) 10^{10}	10^{11}	10^{12}	10^{13}
1 Hydrogen	58 ± 5	47 ± 4	42 ± 6	24 ± 6
2 Helium	28 ± 3	25 ± 3	20 ± 3	15 ± 5
3- 5 Light nuclei	1.2 ± 0.1	1.1 ± 0.1	0.6 ± 0.2	
6- 8 Medium nuclei	7.1 ± 0.4	12.2 ± 0.8	14 ± 2	
10-14 Heavy nuclei	2.8 ± 0.2	6.7 ± 0.5	10 ± 1	
16-24 Very heavy nuclei	1.2 ± 0.2	3.6 ± 0.4	4 ± 1	
26-28 Iron group nuclei	1.2 ± 0.2	4.5 ± 0.5	10 ± 2	24 ± 7
30 Very, very heavy nuclei		0.007±0.004		

TABLE 1.1 : Composition of Cosmic Rays at Different Primary Energies.

Figure 1.2 shows the abundance of elements in cosmic rays in the range of a few hundred MeV per nuclear to about one Gev per nucleon for hydrogen up to iron as given by Meyer et al (1974). For comparison the solar system abundance are also shown in Figure 1.2. A comparison between abundances in cosmic rays and the universe shows that there is an excess of lighter elements (Li, Be and B), in cosmic rays which are believed to come from the fragmentation of the heavier nuclei in passing through the small amount of matter (~ 4 gr cm^{-2}) from their source to the earth. Nuclei heavier than iron have been found in cosmic rays, but with intensities lower by a factor of 10^5 below that of iron.

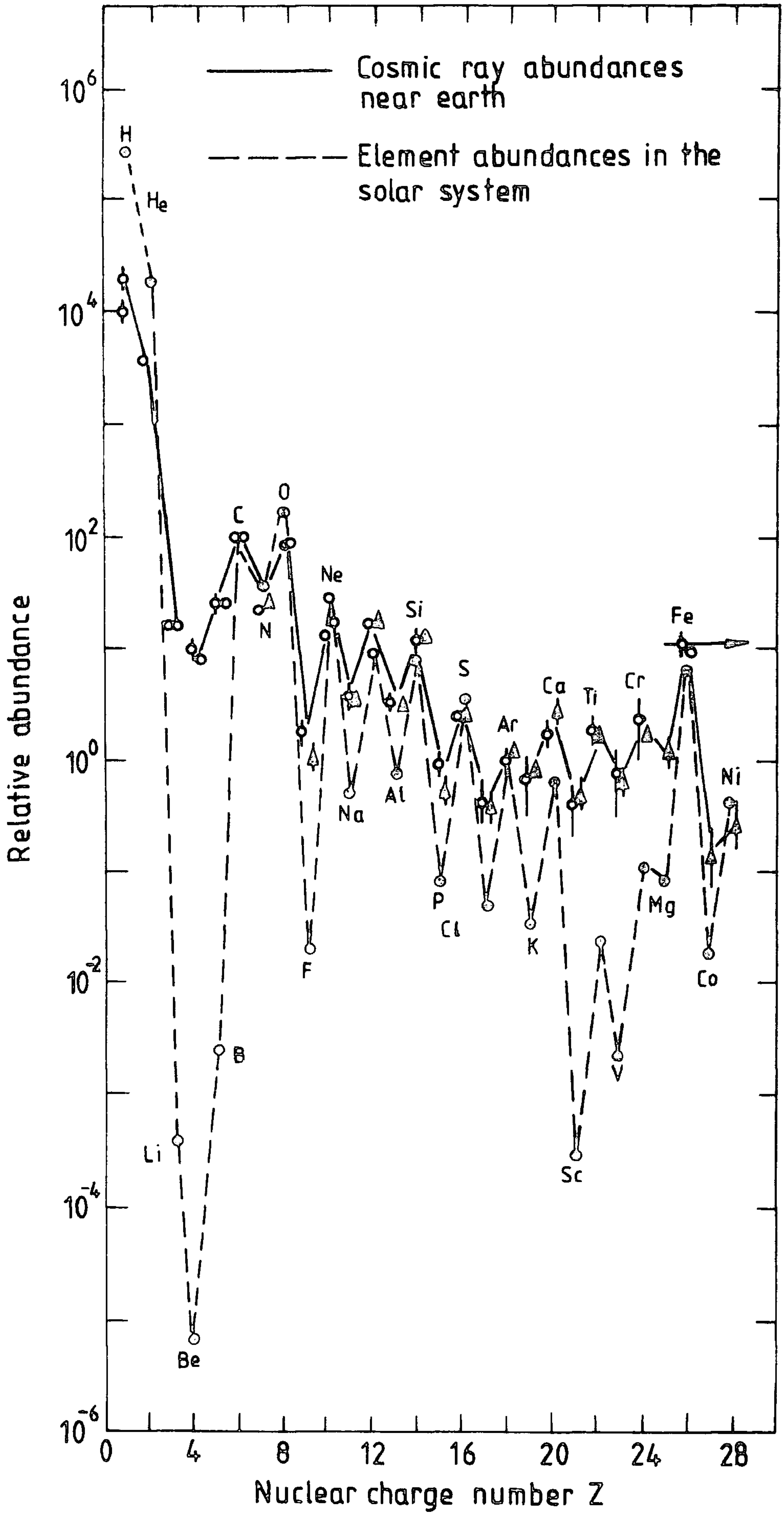

Figure 1.2 : Relative abundance of the elements from hydrogen to the iron group normalized to that of carbon (C=100) (after Meyer et al 1974).

1.5 PROPAGATION OF COSMIC RAYS THROUGH THE ATMOSPHERE - EXTENSIVE AIR SHOWERS

On passing through the earth's atmosphere, the primary cosmic rays interact with the nuclei of the air molecules to produce secondary particles. The primary protons interact, on average, every 80 gr cm^{-2} of the atmosphere and lose about 50% of their energy at each interaction. The secondary particles are mainly composed of pions and a smaller number of kaons, hyperons, and nucleons. The number of secondary particles, n, depends on the energy of the primary particles, E, and this will be adequately discussed in Chapter 7. The pions produced in the interaction exist almost equally in their three modes of π^+, π^- and π^0. The neutral pions have a lifetime, at rest, of about 10^{-16} sec and each decays into two gamma-rays which produce electron-positron pairs by means of pair production. These relativistic electrons produce further gamma rays by bremsstrahlung. These γ-rays then produce more electrons and the shower of particles resulting is known as an electromagnetic cascade. For a primary energy of around 10^{13} eV, this cascade is sufficient by large to reach sea level to produce an extensive air shower (EAS). The shower is detected by the simultaneous arrival of a large number of particles over a large area, and detectors placed at suitable points will record the shower as a coincident signal between several of the detectors.

As the energy of the primary particle increases, the number of particles in the shower and the lateral extent of the shower increase and by measuring the number of particles in a shower an estimate of the primary energy can be made.

The charged pions and kaons produced by the interactions of the primary particles can either interact with an air nucleus to produce further pions or they can decay to produce muons.

$$\pi^{\pm} \rightarrow \mu^{\pm} + e^{\pm} + V_{e}^{\pm}$$

The decay probabilities of pions and kaons are a function of their energy and zenith angle. For a given zenith angle these particles have a greater chance of interacting than of decaying as their energy increases. As the zenith angle increases, the density per unit path length decreases and hence the interaction probability decreases and more numbers of pions and kaons decay into muons. The produced muons have a high chance of reaching sea level without decay or interaction. The Muon Component of E.A.S. would be discussed in Chapter 5.

1.6 ORIGIN OF COSMIC RADIATIONS

1.6.1 Introduction

Since the discovery of the cosmic radiation the question of the origin of these high energy particles and mechanism in which they are accelerated to such high energies has been an astrophysical problem of considerable interest.

The early workers advocated this view that cosmic rays are of solar origin and are kept relatively near the sun by the action of magnetic fields(Teller,1948). Fermi in 1949 was the first to produce an explanation for how cosmic rays are accelerated to high energies and postulated that cosmic rays are repeatedly scattered against the clouds of magnetic plasma that move at about 30 km per sec in interstellar space. His theory, of course, does not agree with more recently observed properties of cosmic rays. There are three different views to investigate concerning the origin of cosmic rays. The first one assumes that the particles originate in our own galaxy and that they are largely confined to it by magnetic fields. In support of this idea, it appears that there are enough sources within the galaxy capable of producing sufficient energy and necessary energetic particles. The second and rather extreme view is to regard the bulk of the cosmic rays as being of extragalactic origin. The third view supports an idea intermediate between 'all galactic' and 'all extragalactic' the possibility of a mixed origin (e.g. Morrison 1961). As far as 'all galactic' sources are concerned, the supernovae and their subsequent remnants, pulsars and more recently white dwarfs, are strong contenders.

1.6.2 Supernova Sources

An extremely attractive suggestion that was made some 25 years ago is that both the nuclear and electronic components of cosmic rays are produced and accelerated in supernova explosions. With 10^{50}- 10^{51} engs emitted as cosmic rays per supernova and one supernova occurring in the Galaxy every 30 years, the injection rate would be $10^{54.5}$ - $10^{55.5}$ engs per 10^{6} years. Cosmic rays have an energy density of about 10^{-12} eng/cm^{3} in the Galactic volume of 10^{67} cm^{3} ; and are to be replaced every million years. The energy needed is 10^{55} engs/10^{6} years in reasonable agreement with the available power. After the initial supernova explosion a shock wave goes out from the core reaching extreme relativistic velocities in the tenuous outer layers of the star. This shock accelerates particles to energies ranging from 10^8 to 10^{21} eV, consistent with the observed power law energy spectrum, (Section 1.3). During the explosion fluxes of neutrons are generated and nuclides extending into ultra-heavy regions may be synthesized by rapid neutron capture. The over-abundance of extremely heavy cosmic rays and the possible existence of trans-uramic cosmic rays thus provide support for the supernova model. Against this positive evidence for supernova sources we must weigh a very unattractive feature. With one supernova explosion detonating every 30 years for the dispersal of cosmic rays from the remnant, at any moment, there are only about 30 supernova in the Galaxy contributing to the local cosmic ray intensity. We also note that the thickness of the disc is less than a thirtieth of the diameter, so that effectively less than one supernova would be contributing to the intensity. Under these circumstances, it is hard to understand the observed high degree of isotropy and constancy in time of the nuclear component.

1.6.3 Cosmic Rays From Pulsars ?

Pulsar observations in the last decade have come out in support of theoretical work on the acceleration of high energy particles near rotating magnetized bodies such as neutron stars. Here the gravitational energy of the collapse is stored as rotational energy of the neutron star. With masses typically comparable to that of the sun, and rotational periods of 10^{-2} sec, the rotational energy that is stored in a neutron star with a radius of 10^{6} cm is about 10^{50} ergs. Intense surface fields ($\sim 10^{12}$ gauss) are believed to be generated during the collapse by the compression of the stellar magnetic field. Calculations indicate that pulsars may be able to generate the highest energy cosmic rays, beyond 10^{14} eV, but do not efficiently generate the majority of the cosmic rays which have energies of only 10^{8} - 10^{12} eV. As in the case of supernova, there are probably too few sources at any moment to generate the remarkable degree of isotropy and constancy of cosmic rays. Finally the surface of the rotating neutron star is probably nearly pure iron, and we meet difficulties in accounting for the composition of the nuclear cosmic rays unless we suppose that gas of the right composition, originating outside of the neutron star, is accelerated in the pulsar field.

However, the absence of any detectable anisotropy in arrival direction of cosmic rays,up to about 5.10^{13} eV, and also the mystery of why the cosmic rays have such a smooth spectrum, suggest that the sources are many and are widely distributed in the galaxy. Indeed, there is no reason to exclude, novas, flare stars, magnetic stars and other active objects, that many also contribute to the flux of cosmic rays in various energy bands. If they do, then we can expect compositional differences to become evident once a sufficiently broad range of energies has been studied.

1.7 SUMMARY

Although many elaborate and well designed accelerators are in operation or under construction, which enable controlled experiments with energies up to about 10^{12} eV or more to be carried out, cosmic rays will be in use for many years to come simply because of its cheap high energy beam of particles.

As mentioned earlier, there are two aspects of cosmic ray studies which physicists are interested in ; nuclear physics and astrophysics. The study of the primary and secondary radiations provides a good opportunity for nuclear physicists to investigate the characteristics of particles and the nature of high energy interactions. For astrophysicists, undoubtedly the most fascinating problem is the origin of cosmic rays and the mechanism in which these particles are accelerated to such high energies as seen in air showers.

CHAPTER TWO

DURHAM EXTENSIVE AIR SHOWER ARRAY AND HADRON FLASH TUBE CHAMBER

2.1 INTRODUCTION

A small air shower array of radius 60m has been constructed around the Physics department of Durham University. The array generally responds to the showers between 10^4 to 5.10^6 particles in size.

In addition to the array, there is a large flash tube chamber (approximately 11000 tubes), situated near to the centre of the array, which by supplying useful information on muonic and hadronic components of extensive air showers provides a good opportunity for cosmic ray studies in Durham. The array comprises of 14 electron density sampling scintillation detectors which seven of them are for fast timing and density measurements while the other seven are only used for shower density measurements. Figure 1 shows the disposition of the scintillation detectors and their relative position with respect to the Physics department and the hadron flash tube chamber.

The areas and exact coordinates of the detectors are shown in Table 2.1, using the centre of detector C as the origin and the line which goes through detector C and detector 52 as the y axis.

Table 2.1 shows that there are four different types of detectors in use, which are grouped according to their areas. The variation in detector area (.75 m^2, 1 m^2, 1.6 m^2, 2.0 m^2) is mainly due to availability. Each detector is generally

Detector	C	Flash Tube Chamber H	11	13	31	33	51	53	12	42	61	62	32	41	52
x Coordinate (m)	0	-12.9	-12.1	-41.8	13.2	45.1	1.0	- 3.6	-22.9	39.1	- 8.7	-43.1	25.2	23.3	0
y Coordinate (m)	0	-1.30	- 6.0	26.3	4.0	14.9	-27.1	-57.3	8.3	-33.1	- 5.8	-18.3	8.3	-16.6	-16.2
z Coordinate (m)	0	-12.2	- 4.9	-13.3	0.20	0.20	0.20	- 9.3	-13.1	- 9.1	- 4.9	-10.3	0.5	-11.3	0.5
Area (m^2)	0.75	2.95	2.0	2.0	2.0	2.0	2.0	2.0	1.60	1.60	1.60	1.60	1.0	1.0	1.0

<u>TABLE 2.1</u> : Coordinates and areas of all detectors in the array; z Coordinate of flash tube chamber refers to the bottom of the chamber.

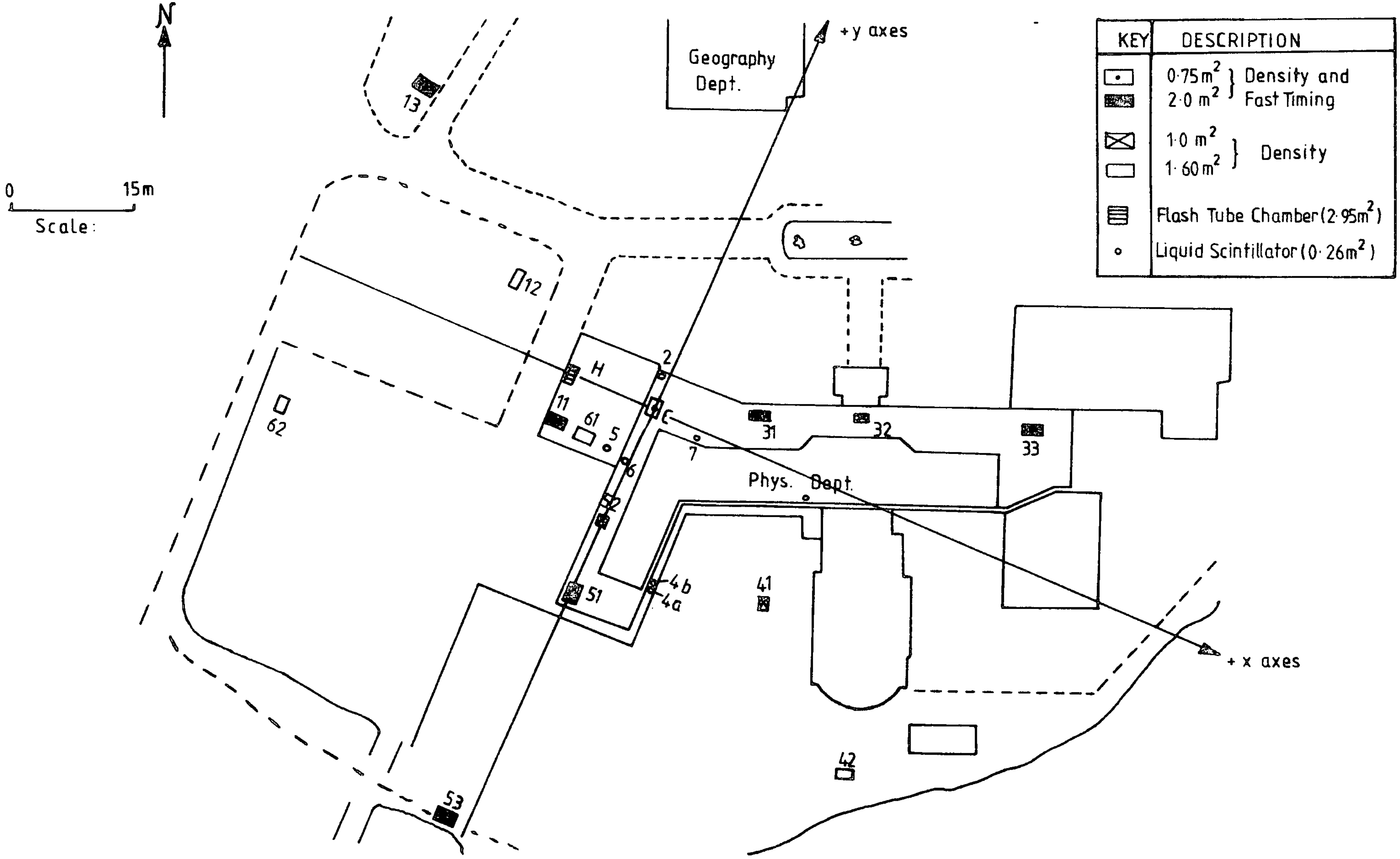

Figure 2.1 : Scale diagram of the Durham Extensive Air Shower Array.

viewed by four photomultiplier tubes for particle density measurements, and in the case of the central detector and 2.0 m^2 detectors an additional fast photomultiplier for timing measurements which will enable the air shower arrival direction to be determined.

The array has a triangular geometry and it has been tried, wherever possible, to put detectors with equal areas, equidistant from the centre of the array. Each of the various types of detector have been constructed in slightly different ways to take full advantage of their size or shape and will be discussed separately.

2.1.1 The Central Detector, C (0.75 m^2)

The central detector is unique in the array in the sense that it is used to define the spatial and temporal origin of the array. As is shown in Figure 2a, it consists of two identical halves where each half is made of a 5 cm thick slab of NE1024 plastic scintillator. There are three photomultiplier tubes attached to each half, two of them being Philips 53AVP and the other one being a Philips 56AVP, fast tube. The latter supplies a time marker to which all of the other timing pulses are referred. This detector has a total area of 0.75 m^2 and is placed on the roof of the Physics department (Fig. 2.1).

2.1.2 The 2.0 m^2 Detectors

There are six of these detectors in the array and they are the most important ones, because apart from detector C, they are the only detectors that send timing measurement pulses to the laboratory and also are used as triggers to establish an event. To preserve symmetry and uniformity, three of these detectors (13,33,53) are placed on the boundary of the array forming an outer equilateral triangle, while the other three (11,31,51) also have a triangular arrangement but near to the centre. Each of these detectors consists of a 2.5 cm thick slab of NE110 plastic scintillator with an area of 2 m^2 (2.0 m x 1.0 m). Each is viewed by a total of five photomultipliers, four of which (EMI 9579B, 5" in diameter) for particle density measurements and the other one (Philips 56AVP 2" in diameter) is used for timing measurements. Figure 2d shows the size and the relative position of tubes on this type of detector.

2.1.3 The 1.60 m^2 Detectors

These detectors of which there are four of them in the array, consist of four identical, individually light proofed quarter each of an area 0.4 m^2. They are made of the same material as the central detector (NE 102 A, plastic scintillator) and each quarter is viewed by a Philips 53AVP photomultiplier tube through a perspex light guide for particle density measurement. As will be discussed later, each quarter operates independent of the other three, and a four input mixer-amplifier adds up the pulses from all quarters and produces a single output from the whole detector. Figure 2b shows the position of the tubes on each quarter.

2.1.4 The 1.0 m^2 Detectors

Three detectors of this type exist in the array and like the 1.60 m^2 detectors consist of four individually light proofed quarters each of an area 0.25 m^2 (50 cm x 50 cm). One photomultiplier tube is viewing each quarter but unlike

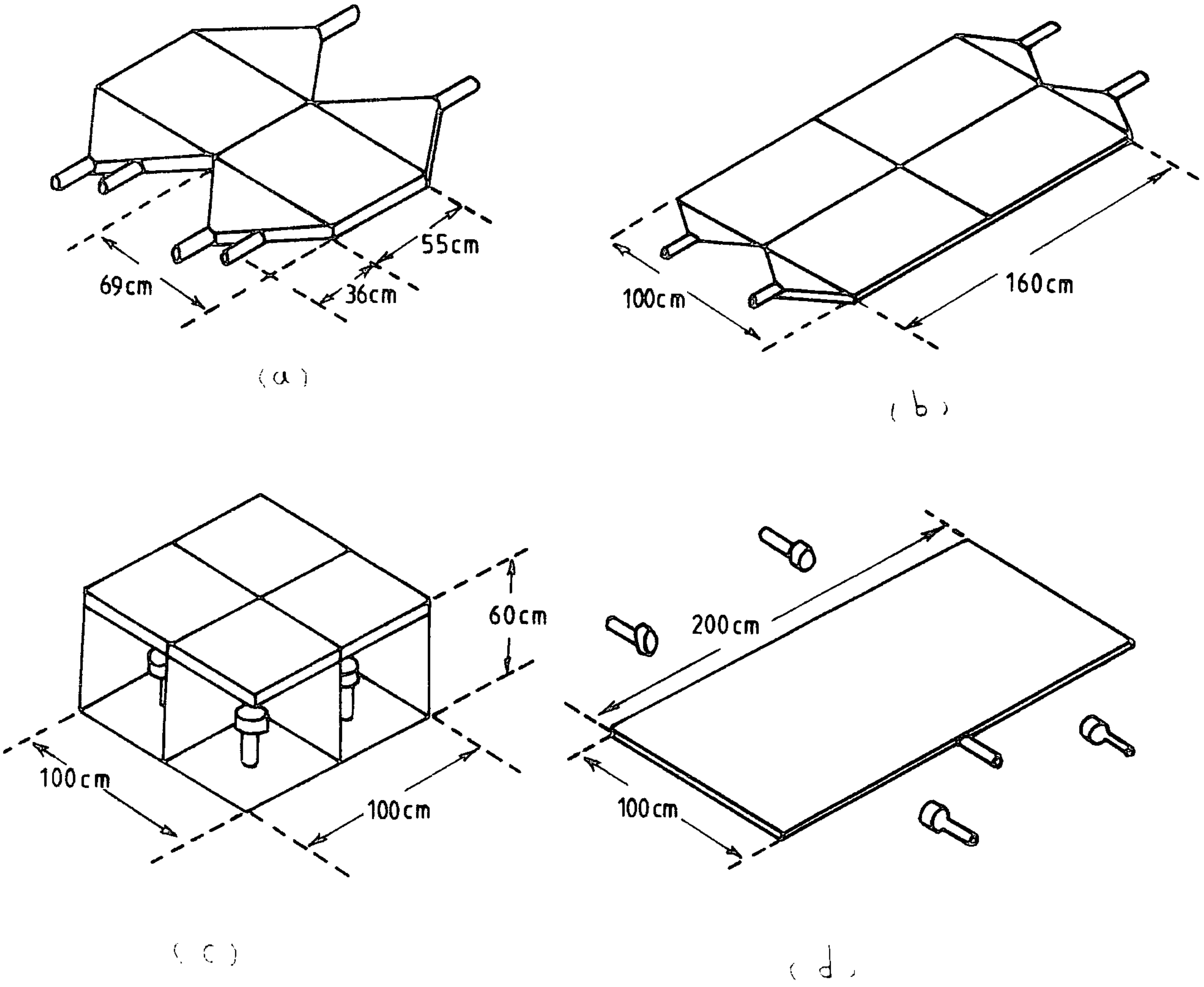

Figure 2.2 : Design of plastic scintillators used in the array

(a): The central detector (0.75 m^2)

(b): A 1.6 m^2 detector

(c): A 1.0 m^2 detector

(d): A 2.0 m^2 detector

the other detectors, the tube views the broad face of the scintillator and not the edge of it, (Figure 2c). Pulses from independent quarters are summed in a mixer-amplifier at the detector and are sent to the laboratory via a 50 Ω cable.

2.2 ESTABLISHMENT OF AN EXTENSIVE AIR SHOWER EVENT

When a number of particles in an air shower, (mainly electrons) hit a piece of scintillator in the array, they dissipate their energy in ionisation and excitation of molecules in their passage through the phosphor. A fraction of this energy is converted into photons which are radiated in all directions. The photomultiplier tubes which are viewing the same piece convert the output light of the scintillator into electrical signals. These electrical pulses (output of 4 tubes) are summed and amplified in a head unit and relayed to the laboratory, via a 50 Ω coaxial cable. At this stage, after discriminating and shaping the pulses from all detectors, events are recorded on an appropriate recording system to be analysed and interpreted later (either on photographic films or magnetic discs).

2.3 PHOTOMULTIPLIER TUBES IN THE ARRAY

There are three different types of photomultiplier tubes in the array and as it has already been stated, they are to convert the output light of scintillators into electrical signals. Two types, EMI 9579B with a 5" diameter photocathode and Philips 53AVP with a 2" diameter cathode, are used for density measurements, while the other type, Philips 56AVP with a 2" photocathode for fast timing.

All the tubes run on a negative E.H.T. and the output of density measuring tubes are negative with an exponential decay and time constant of 20 μsec. The output of fast tubes are also negative pulses of 5 nsec (f.w.h.m.). The base circuits of different types of photomultiplier tubes are shown in Figure 3. It is worth mentioning that the linearity of response, gain variation and temperature dependence of tubes have been fully investigated before constructing the array, (for further information see A. Smith, Ph.D Thesis 1976, Chapter 4).

2.4 E.H.T. SUPPLY UNITS AND E.H.T. DISTRIBUTION BOARDS

E.H.T. supply units send 2.4 kV and 2.7 kV, negative high voltages, to the slow and fast tubes respectively. Since none of the tubes work exactlv at the same voltage, it is necessary to distribute the applied voltages (2.4 kV and 2.7 kV) appropriately amongst the tubes and this has been done by using a chain of resistors and an adjustable potentiometer. As it is clear from Figure 4, each distribution board consists of five or six resistor chains, four of which serve slow tubes, and the rest are used for the fast tubes, if there are any at the detector.

2.5 THE DETECTOR HEAD AMPLIFIERS

The output pulses from each of the four density measuring phototubes are summed in a mixer-amplifier at the detector. The amplifier (Figure 5) essentially consists of four emitter followers whose outputs are summed and amplified in a μA702C - differential amplifier integrated circuit. The output of this device is then fed into another emitter-follower circuit such that the now positive signal can be

Base circuit for EMI 9579B P.M.T.

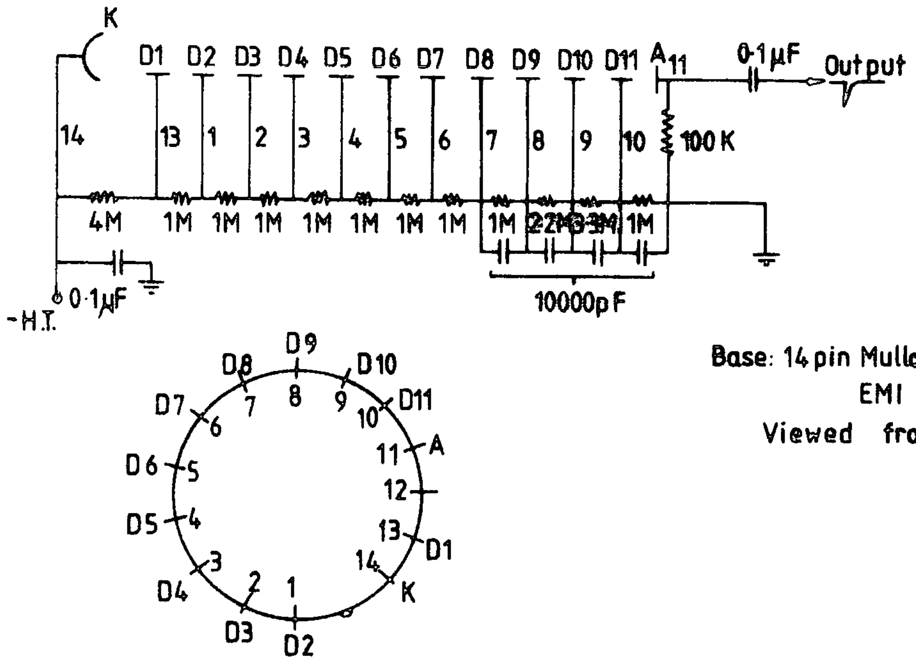

Base: 14 pin Mullard FE 1001
EMI B14A
Viewed from beneath

Base circuit for PHILIPS 53 AVP P.M.T.

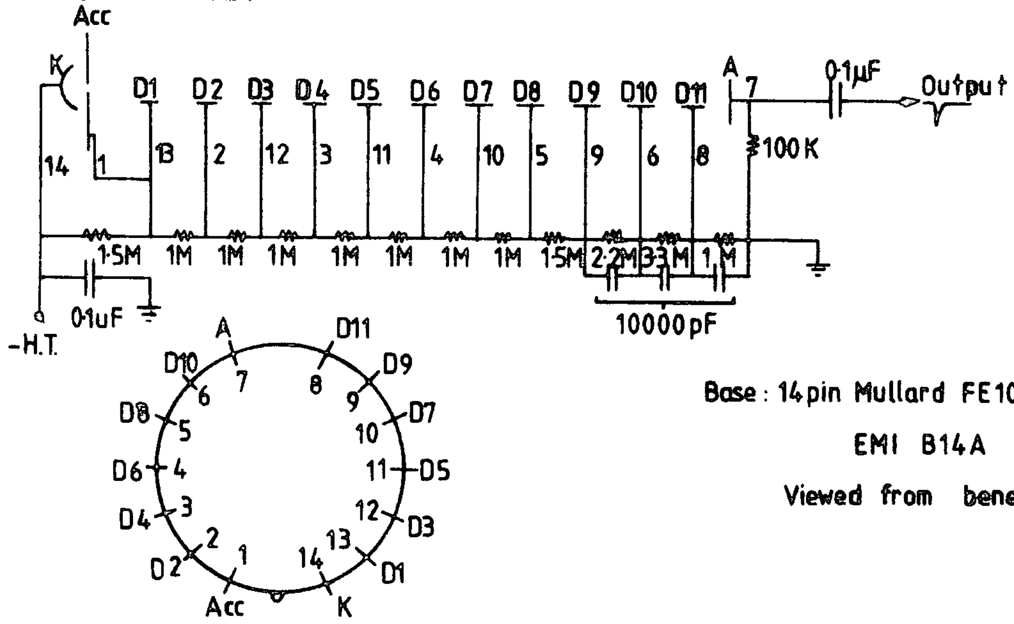

Base: 14 pin Mullard FE1001
EMI B14A
Viewed from beneath

Base circuit for PHILIPS 56 AVP P.M.T.

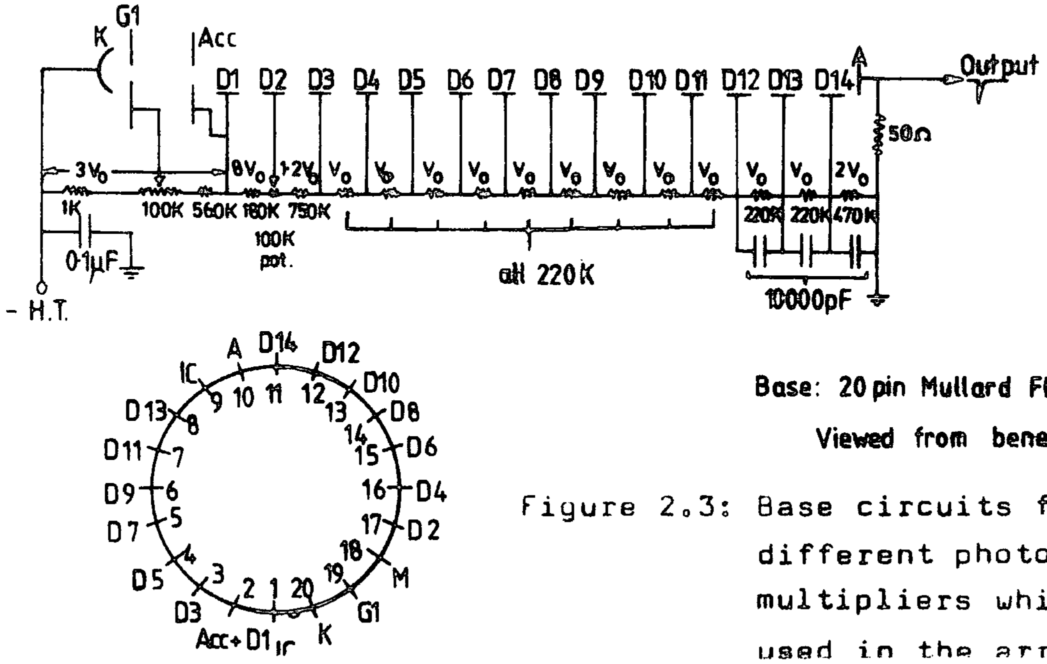

Base: 20 pin Mullard FE 1003
Viewed from beneath

Figure 2.3: Base circuits for different photomultipliers which are used in the array.

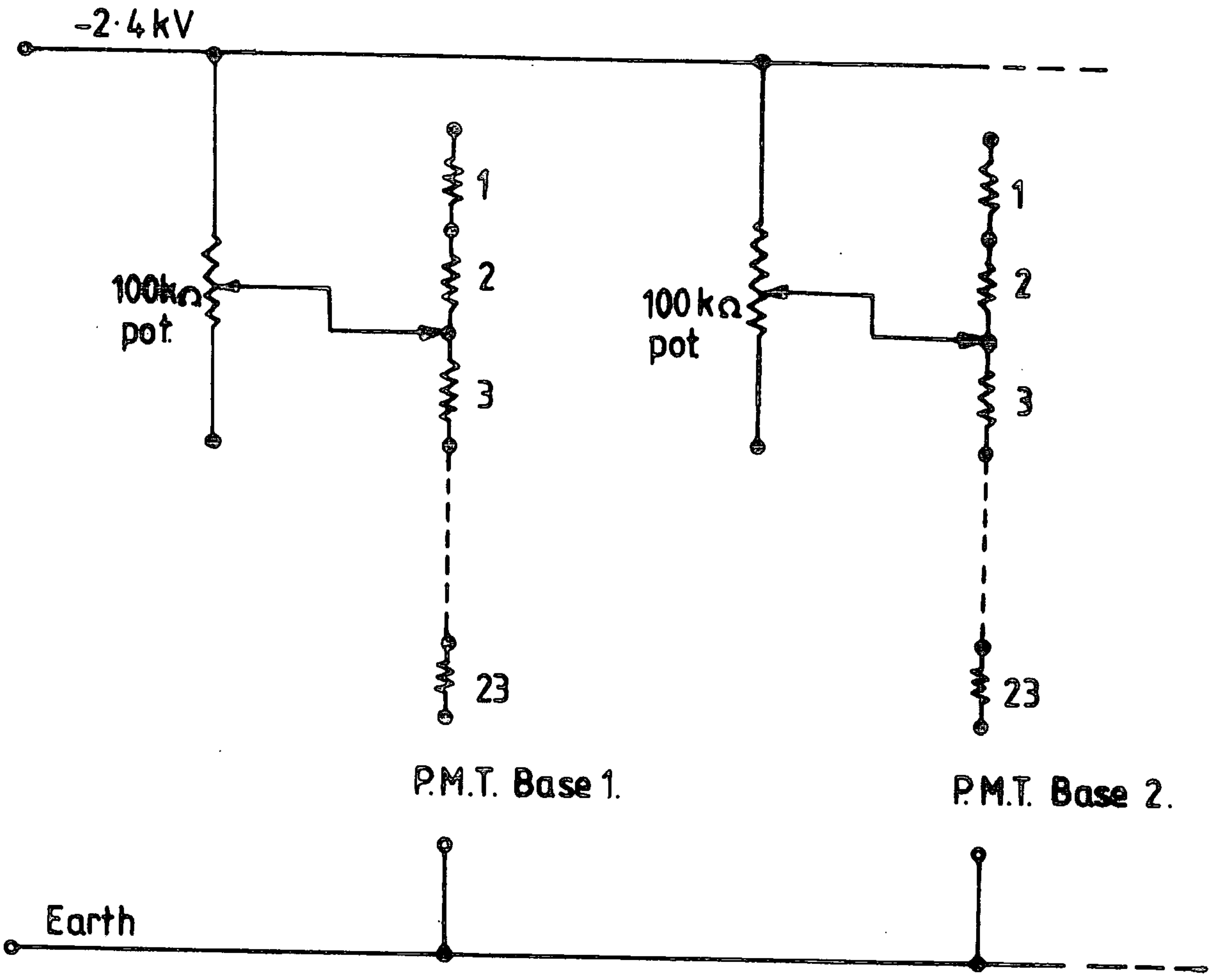

Figure 2.4 : Sections of the four E.H.T. distributions at each detector. All resistors are 100 K Ω.

driven down the long lengths of the cable into the laboratory. An established 24 volt, 3A power supply unit in the laboratory supplies the power to all of the amplifiers in the array.

2.6 CALIBRATION TELESCOPE

The telescope is used for calibrating and checking the density measuring tubes and consists of a slab of NE 102A plastic scintillator (23 cm x 23 cm x 3 cm), viewed by two Philips 53AVP photomultiplier tubes in a light tight duraluminium box.

The interesting point about the telescope is that the same cables which take E.H.T. to the tubes in the telescope carry back the output pulses from the tubes to the laboratory and this has been done by using two charge sensitive amplifiers (Figure 6). The tubes in the telescope run on a positive E.H.T. ($\sim$ 2000 V).

2.7 CALIBRATION OF THE DENSITY MEASURING DETECTORS

According to what has been said earlier, it is clear that each detector has got its own quality, design and dimensions and therefore its own response towards cosmic ray particles. Thus each detector must be calibrated individually. To start with, by using the calibration telescope, a map of each detector's response to a single particle has been prepared. Figure 7 shows these maps and also indicates a point on the scintillator where calibration should be done. In practice, we put the telescope on the calibration mark on the scintillator, trying to form a two-fold coincidence between detector and telescope and get a genuine cosmic ray particle spectrum on the pulse height analyser. The output pulses from two tubes

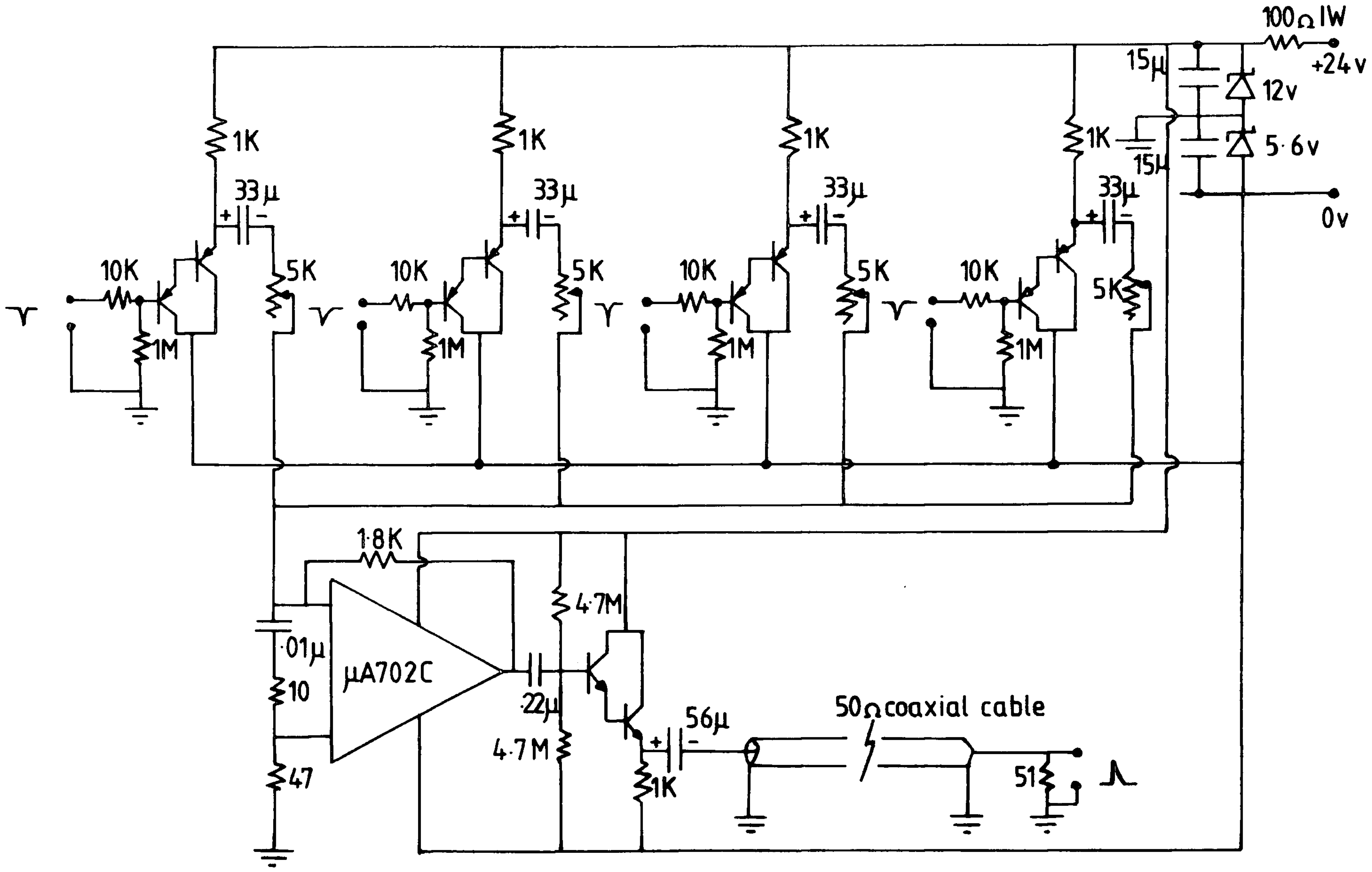

Figure 2.5 : Four input gain five mixer-amplifier in each head unit (Transistors: PNP ZTX301)

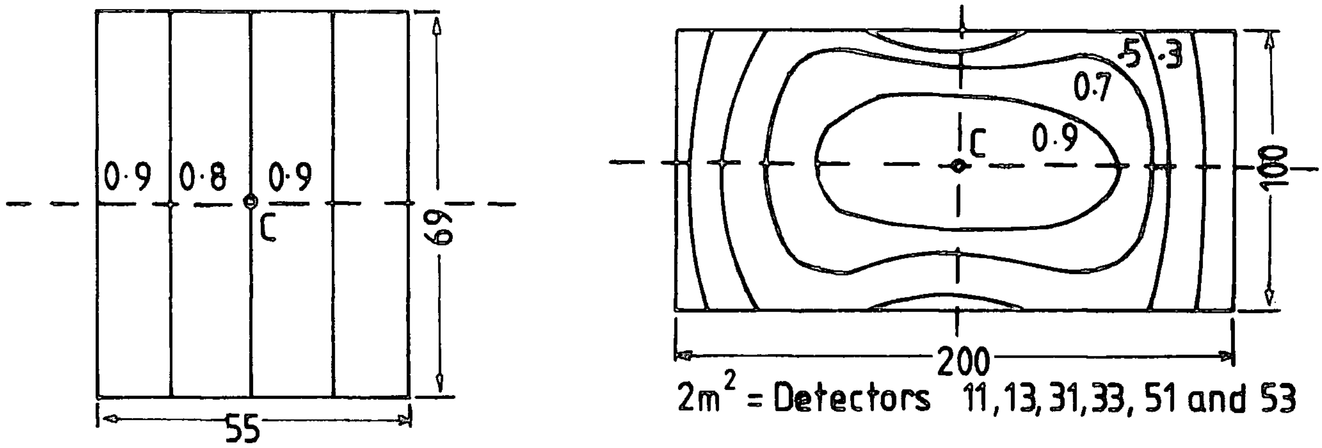

2 × 0·38 m^2 Central Detector

2m^2 = Detectors 11, 13, 31, 33, 51 and 53

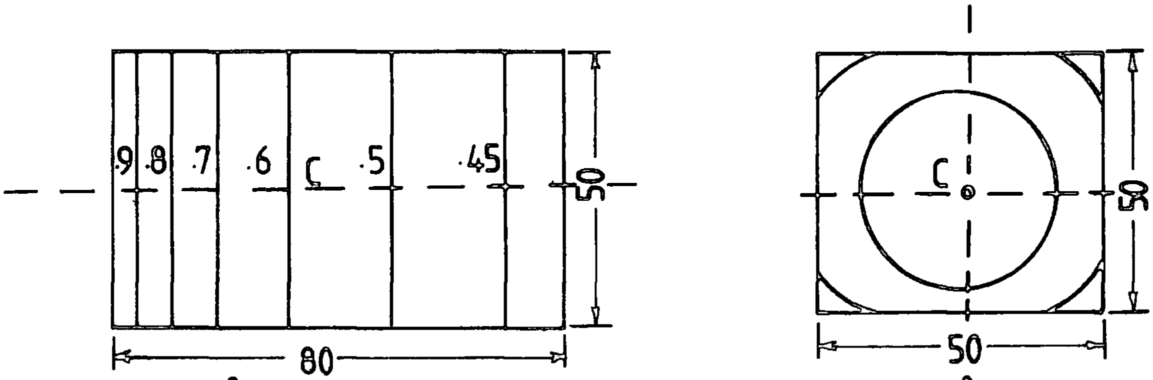

4 × 0·4 m^2 = Detectors 12, 42, 61, and 62

4 × 0·25 m^2 = Detectors 32, 41, 52

Figure 2.7 : Pulse height contour map of the array's scintillators where C represents the calibration points.

of the telescope go through two NE4675 charge sensitive amplifiers (Figure 6) in the laboratory to be amplified and discriminated above a pre-selected threshold level. The logic output pulses of the charge sensitive amplifiers go to a simple coincidence unit whose output opens a gate on the pulse height analyser, letting cosmic ray pulses from the air shower detector be stored in the pulse height analyser. After fifteen minutes or so, a sufficiently accurate pulse height distribution from the region of the detector selected by the telescope will build up on the pulse height analyser display cathode ray tube. By adjusting the E.H.T. to the tubes of the detector, it is possible to fix the position of the peak near enough to the desired calibration value. After a few attempts, when the peak is within ± 2% of the calibration value, that particular phototube is said to be calibrated. Figure 2.8 shows a block diagram ofthe electronic recording system when extensive air showers are detected.

2.8 NEON FLASH TUBE CHAMBER

2.8.1 Introduction

The flash tube chamber is a large visual detector mainly used to observe the track of cosmic ray particles. In the experiment, the chamber is used to study the muon density and consequently the lateral distribution of muons in E.A.S. (Chapter 7). Hadrons interacting in the lead or iron absorbers on top of the chamber, enable a study to be made of the energy and lateral distribution of hadrons in EAS (Chapters 5 and 6). Unlike bubble chambers or spark chambers, which are often used in accelerator experiments, flash tubes, since their introduction

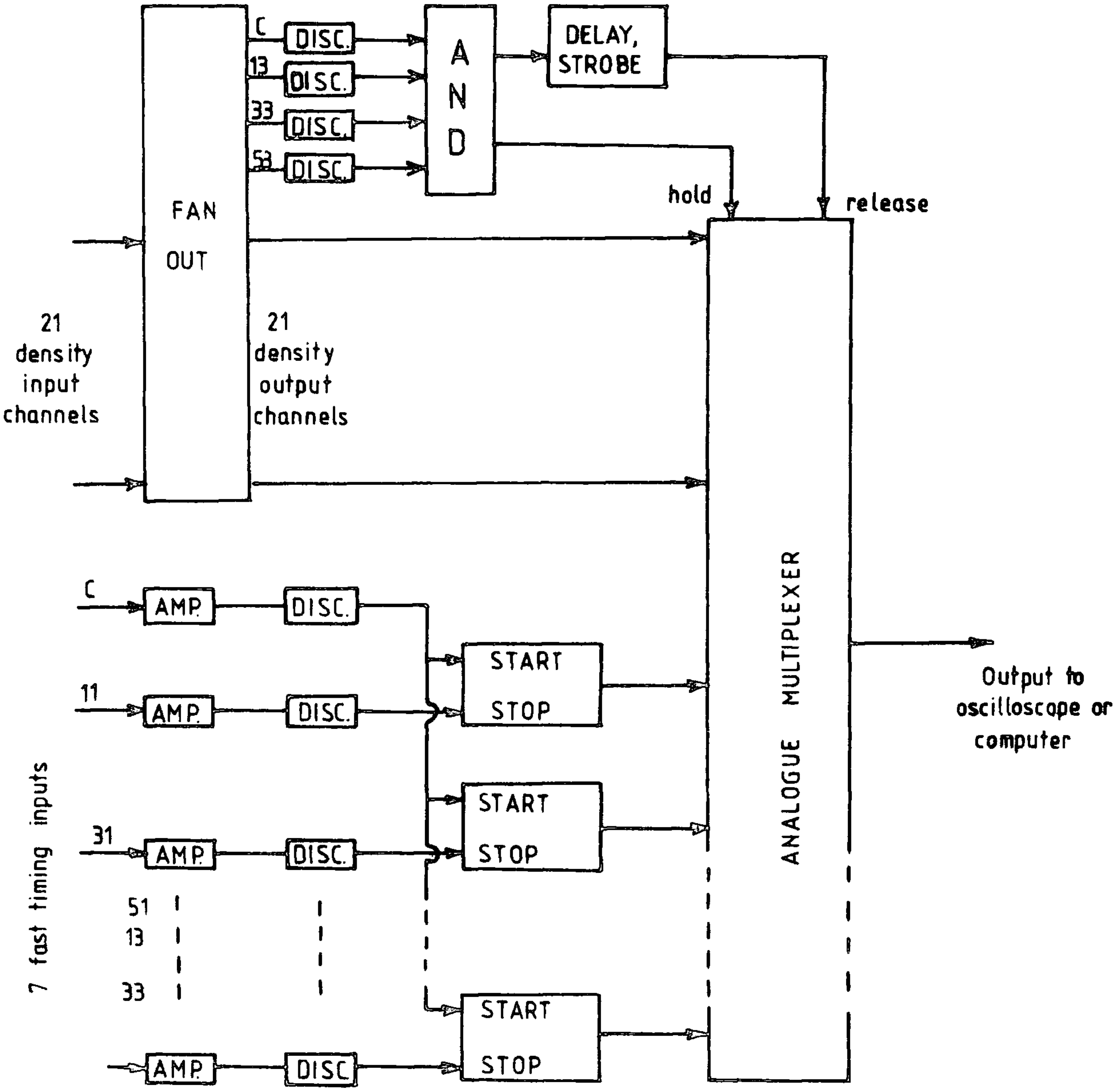

Figure 2.8 : Block diagram of the electronic selection and recording system.

in 1955 by Conversi and Gozzini have been used in cosmic ray experiments. One of the main reasons for this is that flash tubes are made of glass which is a relatively strong material, so they have a long life and are an ideal detector for long experiments, and also their characteristics remain unchanged in a wide range of temperature, pressure and humidity.

2.9 CHARACTERISTICS AND PROPERTIES OF FLASH TUBES

2.9.1 Discharge Mechanism

A flash tube consists of a sealed glass tube normally filled with a low pressure mixture of noble gases, positioned between two parallel plate electrodes. On the passing of an ionizing particle through the tube, the plates are pulsed by an electric field. The electrons left by the primary ionizing particle are accelerated towards the anode plate and by doing so gain sufficient energy to produce secondary electrons via collisions with gas atoms. The avalanches generated, produce luminous discharges which may be photographed, or digitized. Information may be obtained from probes placed on the tube windows. It is understood that the electrons which are produced initially are responsible for the discharge and the secondary electrons released by collision of metastables are usually small in number and can be neglected as far as basic discharge mechanism is concerned. Although the actual numbers will depend on gas composition and pressure, it is normal to expect up to 30 electrons to be produced in a flash tube by the passage of an ionizing particle through it.

2.9.2 Efficiency

The most important and convenient parameter specifying the performance of a flash tube is its efficiency, or the probability that it will discharge after the passage of an ionizing particle through it.

Because of inherent insensitive material present in a flash tube array, two efficiency parameters have been defined. These are the internal efficiency, η , which is defined as the probability of a tube flashing if an ionizing particle passes through the gas of the tube, and the layer efficiency η_L, which represents the probability of a tube flashing and hence registering the passage of an ionizing particle through a layer of tubes.

The layer efficiencies of tubes are normally measured experimentally from which the internal efficiencies can be obtained using the relation

$$\eta = \eta_L \frac{D}{d}$$

where D is the distance between tube centres and d is the internal diameter of the tubes (in the case of our experiment $\eta = \frac{1.81}{1.58} \eta_L = 1.14 \eta_L$). The efficiency of flash tubes is a function of many factors and these have been studied by many authors. Factors include high voltage pulse characteristics, such as magnitude, rise time, width and delay, gas mixtures, temperature and spurious flashing rates.

2.9.3 Sensitive Time

Another important flash tube parameter is the sensitive time, t_d. This is defined as the time delay

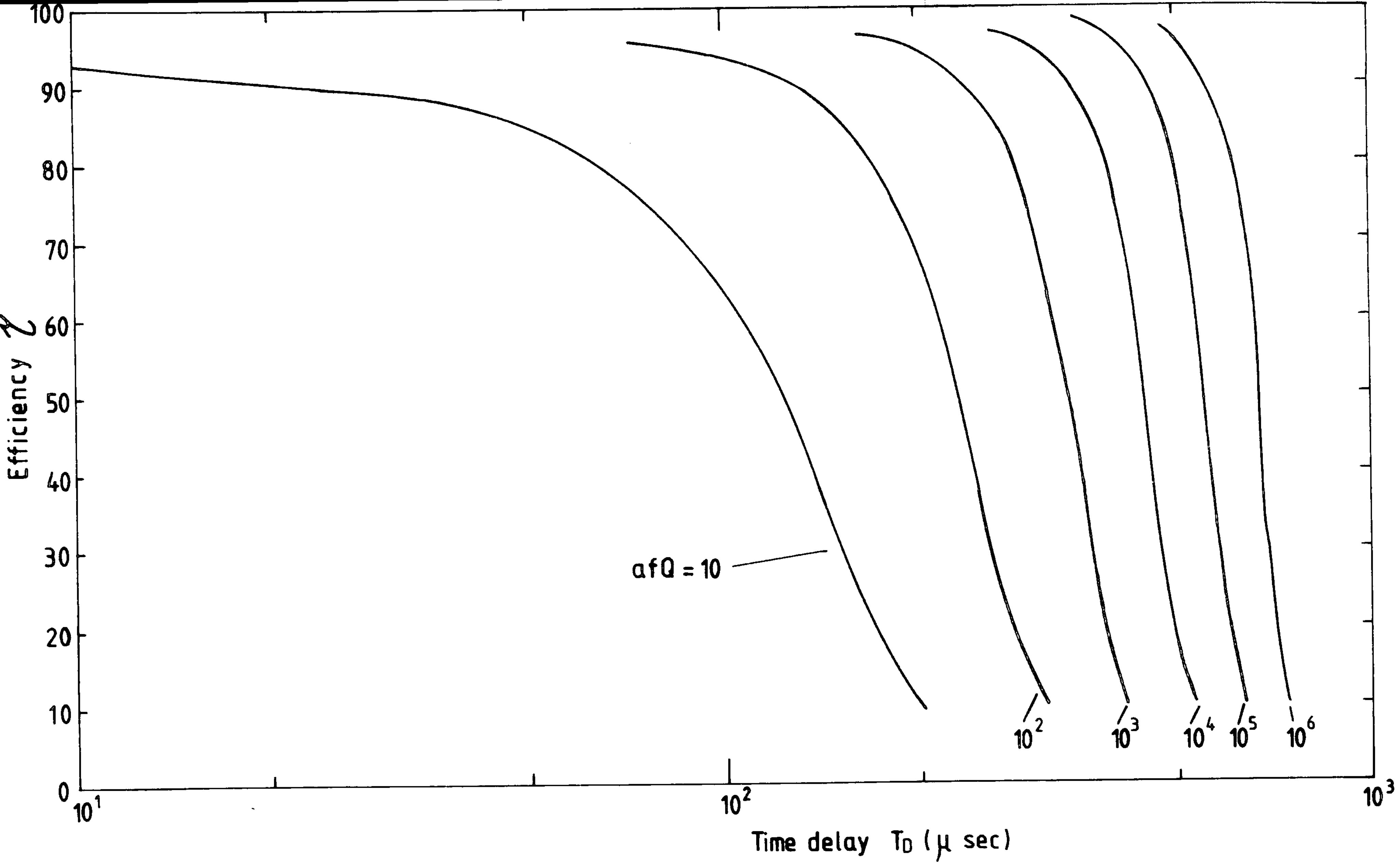

Figure 2.9 : Expected variation of the internal efficiency of the flash tubes with time delay, afq = 10 corresponds to relativistic charge e particles traversing a tube.

between the passage of an ionizing particle and the application of the electric field such that the internal efficiency of the flash tubes falls to 50%. A considerable amount of theoretical work has been done by several authors on this topic, notably by Lloyd (1960). He set up diffusion equations for the electrons produced and solved them to find the probability that a discharge would take place if an electric field were applied t_d μ sec after the passage of the ionizing particle. Lloyd found that the probability of a discharge occurring (internal efficiency) can be expressed as a function of $\frac{Dt_d}{a^2}$ (where D is diffusion coefficient of thermal electrons and a is the internal radius of the tube). The efficiency depends on a f q (where f is the probability that a single electron produces an avalanche and q is the probability per unit track length of primary particle producing an electron-ion pair). Using the calculations of Lloyd, the internal efficiency varia tion has been calculated (for the tubes used in the chamber) as a function of time delay, and is shown in Figure 2.9.

2.10 CONSTRUCTION OF FLASH TUBE CHAMBER

A scale diagram of the flash tube chamber can be seen in Figures 2.10a and 2.10b (front and side views). A total of 10478 flash tubes are used in the chamber. These are cylindrical, soda glass filled with neon gas (98%) and helium (2%) to a pressure of 60 cm Hg. Each tube is 2 metres long, of mean internal diameter 1.58 cms and external diameter 1.78 cms. Alternate layers contain 84 and 85 tubes and the tube positions are staggered with respect to the layers immediately above and below. Each tube is covered with black polythene sleeving to inhibit light transfer to neighbouring tubes. Between every other layer of flash tubes, there is an aluminium electrode, 0.122 cms thick, 3.3 cms apart. In the sections F2 and F3 (Figure 2.9) the electrodes cover an area of 2.95 m^2 while in the sections F1a, F1b, F4a and F4b are shorter in depth by 30 cms, and cover an area of 2.48 m^2.

The chamber from top to bottom comprises of 3 large liquid scintillations, (M, N and S), situated on the roof of the chamber and could form the air shower selection system. These scintillators are each of an area 1.24 m^2, depth 15 cms and each viewed by an E.M.I. 9583B photomultiplier tube. The roof of the chamber is 15 cms of lead which absorb soft components of air showers and let more penetrating particles to be clearly studied in the chamber and also acts as a target for nuclear interactions of hadrons. Below the lead there are 8 layers of flash tubes in F1a, pushed back 15 cms with respect to the front of the main body (F2a and F2b). 15 cms of iron situated between F1a and F1b, allows electromagnetic bursts to be studied in the chamber, charge identification of the parent particle being possible in F1a. Directly below iron, and also below F3a, are three plastic scintillators each of an area 1.05 m^2 and thickness 5 cms and each viewed by five 53AVP photomultiplier tubes and one 56AVP tube. These scintillators could be used as a coincidence unit to select single penetrating particles (muons) and also could measure the number of electrons produced in the electron-photon cascades caused by a nuclear interaction in either targets. There are a further 6 layers of flash tubes in F1b and then the main body of the chamber F2a

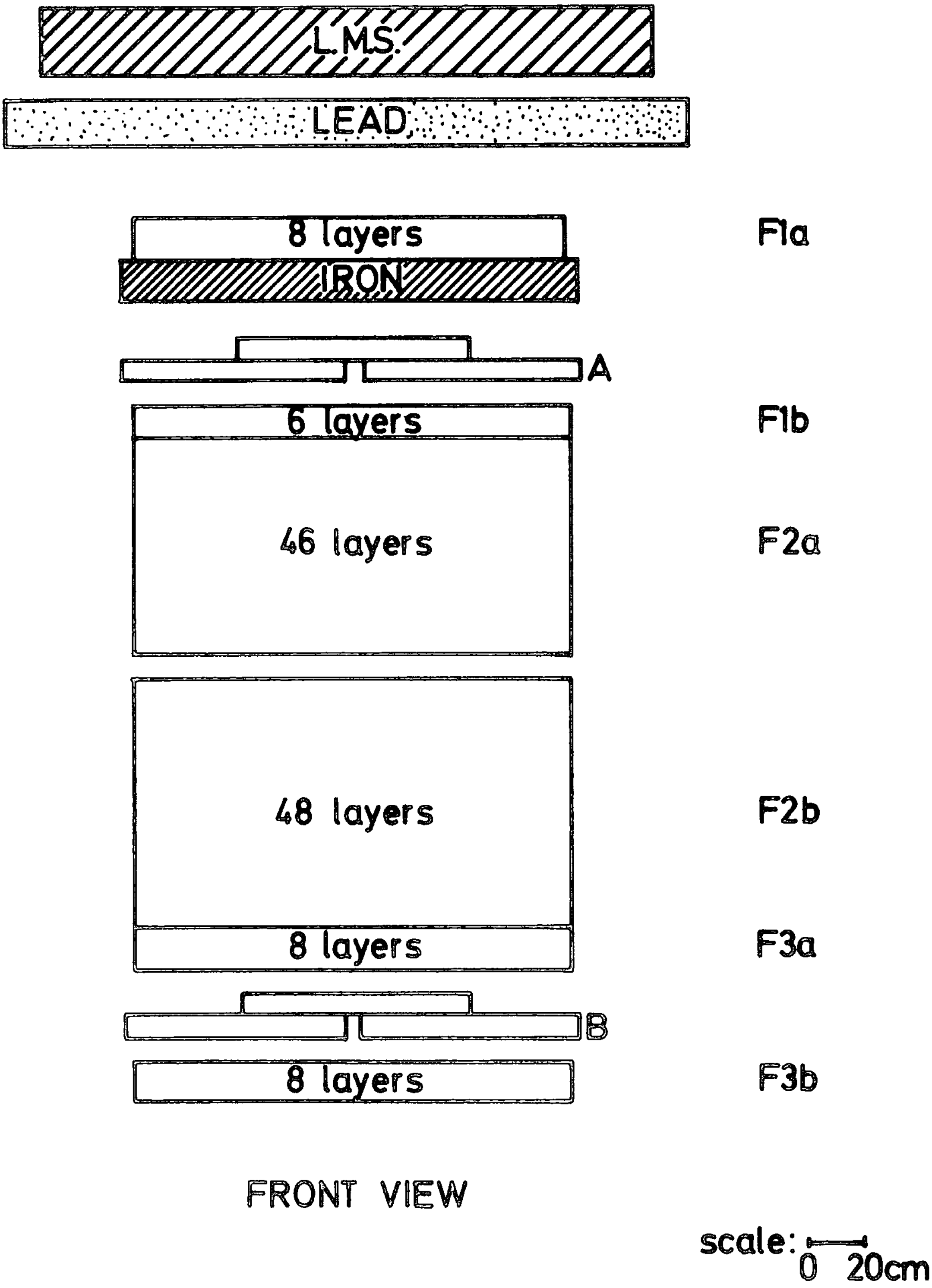

Figure 2.10a : Front view of the flash tube chamber.

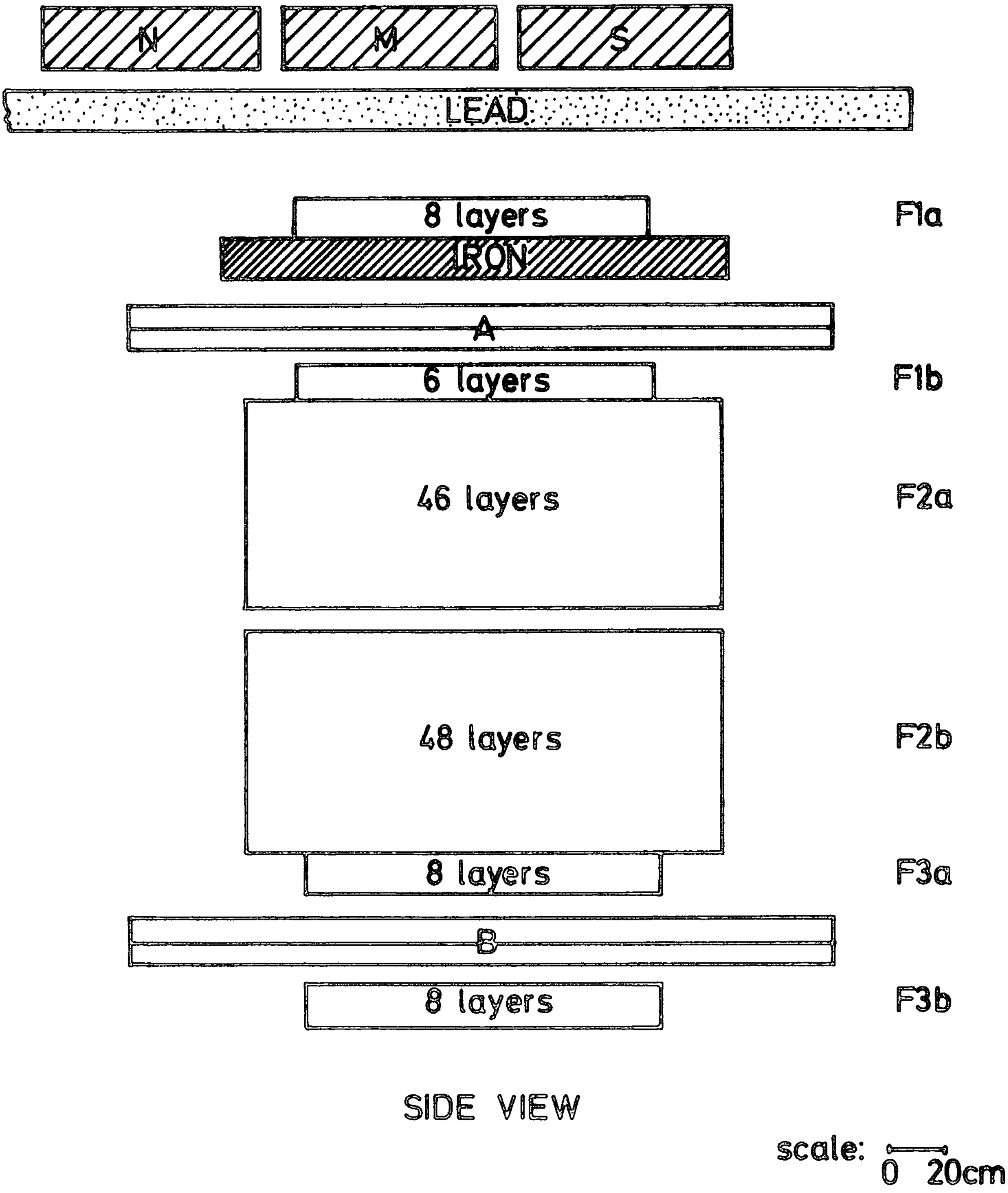

Figure 2.10b : Side view of the flash tube chamber.

(46 layers) and F2b (48 layers). Below these, there are more defining sections, F3a (8 layers) and F3b (8 layers).

The whole chamber is light-tight, allowing the use of a camera without a shutter. This means that the camera is continuously sensitive, the film being wound on by one frame after each event.

2.11 THE HIGH VOLTAGE PULSING SYSTEM

As it was mentioned earlier, when a trigger occurs, a high voltage pulse must be applied to the electrodes, creating the necessary electric field across the neon flash tubes such that in tubes containing ionization due to the recent passage of a charged particle, the neon gas will break down and a visible discharge will occur in the tube. This high voltage pulse is produced by the circuit shown in Figure 2.10a. The 5 volt trigger pulse is used to trigger a thyristor, producing an output pulse of +300 volts. This pulse is fed into a high voltage transformer, the output of which produces the trigger pulse for the "Trigatron" spark gap.

A voltage of 16 kV is applied across the main spark gap and the trigger spark causing the gap to break down largely by the production of photoelectrons.

The pulse applied to the electrodes is approximately rectangular, of height 8 kV and length 10 μ sec, and it is produced by the circuit shown in Figure 2.10b. When the main gap of the trigatron breaks down, the lumped circuit transmission line discharges, through its characteristic impedance, producing a rectangular pulse for a time $2n\sqrt{LC}$ (for n identical L, C stages). The transmission line employed has

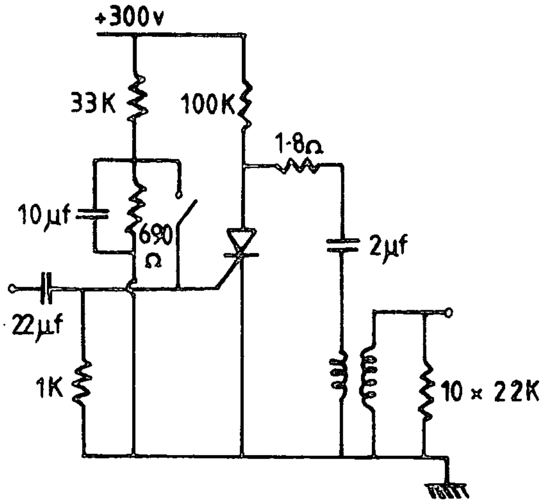

Figure 2.11a : High voltage pulsing unit.

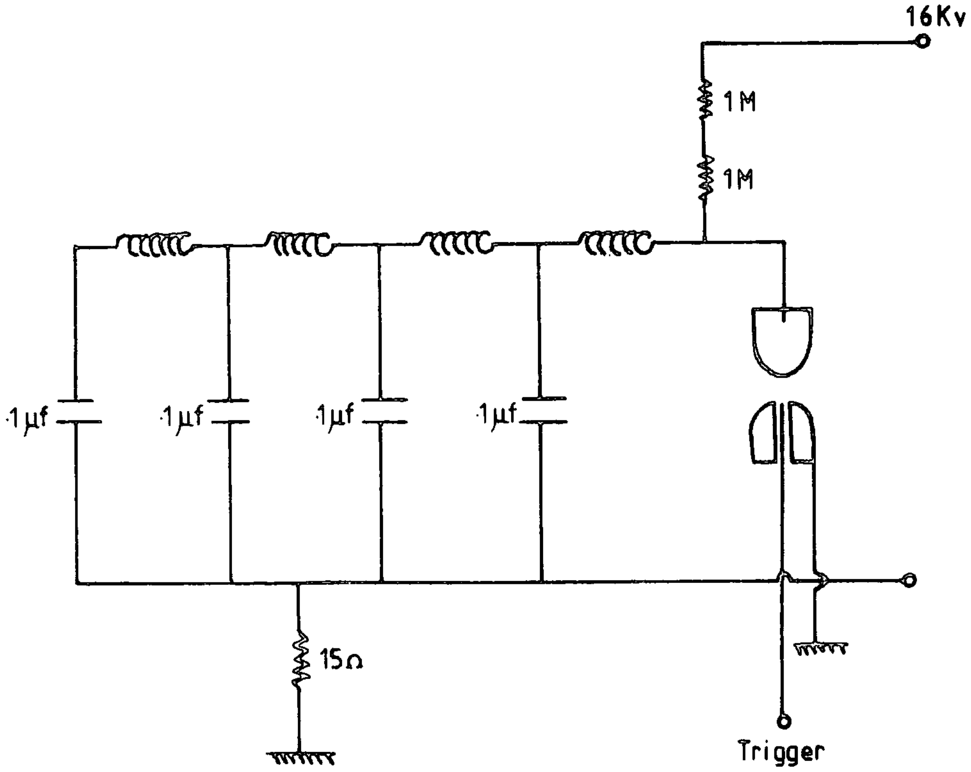

Figure 2.11b : Spark gap and delay line.

four elements, each of capacitance C = 0.1 μF and of inductance L = 22 μH. The capacity of the flash tube chamber which this unit supplies is 0.087 μF.

2.12 SUMMARY AND DISCUSSION

The Durham Extensive Air Shower Array, consists of fourteen plastic scintillators. Each scintillator has got its own advantages and disadvantages and the most important problem associated with any scintillator is its light attenuation length. This is the characteristic length of scintillator down which the light intensity decreases by e^{-1}. Consequently, for large area detectors, accounts must be taken of the non-uniformity in response.

Scintillators do have a great advantage in that they can be made in large areas relatively cheaply, and the associated electronics required to detect the emitted light is capable of long term stability.

Two sets of data are required by the array electronics for each air shower event. One set consists of 14 analogue signals representing the shower particle densities at each detector. The second set represents the timing information which consists of seven time markers which enable us to obtain the zenith and azimuthal angles of the shower front.

The second part of this chapter dealt with the flash tube chamber which, if operated in conjunction with an air shower array could provide valuable information about the muon and hadron components of air showers. It is clear from the work of Lloyd (1960) that the efficiency of flash tubes depends strongly on the charge of the primary ionizing particle. In other words, with a fixed delay time, the higher the charge of passing particle the larger the number of tubes on a particle trajectory will flash. By employing this criterion, the flash tube chamber can be used to search for fractional charge particles, quarks, (D.Cooper, 1974) and the ionizing power of highly charged particles (A. Nasri, 1977).

CHAPTER THREE

METHODS OF DETERMINING CORE POSITION, SHOWER SIZE AND ARRIVAL DIRECTIONS OF EAS

3.1 INTRODUCTION

The main problem in EAS studies is the determination of so called air shower parameters. The experimental data in EAS usually is a number of density measurements which could be used in analysis as independent variables. By using this information and appropriate analysis procedures, one can get an estimate of the core position of the shower. Once the core position is known uniquely for each shower, then by using an assumed lateral distribution function determination of shower size is straightforward. Therefore, the problem of shower analysis mainly deals with the determination of core position and in this chapter two major methods of solving this problem will be discussed. These two methods are :

(i) Method of intersecting loci.

(ii) χ^2 minimization (Computer analysis).

3.2 INTERSECTING LOCI TECHNIQUE

This method of core location was first used by Williams (1948) and leads directly to the core position from the experimental data, if the structure function is known. In this method, basically, the ratio of electron densities from any two detectors is used to determine a locus on which the axis of the incident EAS must have fallen. Three detectors give two independent ratios and the intersection of the two corresponding loci defines the core position of the shower.

Two loci curves usually intersect at two places, and to decide which one of the two is the real core position a fourth detector is needed. The ratio of electron density at this detector to that of any one of the other three, will define a new locus which will intersect the other two loci in a unique position. As it was mentioned earlier this method requires the use of an electron structure function and the one used in our analysis is known as the Griesen function and has the form of :

$$\Delta(N,r) = \frac{0.4N}{r_o^2}\left(\frac{r}{r_o}\right)^{0.75}\left(\frac{r_o}{r_o + r}\right)^{3.25}\left(1+\frac{r}{11.4r_o}\right) \qquad (3.a)$$

where r_o = 79 m at sea level.

It is interesting to note that the position found for the core of a shower is independent of the choice of the electron lateral distribution which is used, but however, as we will see, the analysis procedures necessitate the use of an electron lateral distribution which is an explicit function of shower size N and core distance r.

Now consider two detectors D_1 and D_2 giving electron densities Δ_1 and Δ_2 . By applying eqn (3.a) one can write :

$$\Delta_1 = \frac{0.4N}{r_o^2}\left(\frac{r_o}{r_1}\right)^{0.75}\left(\frac{r_o}{r_1 + r_o}\right)^{3.25}\left(1+\frac{r_1}{11.4r_o}\right) \quad \text{and}$$

$$\Delta_2 = \frac{0.4N}{r_o^2}\left(\frac{r_o}{r_2}\right)^{0.75}\left(\frac{r_o}{r_2 + r_o}\right)^{3.25}\left(1+\frac{r_2}{11.4r_o}\right)$$

$$\frac{\Delta_1}{\Delta_2} = \left(\frac{r_2}{r_1}\right)^{0.75}\left(\frac{r_2 + r_o}{r_1 + r_o}\right)^{3.25}\frac{1+\frac{r_1}{11.4r_o}}{1+\frac{r_2}{11.4r_o}}$$

$$\therefore \quad \frac{\Delta_1}{\Delta_2} = \frac{f(r_2)}{f(r_1)} \qquad (3.b)$$

many pairs of values of r_1 and r_2 satisfy equation (3.b) and their locus defines a curve. In order to plot out such loci curves the ratio $\frac{\Delta_2}{\Delta_1}$ is plotted as a function of r_2 for fixed values of r_1 as shown in figure 3.1. Then for any pairs of detectors D_1 and D_2, by using the information of figure 3.1, a series of loci curves of core positions corresponding to different electron density ratios from the two detectors can be plotted. Figures 3.2a and 3.2b show two examples of such curves for pairs of detectors (62-c) and (33-c) of the Durham EAS array (see Chapter 2). Similar curves drawn for other pairs of detectors, and to locate the core of a shower, it is enough to calculate the density ratios for three pairs of detectors and then the appropriate curves, on which the core must have fallen, can be found. The intersection of these curves would be the core position of the shower. In the course of the experiment, most of the time, information from fourteen detectors were available, so there were many choices of detectors to be used. In practice electron density measurements from a minimum of four detectors were employed to locate the core where information from one of the detectors is repeatedly used in all ratios. Since detector C is located at the centre of the array and required more than 4 p m^{-2} in both the inner and outer ring triggers (see Chapter 2), it was used as the common detector in combination with three other detectors with the largest densities. This method does have the disadvantage of relying very heavily on detector C, even if there are only a few particles detected in C. A more refined choice is to take the four detectors with the largest densities and

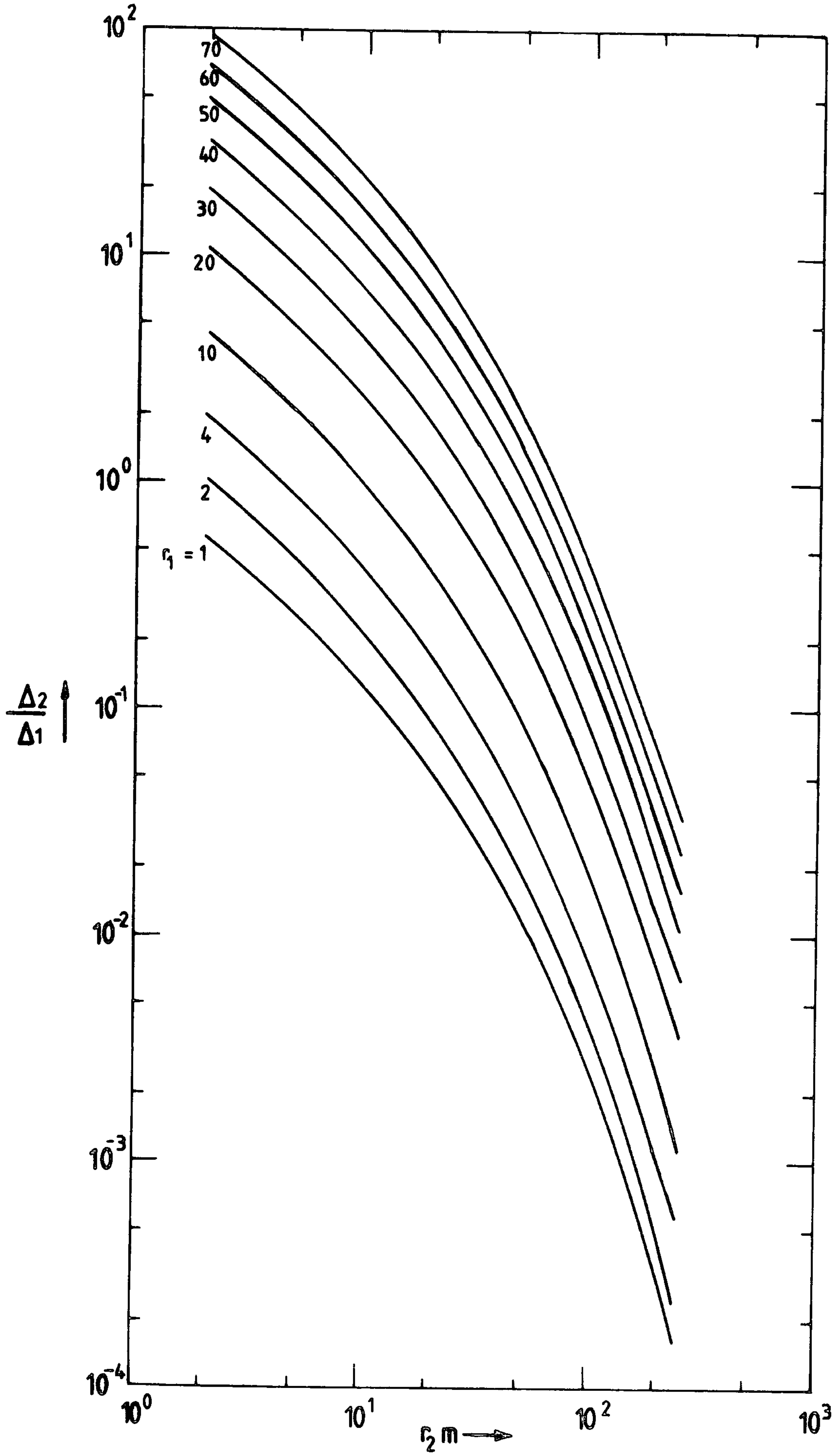

Figure 3.1 : The ratio of densities in detector 2 to 1 $(\frac{\Delta 2}{\Delta 1})$, as a function of r_2 for fixed values of r_1

r_2 = core distance from detector 2

r_1 = " " " " 1

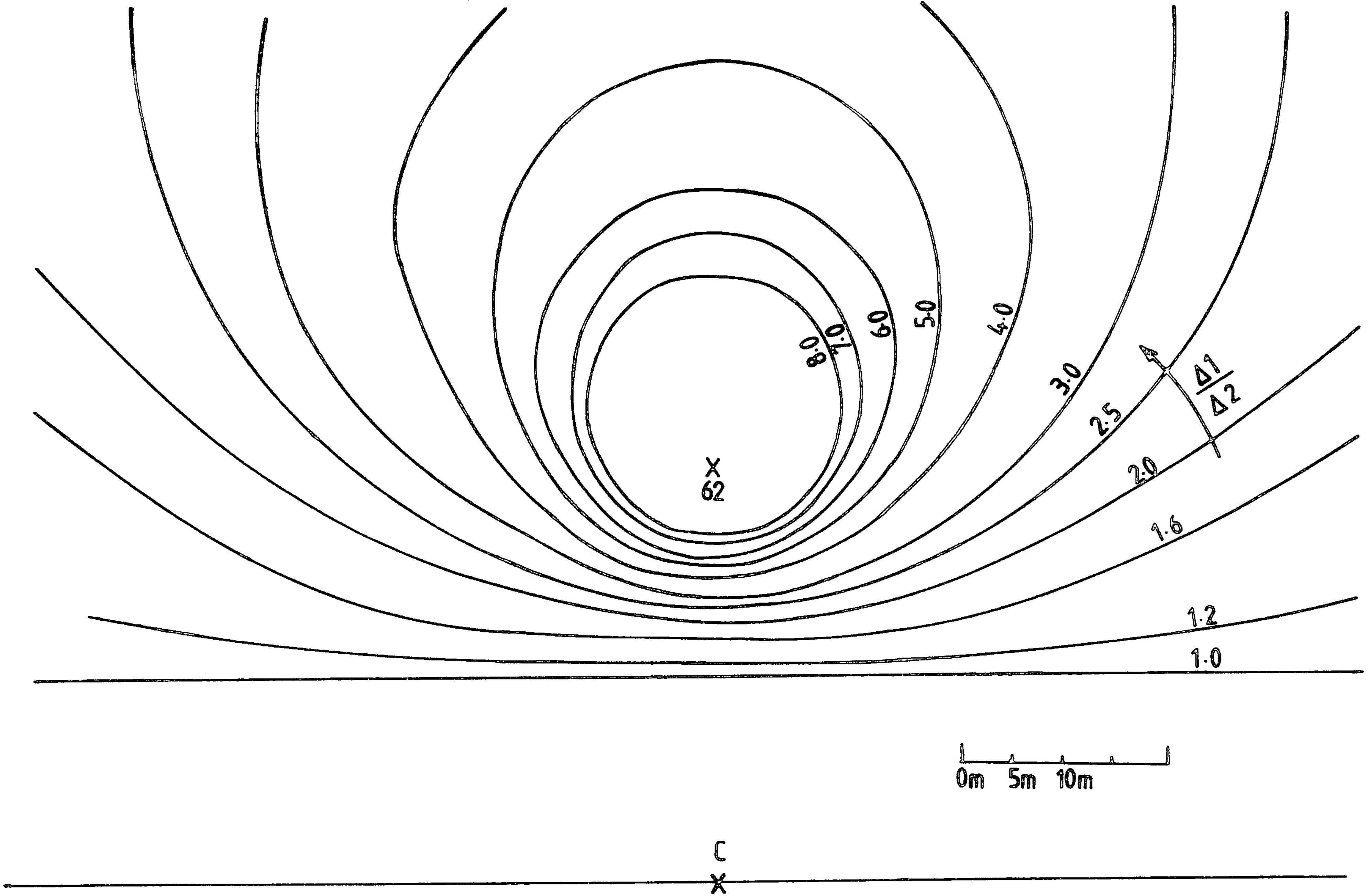

Figure 3.2a : Loci curves on which the core of an air shower must have fallen to give the density ratio, $\frac{\Delta(C)}{\Delta(62)}$, indicated on each curve.

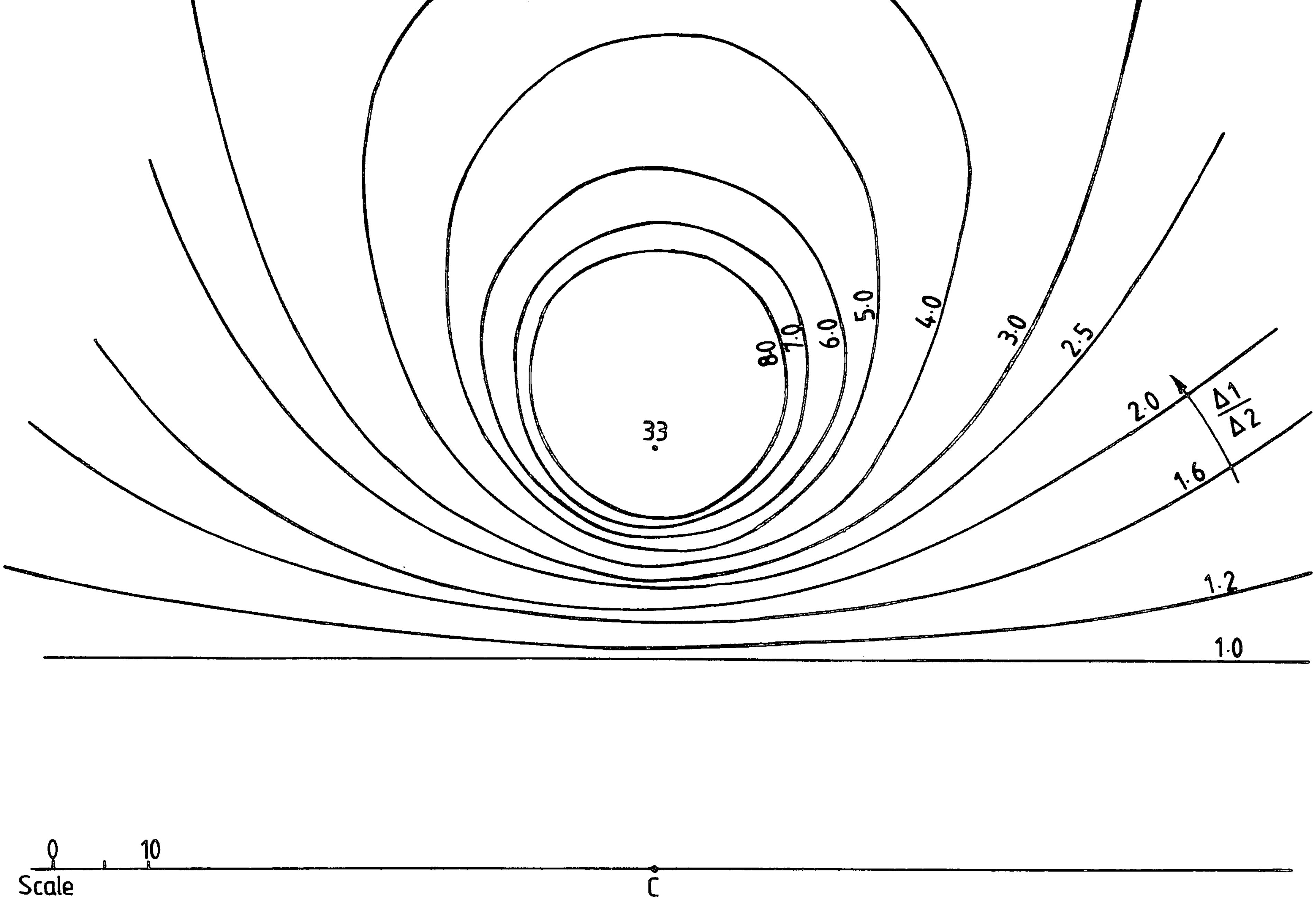

Figure 3.2b : Loci curves on which the core of an air shower must have fallen to give the density ratio, $\Delta(C)$, indicated on each curve.

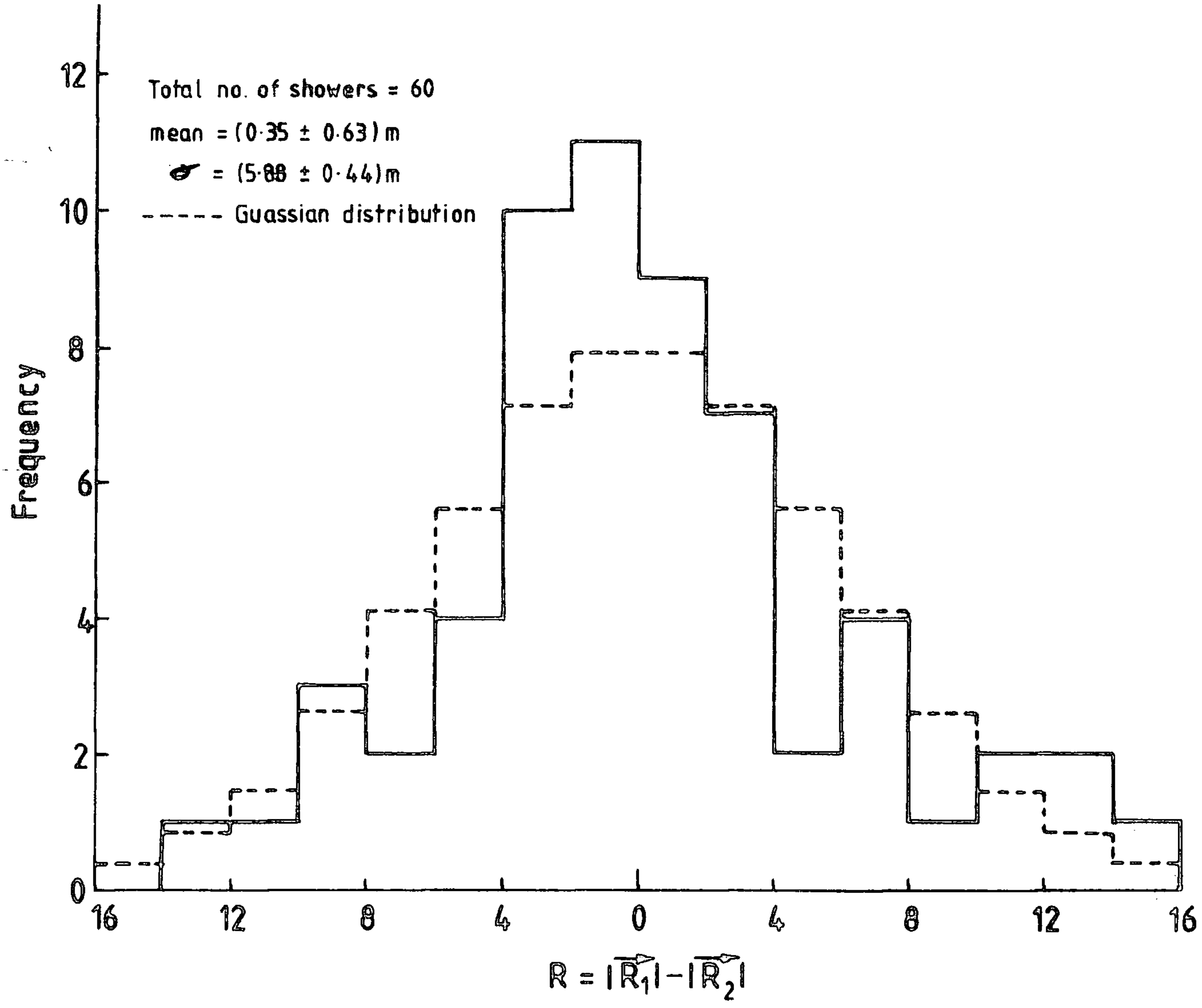

Figure 3.3 : A histogram of the difference between assumed core distance and the core distance determined for simulated showers.

take the detector with the largest signal in combination with each of the other three detectors.

Once the core of the shower is determined, it is a straightforward job to calculate shower size, N_e, by substituting for core distance r in equation (3.a).

3.3 FLUCTUATIONS AND ERRORS

3.3.1 Statistical Fluctuations

Most of the showers at sea level are past the maximum of their development with an age parameter around 1.2, therefore the particles involved in these showers are independent of each other and fluctuations on them can be considered as purely random and follows a Poisson distribution.

Experimental analysis of our data (J. Fatemi, private communication), shows that the observed fluctuations are broader than expected (mainly due to fluctuations in detector response). This analysis suggests that the fluctuation distribution is roughly a Poissonian in shape, but with a broader width and standard deviation of $1.2\sqrt{n}$ (where $\sqrt{n}$ is standard deviation for a normal poisson distribution). Brennan et al (1958) and Clark et al (1961) have made similar studies and found the same results. Smith (1976) has looked at the same problem considering fluctuations due to detector response more accurately and has found results that are consistent with the present work.

Now that the characteristics of the fluctuation distribution is clear, one can simulate real showers in order to investigate the accuracy of the parameter determination. In simulating showers, on sampling n particles, fluctuations were assumed to be Gaussian of standard deviation 1.2 $\sqrt{n}$ where n is average expected number of particles assuming the showers obey the Greisen structure function (eqn.3.a). The size and core distance distributions of simulated showers were similar to those of real showers.

Having generated air showers the cores were located by the method of intersecting loci curves (Section 3.2), and figure 3.3, shows a histogram of the difference in true core distance from the centre of the array and the core distance determined by the method of intersecting loci for a sample of 60 simulated showers. The histogram of figure 3.3 is reasonably well represented by a Gaussian distribution of standard deviation (5.88 ± 0.44)m.

3.3.2 Error in Core Location

In analysing a shower to locate the core, three loci curves are usually used and one of the three following cases may happen.

(i) Three loci curves intersect at, or almost at, one unique point and automatically that point would be the core of the shower. About 20% of the showers are of this kind (Fig. 3.4)

(ii) The three loci curves don't intersect at the same point, but intersecting points make a triangular area in which the core of the shower must have fallen. In this case, the error curve for each locus is drawn and resulting curves usually produce a smaller triangle, inscribed inside the original triangle, where the centre of gravity of the smaller triangle is then taken as the best estimate of the core (Fig. 3.5). (The centre of the triangle is taken to be the intersection of the bisectors of the angles, since this point is equidistance from all three sides of the triangle). The method of calculating error curves is fully described in Appendix A.

(iii) The loci curves either do not intersect in sight or only two of them intersect and one can not find any common area between them (Fig. 3.6). In this case again, the error curves are calculated and drawn and these usually produce a triangular shape where the centre of it would be taken as the best estimate of the core. If even the error curves do not intersect, then the shower would be considered as impossible to analyse. About 20% of the showers are of this kind.

3.4 COMPUTER TECHNIQUE, X^2 MINIMIZATION

Most of the data that was used in the present work has been analysed by this method and analysis details have been fully described by Smith and Thompson (1977).

As it was explained in Chapter 2, the data from the Durham EAS array is assembled and stored in digitised form on magnetic disc within $\underline{2}$ msec of occurrence of an air shower event. Initially, the assembled data on the IBM 1130 Computer is checked and tested to see if it is suitable for full analysis and then converted to a form that can be handled by the IBM 370/168. The so called 'dynamic' data is then converted into meaningful quantities which then could be analysed to get shower parameters.

The main feature of the analysis programs lie within the minimization routines. A versatile and comprehensive CERN minimization package, MINUIT, (James and Roos, 1975), in which the

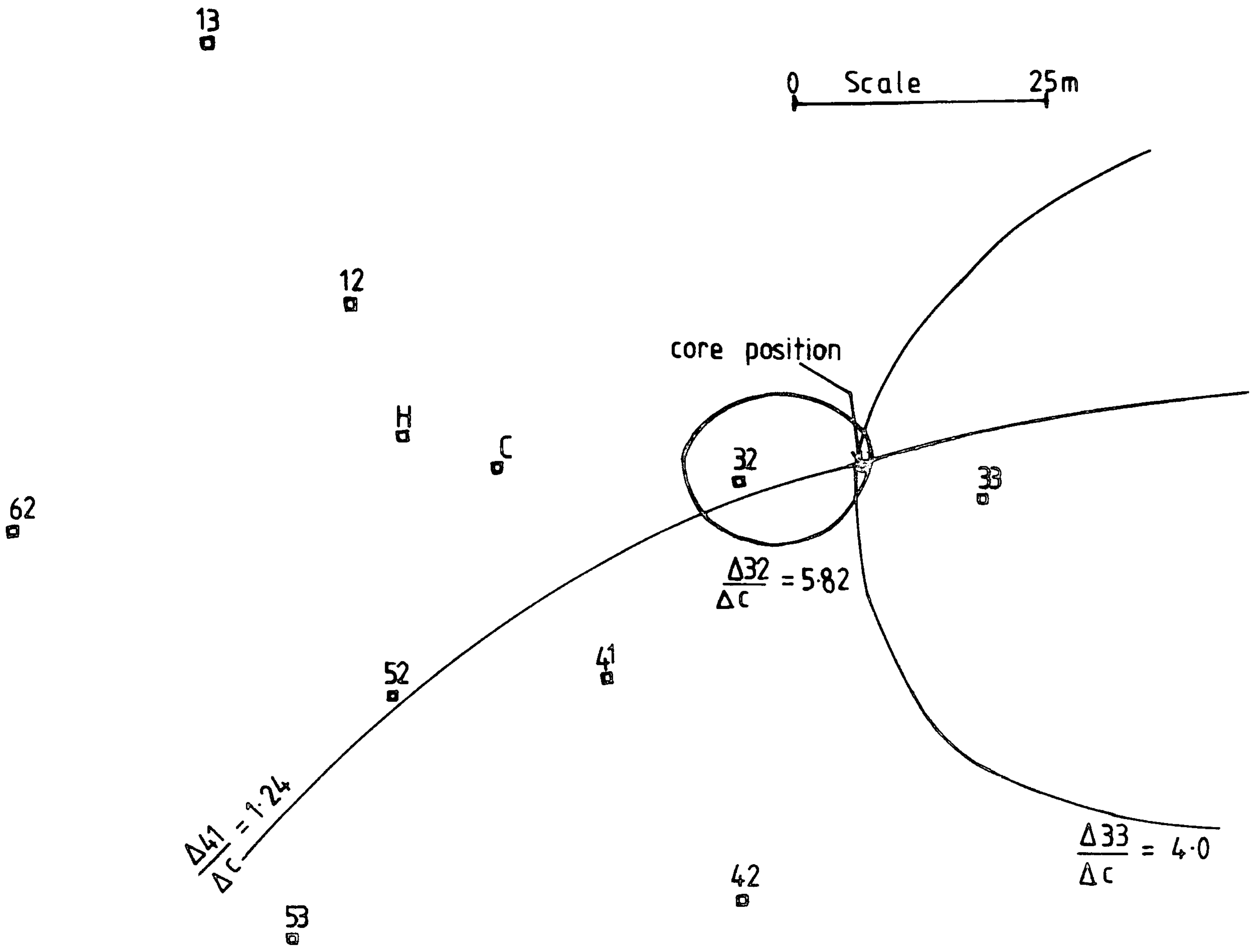

Figure 3.4 : An example of a good shower where core position is found without referring to error curves.

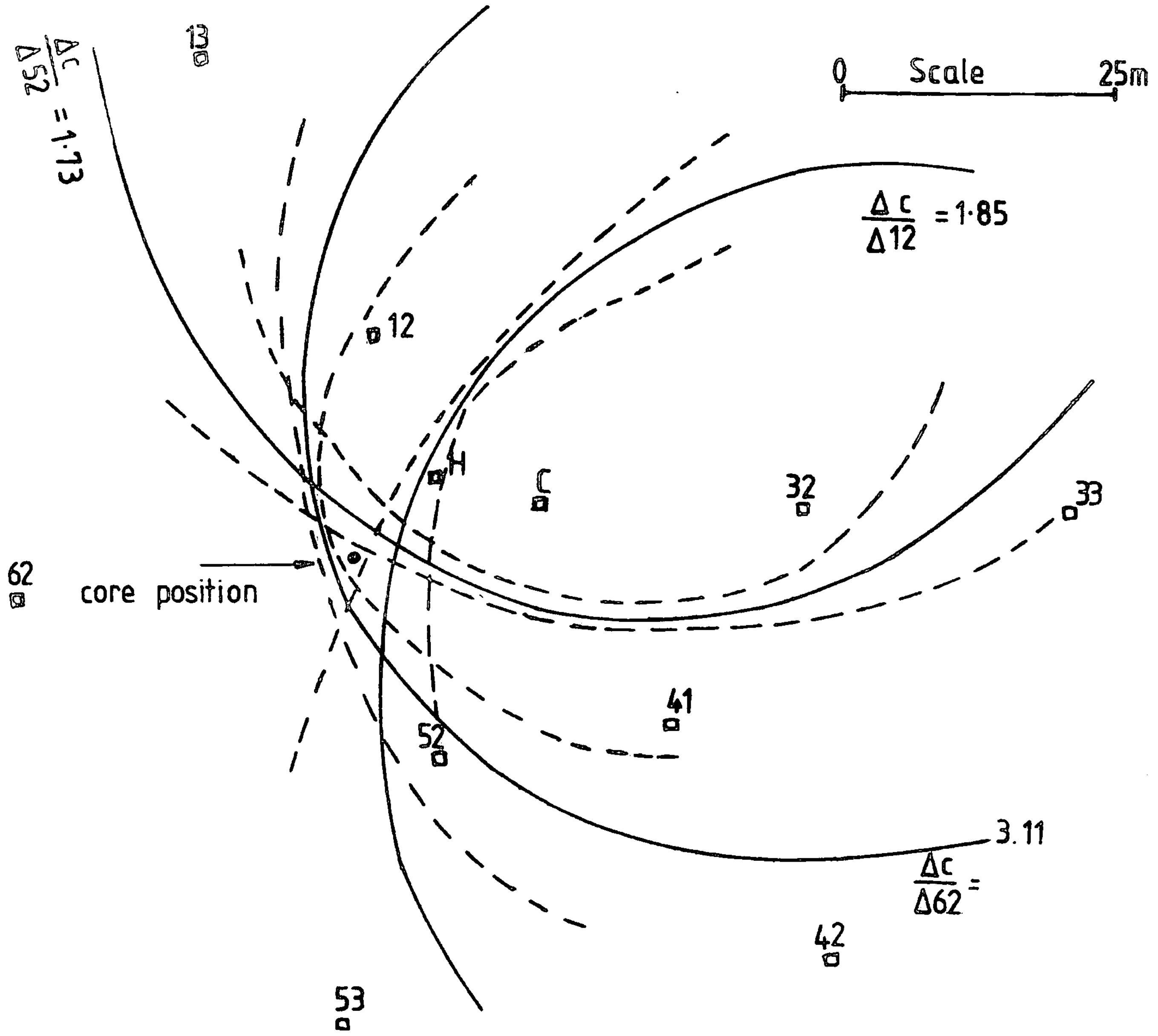

Figure 3.5 : A typical shower analysed by methods of intersecting loci curves where error curves are used to locate the core.

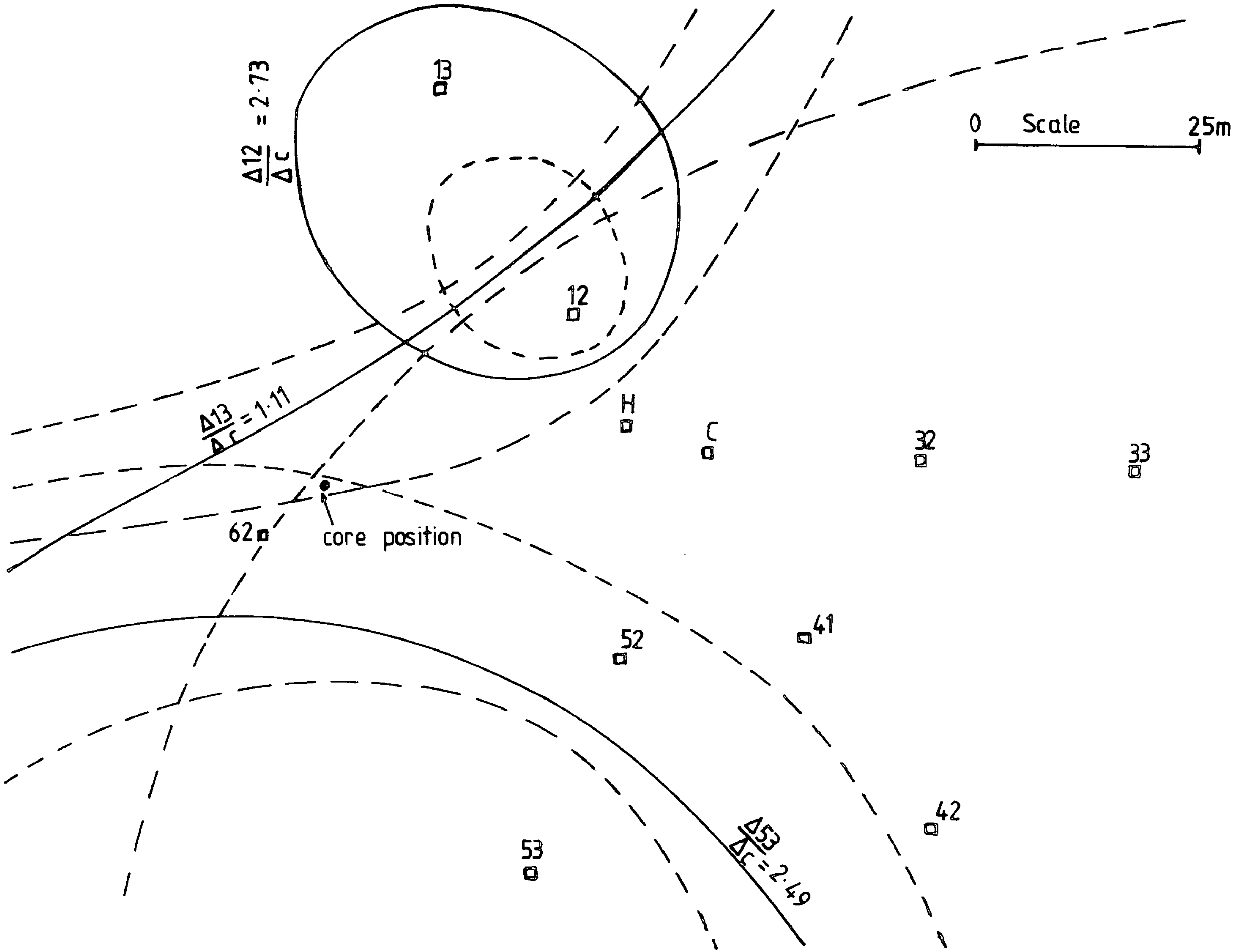
0 Scale 25m
$\frac{\Delta 12}{\Delta c} = 2{\cdot}73$
13
12
H
C
32
33
$\frac{\Delta 13}{\Delta c} = 1{\cdot}11$
62
core position
41
52
42
53
$\frac{\Delta 53}{\Delta c} = 2{\cdot}49$

theoretical description of an air shower's structure is fitted to observed quantities as measured by the detectors in the array is employed. MINUIT uses a variety of minimization techniques which are invoked by calling the appropriate subroutine and combinations of these routines allow for accurate and efficient minimization. Simply, what happens is that by assuming a structure junction and a core position the number of particles at different detectors are calculated and then by moving the core on the collecting area, according to a random distribution, and repeating the process and minimizing a chi squared function of the form

$$Fi = \sum_{i} \Big[(9_{o} - 9_{c})\omega\Big]_{i}^{2}$$

the best values of core position and shower size are found. (9_o and 9_c are observed and calculated number of particles at the ith detector respectively and ω is a weight function). It is interesting to note that in analysis procedures, core position (x'y) and shower size (N) are treated as three independent variables and are minimized together. The structure function used in this method was the one given by Catz et al (1975)and has the form of

$$\Delta(r) = 0.0157\,\frac{N_e\, e^{-r/120}}{(r+1)^{1.62}}\ \mathrm{m}^{-2} \quad \text{where r is in}$$

metres and N_e in units of single particles.

3.5 COMPARISON BETWEEN INTERSECTING LOCI AND X^2 MINIMIZATION METHODS OF CORE LOCATION

The intersecting loci method of core location has been applied to some data in our analysis and it has proved to be a reliable method of obtaining air shower parameters. However, there are occasions where this method breaks down and looks to be inefficient. It is obvious that this technique can only handle small quantities of data and if for example more than 500 events need analyzing, then this technique would prove too laborious. But, on the contrary to computer analysis, with intersecting loci method, one has more control over the data and for example any fault or saturation or even local interaction in a detector is more easily recognizable and information from that detector can be ignored to avoid any trouble in the analysis.

For calculation of intersecting loci curves, all of the showers are assumed to be vertical, so for very inclined showers ($\theta > 50^{0}$), this technique faces major difficulties in locating the core. If one wants to take account of inclination of the showers, one would have to construct a large number of intersecting loci curves corresponding to different angles of inclination of the shower axis. There is no apparent difference in accuracy of both methods in locating the core of a shower, However, the same data have been analysed by both methods and are directly compared. Figure 3.7 is a histogram of the difference in core distance from the central detector C as determined by the method of intersecting loci and computer analysis respectively, for a sample of 189 showers of size in the range

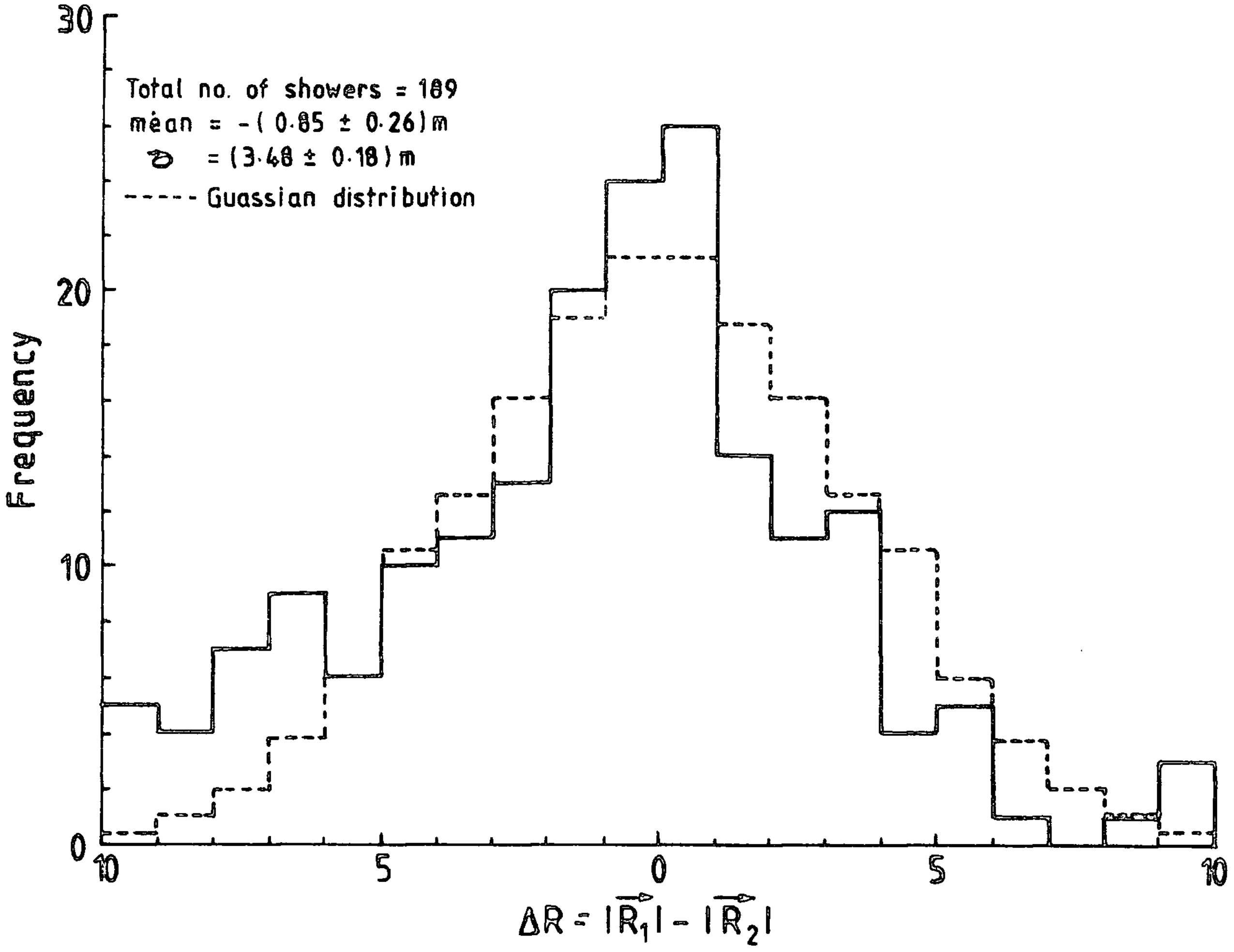

Figure 3.7 : Histogram of the difference in core distance from detector C as determined by the method of intersecting loci and computer analysis.

of 10^5 - 10^6 particles and core distance less than 72 m from C. It is seen that the distribution can approximately be represented by a Gaussian distribution of standard deviation (3.48 ±0.18)m. Of course, ideally the difference should be zero.

3.6 DETERMINATION OF ARRIVAL DIRECTIONS

Using fast timing measurements to determine the arrival direction of an air shower was first introduced by Bassi et al (1952) and soon followed by many people such as Linsley and Scarsi (1962), Wordneck and Bohm (1975) and Crouch et al (1977). In Durham EAS array there are seven detectors, (C,11,31,51,13, 33 and 53), which produce fast timing information, where detector C is used to define the spatial and temporal origin, (see 2.1.1). After electronic adjustment and calibration, fast timing detectors eventually produce time differences, t_i, which is the difference between arrival time of a shower at detector D_i and detector C. Now suppose a shower with zenith and azimuthal angles (θ and ϕ), passes through timing detectors D_i, located at (x_i, y_i, z_i) at time differences t_i, then one has the relationship

$$T_i = \ell\, x_i + m\, y_i + n\, z_i \qquad (3.b)$$

where $T_i = c\, t_i$ ($c = 3.10^8$ msec^{-1} is velocity of light) and

$$\ell = \sin\theta\cos\phi$$

$$m = \sin\theta\sin\phi$$

$$n = \cos\theta$$

are direction cosines of the unit vector normal to the plane of the shower front. (Calculations which lead to equation 3.b is presented in Appendix B). In principle, only three detectors (including C) are enough to determine θ and ϕ . For analytical solution of the problem one can apply equation (3.b) to any two detectors D_1 and D_2 and detector C :

$$T_1 = \ell x_1 + m y_1 + n z_1 \qquad (3.b1)$$

$$T_2 = \ell x_2 + m y_2 + n z_2 \qquad (3.b2)$$

multiplying (3.b1) by y_2 and (3.b2) by y_1 and subtracting gives :

$$\ell = A + B n \qquad \text{where :}$$

$$A = \frac{y_2 T_1 - y_1 T_2}{y_2 x_1 - y_1 x_2} \quad \text{and} \quad B = \frac{y_1 z_2 - y_2 z_1}{y_2 x_1 - y_1 x_2}$$

Similarly by multiplying (3.b1) by x_2 and (3.b2) by x_1 and eliminating ℓ one finds :

$$m = C + D n \qquad \text{where :}$$

$$C = \frac{x_1 T_2 - x_2 T_1}{x_1 y_2 - x_2 y_1} \quad \text{and} \quad D = \frac{x_2 z_1 - x_1 z_2}{x_1 y_2 - x_2 y_1}$$

Since ℓ, m and n are the components of a unit vector then :

$$\ell^2 + m^2 + n^2 = 1 \qquad (3.c)$$

substituting for ℓ and m in (3.c) results :

$$(A + B_n)^2 + (C + D_n)^2 + n^2 = 1$$

$$\therefore \quad A^2 + B^2 + n^2 + 2ABn + C^2 + D^2 + 2CDn + n^2 = 1$$

$$n^2(B^2 + D^2 + 1) + 2(AB + CD)n + (A^2 + C^2 - 1) = 0$$

$$\therefore \quad n = \cos\theta = \frac{-(AB+CD) + \left[(AB+CD)^2 - (B^2+D^2+1)(A^2+C^2-1)\right]^{\frac{1}{2}}}{(B^2 + D^2 + 1)} \qquad (3.d)$$

Recalling that A,B,C and D are given in terms of detector coordinates and time differences, eqn.(3.d) enables the zenith angle of the shower to be calculated. The solution requires cos Θ to be positive, since Θ must lie in the range of $(0\text{-}90^{\circ})$.

The azimuthal angle of a shower can be calculated as following :

$$\frac{m}{\ell} = \frac{\sin\Theta \ \sin\phi}{\sin\Theta \ \cos\phi} = \tan\phi$$

substituting for m and ℓ results :

$$\tan\phi = \frac{C + Dn}{A + Bn}$$

So, in principle, a unique solution for the arrival direction of an air shower can be found with a minimum of three timing detectors. But, as in our case, when the number of timing detectors exceed three, a unique solution is not possible so, a numerical minimization can be applied and this is exactly the technique which is used in Durham. In minimization program, arbitrary values of Θ and ϕ are assumed and by using equations similar to (3.b), the predicted values of time differences, $(t_c)i$, are calculated. The function which is minimized has the form of

$$F = \sum_{i} (t_o - t_c)^2$$

where t_o is the observed time differences in the ith detector and summation extends over all of the timing detectors. The minimum value of F corresponds to the appropriate values for Θ and ϕ . Computer programs such as MINUIT are available for carrying out the above mentioned procedure.

3.7 A NUMERICAL EXAMPLE FOR CALCULATING THE ARRIVAL DIRECTION OF A SHOWER, WHERE TIMING INFORMATION FROM A MINIMUM OF THREE DETECTORS IS AVAILABLE.

Suppose two timing detectors 13 and 33 (Durham EAS Array), give relative time differences of $t_{13} = -94.5 . 10^{-9}$ sec and $t_{33} = 23.4 . 10^{-9}$ sec and detector C which is the temporal origin of the array obviously shows $t_C = 0$ sec. Converting the units gives

$$T_{13} = c\ t_{13} = 3.10^{8} . (-94.5 . 10^{-9}) = -31.5 \quad \text{and}$$

$$T_{33} = c\ t_{33} = 3.10^{8} . (23.4 . 10^{-9}) = 7.8$$

Substituting for coordinates of the detectors (Table 2.1) and time differences in equations 3-b3 and 3-b4 give

$$A = \frac{y_{33}\ T_{13} - y_{13}\ T_{33}}{y_{33}\ x_{13} - y_{13}\ x_{33}} = \frac{(14.9)(-31.5)-(26.3)(7.8)}{(14.9)(-41.8)-(26.3)(45.1)} = \frac{-669.31}{-1808.95} = 0.37$$

$$B = \frac{y_{13}\ z_{33} - y_{33} z_{13}}{y_{33}\ x_{13} - y_{13}\ x_{33}} = \frac{(26.3)(0.2)\ -\ (14.9)(-13.3)}{-1808.95} = -0.11$$

$$C = \frac{x_{13}\ T_{33} - x_{33}\ T_{13}}{y_{33}\ x_{13} - y_{13}\ x_{33}} = \frac{(-41.8)(7.8)-(45.1)(-31.5)}{-1808.95} = -0.61$$

$$D = \frac{x_{33} z_{13} - x_{13} z_{33}}{y_{33}\ x_{13} - y_{13}\ x_{33}} = \frac{(45.1)(-13.3)-(-41.8)(0.2)}{-1808.95} = 0.33$$

Substituting for A, B, C and D in equation 3-d gives

$$n = \cos\theta = \frac{0.24 \pm\sqrt{0.6 + 0.55}}{1.12} = \frac{0.24 \pm (0.78)}{1.12}$$

Since θ lies in the range $(0-90)^o$, therefore $\cos\theta$ should be positive so

$$\cos\theta = 0.91$$

$$\theta = 24.3^o$$

Substituting for $\cos\theta$ in equation 3-e gives

$$\tan\phi = \frac{C+D\cos\theta}{A+B\cos\theta} = \frac{-0.61 + (0.33)(0.91)}{0.37 + (-0.11)(0.91)} = -1.15$$

which implies either $\phi = 131.01^o$ or $\phi = 311.01^o$

Obviously there must be a unique solution for Θ and ϕ and this will be found by looking at $\cos\phi$ by means of calculating ℓ

$$\ell = A + B\cos\Theta = 0.27$$

on the other hand

$$\ell = \sin\theta\cos\phi = 0.27$$

Since $\sin\theta$ is always positives then $\cos\phi$ must be positive and out of the two above answers for ϕ only $\phi = 311.01^o$ satisfies this. So $\theta = 24.3^o$ and $\phi = 311.01^o$ is the unique solution. It is shown that three detectors are adequate to find the arrival direction of a shower, but as stated earlier, in the Durham E.A.S. Array there are a total of seven timing detectors which at least four of them have been working at any moment. Table 3.1 gives examples of three events where information from four timing detectors (C,13,33 and 53) were available and therefore three independent values of θ and ϕ are calculated numerically for each event. The mean calculated zenith and azimuthal angles are compared with the values determined by computer technique using MINUIT package. Comparison between the results of both methods indicates that they are in reasonable

		Event No.		
		1	2	3
Given arrival time relative to C	t_{13} (n sec)	- 7.02	- 12.9	- 71.3
	t_{33} (n sec)	- 3.94	41.7	142.3
	t_{53} (n sec)	32.1	113.2	15.8
Calculated arrival directions	θ_{13-33} (degree)	12.8	34.79	17.3
	θ_{33-53} (degree)	14.2	49.3	19.3
	θ_{53-13} (degree)	11.7	40.1	21.7
	ϕ_{13-33} (degree)	163.1	38.1	204.7
	ϕ_{33-53} (degree)	175.3	47.1	224.0
	ϕ_{53-13} (degree)	171.8	39.2	232.0
	mean of the calculated zenith angles	12.9	41.6	19.7
	mean of the calculated azimuthal angles	170.1	41.5	220.3
	θ determined by the computer (MINUIT)	12.3	46.2	18.9
	ϕ determined by computer technique (MINUIT)	177.0	40.3	211.0

TABLE 3.1 : Examples for calculating zenith and azimuthal angles where arrival times at three detectors (relative to C) are available.

agreement and the differences are within 5^{o} for θ and 10^{o} for ϕ .

3.8 SUMMARY

A method of determination of shower parameters has been discussed based on the intersecting loci curves, first introduced by Williams (1949). However, this technique can not handle large quantities of data, for which case an analysis using a numerical minimization technique has been discussed. The error in core location by both methods is on average about ± 6m and a comparison between the results from both methods is made. An analytical approach to determine arrival direction of the showers (θ and ϕ), is also discussed for a minimum of three detectors. If there are more than three timing detectors then a χ^2 minimization technique is applied.

CHAPTER FOUR

STUDY OF THE SIZE SPECTRUM AT SEA LEVEL

4.1 INTRODUCTION

One of the main problems in investigating air showers is to evaluate shower parameters, including shower size, as it was fully described in the previous chapter. Using the information on the size of the showers makes it possible to study the size spectrum or as it is sometimes called the number spectrum. The size spectrum of air showers is studied mainly for the information that it bears on the primary energy spectrum. However, conversion from shower size to primary energy is not a straightforward process and is very much dependent upon the model of air shower development used to derive the relationship between them. This aspect of air showers, which is out of the scope of this work, has been and continues to be investigated by many workers (e.g. Dixon et al (1973), Shibita (1975), Popov (1975) and Kempa (1976)) and is still the subject of some uncertainty due to the lack of knowledge of the appropriate nuclear physics.

There are two common methods used to measure the size spectrum. The first and more reliable is direct measurement of shower size from air shower information and the second method is to measure the density spectrum first and then convert it to a size spectrum using appropriate relations. In the following section a survey of measurements of size spectrum at different altitudes is described.

4.2 PREVIOUS MEASUREMENTS OF THE SIZE SPECTRUM

The results of size spectrum measurement, like any other measurement in EAS studies, could be dependent upon the altitude at which the experiment is carried on. To avoid this and any other possible phenomena, especially attenuation in the atmosphere, the size spectrum of EAS has been measured at mountain altitudes as well as at sea level.

4.2.1 R. Norman (1956), Sea Level

A proportional counter was used to measure the integral density spectrum of EAS in the range of $\Delta = 20\text{-}1000\ m^{-2}$. The experimental arrangement comprised three proportional counters of the control grid type each of area .05 m^2, located in a horizontal plane at the three corners of a 5 m equilateral triangle. A three-fold coincidence was used as EAS selection. After measuring the density spectrum, Norman expressed his results for the number spectrum

$R(>N) = 2.3 \cdot 10^{-4} \left(\frac{N}{10^6}\right)^{-1.40 \pm 0.1}$ $hr^{-1}\ m^{-2}$ for $N < 10^6$ and with evidence of a rapid increase in the exponent for $N > 10^6$. In his calculations he used the following formula :

$S = 1.4 - 0.7 \log \frac{N}{200}$ where S is the age parameter and N is the shower size.

4.2.2 Summary of Hillas (1970)

Hillas (1970) has summarised the available data on measurements of the sea level number spectrum using Extensive Air Shower arrays (Figure 4.1). From his survey he concludes that many experiments at sea level and at other altitudes, show that the spectrum of shower size, N, steepens suddenly at an energy near 3 or 4.10^{15} eV, the same happens to the spectrum of the total

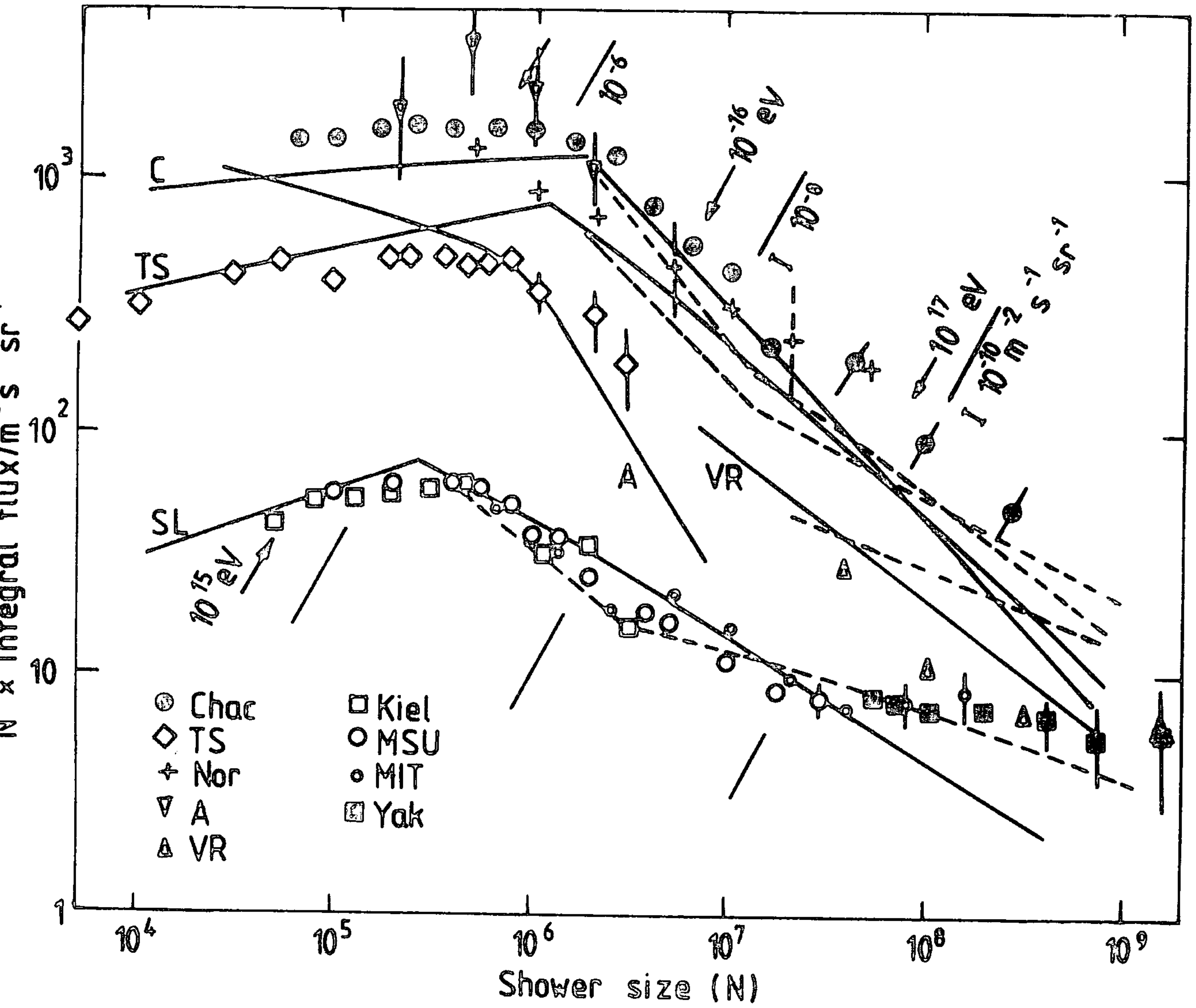

Figure 4.1 : The integral shower size spectrum at various altitudes. The lines show the approximate fluxes to be expected according to a conventional shower model of Hillas (Hillas 1975).

of muons, N_μ. As this occurs even at mountain altitudes, it does not represent simply an increased attenuation of showers, but rather directly reflects a sharp steepening or "knee" in the primary energy spectrum. After careful investigations, Hillas suggested the following expressions for the size spectrum

$R(>N) = 52.0\ N^{-1.5}\ m^{-2}\ sec^{-1}\ st^{-1}$ for $N_e \leq 5.10^5$

$R(>N) = 36920.0\ N^{-2.0}\ m^{-2}\ sec^{-1}\ st^{-1}$ for $5.10^5 < N_e < 3.10^7$

$R(>N) = 6.76\ N^{-1.50}\ m^{-2}\ sec^{-1}\ st^{-1}$ for $N_e \geq 3.10^7$

4.2.3 Aseikin et al (1971), 3340 m. above sea level

The data concerning EAS information were obtained at the Tien Shan array in Russia. The 64 scintillation counters, each of area 0.25 m^2 which are regularly spaced over an area 110 m^2 in the centre of installation and four fast timing scintillators (each of area 7.0m^2) situated at 20m from the centre and 10 counters located at 70 m from the installation centre, provide air shower parameters. The showers with $N_e \geq 10^5$ and zenith angle $\theta < 30^\circ$ were chosen for analysis. The shower size was determined from the density of particles flux at the 70m counters. The age parameter was estimated by the comparison of the particle densities at various distances from the shower axis using the Nishimura-Kamata lateral distribution. This measurement, similar to sea level measurements, did not fail to produce a power law function with a single constant exponent for the whole range of shower sizes. The size spectrum suggested by this group has the following form :

$$R(\geq N) = (2.7 \pm 0.3)\ 10^{-3} \left(\frac{N}{7.5.10^5}\right)^{-\gamma} m^{-2}\ hr^{-1} st^{-1} \text{ where}$$

$\gamma = (1.54 \pm 0.8)$ for $1.8.10^5 < N \leq 7.5.10^5$ and

$\gamma = (2.11 \pm 0.3)$ for $7.5.10^5 < N < 3.10^6$

4.2.4 Antonov et al (1971), Aircraft Experiment

Airborn equipment, consisting of 20 scintillators of 0.07 m^2 area, 2 counters of 0.25 m^2 area and a spark chamber block were installed in the fuselage and wings of an aircraft to study EAS characteristics at altitudes of 5280 m (530 gr cm^{-2}), 7320 m(400 gr m^{-2}) and 10000 m (269 gr cm^{-2}). The installation was triggered when at least seven relativistic particles passed simultaneously through each of three counters of .07 m^2 area located at the corners of a triangle with 0.5m sides. The spark chamber was used to select showers with zenith angle $\leq 30^0$.

The total number of particles in a shower was evaluated on the basis of the value of N_{20}^{*}. It was assumed that at core distances greater than 20m the lateral distribution function might be approximated by Nishimura-Kamata function. It was also assumed that the value of age parameter S was within (.2-1.0). The values of thecoefficients of transitions from N_{20} to total number of particles, were found for various altitudes to be about 3 to 5. The accuracy of these coefficients is 50%.

The vertical integral spectrum of showers for 10000m altitude was measured using events that their effectiveness of detection are close to 100%. It is suggested that for showers in the range of 5.10^5 - 5.10^6 the spectrum may be approximated by a power law function with an exponent of 2.1 ± 0.3.

4.2.5 Krasilnikov et al (1973), Yakutsk Array

The differential and integral size spectrum of large showers in the range of (10^7 - 10^9) particles, at sea level, is obtained at the Yakutsk EAS array (Egorov et al, 1973).

---

* N_{20} is the total number of particles in the shower found from density at 20 m from the core.

The events with core distance in the range of (200-600)m and zenith angle less than 30^{o} were selected. An effective area, S_{eff}, was determined in such a way that the probability to record the shower of size $\geq N$ inside S_{eff} was ≥ 0.94.

The differential and integral EAS size spectra in the range of $3.10^{7} < N < 10^{9}$ at sea level are suggested to have the form of :

$$R(N,0) = (1.17 \pm .24)10^{19} \left(\frac{N}{10^{8}}\right)^{-2.75 \pm 0.08} \quad m^{-2}sec^{-1}st^{-1}$$

$$R(>N,0) = (7.94 \pm 0.72)10^{-12} \left(\frac{N}{10^{8}}\right)^{-1.68 \pm .05} \quad m^{-2}sec^{-1}st^{-1}$$

It is interesting to note that the exponent found in this experiment is considerably lower than was found in other measurements.

4.2.6 Ashton and Parvaresh (1975), Sea Level

A proportional counter of rectangular cross-section was employed initially to measure the density spectrum of EAS. The counter was made of aluminium walls with external dimensions of (15,15 and 101)cm filled with a 90% argon and 10% methane gas mixture at atmospheric pressure. EAS are selected by the simultaneous passage of a predetermined number of particles through each of three liquid scintillators each of an area $1.24\ m^{2}$, placed in close proximity of one another. Assuming the lateral structure function of EAS particles is independent of shower size, three different lateral structure functions, the Greisen, the Kiel and the Sydney groups, were used independently to interpret the data. The analytic expressions for these functions, respectively, are as follows :

$$\Delta(r) = \frac{0.4}{r_1^2}\left(\frac{r_1}{r}\right)^{0.75}\left(\frac{r_1}{r + r_1}\right)^{3.25}\left(1+\frac{r}{11.4\ r_1}\right) \text{where } r_1=79\text{m}$$

$$\Delta(r) = 1.08 \cdot 10^{-2}\ (r + 1.0)^{-1.5}\ \exp\ (-^r/120)$$

$$\Delta(r) = 2.12 \cdot 10^{-3}\ (r + 1)^{-1.0}\ \exp\ (-^r/75)$$

After measuring a density spectrum, the best estimate of the size spectrum was suggested to be :

$R(>N) = 3.0\ N^{-1.30}\ m^{-2}\ sec^{-1}\ st^{-1}$ for $N < 7.10^5$

$R(>N) = 36720\ N^{-2.0}\ m^{-2}\ sec^{-1}\ st^{-1}$ for $7.10^5 \leq N < 3.10^7$

$R(>N) = 6.76\ N^{-1.5}\ m^{-2}\ sec^{-1}\ st^{-1}$ for $N > 3.10^7$

4.2.7 Catz et al (1975), Sea Level

The results of this measurement is obtained from experiments carried on at Verrieres le Buisson in France. The basic electron detectors are scintillators, but the apparatus also consists of a certain number of Geiger counters. The Geiger counters allow to estimate the true size of showers, namely the sizes of showers directly comparable with those obtained from calculations of EAS development.

Detailed analysis of experimental data showed that the lateral distribution of particles as registered by the scintillator counters can be described at distances from about 2m to at least 70m from the axis by the formula :

$$\Delta(r) = N \times 0.015 \times \frac{\exp(^{-r}/120)}{(r + 1)^{1.62}}$$

where N represents the total number of electrons in a shower. Assuming the lateral distribution given above, the core position for 25000 showers were obtained and after making allowances for the type of detector, (i.e. correction for G-M to scintillator densities), the individual shower sizes were found by extrapolating the lateral distribution to larger distances from the core.

Assuming the size spectrum has a form of $AN^{-\gamma}$, then Catz et al suggested a change of slope from $\gamma = 1.59 \pm 0.02$ to $\gamma = 2.19 \pm 0.02$ at N_e around 10^6.

4.2.8 Kiel Group (1977) Sea Level

The recently modified EAS array in Kiel, Germany, mainly consists of 27 unshielded scintillation counters for core position and shower size determination. 11 scintillation counters connected to 22 fast timing channels supply arrival direction of the showers and a 31 m^2 neon hodoscope with 176400 flash tubes under about 2.5 gr cm^{-2} of wood to study electron core structure. Besides the conventional parameters such as core position, shower size and arrival direction, the scintillator data yield several parameters corrolated to the shower age. Investigations showed that, for the range of 10^5- 10^6, on the average the showers become continuously steeper and that the fluctuations decrease. There is an indication of a flattening of the showers above 10^6. Assuming the integral size spectrum follows a power law function, this measurement suggested an exponent of $(1.61 \pm .02)$ in the size range 10^5- 10^6 and (1.91 ± 0.03) above 2.10^6. The intensities in units of $cm^{-2}sec^{-1}st^{-1}$ are $(4.0 \pm 0.9)\ 10^{-10}$ at 10^5, $(9.7 \pm 2.3)10^{-12}$ at 10^6 and $(1.1 \pm 0.5)\ 10^{-13}$ at 10^7.

4.3 PRESENT WORK

4.3.1 Experimental Arrangement

In the present work data from the Durham EAS array has been used to produce a size spectrum in the range of 10^4-4.10^6 particles. Briefly, EAS have been selected using both an inner ring trigger, $\Delta_c(\geq 4\ m^{-2})$, $\Delta_{11}(\geq 2\ m^{-2})$, $\Delta_{31}(\geq 2\ m^{-2})$, $\Delta_{51}(\geq 2\ m^{-2})$ & an outer ring trigger, $\Delta_c(\geq 4\ m^{-2})$, $\Delta_{13}(\geq 2\ m^{-2})$, $\Delta_{33}(\geq 2\ m^{-2})$, $\Delta_{53}(\geq 2\ m^{-2})$ of the Durham EAS array, (Chapter 2, and Figure 2.1), where the numbers in brackets refer to the minimum electron density requirement from each detector. The core position and shower size for 4819 showers has been found using the computer analysis method explained in the previous chapter. But before dealing with the results of the size spectrum it is useful to evaluate the rate of showers $> N$ which produce a certain trigger and also the rate of showers whose cores fall at a distance greater than r from a certain point (e.g. a detector) as a function of r.

4.3.2 Rate of Showers of Size > N which satisfy the EAS Selection Criteria

For any detector, with a given threshold, there is an area around it which a shower of size N can fall and satisfy the given threshold. If we plot this area for all the triggering detectors, the intersection of these areas produce a common area (collecting area, A_N) in which the core of a shower of size N can fall and produce the trigger. Figure 4.2 displays examples of these areas for the outer ring trigger while the same has also been done for the inner ring trigger. These curves were elevated assuming all showers obey the Greisen(1960) electron structure function which is

$$\Delta(r,N) = \frac{0.4\ N}{r_1^{\ 2}} \left(\frac{r_1}{r}\right)^{0.75} \left(\frac{r_1}{r_1 + r}\right)^{3.25} \left(1+ \frac{r}{11.4 r_1}\right) m^{-2}$$

where r_1 = 79 m at sea level and $\Delta(r,N)$ is the density of a shower of size N at distance r from the axis. The dependence of the collecting area, A_N, on shower size for both inner ring and outer ring triggers are shown in Figure 4.7. It is necessary to mention that in this particular section, the zenith angle dependence of collecting area is neglected, in other words we have assumed that all shower axes are perpendicular to the ground. It is also necessary to use an established integral size spectrum and the one given by Ashton and Parvaresh (4.2.6) which can be summarized as :

$$\begin{aligned} R(\geqslant N) &= 3.0 \quad N^{-1.30}\ m^{-2}\ sec^{-1}\ st^{-1} \text{ for } N \leqslant 7.10^5 \\ R(\geqslant N) &= 36920.0\ N^{-2.0}\ m^{-2}\ sec^{-1}\ st^{-1} \text{ for } N \geqslant 7.10^5 \end{aligned} \qquad (4.a)$$

has been used.

The differential rate of showers of size N is calculated by differentiating eqns (4.a).

$$R(N) = 3.9 \quad N^{-2.30}\ m^{-2}\ sec^{-1}\ st^{-1}\ N^{-1} \quad \text{for } N \leqslant 7.10^5$$

$$R(N) = 73840.0\ N^{-3.0}\ m^{-2}\ sec^{-1}\ st^{-1} \quad \text{for } N \geqslant 7.10^5$$

Using the following formula the differential triggering rate is calculated and shown in Figure 4.3 :

$$R(N) = R(N) \times A_N \quad sec^{-1}\ st^{-1}\ N^{-1}$$

As it is clear from Figure 4.3, the differentiation of the integral size spectrum, (4.a) caused a discontinuity at $N = 7.10^5$ and since our calculation based on graphical solutions, the discontinuity was smoothed out. The area under the curve of Fig 4.3 is evaluated numerically assuming each pair of points are connected by a straight line. The results which are the rate of shower of size N that produce an EAS trigger for both the inner ring and the outer ring triggers are shown in Figure 4.4.

4.3.3 Rate of Showers Whose Cores Fall at a Distance >r From the Centre of the Array, (Detector C), as a Function of r

To start with, an important assumption is made and that is, the areas shown in Figure 4.2 (collecting area, A_N) are approximated by circles of radius r_N centred at detector C where $\pi r_N^2 = A_N$. It is understood that any shower size, N, corresponds to an area A_N, (Figure 4.2) and a radius r_N. Considering the following integral

$$R(>r) = \int_{r_N}^{\infty} R(>N(r))\ 2\pi r\, d r \qquad (4.b)$$

where $R(>N(r))\ 2\pi\, rdr$ is the rate of showers of size greater than N, corresponding to core distance r, which fall in the area $2\pi rdr$, a plot is made of $R(>N(r))2\pi rdr$ as a function of r (Figure 4.5). To evaluate equation (4.b) the area under the curve of Fig 4.5 is numerically calculated and the result which is the required rate is plotted in Figure 4.6.

4.4 RESULTS

To obtain the vertical differential size spectrum R(N,0) from the experimental data assume that the differential size spectrum at zenith angle θ is given by :

$$R(N,\theta) = R(N, 0)\cos^n\theta \ m^{-2}\ sec^{-1} st^{-1}/\text{unit } N \qquad (4.c)$$

The number of showers, x, of size N/unit N traversing a collecting area, $A(\theta)$, in the horizontal plane in time t that have

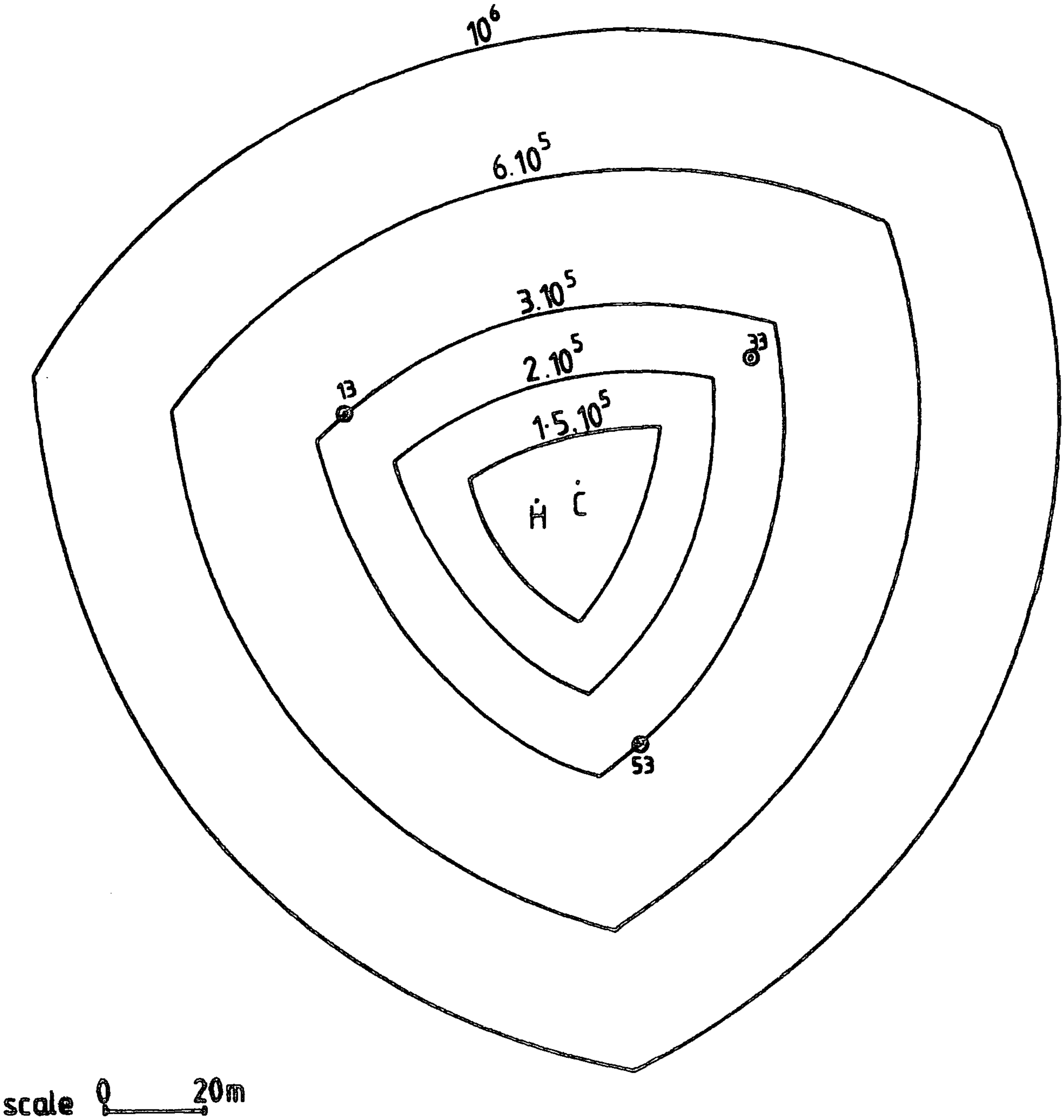

Figure 4.2 : A scale diagram showing the outer ring triggering detectors. Air showers of size indicated on the curves must fall inside the area defined by the curve to satisfy the trigger conditions, $\Delta_C (\geq 4\ m^{-2})$, $\Delta_{13} (\geq 2m^{-2})$, $\Delta_{33} (\geq 2m^{-2})$ $\Delta_{53} (\geq 2m^{-2})$

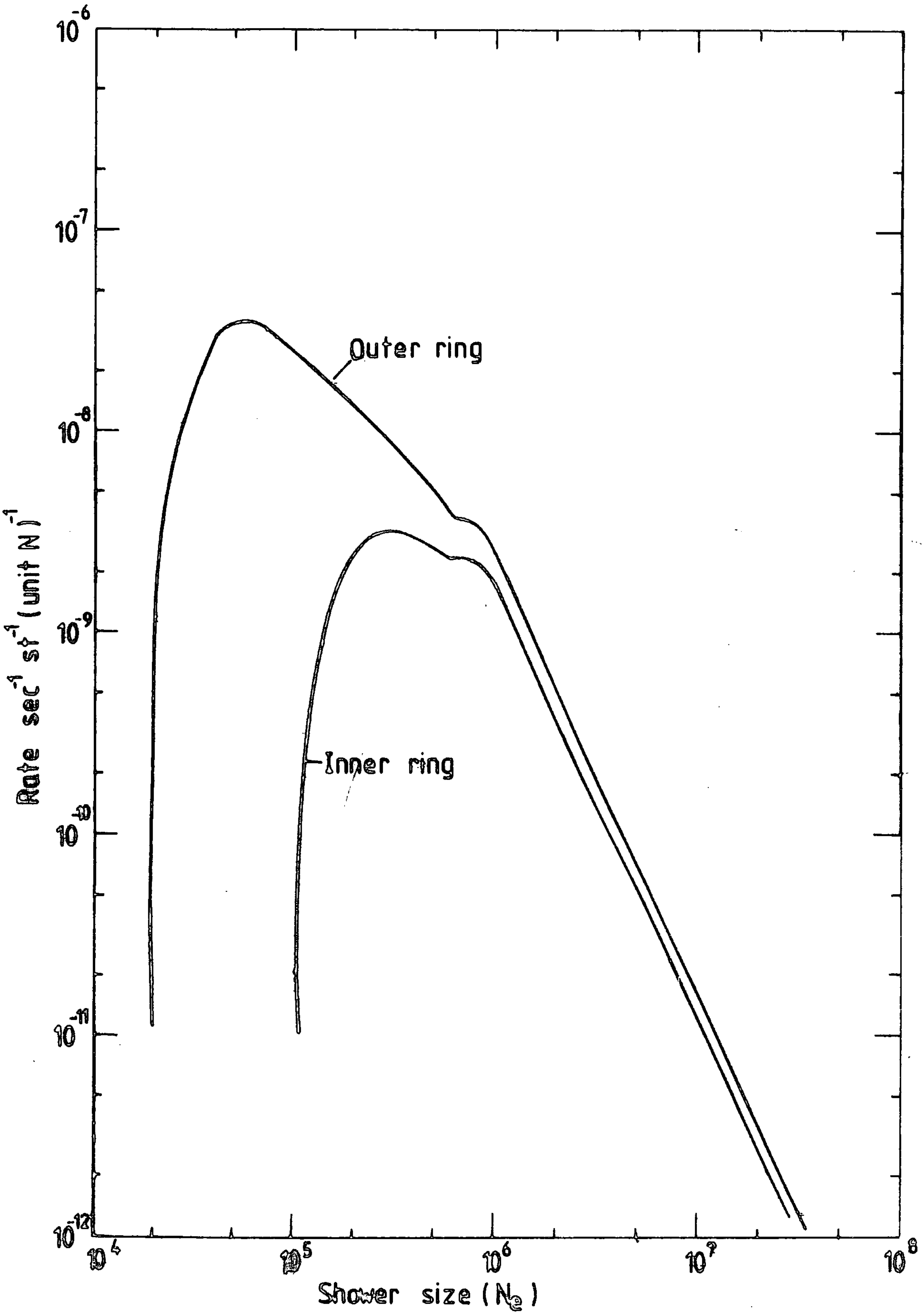

Figure 4.3 : Differential triggering rate for the inner and outer ring triggers.

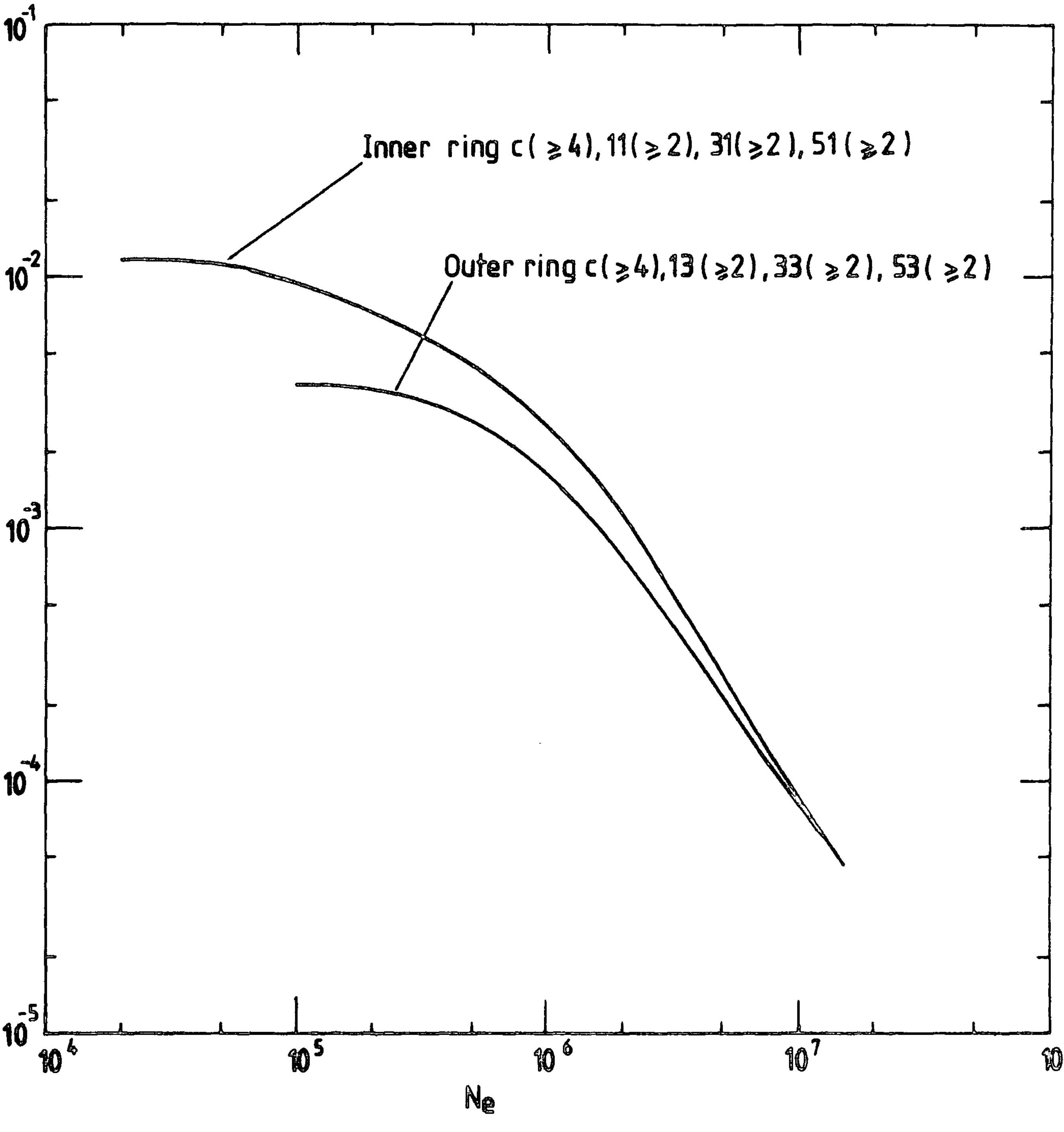

Figure 4.4 : A plot which indicates the rate of showers of size N that produce the indicated EAS trigger. The numbers in brackets are the triggering particle densities (m^{-2}).

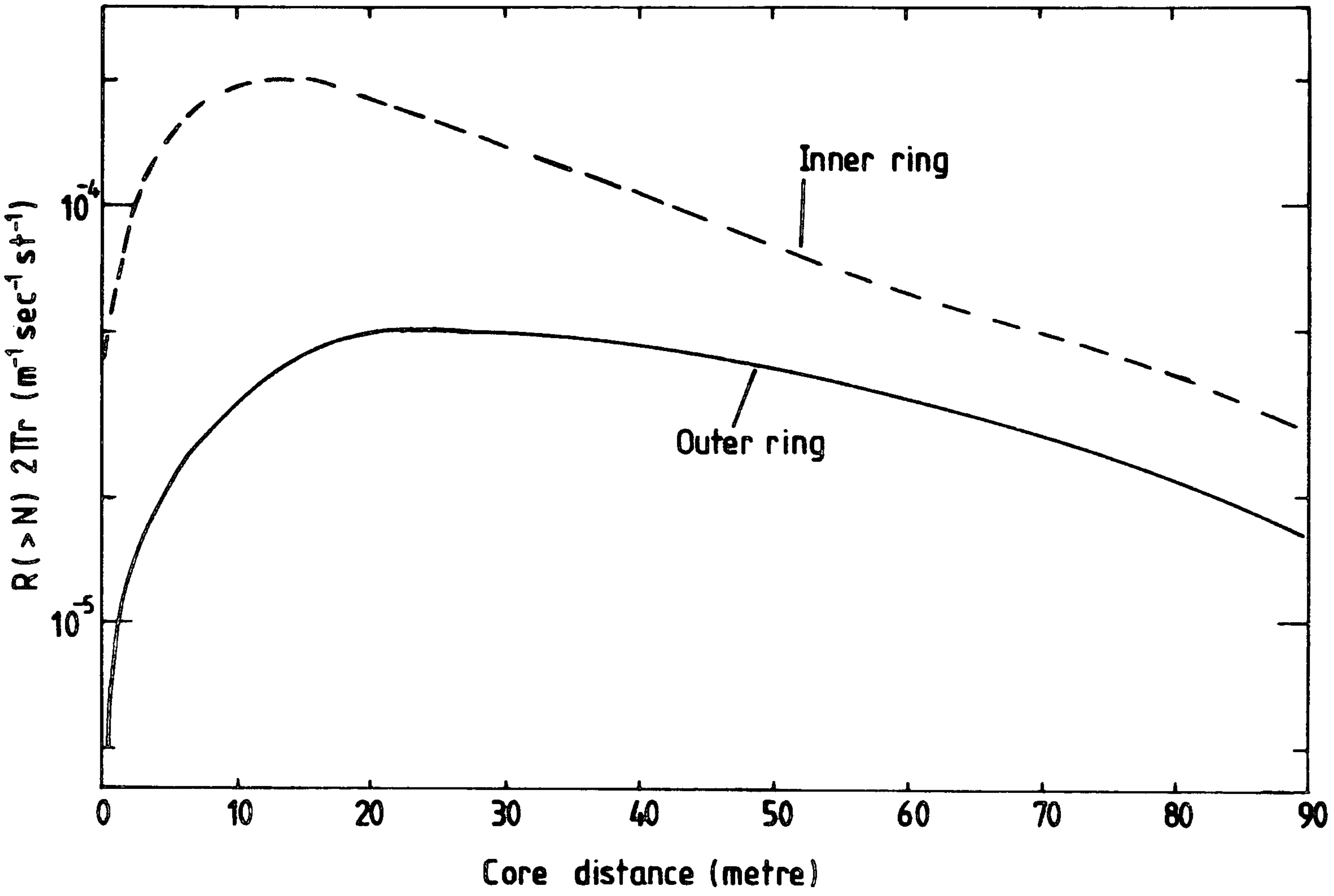

Figure 4.5 : The plot of R(> N) 2π r as a function of core distance.

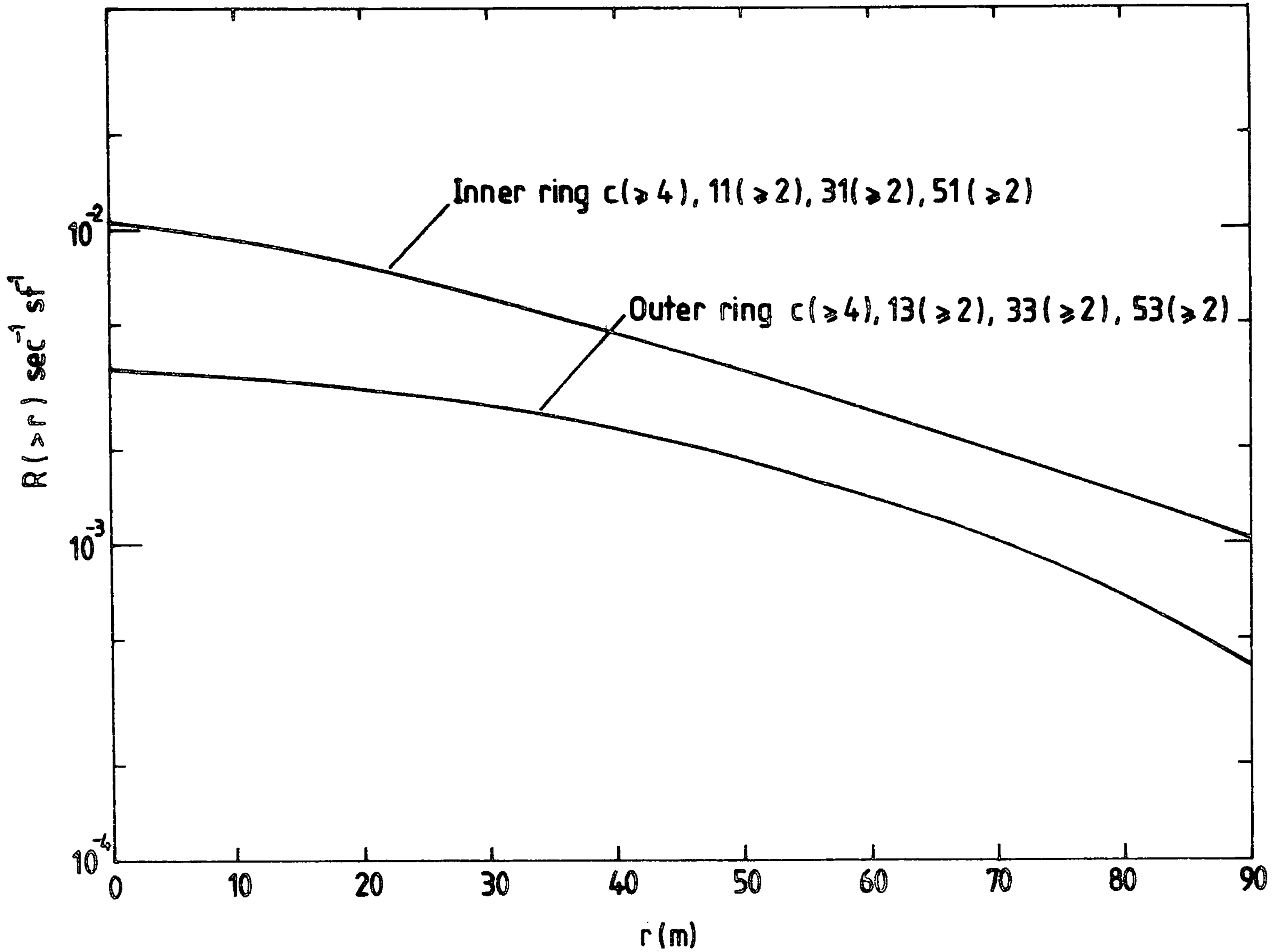

Figure 4.6 : Rate of showers whose cores fall at a distance > r from the centre of the array (detector C), as a function of r. The numbers in brackets are particle densities (m^{-2}).

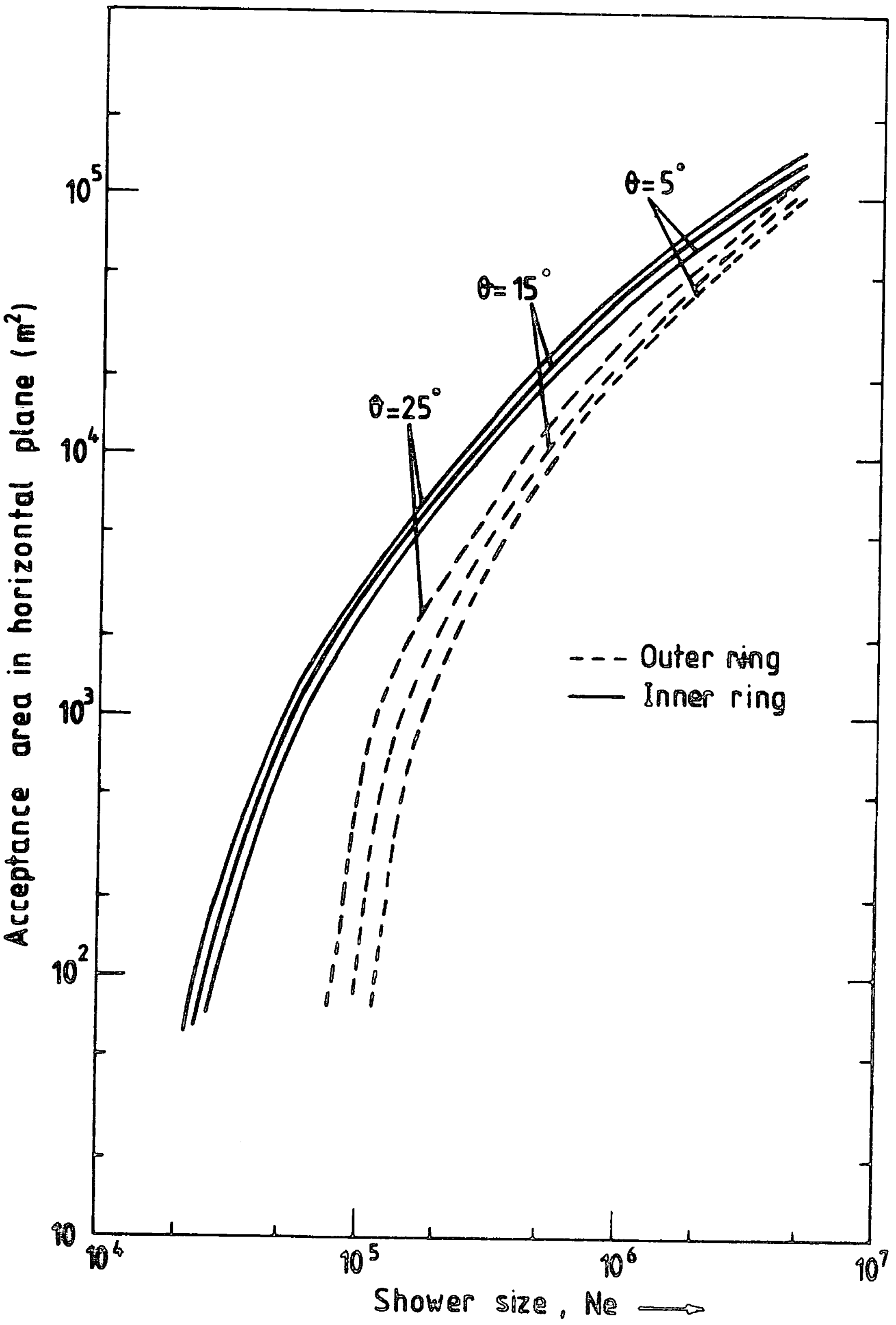

Figure 4.7 : Variation of collecting area with shower size for different zenith angles for both the inner and outer ring triggers.

zenith angle θ is given by :

$$x = \int_0^\theta R(N,\theta) . A(\theta) . \cos\theta . t . 2\pi \sin\theta \, d\theta$$

substituting eqn. 4.c in this equation gives :

$$x = R(N,o).t.2\pi \int_0^\theta A(\theta) \cos^{n+1}\theta \sin\theta \, d\theta$$

$$\therefore \quad R(N,o) = \frac{x}{t.2\pi \int_0^\theta A(\theta).\cos^{n+1}\theta .\sin\theta \, d\theta} \qquad (4.d)$$

It is clear that the collecting area is dependent on zenith angle θ and figure 4.7 shows this dependence. For near vertical showers one can assume $A(\theta) = A =$ constant and eqn. 4.d becomes :

$$R(N,0) = \frac{x}{t.2\pi.A\left(\frac{1-\cos^{n+2}\theta}{n+2}\right)}$$

Using the information of the curves in Figure 4.8 and assuming $n = 8.3$, (Ashton et al (1979)) eqn. (4.d) can be numerically evaluated to find the differential rate of showers of size N/unit N incident vertically at sea level.

The 4819 showers used in the analysis were required to have zenith angle $\theta < 50^o$ and core distance from the central detector of the Durham EAS array of $<$ 75 m.

4.5 DISCUSSION AND CONCLUSION

The results for the differential rate of showers incident vertically at sea level is shown in Figure 4.8 where lines (a) and (b) are best estimates from EAS density spectrum and EAS measurements respectively. Figure 4.9 shows the integral size spectrum of showers incident vertically at sea level as obtained from Figure 4.8 and again a comparison is made with previous work.

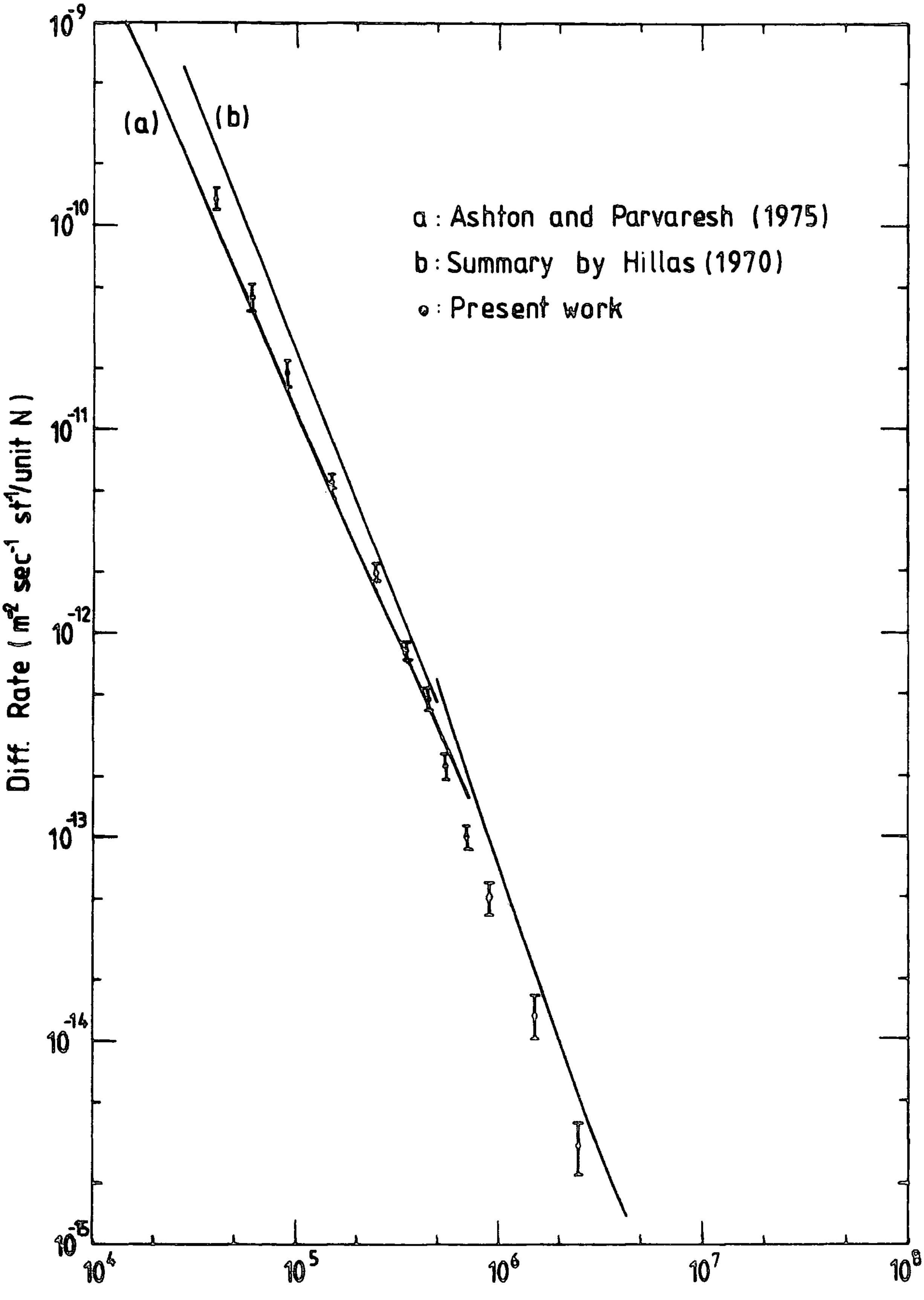

Figure 4.8 : The differential size spectrum of EAS incident vertically at sea level.

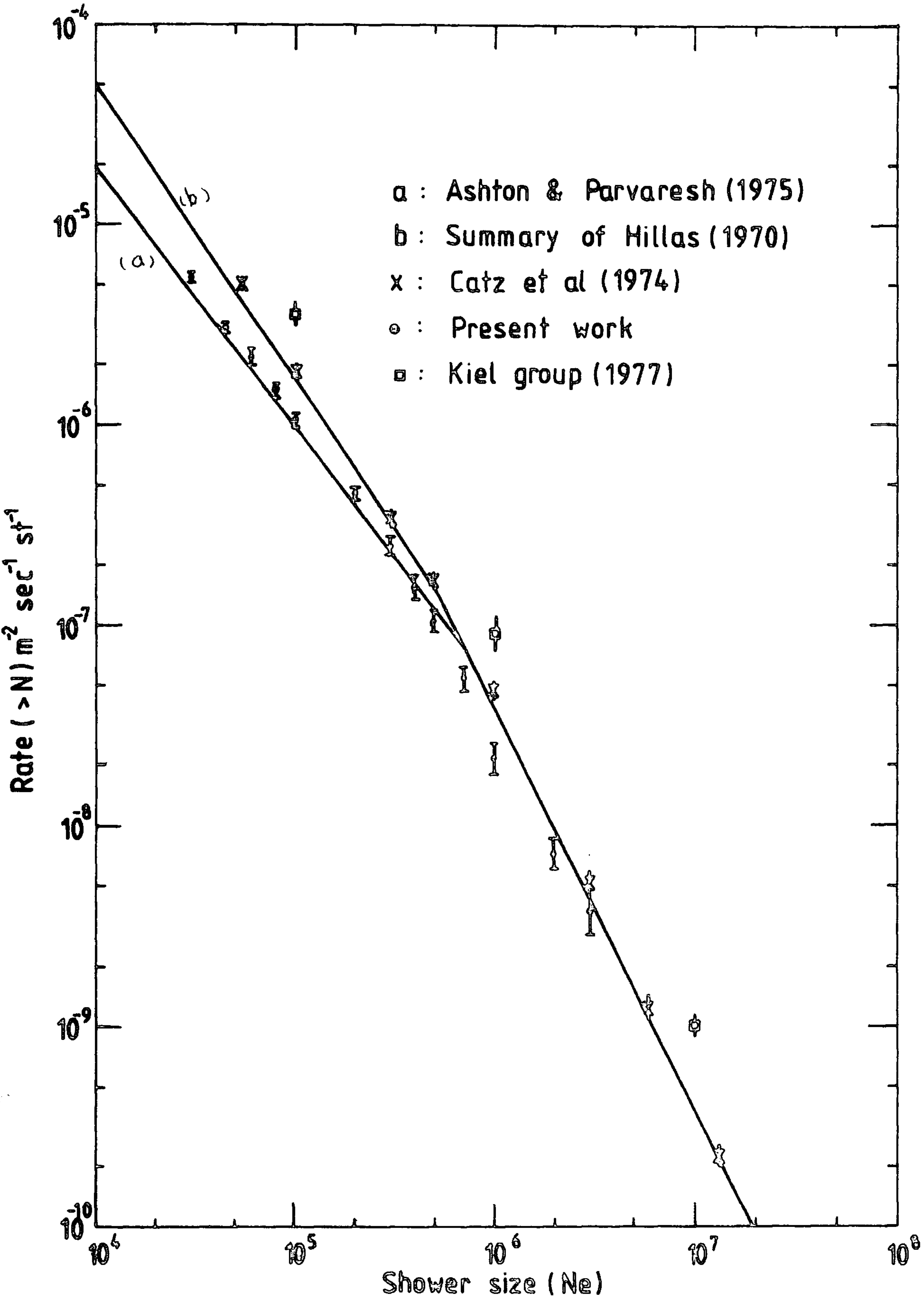

Figure 4.9 : The vertical, integral size spectrum at sea level.

In this chapter the rate of showers of size $\geq N$ which produce the air shower trigger and the rate of showers whose cores fall at distances greater than r are calculated. Looking back at Figure 4.9, it is clear that the present measurement of the vertical sea level integral size spectrum, over the size range of 2.10^4 to 4.10^6 particles, gives intensities that are significantly lower than previous measurements using EAS arrays.

CHAPTER FIVE

MUON COMPONENT OF E.A.S.

5.1 INTRODUCTION

Although it is many years since muon was discovered, its relation to the other particles and the role it plays in the structure of the matter is still far from clear. Muon is identical to electron in many ways, except that it is about 200 times as massive and decays as follows :

$$\mu^{\pm} \rightarrow e^{\pm} + \nu_{\mu} + \bar{\nu}_{e}$$

The majority of muons in EAS are the product of decay of charged pions and kaons high in the earth's atmosphere. The study of muon components of EAS is of interest from many points of view. Because muon only interacts weakly with matter and has a relatively low probability of decay, it is a suitable conveyor of information from high energy interactions of cosmic rays and from early stages of EAS development. Besides, the study of lateral distribution of muons at sea level reveals a lot about the mean transverse momentum of the particles produced in the late interactions, as well as the height of the production of muons and multiplicity of the pion productions.

However, the appearance of muon as a product of the decay of pions and kaons makes it certain that a detailed knowledge of its nucleonic interactions will be of great value in finding a satisfactory theory for the whole family of unstable particles produced in high energy nuclear interactions. In this chapter, measurement of the lateral distribution of muons, the relation between the number of muons and electrons in a shower and the spatial separation distribution of neighbouring muons in flash tube chamber will be discussed.

5.2 DATA ACQUISITION

The flash tube chamber of the Durham EAS array is used as a vidual detector to study muons. Extensive air showers were selected by the inner or outer ring triggers which demanded 4 p m^{-2} at detector C and 2 p m^{-2} in either inner ring detectors, 11, 31, 51, or outer ring detectors, 13, 33, 53 (Chapter 2).

Shower size, core distance and arrival direction of each air shower is determined by employing computer analysis technique (Section 3.9). Muon densities were measured at the plane situated between the two sections F2 and F3 in Figure 2.9. To be accepted for analysis, muons are required to have a track length of greater than 60 cm in the flash tubes and be parallel to within $\pm 5^{\circ}$. The lead and iron absorbers on top of the chamber provide an energy threshold of 500 MeV for muons to reach the level of measurement. Only events with core distance less than 75m and zenith angle less than 50° were accepted, and with these criteria, a total of 4483 events were analysed.

5.3 LATERAL DISTRIBUTION OF MUONS

5.3.1 Introduction

A detailed theoretical analysis has shown that the lateral distribution of muons can give information about the mean transverse momenta of pions produced in interactions of energy around 10^{14} - 10^{15} eV (Adcock et al (1970)) and that the spectrum of numbers of the recorded parallel muons is related to the multiplicity of pion production at the primary energies quoted.

The best method of measuring lateral distribution of muons is to measure the distribution for every single shower and then average the results but this requires a large number of detectors and practically is impossible. However, the experimental measurements of the lateral distribution of muons seem to be on average slightly flatter than expected, especially for events with core distance below 20m. This broadness perhaps is partly due to error in core location and partly could reflect a larger transverse momentum than it is usually assumed. More recent studies of muons reveal that it is not possible to postulate that the wide lateral distribution observed is merely arisen because of the high transverse momentum, but greater heights of origin must be assumed. This is confirmed especially in energy region (1-50) GeV, where accelerator data is available.

5.3.2 Survey of Previous Measurements

All the measurements on the lateral distribution of muons at sea level are restricted to certain core distances, shower sizes and energy threshold and also depend on altitude of observation which all of these factors make a direct comparison difficult. However, experimental measurements are in good agreement with each other, but facing discrepancies when it comes to compare them with theoretical predictions. So here experimental works as well as theoretical analysis will be discussed.

A summary of some of the previous measurements on the low energy muons ($1 < E_\mu < 10$) GeV is shown in Figure 5.1,

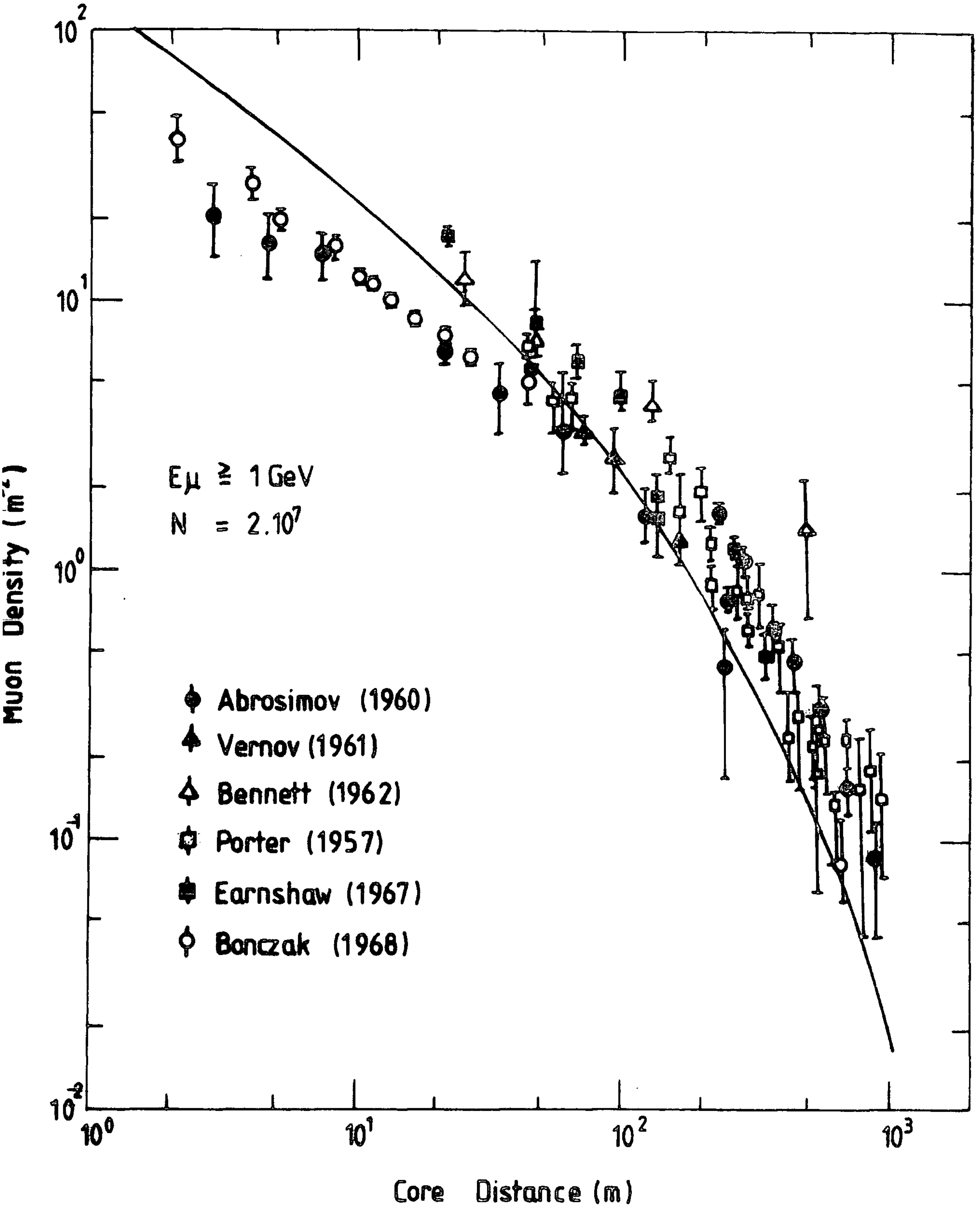

Figure 5.1 : A summary of measurements on lateral distribution of muons where $E_{\mu} \geq 1$ GeV. All the data are normalized to $N_e = 2.10^7$ particles. The continuous curve was calculated according to Greisen's formula (After Wdowczyk, 1973).

(Wdowczyk, (1973)), where experimental data are compared with Greisen lateral distribution function which has the form of

$$\rho_\mu\,(N_e, r) = \frac{14.4\ r^{-0.75}}{(1 + r/320)^{2.5}} \left(\frac{N}{10^6}\right)^{0.75} \left(\frac{51}{E_\mu + 50}\right) \left(\frac{3}{E_\mu + 2}\right)^{0.14\ r^{0.37}} \tag{5.1}$$

where r is expressed in metre and E_μ in GeV. This formula is valid for E_μ = 1-10 GeV.

Looking at Figure 5.1, indicates that the measured distributions, especially for $r < 20$m, are slightly broader than expected, and indeed this is the case for any measurement compared with predictions based on the standard (CKP) model. In order to get better consistency between the two, it is necessary to assume either higher pion transverse momentum or an increasement in the height of the muon productions, and as it was mentioned earlier for low energy muons where accelerator data is available it is proved that the more likely possibility is the second one.

Many people such as Grieder (1976), Kempa et al (1977), and Gaisser et al (1978) have attempted to predict lateral distributions based on new models (isobar-fireball models, scaling,..) or a reformed CKP model.

Figure 5.2 shows a collection of low energy muon data at sea level, normalized to $N_e = 10^5$, compared with the theoretical predictions by Grieder (1976). In Figure 5.2 curves 1 and 2 are the result of calculations with the slow multiple fireball model (SMFB) and single fireball model (SFB) respectively with constant cross sections where curve 3 is for the intermediate double fireball model (IDFB) with rising cross sections. These three curves are for proton initiated showers. Curve 4 is

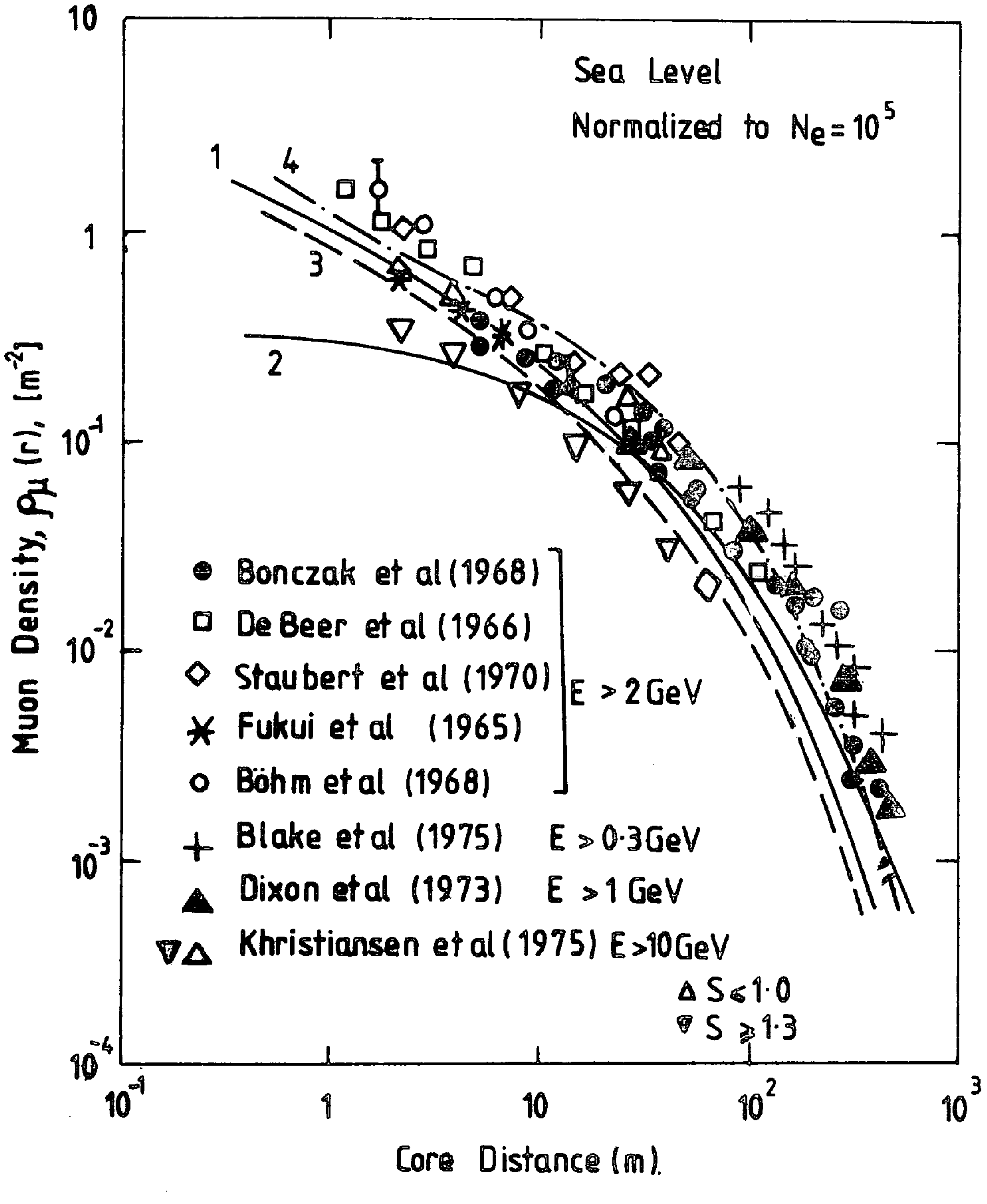

Figure 5.2 : Lateral density distribution of low energy muons ($E_\mu > 1$ GeV) at sea level. Curves 1 to 4 correspond to different models and experimental data are normalized to $N_e = 10^5$ (After Grieder 1976).

for showers initiated by primary iron nuclei, and is obtained by means of SMFB model with constant cross sections. It should be noted that the transverse momentum distribution for all the curves are the same (more information about the models can be found in Chapter 6 and also in reports by Grieder (1976)).
In Figure 5.2, curve 1 agrees quite well with most of the data throughout the distribution and curve 2 disagrees with the bulk of the experimental data within the 15m from the core. Curve 3 yields an acceptable fit around 100 metres while Curve 4, which is initiated by iron nuclei primary, shows an excess of particles at some ten metres from the axis. However, it seems that the experimental data tend to agree with those models which support a mean multiplicity dependence of the form $< n > \alpha\ E^{0.37}$ or $< n > \alpha\ E^{0.50}$ rather than $<n> \alpha\ E^{0.25}$ which is originally assumed in the standard (CKP) model.

5.4 PRESENT WORK ON LATERAL DISTRIBUTION OF MUONS

5.4.1 Method of Analysis

In order to obtain lateral distribution of muons, a number of assumptions and pre-calculations are made. It is assumed that the lateral distribution of muons has the following form of

$$\Delta_\mu (E,r) = g (N) f (r)$$

In other words, the density of muons can be shown as a product of two independent functions of N and r (g(N) and f(r)). Therefore, to construct the lateral distribution of muons, at first the relation between muon density and shower size has to be determined. To do this, Figure 5.3 which shows the relation between the number of muons observed in the flash tube chamber and shower size for showers with core distance in the range of (0-10)m is prepared.

There are two reasons why the limited range of core distances and in particular (0-10)m is used. Firstly, in order to be sure that the data which is shown in Figure 5.3 is independent of the core distance, showers with almost the same core distances were required. The second and more important reason is that, as it has already been discussed, the probability of detecting a shower of size N strongly depends on the acceptance area or indeed the core distance (Figure 4.7). Therefore, if all the data was used, it would have needed a correction due to this fact that smaller showers have less probability of being detected and to avoid this the core distance range of (0-10)m was used, because almost all showers with any size in the range $1.5.10^4 - 4.10^6$ particles which fall within this range of core distance could trigger the array. A linear regression fit to the data of Figure 5.3 gives :

$$\bar{n}_\mu = 0.63 \; N_e^{0.69 \pm 0.08}$$

This relation is used to normalize the showers to the appropriate values.

Assuming $N_\mu = A \; N_e^\alpha$, other measurements on the dependence of the number of muons N_μ on shower size N_e, (e.g. Wdowczyk et al,(1973) and Gaisser et al(1976) suggest a value for α around 0.75 which is in good agreement with present work.

5.4.2 Results

After normalizing all the data to a median shower size of 3.10^5, the lateral distribution of muons at sea level is

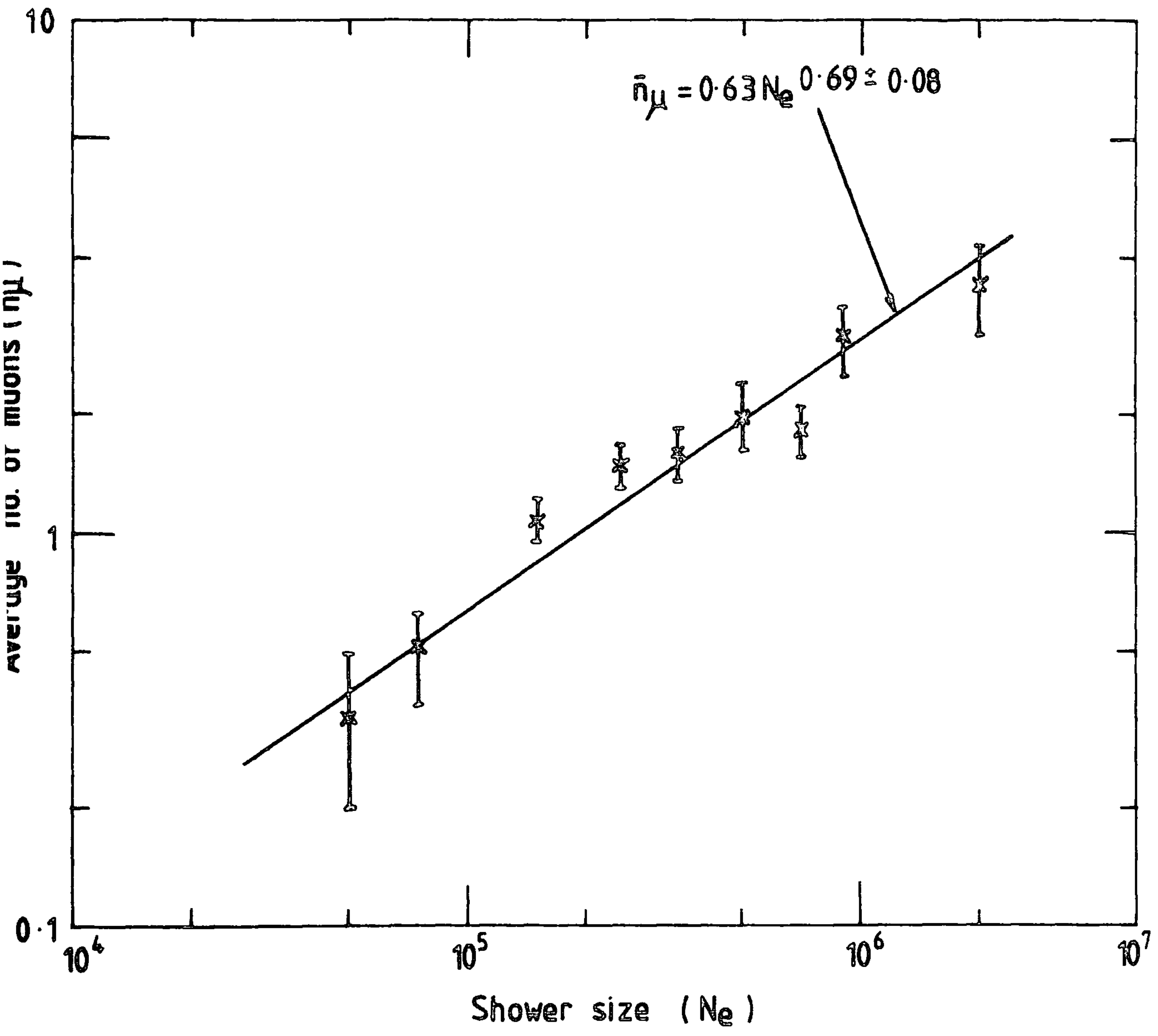

Figure 5.3 : Average number of muons in chamber as a function of shower size for events with the orthogonal core distance in the range of (0-10)m.

plotted in Figure 5.4, where for comparison predictions of Greisen (Equation 5.1) is also shown.

As it is clear from Figure 5.4, similar to most of other measurements, our results show a broader distribution than expected and especially over the core distance range of (25-75)m the measured density is consistently larger than the values given by the Greisen formula, the mean excess being a factor of 1.36. In order to see the zenith angle dependence of the lateral distribution, the data is divided into two groups of near vertical showers ($\theta \leq 25^0$) and showers with large zenith angles ($\theta > 25^0$) and plotted in Figure 5.5. It is seen from this figure that there is no evidence for a significant change of the muon lateral structure function for showers in the range ($1.5.10^4$ - 4.10^6) particles. Figure 5.6 displays the same data, but grouped into different ranges of shower sizes.

5.5 SPATIAL SEPARATION DISTRIBUTION BETWEEN NEIGHBOURING MUONS IN THE FLASH TUBE CHAMBER

5.5.1 Introduction

The most frequent type of event observed in the hadron flash tube chamber, which is triggered by the usual EAS trigger, is one, two or more muon tracks traversing the chamber. The object of this section is to compare the experimental distribution of spacing between muons observed in one plane with that expected for a spatially random flux of EAS muons. At first the simplest case of two parallel muon tracks will be considered and then the problem will be generalised. Assuming the muon tracks are randomly related the probability that two parallel muon tracks have separation t, measured at the level MN of Figure 5.7, can be calculated. Let α be the probability that a muon track falls per unit distance anywhere along xy. If

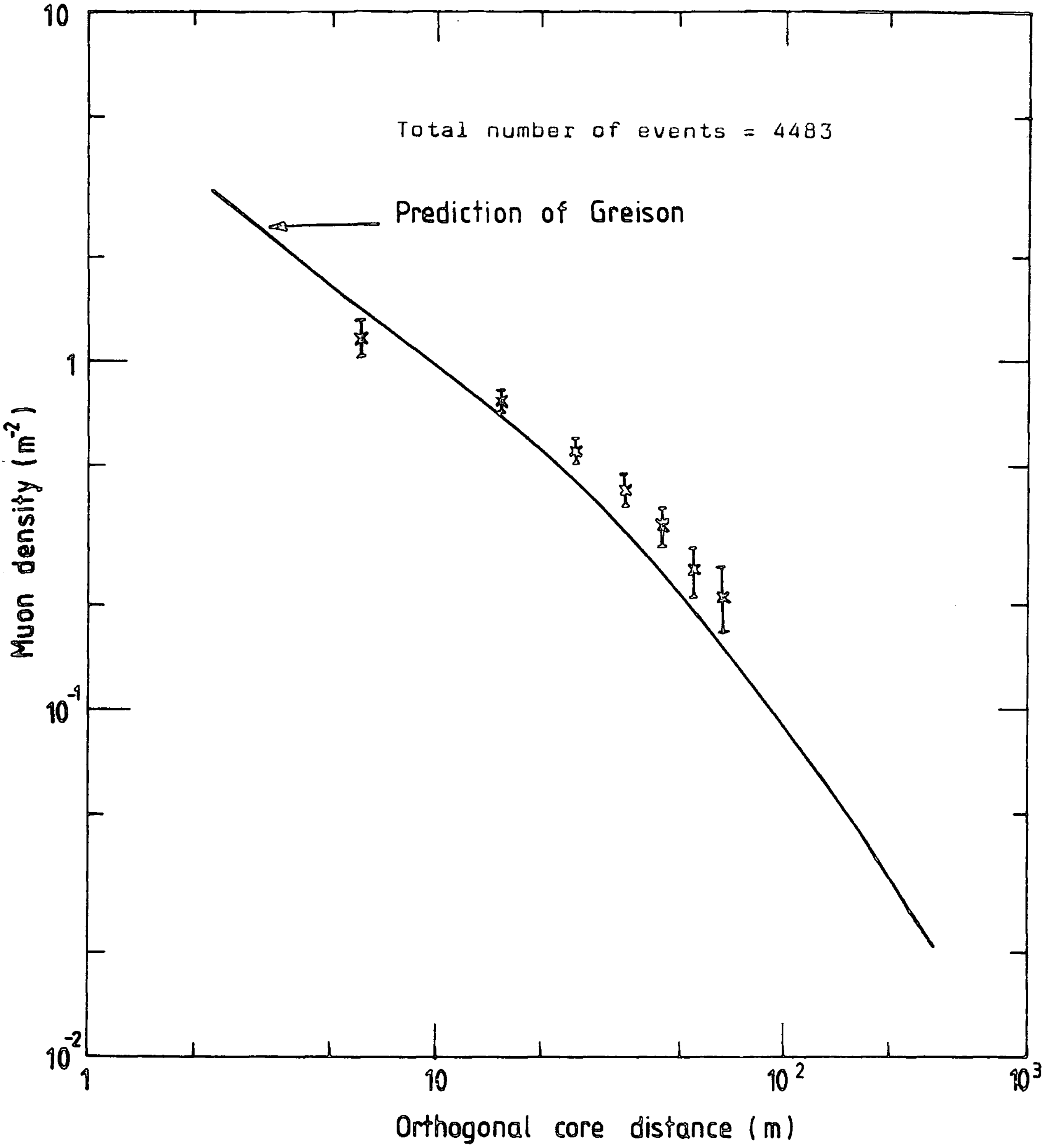

Figure 5.4 : Measurements on the lateral distribution of muons where the solid line is plotted according to the Greisen prediction.

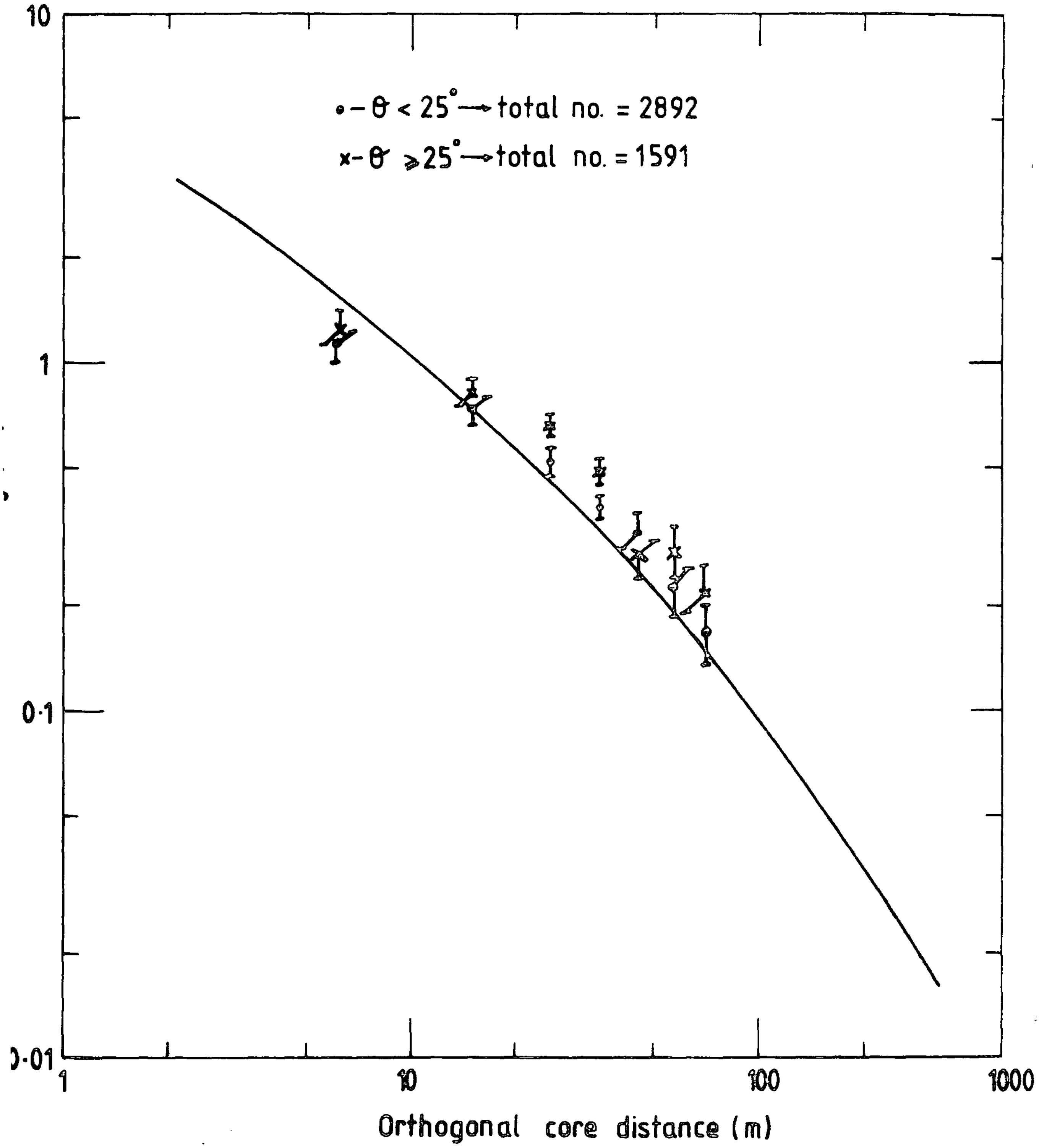

Figure 5.5 : Dependence of the lateral distribution of muons on zenith angles. The solid line is based on predictions of Greisen.

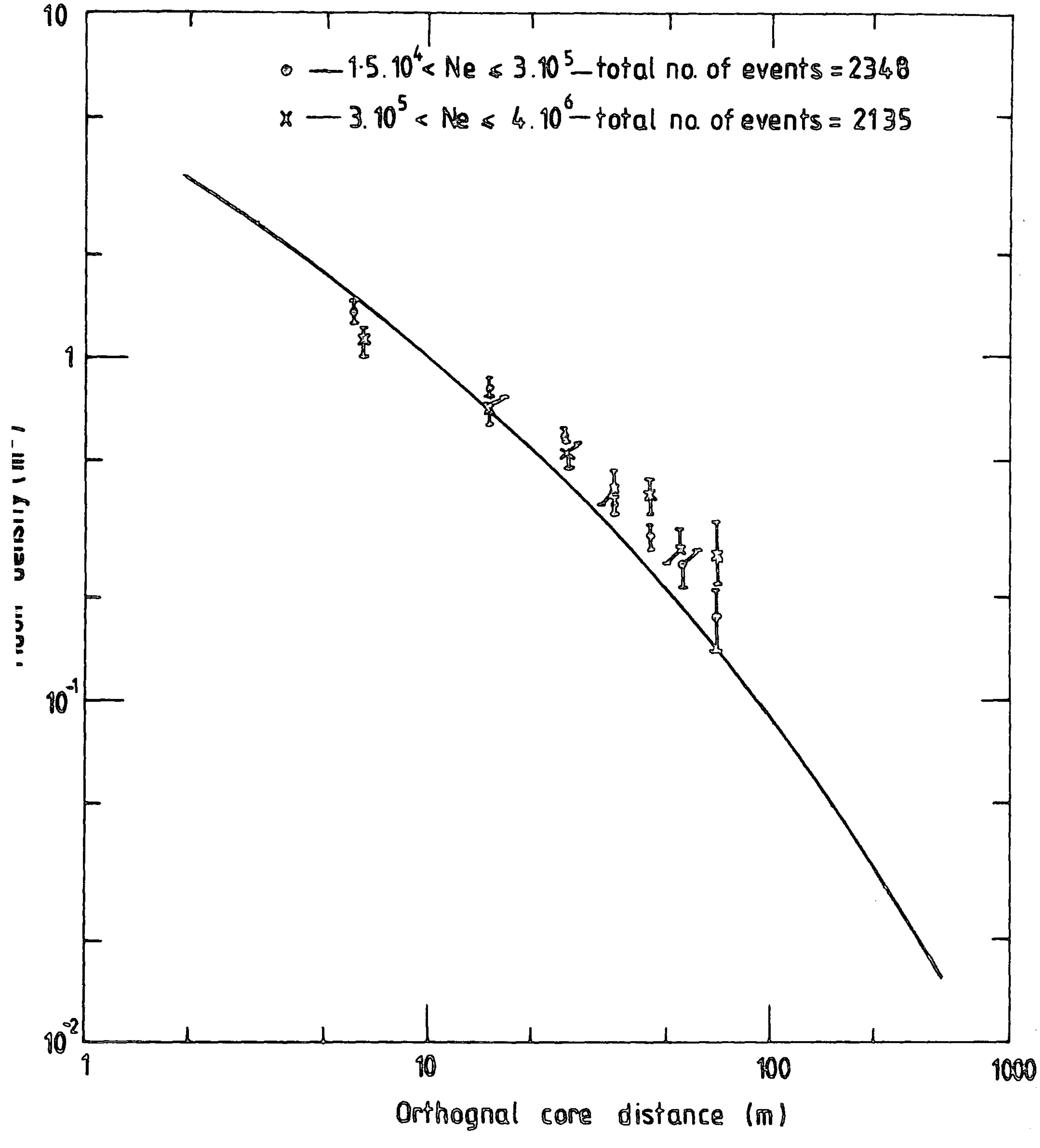

Figure 5.6 : Lateral distribution of muons for two ranges of shower size. The solid line is based on predictions of Greisen.

the first muon track crosses the line xy between x and x +dx and the second muon track between x + t and x + t + dt, as shown in Figure 5.7, then the probability of this occurring $= \alpha\, dx.\alpha dt$. For a separation t the first muon can fall anywhere in the distance 0 to $\ell - t$ where ℓ = 151 cm (the width of the flash tube chamber) and the probability p(t) is given by

$$p(t)\, dt = \alpha^2 \int_0^{\ell - t} dx dt = \alpha^2 (\ell - t)\, dt$$

Requiring $\int_0^{\ell} p(t)dt = 1$ gives $\alpha^2 = \frac{2}{\ell^2}$, thus

$$p(t) = \frac{2}{\ell^2} . (\ell - t)$$

For N observations the number of events n(t) expected with separation t per unit separation is given by

$$n(t) = N. \frac{2}{\ell^2} . (\ell - t)$$

Extending the argument to calculate the probability that the separation between neighbouring random muons is t when 3,4, ...n muons traverse the chamber gives the results shown in Table 5.1.

5.5.2 Results

The frequency of observing 0,1,2, etc. parallel muons in the chamber from a sample of 5014 showers is shown in Figure 5.7. Figures 5.8 (a,b,c and d) show the measured frequency distribution of projected spatial separation t of neighbouring muons for events with muon multiplicities 2,3,4 and 5. The expected distributions, assuming that the muon

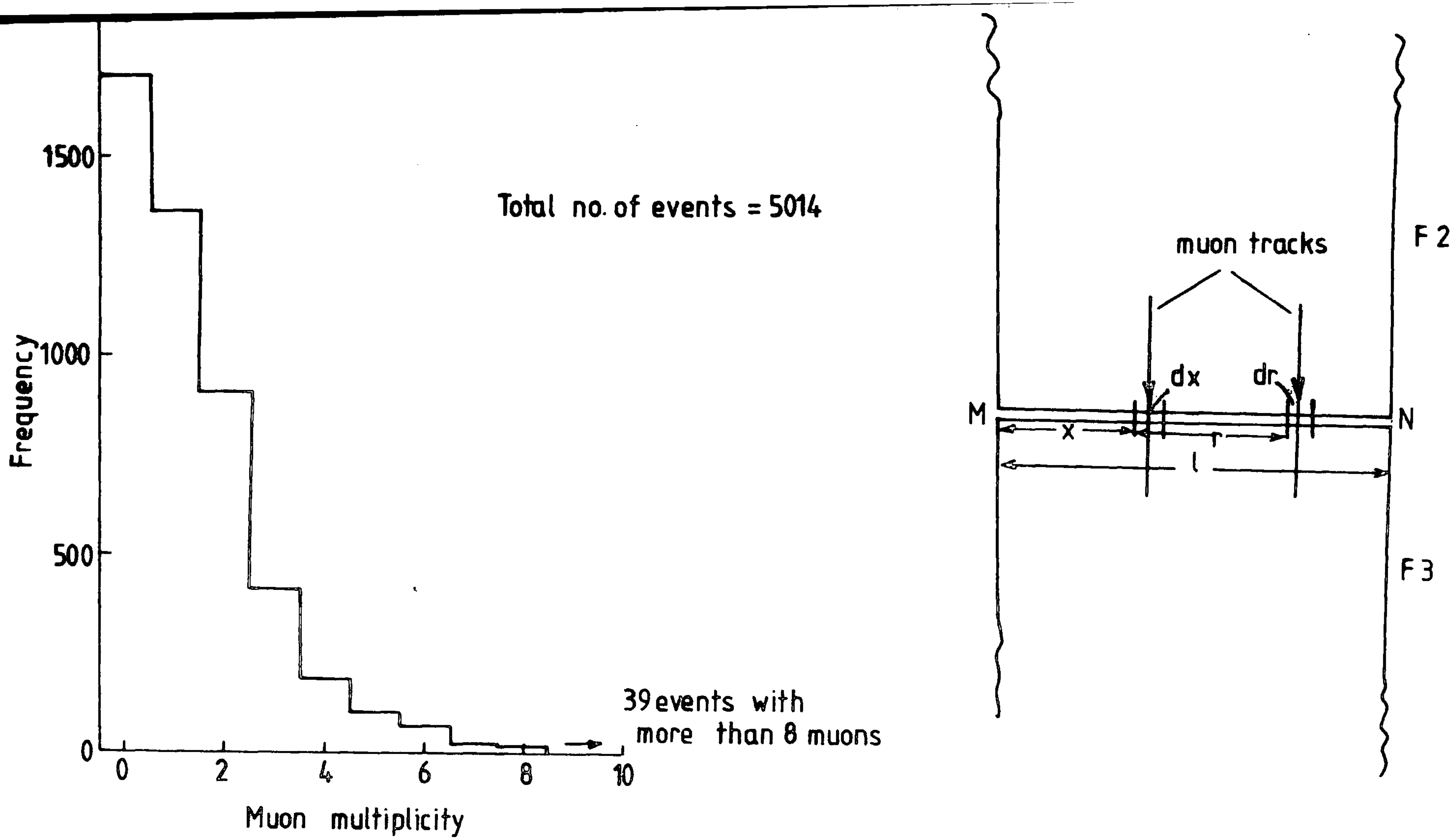

Figure 5.7 : (a) Frequency distribution of observing 0, 1, 2, etc. muons traversing the chamber in a sample of 5014 shower triggers.

(b) Diagram showing 2 muon tracks traversing the flash tube chamber. The separation r is measured.

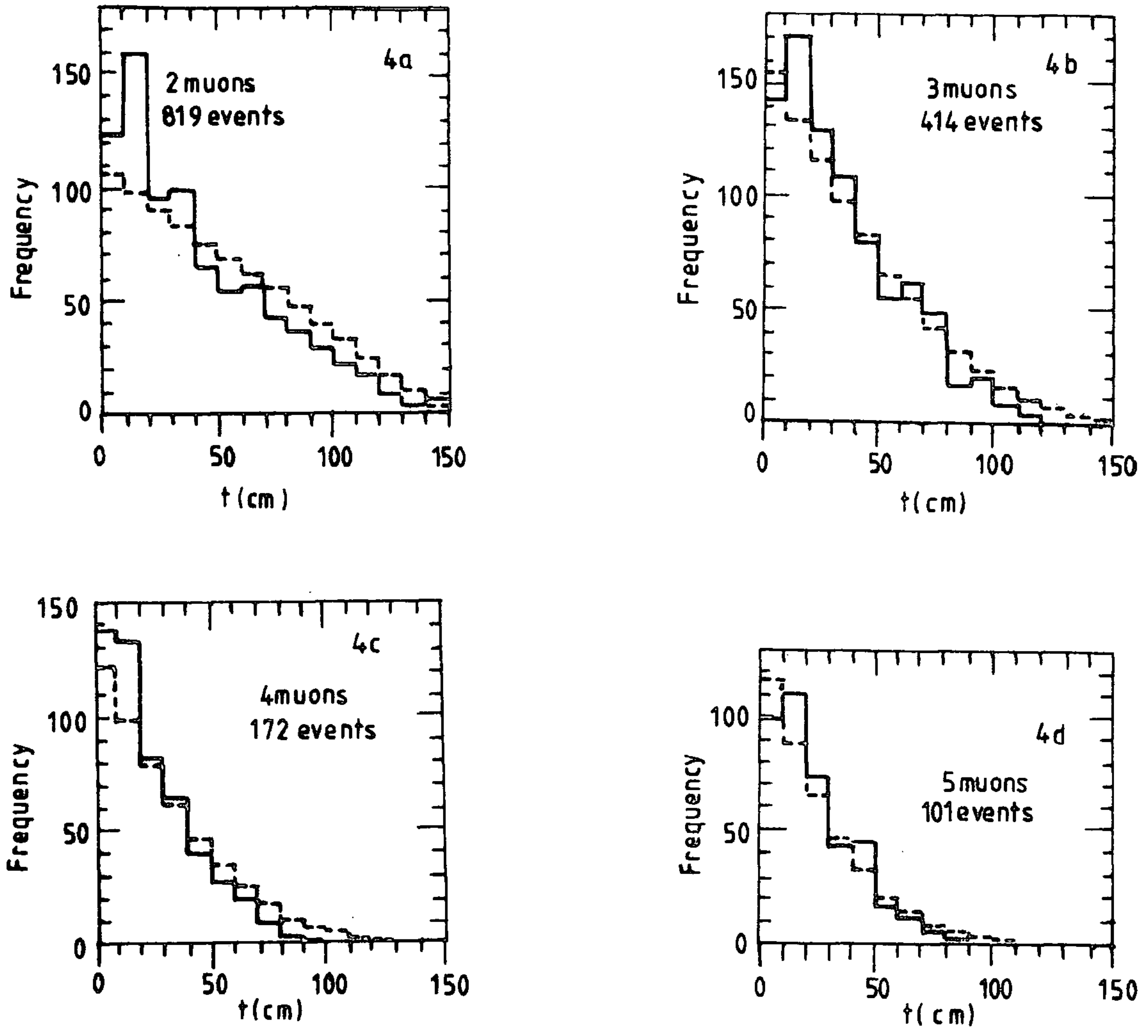

Figure 5.8 : Frequency distribution of projected spatial separation t, of neighbouring muons for events with 2, 3, 4 and 5 muons traversing the flash tube chamber. The dashed lines are the expected distributions, assuming the muons are randomly separated.

No. of unrelated muons in the chamber	Probability P(t) that any 2 neighbouring unrelated muons are separated by a distance t	Mean separation of muons
2	$\frac{2}{\ell^2} \cdot (\ell - t)$	$\ell/3$
3	$\frac{3}{\ell^3} \cdot (\ell - t)^2$	$\ell/4$
4	$\frac{4}{\ell^4} \cdot (\ell - t)^3$	$\ell/5$
5	$\frac{5}{\ell^5} \cdot (\ell - t)^4$	$\ell/6$
n	$\frac{n}{\ell^n} \cdot (\ell - t)^{n-1}$	$\ell/n+1$

TABLE 5.1 : The probability that the separation between random muons is t when 2, 3, 4.....n muons traverse the flash tube chamber.

tracks are unrelated to one another, is also shown in Figure 5.8. It is seen that the assumption that the muons are unrelated gives a reasonable fit to the measurements where the muon multiplicity is 3 and 5, but not for multiplicities 2 and 4.

During the course of the experiment an unusual event is observed and shown in Figure 5.9. The accompanied shower has a size of $N = 1.6.10^6$ particles with a zenith angle $\theta = 7.5^0$, azimuthal angle $\phi = 265^0$ and the orthogonal core distance from the flash tube chamber is 71.4m. Usually, single muon tracks show only one tube flashed per layer of flash tubes, and it is seen for this event that a large number of side by side flashes are observed. It is likely that this event was produced by two closely separated muons, but a further possibility is that it was produced by a single penetrating particle of large Z where Ze is the charge on the particle. Measurements on relativistic muon tracks traversing the chamber show that the average number of side by side flashes produced by knock on electrons is ~ 1.6. For the track shown in Figure 5.9, 53 out of the 96 layers of flash tubes show side by side flashes.

As the number of knock on electrons is expected to increase as Z^2, it is possible that the track is produced by a relativistic penetrating particle with $Z = 5.7$. Fundamental particles with large Z have been produced by Yock (1975) on theoretical grounds.

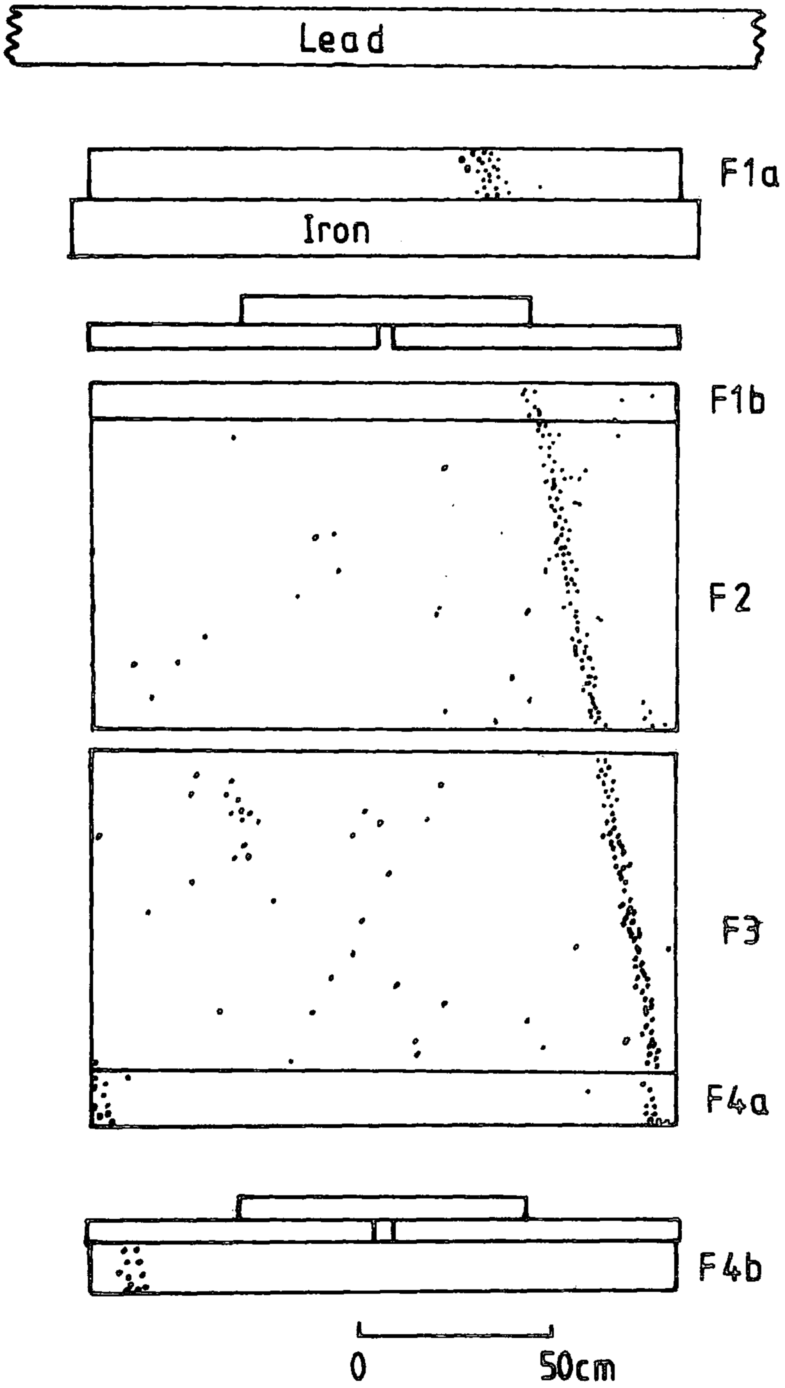

Figure 5.9 : An unusual event seen in the flash tube chamber.

5.6 SUMMARY AND CONCLUSION

Lateral distribution of muons at sea level is studied and measurements show that the absolute density of muons of energy > 0.5 Gev is on average 36% larger than predicted by the Greisen formula, for core distances in the range of 25-75m. The relation between a number of muons and a number of electrons in a shower is investigated and a value of $\alpha = 0.69 \pm 0.08$ is found where $N_\mu = A N_e^\alpha$ is assumed. The distribution of the separation of neighbouring muon groups in the flash tube chamber is studied and the results indicate that the assumption that muons are unrelated fits reasonably well with the data where the muon multiplicity is 3 and 5, but not for multiplicities 2 and 4.

CHAPTER SIX

STUDY OF HADRONS IN EXTENSIVE AIR SHOWERS

6.1 INTRODUCTION

The study of nuclear active particles (NAP) in extensive air showers is a unique source for gathering information in various fields of high energy and particle physics over an enormous range of energy, covering regions many orders of magnitude beyond that of present accelerators. Although hadrons in EAS are the least numerous of all particles, they form the backbone for the development of an EAS and carry the largest percentage of energy in a shower. For many years the study of hadrons has provided a lot of information on the nature of primary cosmic rays, and the development of new ideas such as gammanization and high transverse momenta. Primary cosmic rays that enter the atmosphere interact strongly with the components of an air nucleus and a large number of secondaries are produced in the process of multiple secondary particle production. A simple and well known picture of the development of an air shower is as follows. A primary nucleus collides with a target air nucleus high in the atmosphere and fragments into separate nucleons as well as producing secondary mesons. In this process the surviving nucleons have a much higher energy than the other secondaries and carry off on the average about 50% of the incident energy. The majority of secondaries produced in the interactions are pions in equal numbers of both charges ($\pi^{\pm}$) and neutrals (π^{0}). The neutral pions decay into two photons with a mean lifetime of about 10^{-16} sec. If these photons are energetic enough they give rise to an electron photon cascade in the atmosphere by means of pair production.

$$\gamma + \gamma \rightarrow e^+ + e^-$$

The relativistic electrons produce further γ-rays by bremesstrahlung and the new photons produce further electrons and this cyclic process goes on until the whole electromagnetic cascade reaches sea level. On the other hand charged pions have a lifetime about 10^{-8} sec, within which they may decay into muons and neutrinos

$$\pi^{\pm} \rightarrow \mu^{\pm} + \nu_{\mu}$$

or interact with air nuclei producing more pions. The nuclear interaction of pions appears to resemble those of nucleons except that the leading particle is a pion which may equally be positive, negative or neutral. The muons produced by pion decay have a lifetime of 2.10^{-6} sec. Low energy muons decay into electrons (positrons) and neutrinos $\mu^{\pm} \rightarrow e^{\pm} + \nu_{\mu} + \nu_e$ Muons have got a good chance of reaching sea level or even be detected underground as they are not strongly interacting particles as are nucleons and pions. This is a simple and brief explanation of the essential elements and factors in forming an EAS. Owing to the high degree of complexity of the phenomena, a very important role in understanding EAS is played by detailed theoretical models and calculations of EAS development in the atmosphere.

6.2 DIFFERENT MODELS USED IN EAS SIMULATIONS

6.2.1 Introduction

An air shower model in general consists of two main parts, the particle production and propagation model. In principle, any high energy particle production and propagation model could be used and this is almost exactly what has happened in the past. Since all details of the nature of interactions and particle production are not well known, it seems necessary to perform the calculations by a method of successive approximations. At first a simple model is derived by extrapolating the results from the lower energy regions where direct and accurate measurements are available and then the calculations are compared with the experimental data. The deviation of observations from the prediction of the model are used for the modification of it in later stages. The necessary modifications should be suggested on the basis of a detailed understanding of the sensitivity of various parameters of EAS to different features of the high energy interaction model. In the following a number of models will be discussed and wherever necessary the results of simulations based on these models will be presented for comparison.

6.2.2 Standard CKP Model

The standard CKP model which is named after Cocconi, Koester and Perkins, is undoubtedly one of the first and most popular models that has been used in cosmic ray simulations and calculations. Properties of this model can be summarized as follows (after De Beer et al (1969)).

(i) High energy nucleons lose on average 50% of their energy in each collision and have an interaction mean free path in the atmosphere of 80 gr cm^{-2} ; both these quantities being independent of energy.

(ii) The secondary particles are mainly pions, there being on average equal numbers of $\pi^{\pm}$, π^{-} and π^{0} mesons produced.

(iii) The pions have an energy distribution in the laboratory system given by an empirical relation, which when allowance is made for particles emitted in the 'backward cone' can be written as :

$$S(E,E_0) = \frac{1}{2}\left\{ \frac{n(E_0)}{\Gamma} \exp\left(-\frac{E}{\Gamma}\right) + \frac{n(E_0)}{G} \exp\left(-\frac{E}{G}\right) \right\}$$

where $n(E_0)$ is the multiplicity of pions produced, E_0 is the transferred energy, G is the average energy of pions in the backward cone and, $\Gamma = 2(E_0 - \frac{1}{2}\, n(E_0)\, G)/n(E_0)$ is the average energy in the forward cone.

(iv) It is assumed that the fraction of energy lost by a nucleon which does not appear as pions is negligible.

(v) The multiplicity of secondary pions, ns is given by ns = $2.7\, E_p^{\frac{1}{4}}$ with E_p in GeV for k = 0.5 and ns = $2.7 . 2^{\frac{1}{4}}(kE_p)^{\frac{1}{4}}$ for all k. k is the inelasticity of the interacting primary.

(vi) The distribution in transverse momentum, P_t, of the produced pions is given by the expression suggested by Cocconi, Koester and Perkins :

$$f(P_t) = \frac{P_t}{P_0^2} \exp\left(-\frac{P_t}{P_0}\right)$$

the mean transverse momentum $2p_0$ is assumed to be independent of energy and equal to 0.4 GeV/c.

(vii) Pion interactions are assumed to differ from nucleon interactions in that they are catastrophic with interaction length of 120 g cm^{-2}. The energy spectrum of the pions produced in pion production is taken to be that given by the same relation as for protons but with K = 1, in other words :

$$n_s = 3.2 \; E_p^{\frac{1}{4}}$$

(viii) Fluctuations are allowed for in the calculations to the extent that variations in the inelasticity of nucleon-air nucleus are included, as well as the normal statistical fluctuations in the depth in the atmosphere of the interactions. The adopted form for the inelasticity distribution is : $f(k) = -(1-\alpha)^2 \; (1-k)^{\alpha} \; \ell n(1-k)$ with $\alpha = 1.414$. Predictions and results of simulations based on this model will be used in subsequent discussions and comparisons.

6.2.3 Isobar-Fireball Models

Simulations based on different fireball models have been carried out by Grieder (1976) and the results have been compared with experimental data. The essential features of the showers and high energy models will now be discussed.

Four different models that follow different high energy multiplicity laws have been used to simulate the strong interactions. The interactions are considered as nucleon-nucleon or pion-nucleon interactions whichever applies to the particular case. Usually an interaction mean free path of 75 g cm^{-2} has been used for nucleons and 120 g cm^{-2} for pions. Each interaction is treated individually. The type of interaction depends on the type of particle which initiated it and on the energy which is available in the centre of mass.

It is necessary here to explain briefly about the so called two component model (isobars and fireballs, or diffraction and pionization) which can be summarized as follows :

The isobar component has a very limited energy dependence and is the same for all models. Isobars are assumed to decay into a nucleon and one or several pions, depending on the type of isobar. Therefore the difference lies essentially in the treatment of the fireball component. In the single fireball model (SFB), the fireball is stationary in the centre of mass and its total energy is just its rest mass. The fraction of the total centre of mass energy given to the fireball component is described approximately by a Gaussian distribution, whose mean value is an energy independent parameter. For an energy-independent transverse momentum, the average asymptotic multiplicity is proportional to $E_{lab}^{\frac{1}{2}}$. In the other three models : double fireball (DFB), intermediate double fireball (IDFB) and slow multiple fireball (SMFB), the computed average fireball energy portion is the same as the SFB version but this energy is now shared among two or more fireballs and each share is divided into a kinetic and a mass portion. The resulting multiplicity, which is dominated by the fireball component at high energy, is now a function of the energy dependence of the fireball velocity in the centre of mass. The latter has been chosen such that the asymptotic relations, $<n> \alpha E_{lab}^{1/4}$, $<n> \alpha E_{lab}^{3/8}$ and $<n> \alpha E_{lab}^{3/7}$ result for the DFB, IDFB and SMFB models respectively. Nucleon-antinucleon production is considered in each case and kaon production in some cases. The gross features of the DFB model are very similar to the CKP formula, except that isobar excitation and leading particle effects are considered.

6.3 LATERAL DISTRIBUTION OF HADRONS

6.3.1 Introduction

Measurements of the lateral distribution of hadrons are of interest for two main reasons. The first is that by integrating the lateral distributions the total number of hadrons in a shower can be obtained. Accuracy in the estimation of this parameter depends very strongly on our knowledge of the lateral distribution of hadrons. The second is that since the lateral distribution is determined mainly by the mean transverse momentum, a study of the lateral distribution can give information about the mean value of transverse momentum ($\langle p_t \rangle$) in high energy interactions.

6.3.2 Summary of Some of the Measurements and Theoretical Calculations

(a) Kempa et al

A theoretical analysis of hadrons and their characteristics in EAS has been made using the standard model of EAS development (CKP) described in the previous section, for two multiplicity laws $n_s \alpha E^{\frac{1}{4}}$ and $n_s \alpha E^{\frac{1}{2}}$. Two different approximations were used for the relation between the hadron density and core distance. The first one is $\rho_H \alpha \exp(-{}^{r}/{r_0})$ and the second one is $\rho_H \alpha \exp(-\sqrt[4]{{}^{r}/{r_0}})$. A comparison between experiments and these two theoretical calculations has been made in Figure 6.1a. A comparison of experimental data with the theoretical lateral distribution of hadrons based on $\rho_H \alpha \exp(-\sqrt[4]{r/r_0})$ for two multiplicity laws of $n_s \alpha E^{\frac{1}{4}}$ and $n_s \alpha E^{\frac{1}{2}}$ is shown in Figure 6.1b. The experimental points are seen to be clearly above theoretical calculations and this indicates that $\langle p_t \rangle$

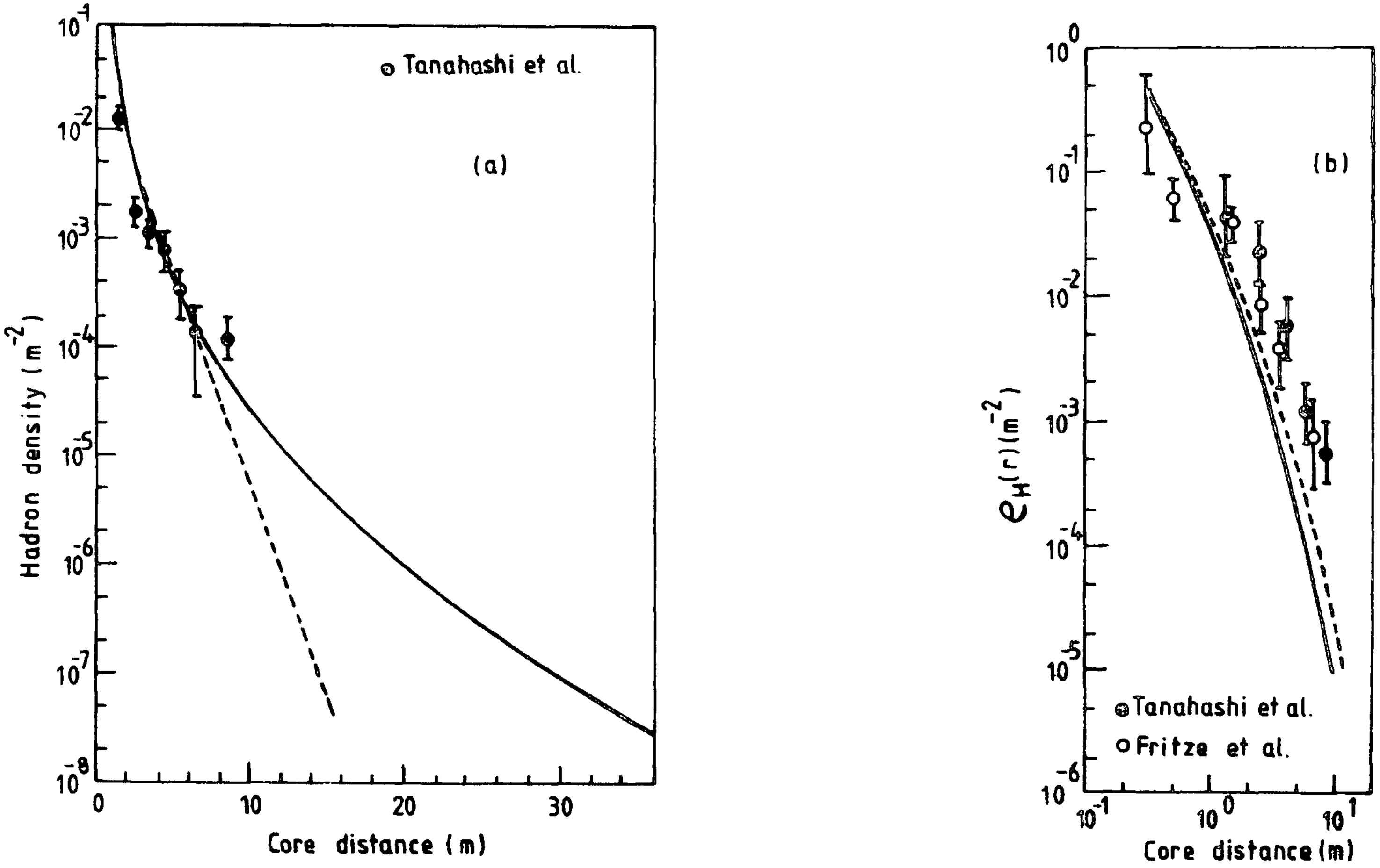

Figure 6.1 (a) Lateral distribution of hadrons for showers of size $N_e = 10^5$ where — $\rho_H \sim \exp(-\sqrt[4]{\frac{r}{r_o}})$ and --- $\rho_H \sim \exp(-\frac{r}{r_o})$

(b) Lateral distribution of hadrons in showers of is above the adopted value of 0.4 GeV/C. Thus an increase of $< P_t >$ with energy can be expected. It is worth mentioning that this discrepancy can also be partly explained by the effect of inaccuracy in core location (the accuracy is usually not better than 1 m). Furthermore theoretical calculations were made only for vertical showers, while the experimental points include inclined showers as well.

(b) Grieder (1977)

Results of simulated distributions together with experimental data from different groups are shown in Figure 6.2. The simulated distributions shown apply to 10^6 GeV, proton initiated showers and were obtained with the SMFB model, constant cross sections and a standard transverse momentum distribution with a cut-off at 5 GeV/C. The results of Kameda et al and Fritze et al have been normalized to a shower of size 10^5, whereas the remaining data have not been modified. A comparison of the experimental and theoretical distributions presented in Figure 6.2 shows that the two sets of data of Kameda et al for hadrons with energy larger than 100 GeV are in excellent agreement with predictions at distances larger than one metre from the shower core. The deviations from the predicted distribution in close proximity of the shower axis is more pronounced for events belonging to the smaller size group (represented by diamonds). This may be due to uncertainties in core location that are getting worse with decreasing size. The data of Fritze et al for 800 GeV hadrons agree roughly with expectation near thecore, but the average slope of the distribution is smaller, the higher-energy data of Matano et al and Baruch et al for distances that are less

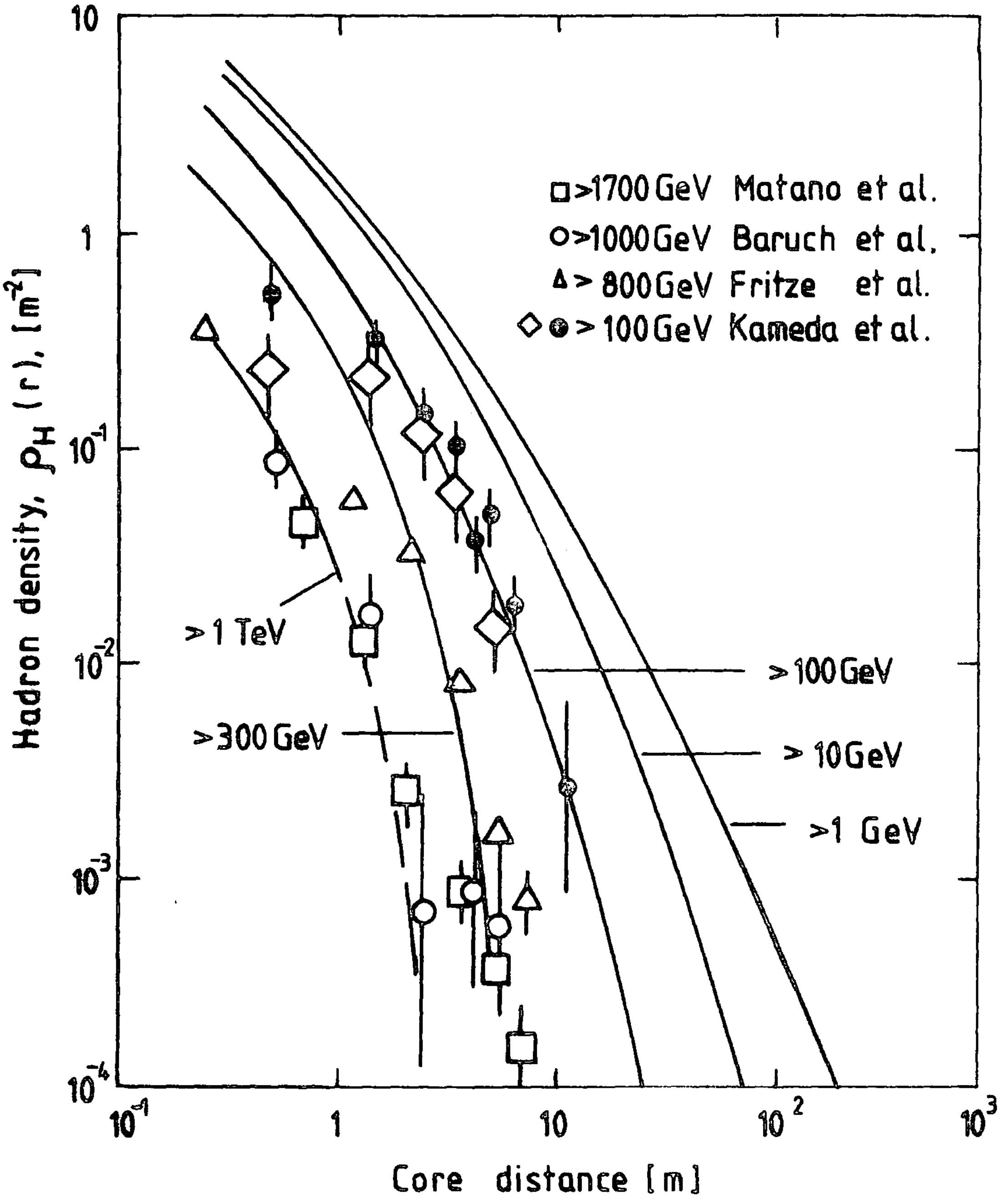

Figure 6.2 : Lateral distribution of hadrons for different energy thresholds. The simulated distributions are for proton initiated showers calculated with the SMFB model and a standard transverse momentum distribution with a cut-off at 5 GeV/C (After Grieder, 1977).

than two metres from the shower axis yield densities that are comparable to those expected from simulations for proton initiated showers and constant cross sections.

6.4 PRESENT MEASUREMENT

6.4.1 Experimental Arrangements

A large flash tube chamber of approximately 11000 tubes has been employed as a visual hadron detector. The flash tube chamber is located near the centre of the Durham Extensive Air Shower Array (Chapter 2) and has been running in conjunction with EAS detectors where information on shower size and core position as well as arrival direction were available. A hadron associated with an air shower interacts in 15 cm lead or 15 cm iron absorbers on top of the chamber to produce an electron-photon cascade developing into the flash tubes below. (Examples of the events obtained are shown in Appendix D). Figure 6.3 shows the front view of flash tube chamber. The acceptance geometry in the back plane is determined by the electrode length of 1.5m used for the flash tubes in F1a and F1b. The normal length of electrodes of flash tubes in F2 and F3 are 2 m. and are symmetrically placed with respect to the electrodes in F1a and F1b. They are a useful aid in determining whether hadron initiated bursts in the iron, are truly charged or neutral when edge effects are considered. As shown in Figure 6.3, for a burst to be accepted the core should lie between but not in the shaded area.

A delay time of 20 μsec has been used between the arrival of the front of the shower and the application of the high voltage to the plates in the flash tube chamber. The

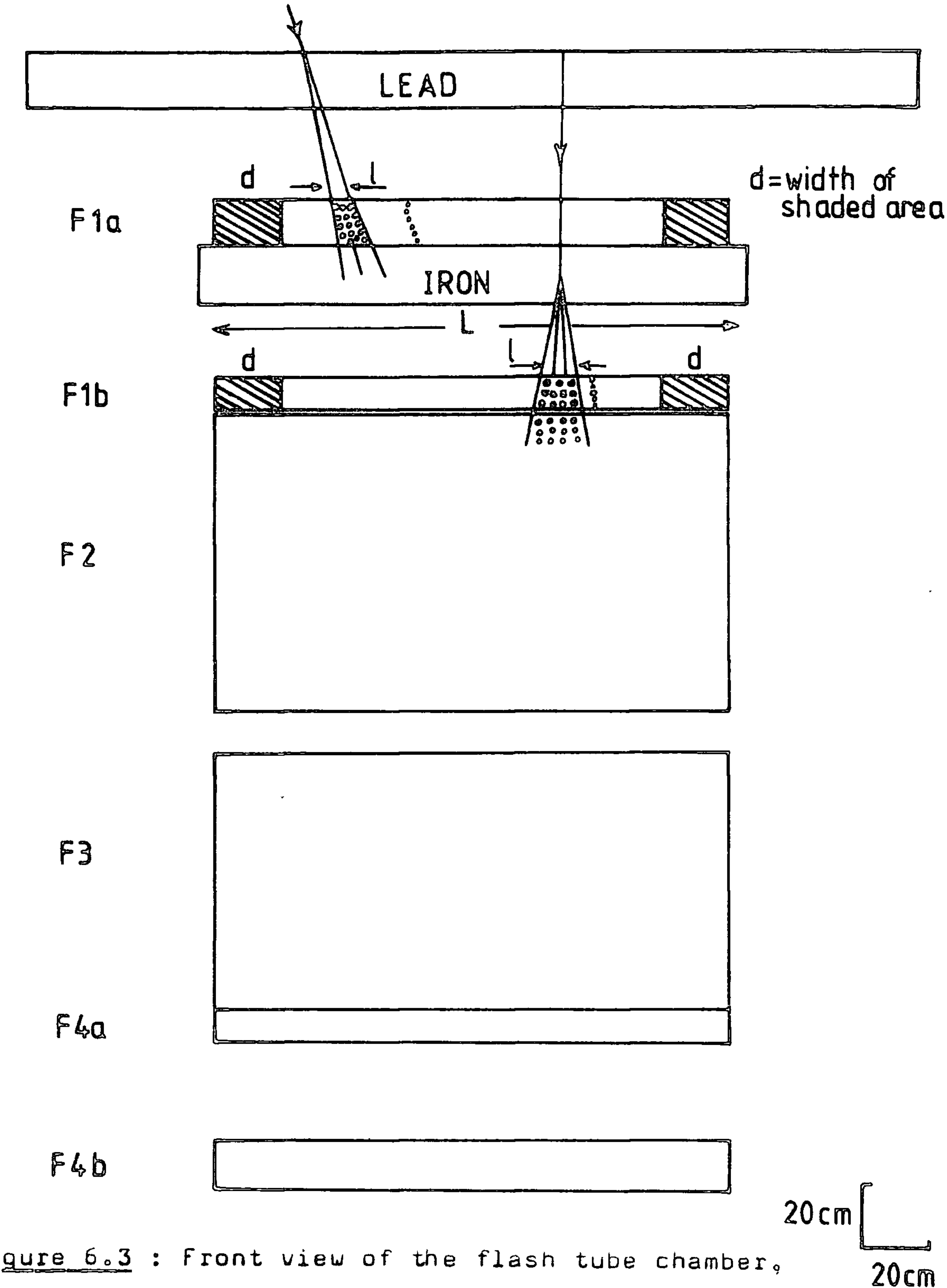

Figure 6.3 : Front view of the flash tube chamber. For a burst to be accepted, it should fall between but not in the shaded area. The shaded area is a function of burst size.

Time delay on high voltage pulse	20 μ sec
Cut on orthogonal core distance from FIT Chamber	$r < 75m$

EAS selection	inner ring trigger	outer ring trigger	Total
No. of EAS triggers	1870	3665	5535
Run time	119.1 hr	607.9 hr	726.90 hr
Trigger rate	$15.70 \pm 0.36 hr^{-1}$	$6.03 \pm 0.10 hr^{-1}$	-
No. of analysable showers with $r<75m$ and $\theta < 50^o$	1617	2866	4483
% of shower triggers with $r < 75m$ and $\theta < 50^o$	86%	78%	81%
No. of detected hadrons with $E > 13$ GeV	81	105	186

No. of bursts observed under the lead or iron	lead	103
	iron	65
	undetermined	18
Ratio of bursts produced in lead to those produced in iron, $\frac{n(Pb)}{n(Fe)}$, determined from F/T		$1.58 \pm .13$
Expected $\frac{n(Pb)}{n(Fe)}$ assuming all bursts are produced by hadrons	nucleons	2.17
	pions	2.24
No. of charged and neutral hadrons that interacted in iron	charged	57
	neutral	8
Ratio of charged to neutral hadrons determined from flash tube chamber		7.1 ± 2.7

TABLE 6.1 : Summary of basic data concerning experiment on hadrons in EAS.

EAS have been selected by a fourfold coincidence between central detector C($\gtrsim$ 4 m^{-2}) and either of three detectors 13,33, 53 ($\geqslant$ 2 m^{-2}), outer ring or 11, 31, 51 ($\gtrsim$ 2 m^{-2}), inner ring.

In the course of the present work, a total of 4483 showers (1617 inner ring and 2866 outer ring) with $r < 75$m and $\theta < 50^0$ have been analysed and 186 hadrons of energy $\geqslant$ 13 GeV have been detected.

Details of the basic data are listed in Table 6.1. Figure 6.4a displays the orthogonal core distance distribution of analysed inner ring and outer ring triggers where for comparison the same core distances but measured in the x y plane are shown in Figure 6.4b. In Figures 6.5a and 6.5b the core distance distribution of the inner ring and the outer ring triggers as well as the core distance distribution of the showers with a detected hadron in the flash tube chamber are shown. Figure 6.6 displays the shower size distribution of the inner ring and the outer ring showers with a detected hadron in the flash tube chamber.

6.5 RESULTS

6.5.1 General

The main purpose in this section is to know how the density of hadrons in a shower depends on the energy, the core distance and the shower size and try to get an exact expression relating them together ($\Delta(E, r, N)$).

To see the dependence of the density on the shower size, the data is divided into two ranges of $1.5.10^4 < N \leqslant 2.3.10^5$ and $2.3.10^5 < N \leqslant 4.10^6$ and then the lateral distribution of hadrons for both cases are plotted in Figure 6.7.

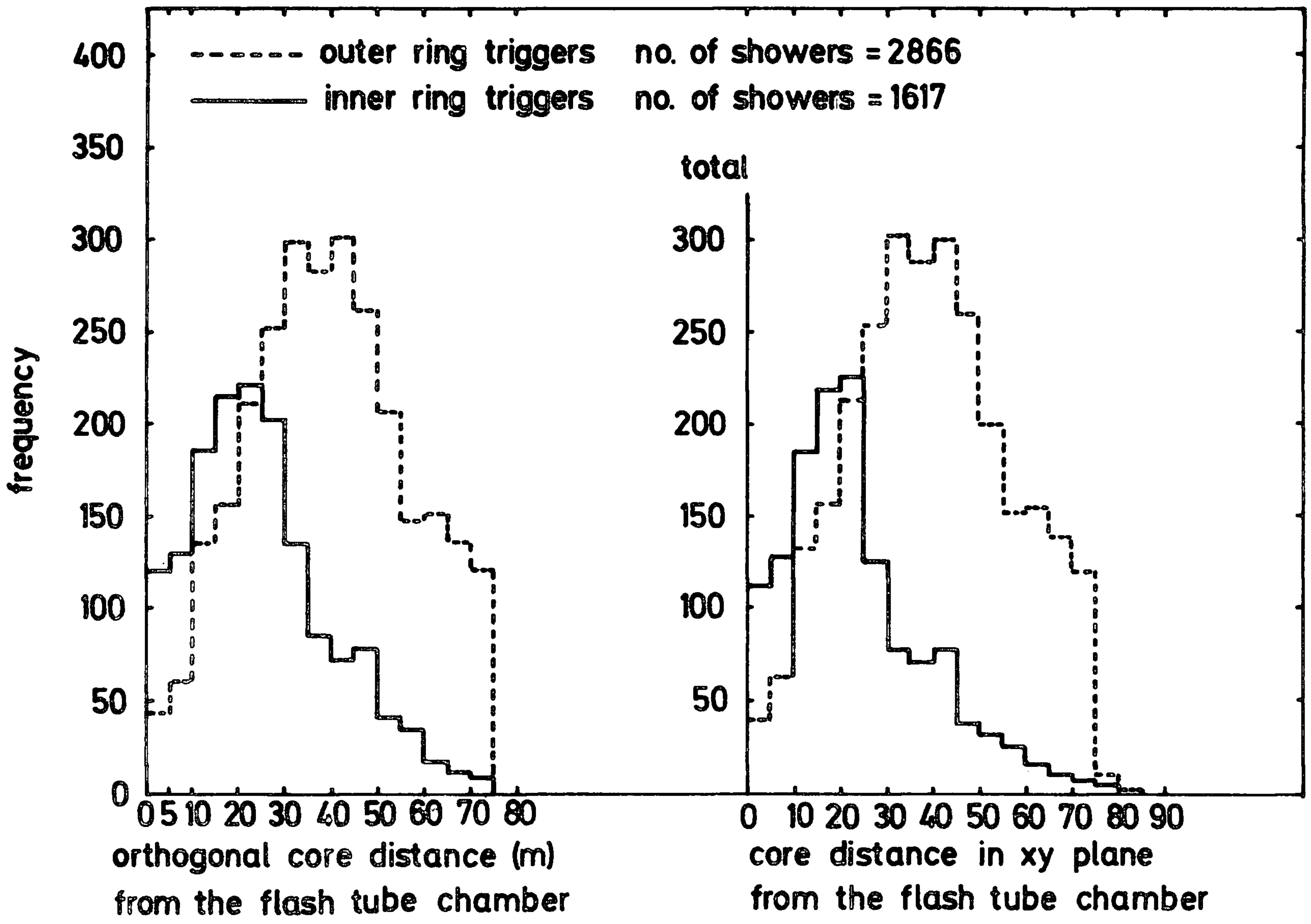

Figure 6.4 : (a) Orthogonal core distance distribution for inner ring triggers measured from the flash tube chamber.
(b) Core distance distribution for inner ring and outer ring triggers measured in xy plane.

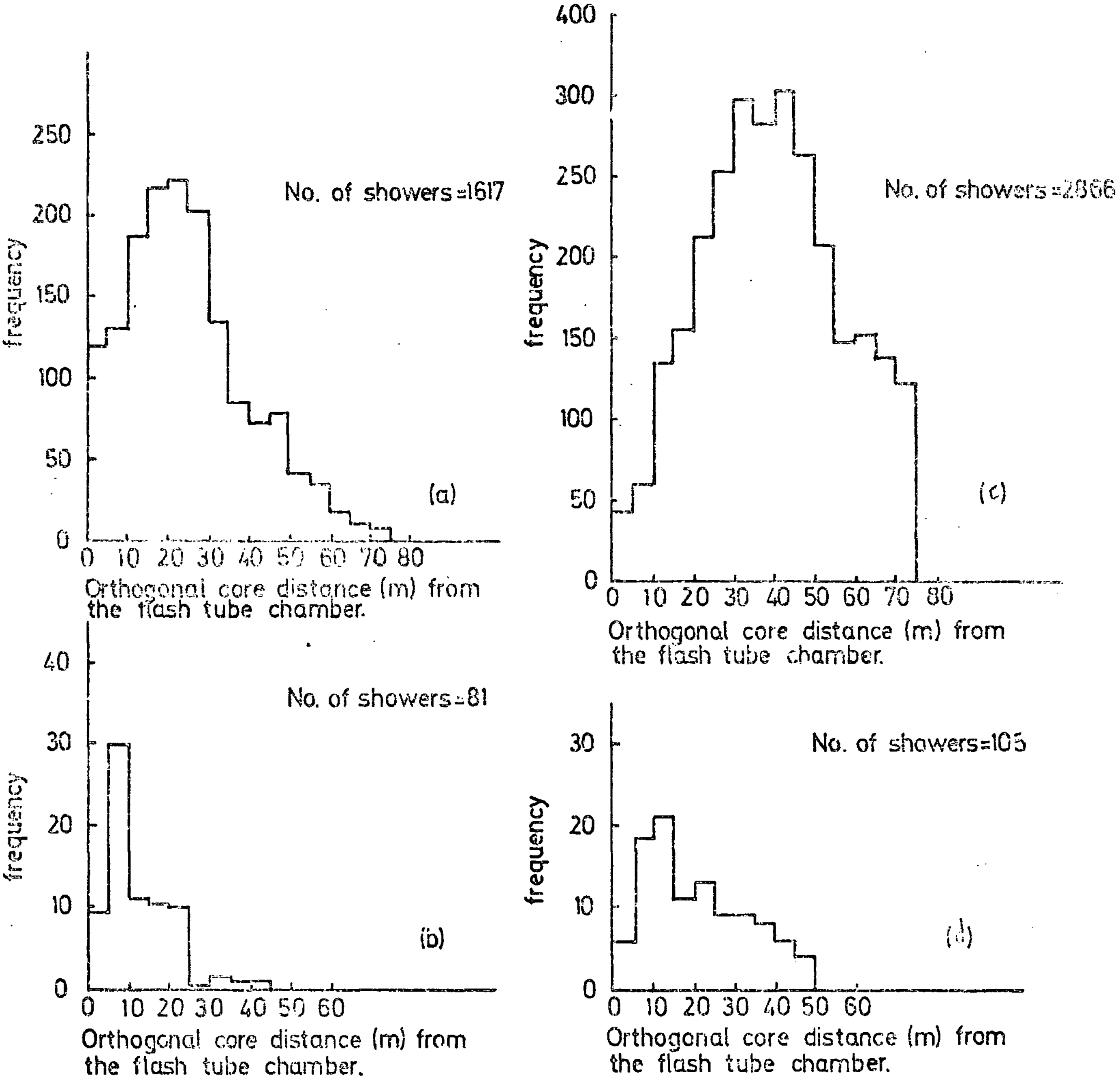

Figure 6.5: Distribution of orthogonal core distance from the flash tube chamber for

(a) all analysable inner ring triggers

(b) inner ring triggers with a detected hadron in the flash tube chamber

(c) all analysable outer ring triggers

(d) outer ring triggers with a detected hadron in the flash tube chamber.

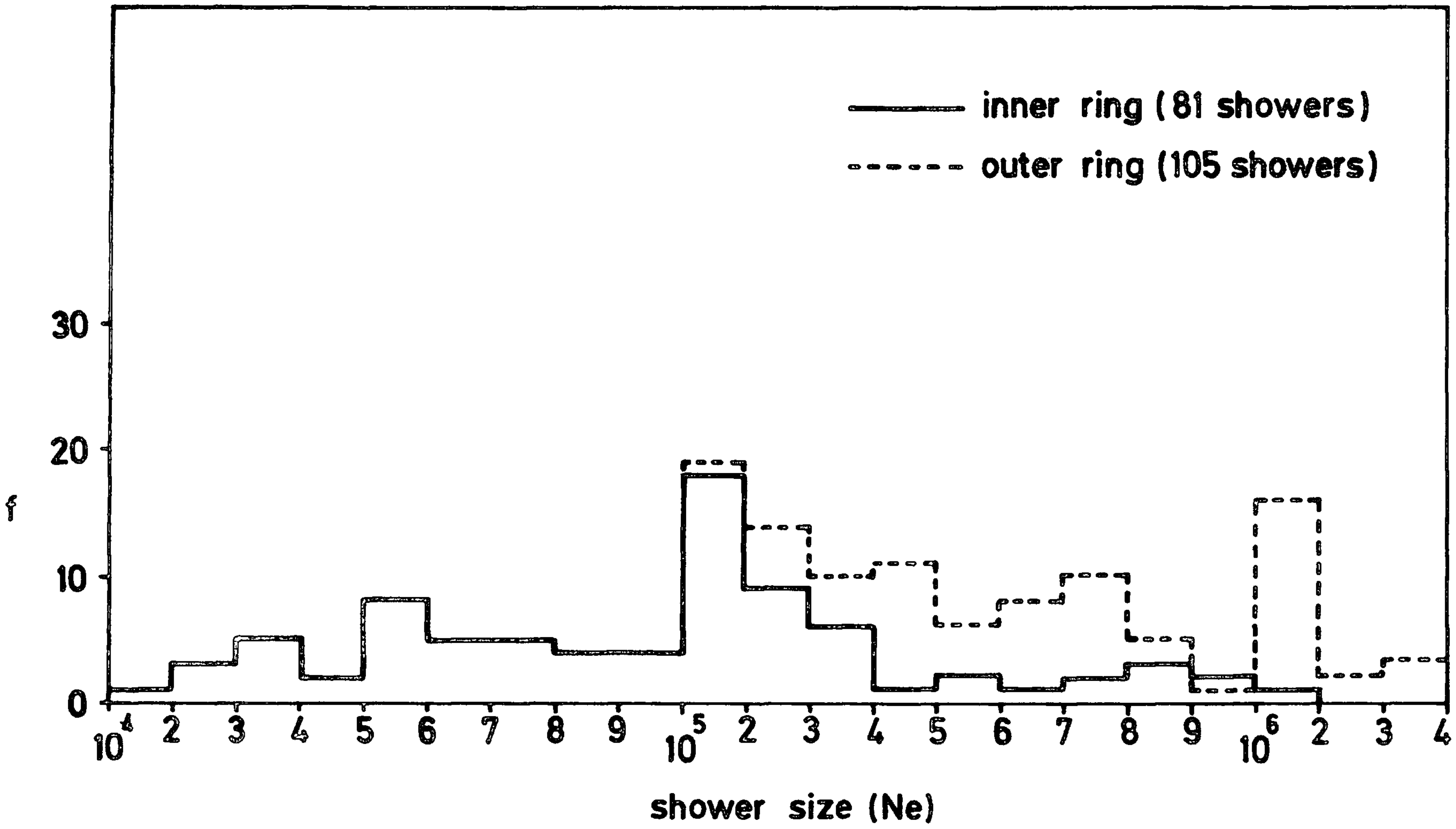

Figure 6.6 : Distribution of shower size for showers with a detected hadron in the flash tube chamber.

After determination of the energy for each hadron(7.3.3) to investigate the energy dependence of the lateral distribution of hadrons, the data is divided into two groups of $13 \leq E < 82$ GeV and $82 \leq E < 1500$ GeV and the results are plotted in Figure 6.8.

Assuming $\Delta(E,r,N) \sim e^{-\frac{r}{r_o}}$ the best line through the points in Figures 6.7 and 6.8 are also shown. Figure 6.9 shows the lateral distribution of hadrons for all of the hadrons observed in the flash tube chamber.

6.5.2 Total number of Hadrons with Energy $\geq E$ in a Shower of Size N

As mentioned earlier and it is clear from Figure 6.7, the lateral distribution of hadrons can be represented as :

$$\Delta(E,r,N) = C \; e^{-\frac{r}{r_o}}$$

By integrating this equation over the whole range of core distances the total number of hadrons with energy $\geq E$ in a shower of size N can be calculated.

$$\Delta(E,r,N) = C \; e^{-\frac{r}{r_o}}$$

$$n_H(\geq E,N) = \int_0^\infty C \; e^{-\frac{r}{r_o}} \; 2\pi r dr$$

$$= 2\pi C \int_0^\infty r \; e^{-\frac{r}{r_o}} \; dr$$

$$\text{since} \int_0^\infty x \; e^{-\alpha x} \; dx = \frac{1}{\alpha^2} \quad \text{then :}$$

$$n_H(\geq E,N) = 2\pi C \; r_o^2 \qquad (6.a)$$

where n_H is the total number of hadrons in a shower of size N

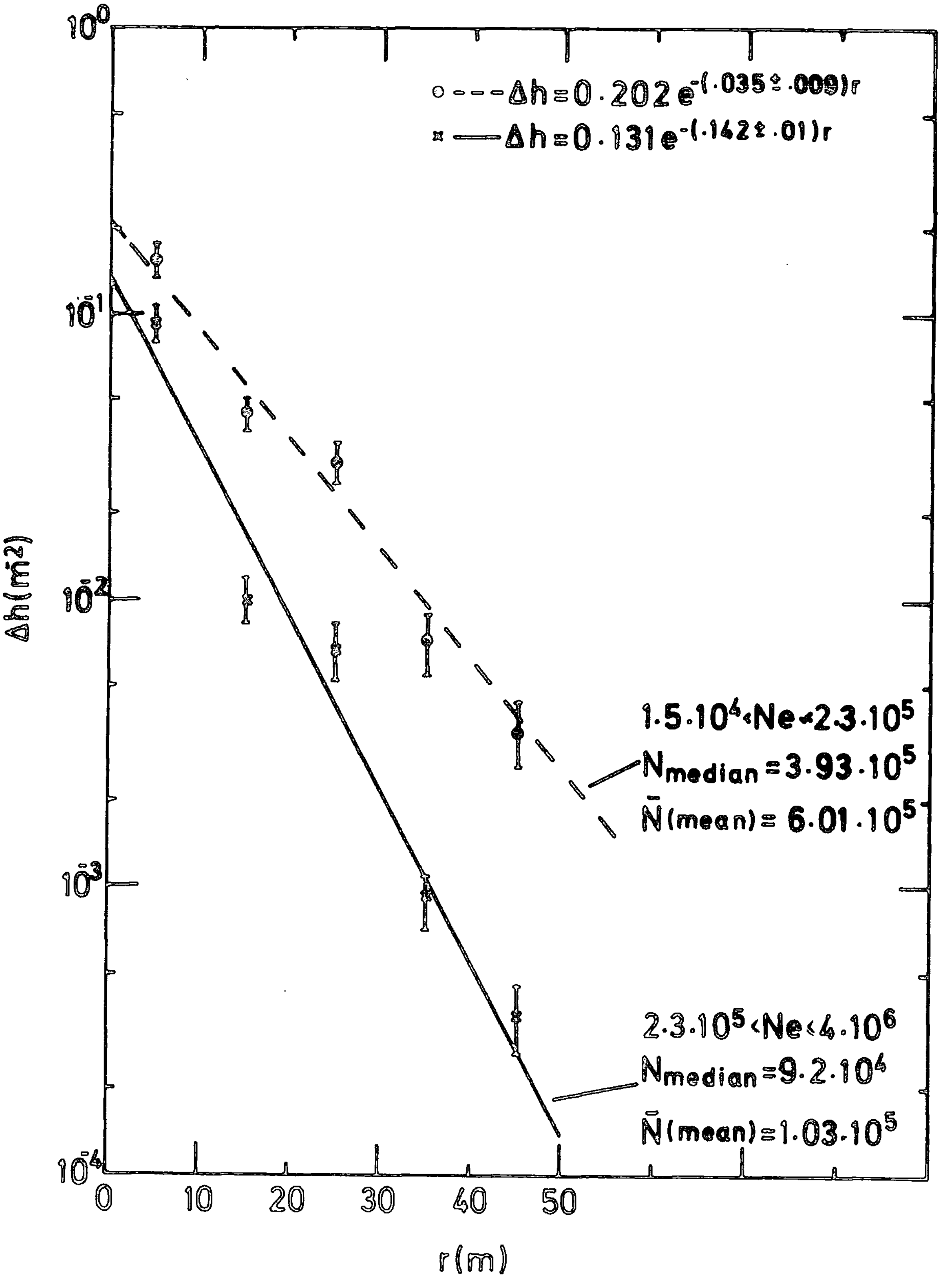

Figure 6.7 : Dependence of the lateral distribution of hadrons on shower size. The lateral distribution function is expressed in the form of exp $(-\frac{r}{r_0})$.

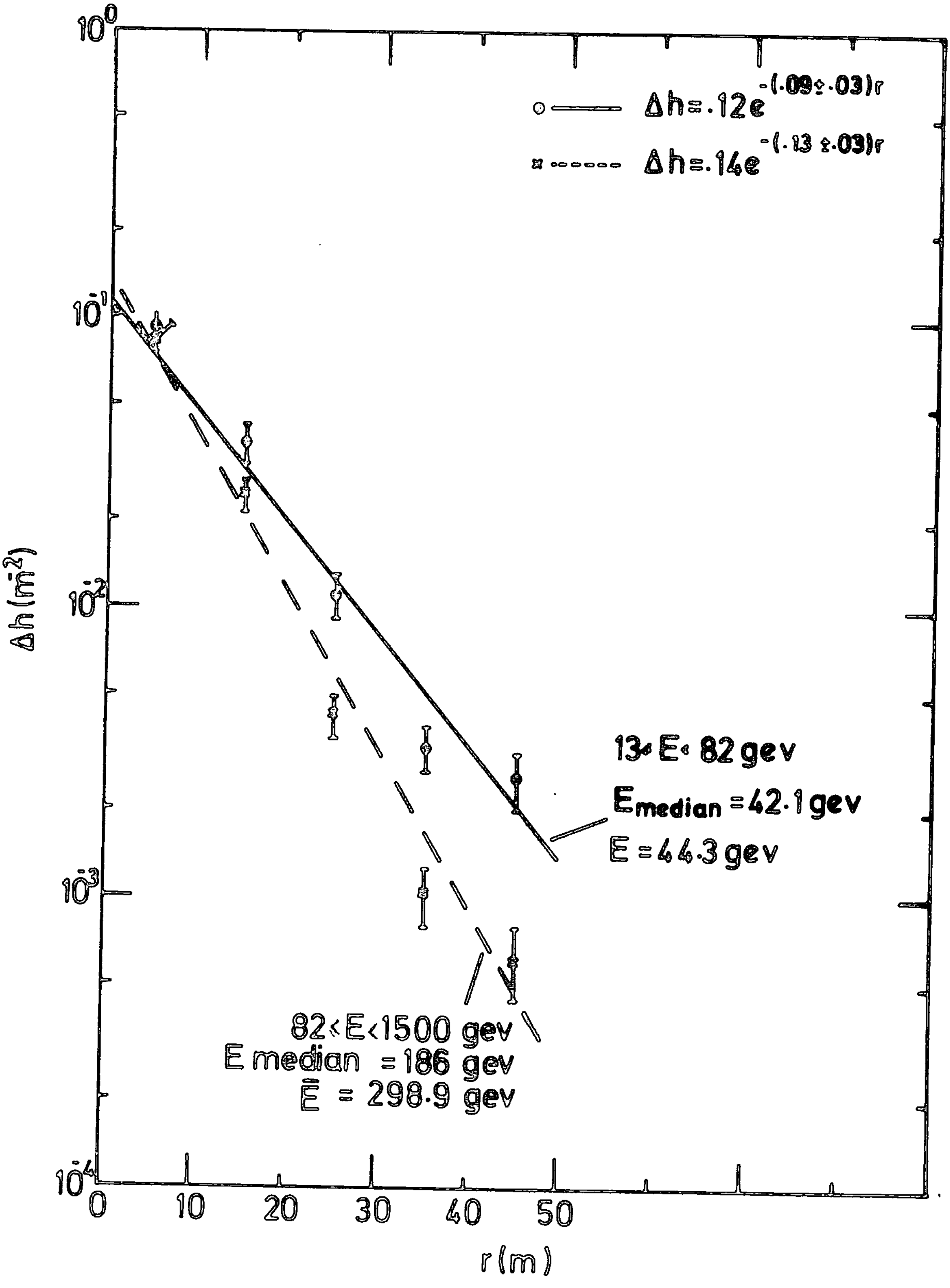

Figure 6.8 : Dependence of the lateral distribution of hadrons on energy threshold.

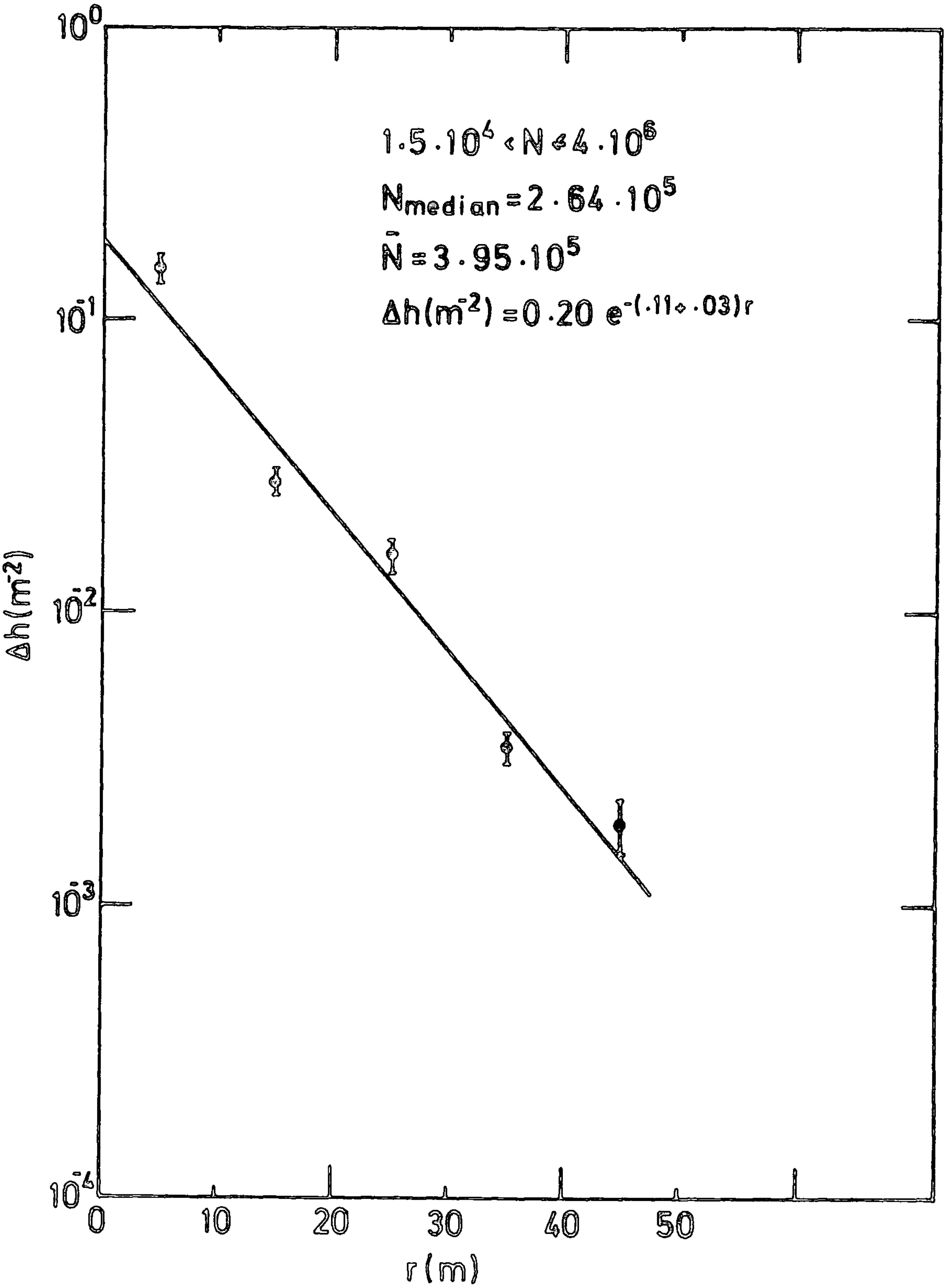

Figure 6.9 : Lateral distribution of hadrons for all of the hadrons observed in the flash tube chamber.

and C is the ordinate of the lateral distribution of hadrons at $r = 0$. Using equation 6.a and employing the results of Figure 6.7, the relation between the total number of hadrons with energy ≥ E in a shower of size N is calculated to be

$$n_H(\geq 13 \text{ GeV}) = 3.18.10^{-3} \quad N^{0.82 \pm .05} \qquad (6.b)$$

and the result is plotted in Figure 6.10a.

6.5.3 Dependence of r_0 on Shower Size and Energy

Inspection of Figures 6.7 and 6.8 reveal that the lateral distribution of hadrons is flatter for showers with larger size while the situation is reversed in the case of energy, i.e. the lateral distribution of hadrons is steeper for higher energy threshold. Therefore the characteristic length r_0 which appears in $\Delta h \sim e^{-\frac{r}{r_0}}$ increases as shower size increase and decreases with increasing hadron energy. Using the results of Figures 6.7 and 6.8 the variation of r_0 with shower size and energy are shown in Figures 6.10b and 6.10c. The lines through the points have the form of

$$r_0 = 0.25 \quad N^{0.29 \pm .03} \qquad (6.c)$$

$$r_0 = 22.7 \quad E^{-0.19 \pm .03} \qquad (6.d)$$

where r_0 is in metres, N is in units of single particles and E is in GeV.

The points represented in Figures 6.10(a, b and c) are evaluated at the mean as well as the median shower size and energy of the corresponding ranges but in the rest of the calculations the results with mean values will be used.

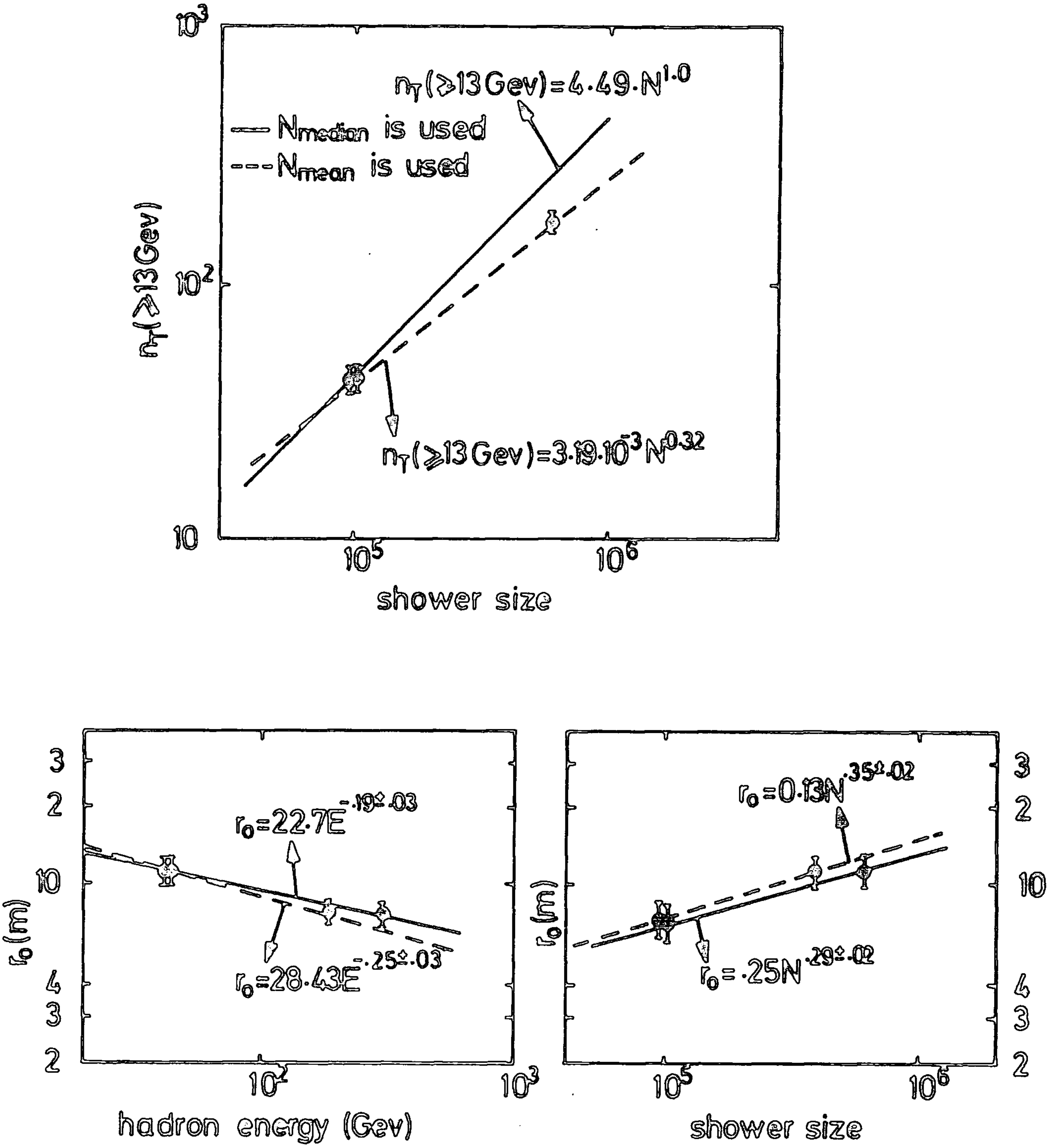

Figure 6.10 : (a) Variation of the total number of hadrons in a shower of size N as a function of shower size.

(b) The relation between r_o in $(r)= A\ e^{-r/r_o}$ and shower size.

(c) Variation of r_o in $(r)= A\ e^{-r/r_o}$ with hadron energy.

6.5.4 Density of Hadrons of Energy E/unit E at a Distance r from the Axis of a Shower of size N.

Assuming $\Delta h \sim e^{-\frac{r}{r_0}}$, from earlier measurements it is quite straightforward to work out the dependence of r_0 on shower size and energy (following Kameda et al (1965)).

By quoting equations 6.c and 6.d

$$r_0 = 0.25 \quad N^{.029 \pm 0.03}$$

$$r_0 = 22.7 \quad E^{.019 \pm 0.03}$$

where r_0 in metres, E in GeV and N in units of single particles one can deduce that

$$r_0 = 0.25 \times 22.7 \; N^{0.29 \pm 0.03} \; E^{-0.19 \pm 0.03}$$

$$r_0 = 5.67 \; N^{0.29 \pm 0.03} \quad E^{-0.19 \pm 0.03}$$

and therefore the expected lateral distribution, $\Delta (r,E,N)$, contains a term

$$e^{-\frac{r}{5.67 \, N^{0.29} \, E^{-0.19}}}$$

Other observations which have to be used in calculating the density of hadrons are

(i) Total number of hadrons in a shower of size N with energy ≥ 13 GeV which is measurable from equation 6.b

$$n_r \; (\geq 13 \text{ GeV}) = 3.18.10^{-3} \quad N^{0.82 \pm 0.05}$$

(ii) Observed integral energy spectrum of hadrons (7.3.3) which is well represented by

$$n_h\ (\geq E) \sim E^{-0.73\ \pm\ .04} \qquad (6.e)$$

where E is in units of GeV.

It is shown in Figure 6.11 and 6.12 that E_h does not vary strongly with N which means that the shape of the energy spectrum does not change significantly with shower size Therefore equation 6.e is valid for the whole range of size in the present work.

Thus the expected number of hadrons per m^2 with energy E per unit E at a distance r from the shower size in a shower of size N can be expressed as

$$\Delta h(E,r,N) = k\ \ E^{-\alpha}\, N^{\beta}\, e^{-\,r/r_o}\quad m^{-2}\ GeV^{-1} \qquad (6.f)$$

where $r_o = 5.67\ E^{-0.19}\ \ N^{0.29}$ and k is a constant.

Now the problem is to find numerical values for α , β and k. Integrating the above expression (equation 6.f) over core distance and energy gives the total number of hadrons with energy greater than E_o in a shower of fixed size N.

$$N(>E_o,N) = \int_{E_o}^{\infty}\int_{r=o}^{\infty} \Delta_h(E,r,N)\ 2\pi r dr\ dE \quad =$$

$$\int_{E_o}^{\infty}\int_{r=o}^{\infty} k\ E^{-\alpha} N^{\beta}\ e^{-\ r/r_o}\ \ 2\pi r dr\ dE =$$

$$2\ \pi k\ N^{\beta} \int_{E_o}^{\infty} \left\{ \int_{r=o}^{\infty} r\ \ e^{-\ r/r_o}\ \ dr \right\} dE$$

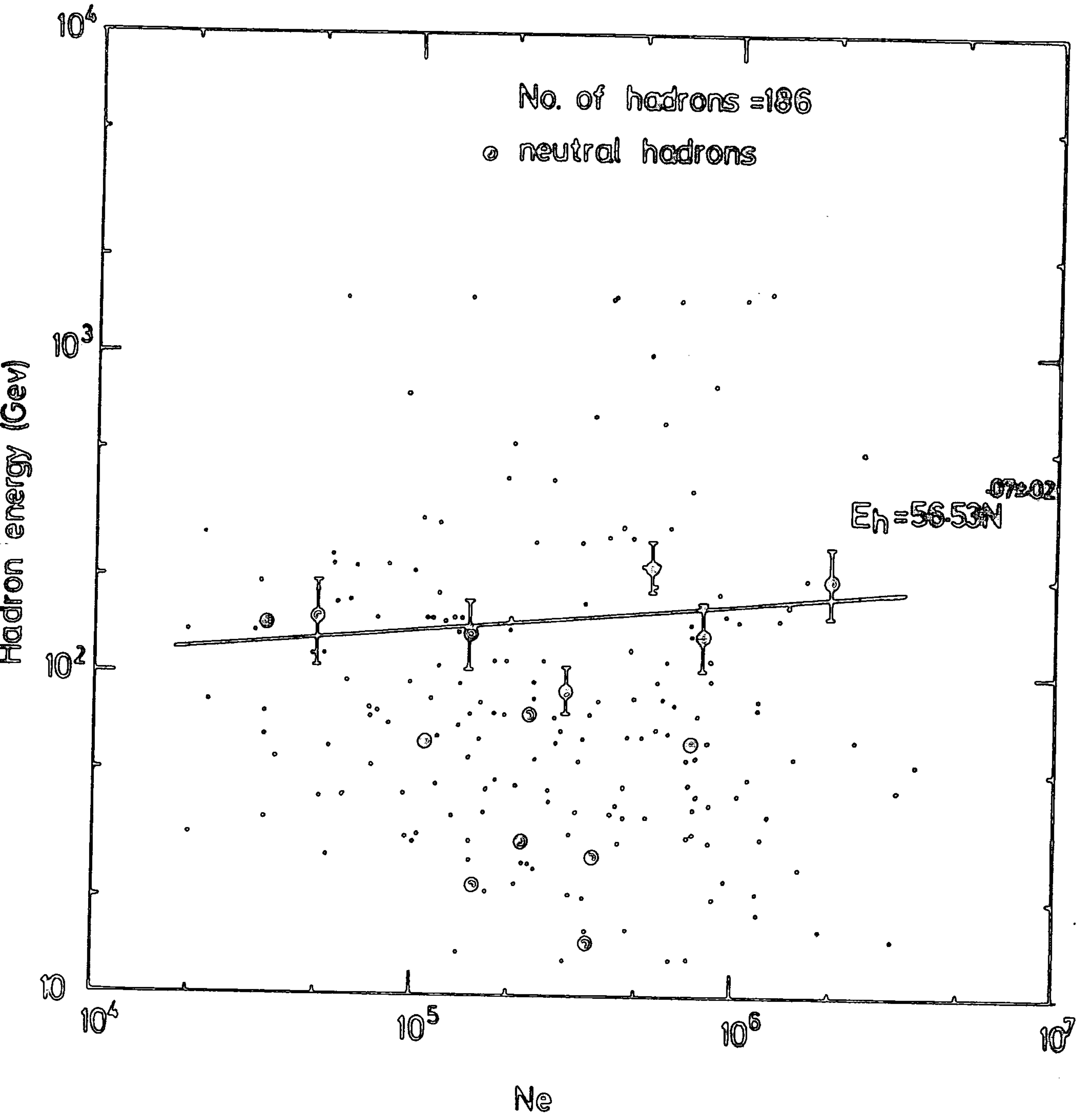

Figure 6.11 : Variation of hadron energy with the size of the accompanied shower.

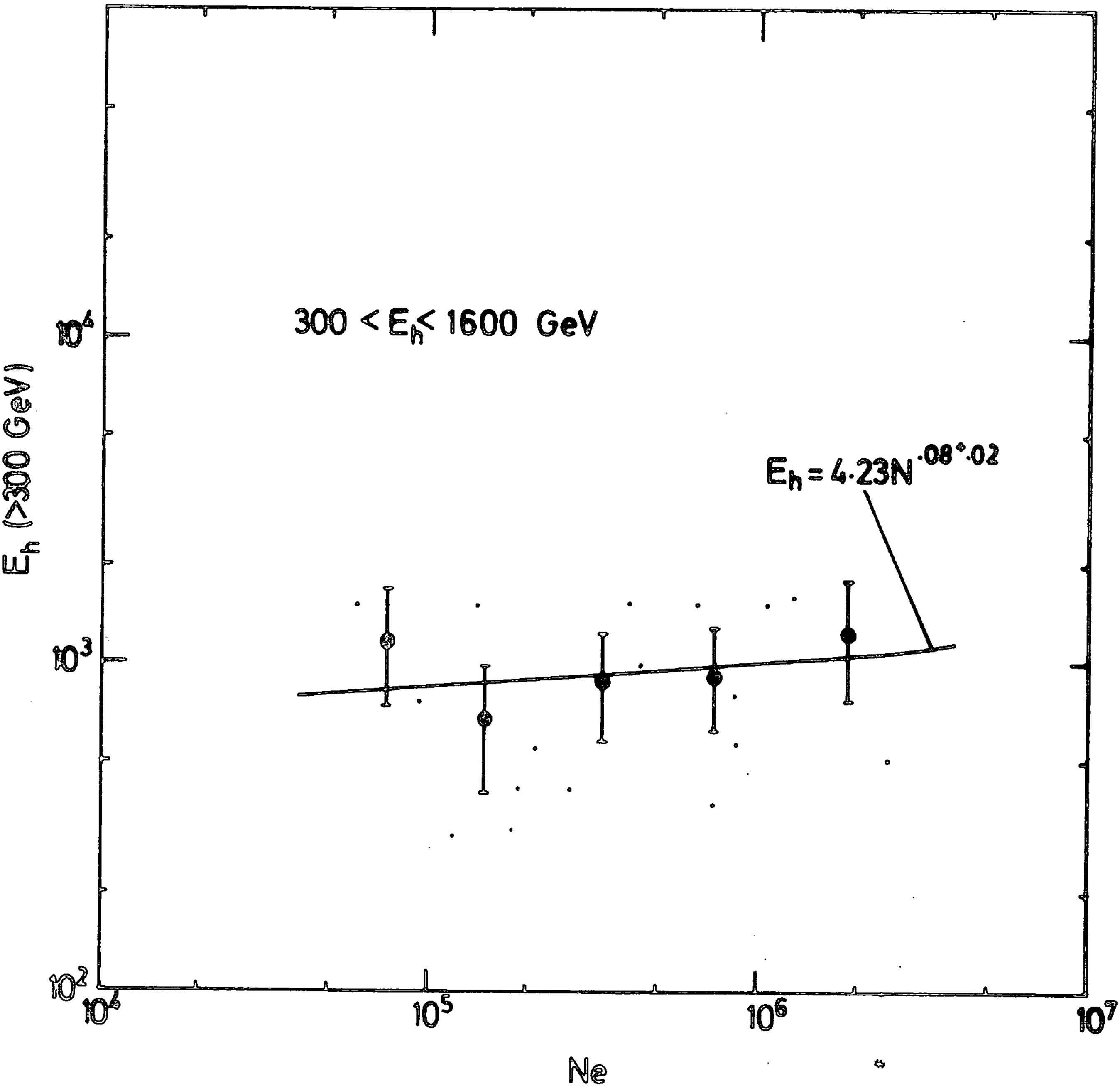

Figure 6.12 : Variation of hadron energy with shower size where only hadrons with energy in the range of 300< E_h< 1600 GeV are used.

where $r_o = 5.67\, E^{-0.19}\, N^{0.29}$

Since $\int_{r=0}^{\infty} r\, e^{-r/r_o}\, dr = r_o^2$ then :

$$N(> E_o, N) = 2\pi k\, N^{\beta} \int_{E_o}^{\infty} E^{-\alpha}\, r_o^2\, dE =$$

$$2\pi k\, N^{\beta} \int_{E_o}^{\infty} E^{-\alpha} (5.67)^2\, N^{0.58}\, E^{-0.38}\, dE =$$

$$2\pi k\, N^{\beta+0.58}\, (5.67)^2 \int_{E_o}^{\infty} E^{-\alpha\ -0.38}\, dE$$

Therefore :

$$N(>E, N) = \frac{2\pi k (5.67)^2}{\alpha - 0.62}\, N^{\beta + 0.58}\, E^{-(\alpha - 0.62)} \qquad (6.g)$$

Comparing this equation with (6.b) and (6.e) requires

$$\beta + 0.58 = 0.82 \pm 0.05$$

$$\beta = 0.24 \pm 0.05$$

and

$$\alpha - 0.62 = 0.73 \pm .04$$

$$\alpha = 1.35 \pm 0.04$$

Substituting for α and β in equation (6.g) gives

$$N(> E, N) = 277.0\ k\ N^{0.82}\ E^{-0.73}$$

Evaluating this expression for E= 13 GeV and N = 1

$$N(> 13\ \mathrm{GeV}, 1) = 277.0\ k\ (1)^{0.82}\ (13)^{-0.73} = 42.59\ k \qquad (6.h)$$

Comparing equations (6.h) and (6.b) gives

$$3.18.10^{-3} = 42.59\ k$$

$$k = 7.5.10^{-5}$$

Substituting for α, β and k in equation 6.f gives a formula for the density of nuclear active particles, of energy E per unit E in EAS of size N at a distance r from the shower axis as follows :

$$\Delta h(E, r, N) = 7.5.10^{-5}\ E^{-1.35\pm0.04}\ N^{0.24\pm.05}\ e^{-\frac{r}{5.67\ N^{0.29} E^{-0.19}}}\ m^{2}\ \mathrm{GeV}^{-1}$$

where E is in GeV, r is in metres and N is in units of single particles.

6.6 SUMMARY AND CONCLUSION

The lateral distribution of hadrons in showers of size $1.5.10^4 - 4.10^6$ particles has been measured and it has been fairly well represented by the expression $\Delta h \sim e^{-r/r_0}$ where $r_0 = 9.1 \pm 2.01$ metres. It is also shown that the lateral distribution of hadrons is steeper for hadrons in larger showers than for hadrons in smaller ones. However the same distribution is flatter for a higher hadron energy threshold. Using the results of the hadron lateral distribution the relation between the total number of hadrons with energy greater than E in a shower of size N is worked out. This relation has the form of $n_H \alpha N_e^{\alpha}$ where $\alpha = 0.82 \pm .05$.

An empirical expression giving the density of hadrons of energy E per unit E at a distance r from the axis of a shower of size N is calculated to be :

$$\Delta_h(E,r,N) = 7.5.10^{-5}\ E^{-1.35}\ N^{0.24}\ \exp\left(-\frac{r}{r_o}\right)\ m^{-2}\ GeV^{-1}$$

where $r_o = 5.67\ N^{0.29}\ E^{-0.19}$

and E is in GeV, r in metres and N is in units of single particles.

In the following chapter, the significance of study of lateral distribution of hadrons in connection with transverse momenta will be discussed.

CHAPTER 7

FURTHER RESULTS AND DISCUSSIONS ABOUT THE HADRON COMPONENT IN EAS

7.1 INTRODUCTION

The hadron component of an extensive air shower determines the way in which the shower as a whole develops. Measurements of the hadron component provide the most direct way of studying the nuclear physical process occurring at these extremely high energies, thus obtaining information about this component is of considerable importance. In addition, one of the most important questions to be answered with regard to the astrophysical aspects of high energy cosmic ray particles is'what is the mass composition of these high energy particles ? ' Hadron measurements can provide a means of determining the answer.

Probably the reason why few reliable experiments have been performed to study the hadron component of EAS is the difficulty in making accurate measurements. In this chapter, a measurement of the hadron energy spectrum and other important issues such as transverse momentum and the ratio of charged to neutral hadrons in a shower, will be discussed. But before that, a survey of theoretical calculations and simulation results and their comparison with experimental data will be presented.

7.2 THEORETICAL CONSIDERATIONS

In this section the simulation results (P. Grieder, 1976) based on four different fireball models (Table 7.1) and also results of the Monte Carlo simulations based on the CKP model (Kempa et al, 1976) will be discussed. Figure 7.1 shows the integral energy spectrum of hadrons in air showers at sea level, and for comparison, different experimental results are also presented. Table 7.1 displays the properties of models which have been used in simulations. To summarize briefly, curves 1, 2 and 3 are for proton initiated showers and curve 4 applies to events initiated by iron nuclei. Curves 1 and 4 were obtained with a slow-multiple fireball model (SMFB) while curve 2 with intermediate double fireball model (IDFB), and constant cross sections were considered in either case. Curve 3 is for the IDFB model with rising cross sections. All the simulation results are for 10^6 GeV primaries ($\sim 10^5$ shower size) and experimental data have not been normalized but all belong to the showers of almost similar size groups with $< N > \simeq 10^5$. It is interesting to note that the results obtained by the different experiments agree fairly well at lower energies and diverge more and more with increasing energy. It is worth mentioning that methods of determining core position, size and energy of the showers, differ from one experiment to the other and could cause considerable disagreement in the results. Figure 7.2 shows an analogous simulation and computation of hadron data for mountain altitude. The calculated spectra are for an altitude of 3000 metres above sea level and primary energies of 10^5 GeV and 10^6 GeV while

No.	Model	Cross Section σ	Multiplicity α $n_s \sim E^{\alpha}$
1	SMFB	Const.	0.2
2	IDFB	Const.	0.2
3	IDFB	Rising	0.2
4	SFB	Const.	0.15
5	SFB	Const.	0.25

TABLE 7.1 : Properties of different models used in simulations by Grieder (1976), the results of which are shown in Figures 7.1 and 7.2.

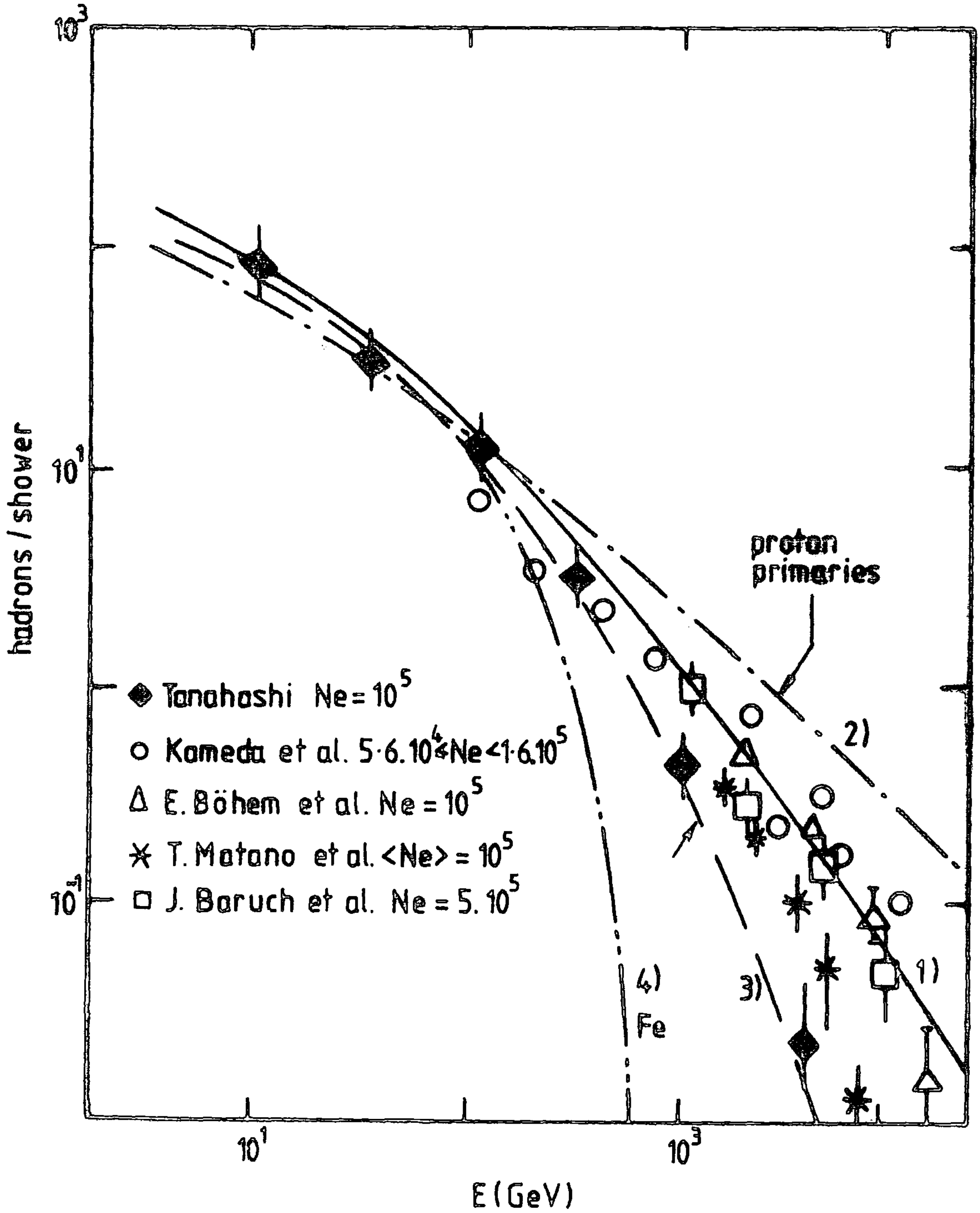

Figure 7.1 : Integral energy spectra of hadrons in air showers at sea level. Curves 1, 2 and 3 are based on theoretical models for primary protons of energy $E_0 = 10^6$ GeV. Curve 4 is for primary iron nuclei. (After Grieder, 1976).

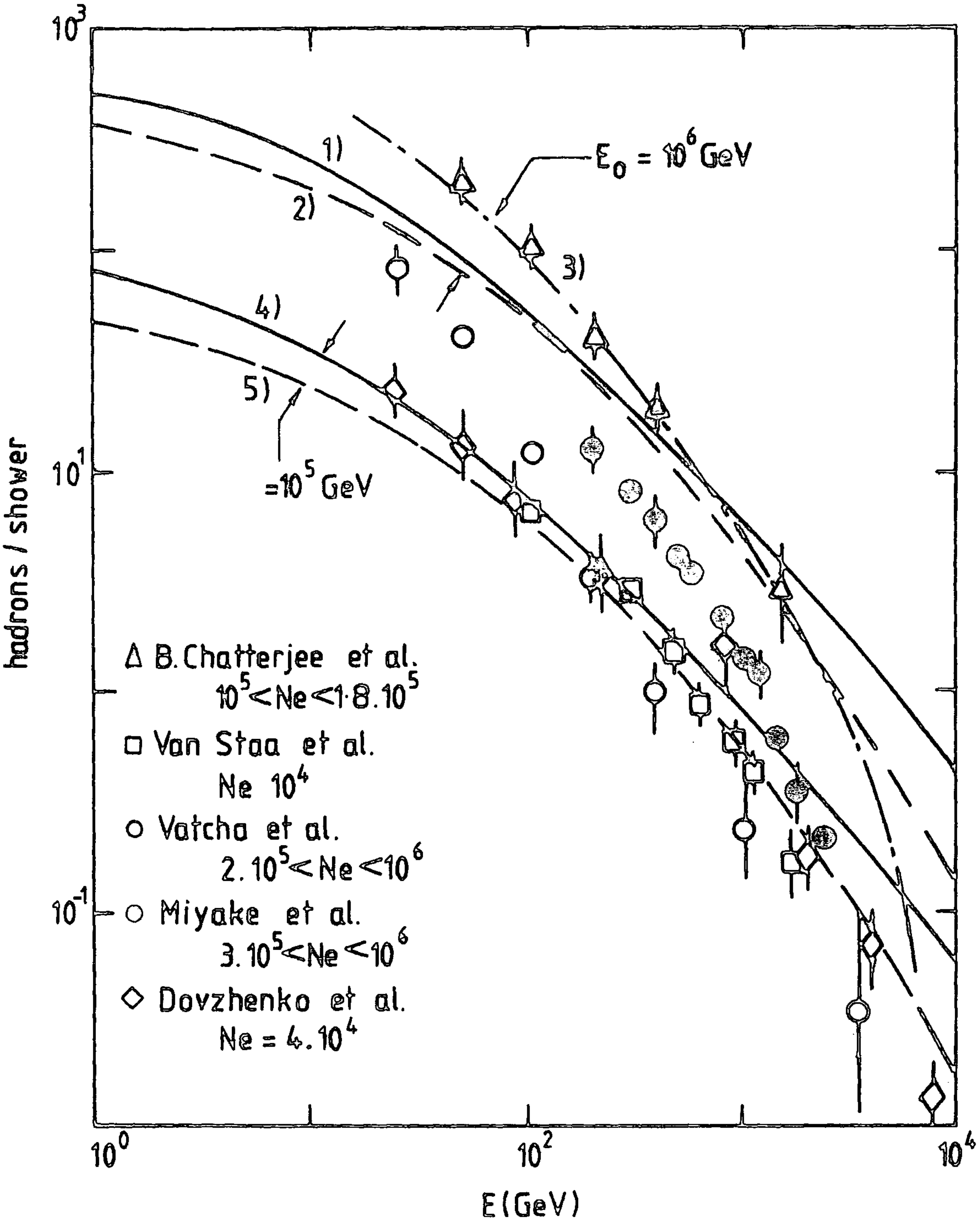

Figure 7.2 : Integral energy spectra of hadrons at mountain level. The calculated spectra are for an altitude of 3000m.

(After Grieder, 1976).

the experimental data have been obtained at altitudes (2200-3800) m. A quick look at Figure 7.2 indicates that, although some of the data appear to fall off a little faster than predicted and might suggest the presence of a considerable fraction of heavy primaries, but one can say that most of the data are adequately described by proton initiated showers in conjunction with a high multiplicity model and a continuously increasing cross section. However, the addition of a large fraction of heavy primaries increases not only the slope of the spectrum but also the total number of hadrons per shower, which causes a major disagreement between observed and predicted particle fluxes. Comparing Figure 7.1 and Figure 7.2 indicates that the slope of the high energy portion of the sea level spectrum is about equal or even slightly smaller than that at mountain level. This is in contradiction with what we expect from simulation calculations which indicate larger slopes at sea level. Moreover, the number of high energy hadrons that are observed in medium and large size showers at mountain level is lower in comparison to simulated results whereas the low energy hadrons appear to be over-abundant. At sea level the respective hadron numbers very nearly correspond to expectation. These particular features of the experimental data suggest that the nature of high energy interactions begin to change gradually at energies around 10^5 GeV. Either the multiplicity of secondaries increases more rapidly or the rate of rise of the cross section proceeds faster than expected at these energies.

Kempa et al (1975) have done some simulations based on the standard CKP model (6.2.1). A combination of Monte Carlo and analytical methods is used to derive the characteristics of individual EAS. The Monte Carlo method is used to obtain the points of each interaction of the leading particle and the energy released in these interactions. The characteristic values of pion and electron cascades started at each point of the interaction of the leading particle are obtained analytically. Figures 7.3a and 7.3b display the integral energy spectra of hadrons at sea level and mountain altitude respectively. The experimental points, at sea level, are from Tanahashi (1965) and the data at mountain level is from Dovzhenko et al (1959) which is measured at an altitude of 3860 in the Pamir. The spectra are calculated for two models of $n_s \alpha E^{\frac{1}{4}}$ and $n_s \alpha E^{\frac{1}{2}}$ and it is interesting to note that the differences in values of hadron densities predicted by the two analysed models are small compared to the experimental precision. At an energy threshold of 100 GeV (sea level) both models predict the same number of hadrons and this is true at all sizes. The energy threshold of 100 GeV is the'optimum energy' for a measurement of hadron content in EAS.

7.3 ENERGY SPECTRA MEASURED IN THIS EXPERIMENT

7.3.1 Analysis of the data

The integral intensity of hadrons with energy ≥ 13 GeV in EAS at sea level has been measured over the size range of $1.5.10^4$-4.10^6 particles. As mentioned earlier, the hadrons were detected after interacting in either lead or iron absorbers on top of the flash tube chamber. After recording a burst, the burst width was measured in the flash tube layers below

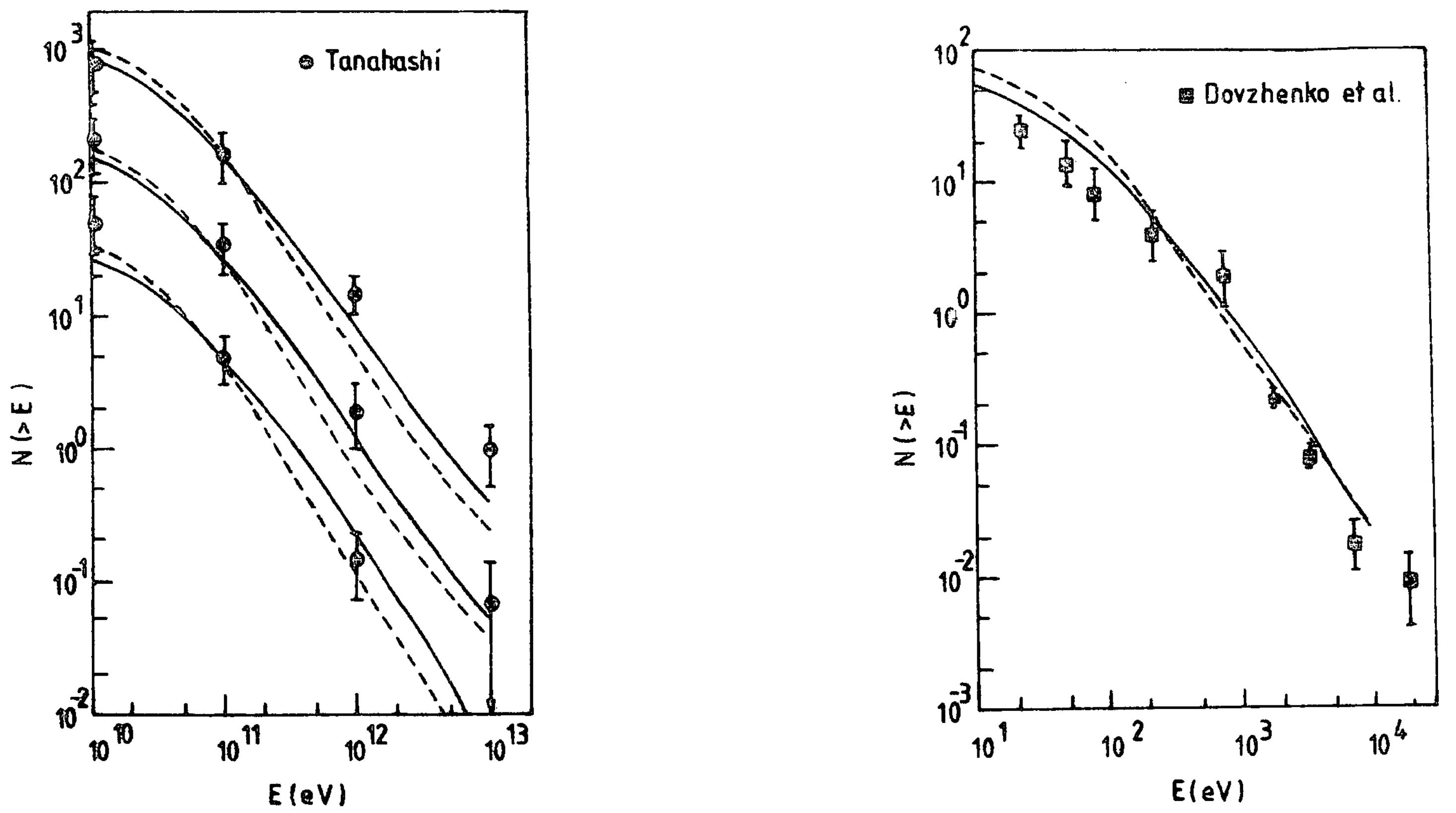

Figure 7.3 : Integral energy spectra of hadrons at sea level (a) and mountain altitude (b) (After Kempa et al, 1976).

the lead or iron and a conversion of burst width to burst size and then to energy was carried out. The relation between burst width and burst size of the bursts under the lead and iron absorbers has already been measured (Cooper, 1974). The conversion curve from burst size to energy of the incident hadron has also been measured, and using the results of these two measurements Figures 7.4 and 7.5 are calculated which give a direct relation between burst width and energy of the incident hadron for lead and iron absorbers respectively (pion and proton primaries are considered in each case). Although it is obvious that a number of bursts are produced by proton primaries, charged bursts are assumed to be produced by pions and neutral bursts by neutrons as pions and protons of the same energy give almost the same burst width.

7.3.2 Correction to the Energy Distributions of Hadrons

Figures 7.6a and 7.6b show the differential and integral frequency distribution of energy for all hadrons observed in the chamber. A correction was applied, however, since for a certain burst size there is a bias toward smaller burst widths. This arises because the probability that an event is accepted is a function of the width of the burst. An acceptable event is one in which the whole width of the burst can be seen in the flash tubes, while as the burst width increases the probability that the whole of the burst will be contained in the flash tubes, decreases. Looking back at Figure 6.3 and assuming that the burst width measured at the centre of F1a and F1b to be ℓ, then the probability of acceptance is $\frac{L - \ell}{L}$. Considering these points and using the results of Figures 6.4 and 6.5, the acceptance probability of a burst produced in the lead or iron

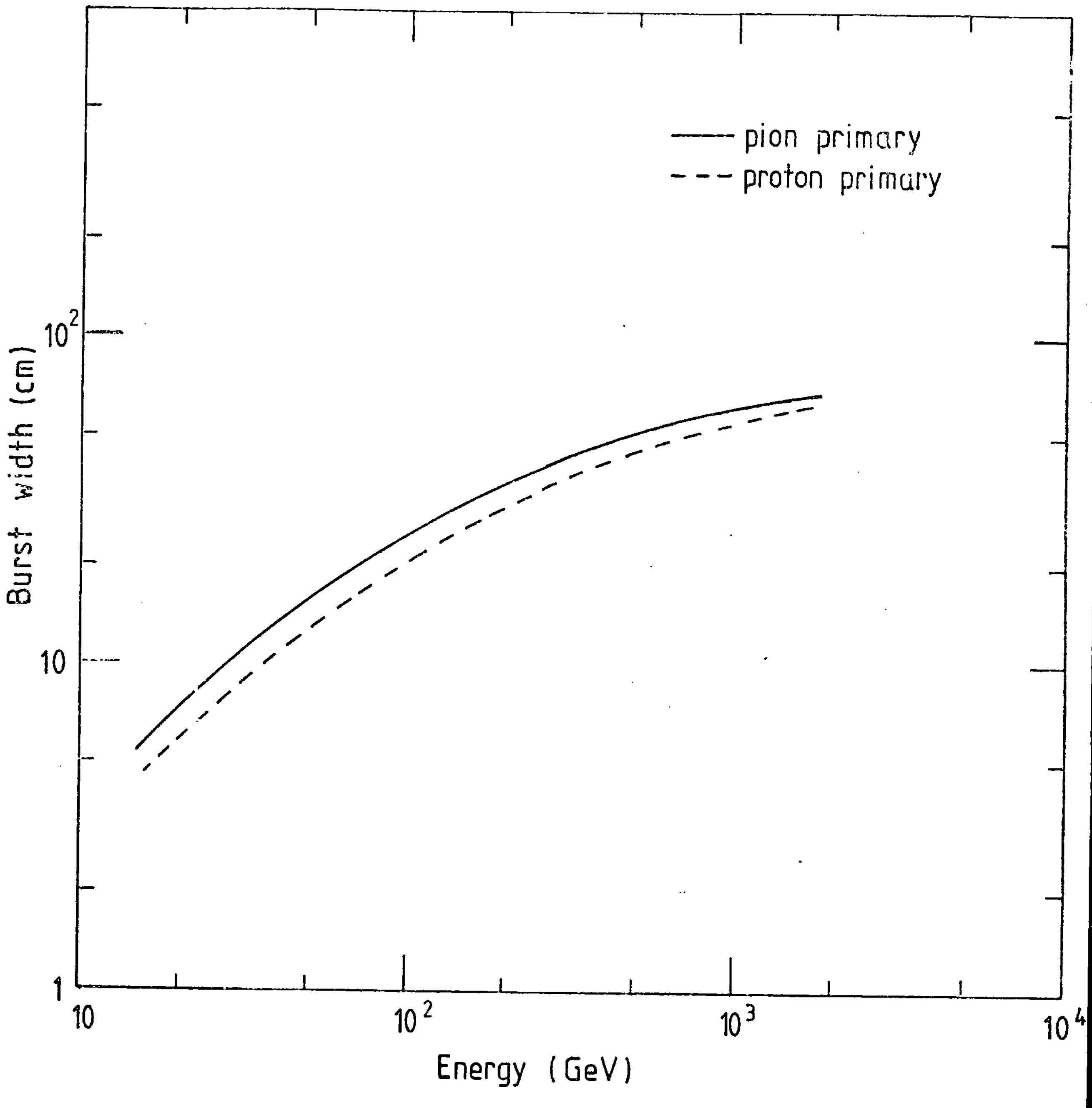

Figure 7.4 : The variation of burst width (measured in the flash tube chamber) with energy of incident pions and protons for a 15cm thick lead absorber. Time delay = 20 μs.

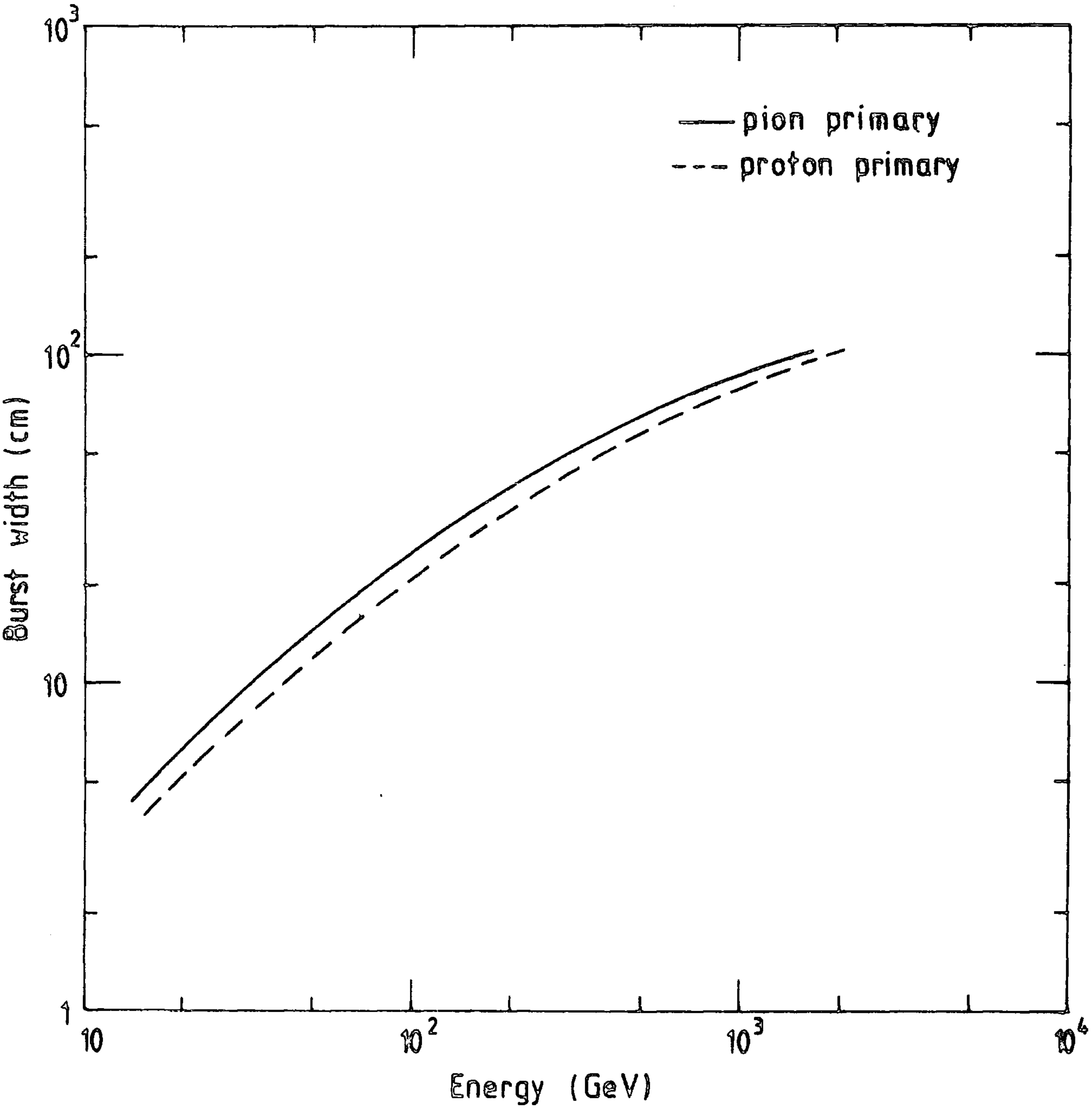

Figure 7.5 : The variation of burst width (measured in the flash tube chamber) with energy of incident pions and protons for a 15 cm thick iron absorber. Time delay = 20 μs.

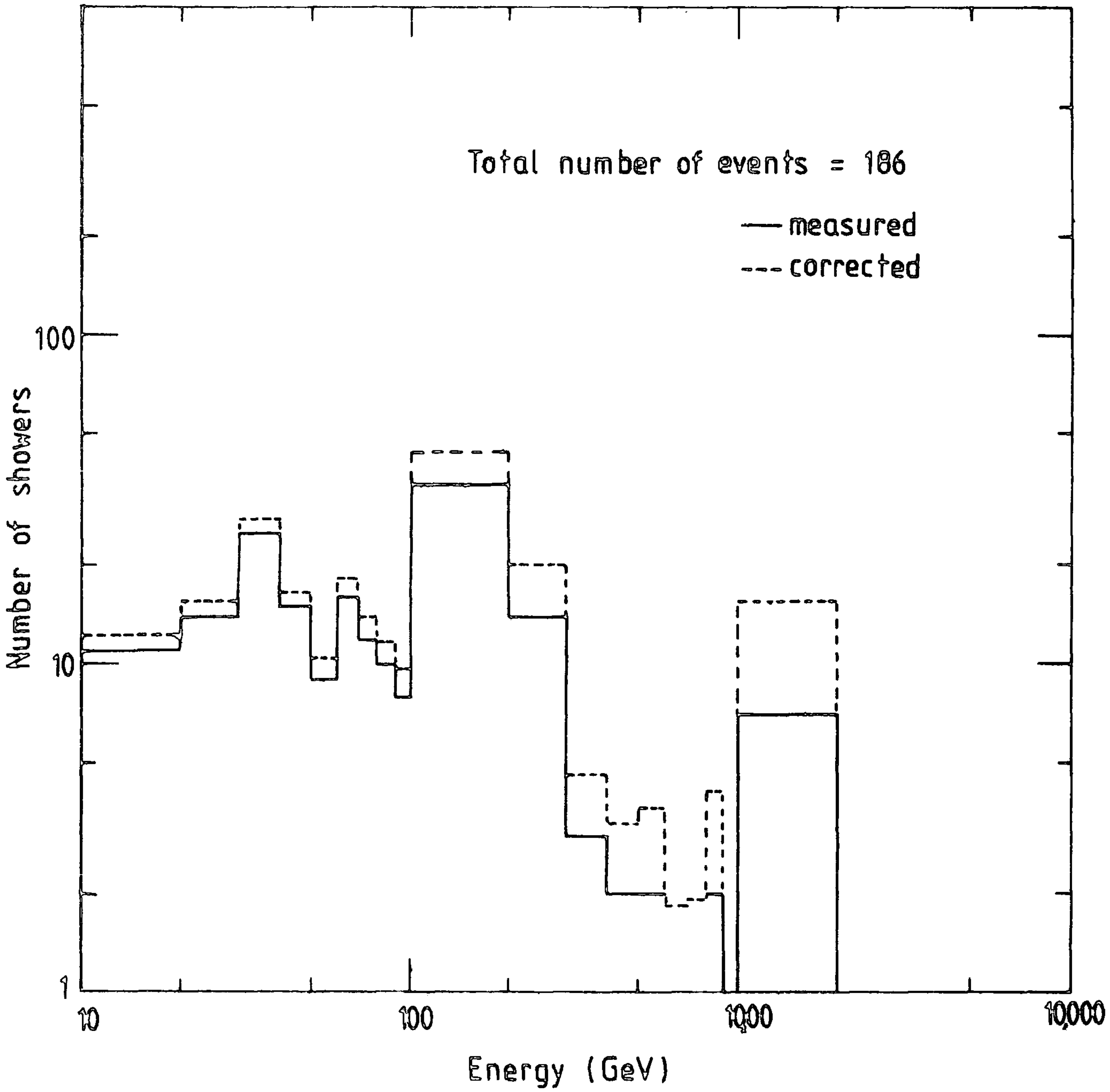

Figure 7.6a : Differential energy distribution of hadrons observed in the flash tube chamber.

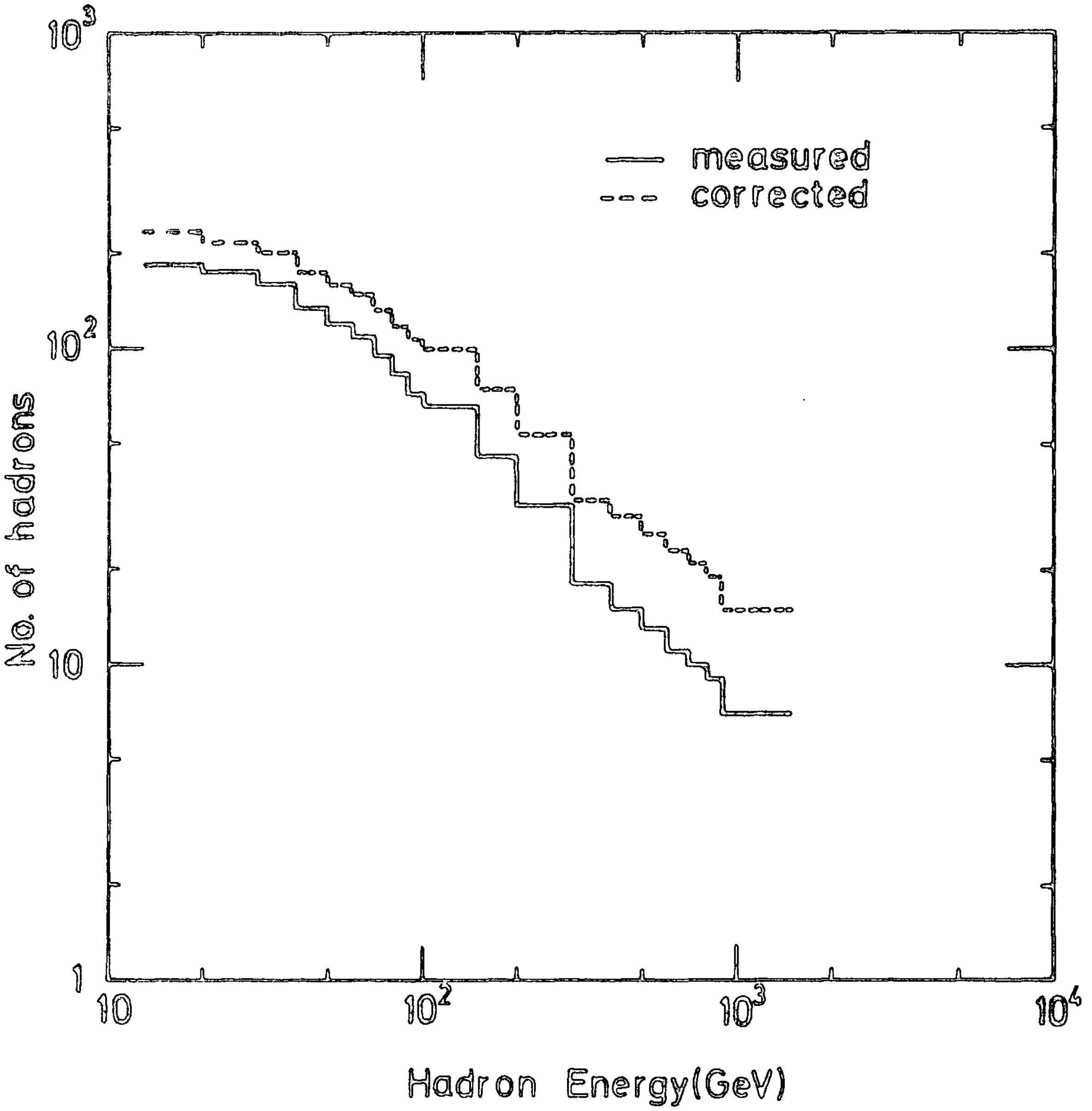

Figure 7.6b : Integral energy distribution of hadrons observed in the flash tube chamber.

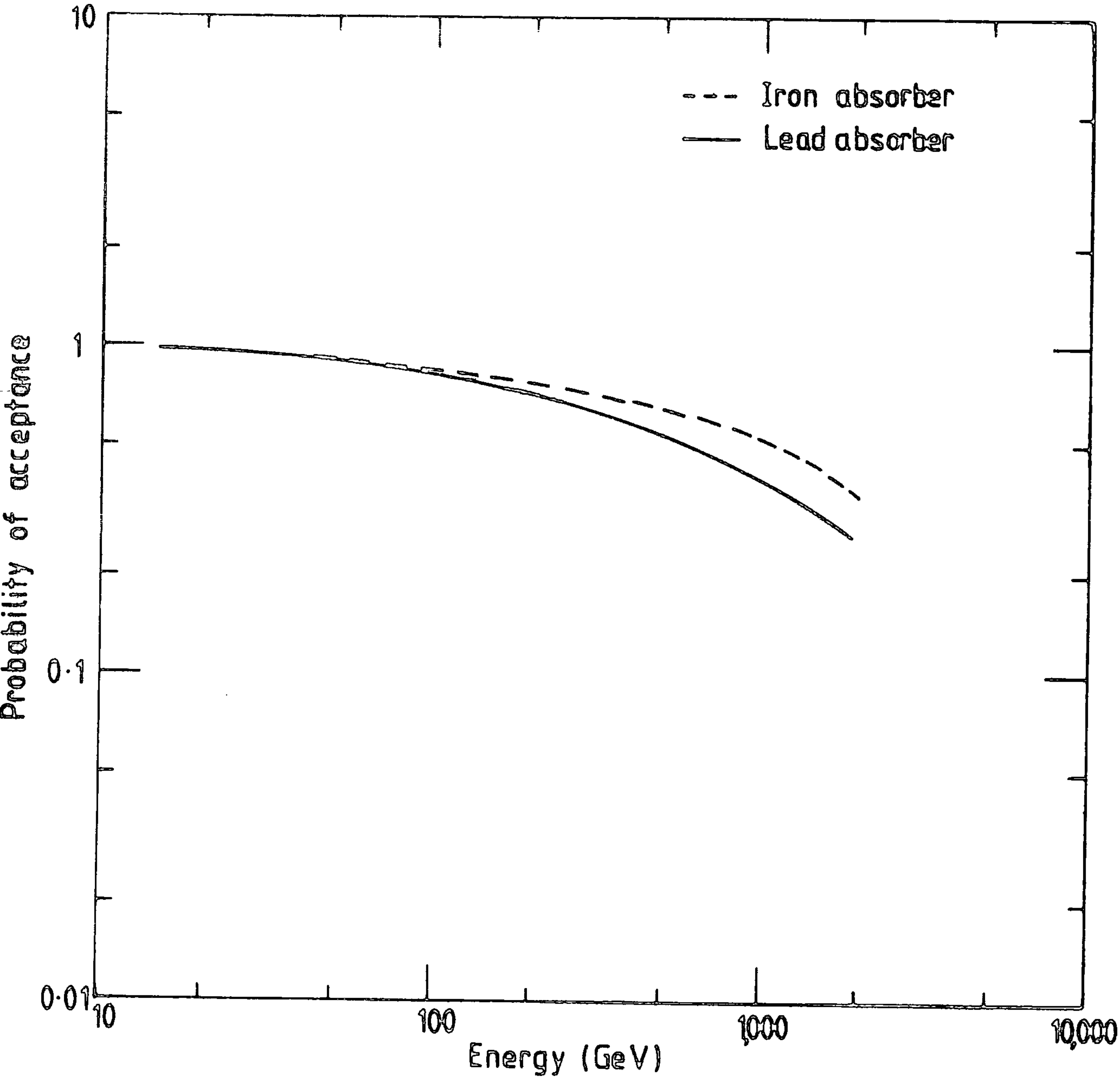

Figure 7.7 : The acceptance probability of a burst produced in the lead or iron absorbers as a function of the energy of the incident pion.

targets as a function of the energy of the incident hadron has been calculated and plotted in Figure 7.7. This has been used to correct the measured energy distribution of hadrons and the dashed lines in Figure 7.6 shows this correction.

7.3.3 Results

The measured integral energy spectrum of hadrons is shown in Figure 7.8 and the best line through the points has the form of

$$n_H\ (\geq 13\ \mathrm{GeV}) = 2.3\ 10^3\ \ E^{-0.73\ \pm\ 0.04}$$

where E is in units of GeV

Using the results of Figure 6.9a which gives the total number of hadrons in a shower of size N, the data is normalized to appropriate values, and compared with the energy spectrum in the summary of Greisen (1960), Figure 7.9.

Figure 7.10 shows the present measured energy spectrum alongside other measurements and compared with the simulations of Grieder (1976). It is clear from Figure 7.9 and Figure 7.10 that the present experimental results agree reasonably well with other measurements as well as with theoretical predictions.

7.4 ANGULAR DISTRIBUTION OF HADRONS IN EAS

Figure 7.11a shows the zenith angle distribution of hadrons observed in the flash tube chamber, where for comparison the zenith angle distribution for all shower triggers is also shown (Figure 7.11b). Assuming the angular distribution of hadrons in EAS follows the form of $I(\theta) = I(o)\cos^n\theta$, then the best value for n from the measured hadron angular distribution is calculated to be $n = 8.7 \pm 0.9$. Since for near

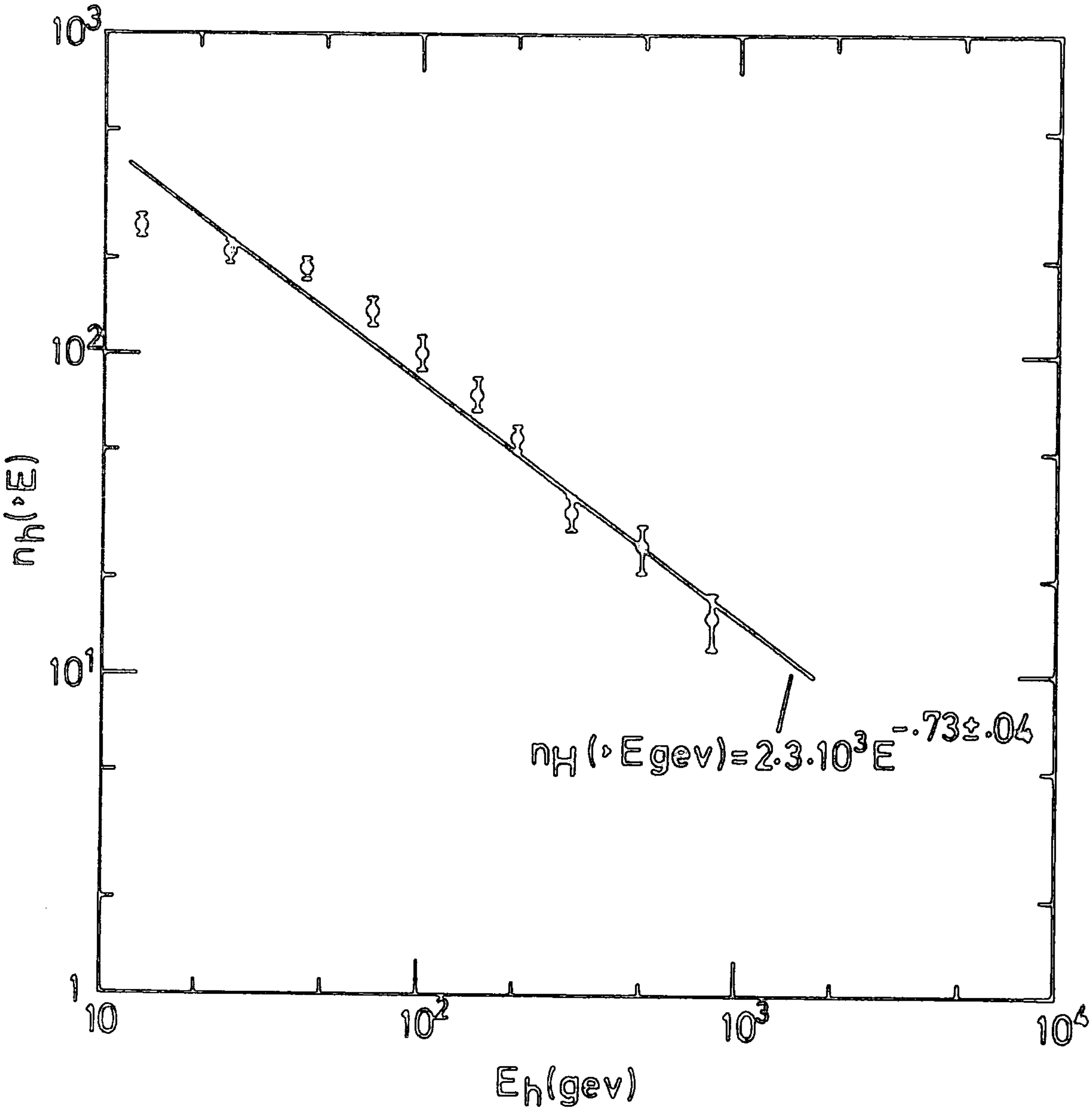

Figure 7.8 : Measured integral energy spectrum. An analytical fit to the measurement is $n_H\ (>E) = 2.3.10^3\ E^{-.73\ \pm\ .04}$ with E in GeV.

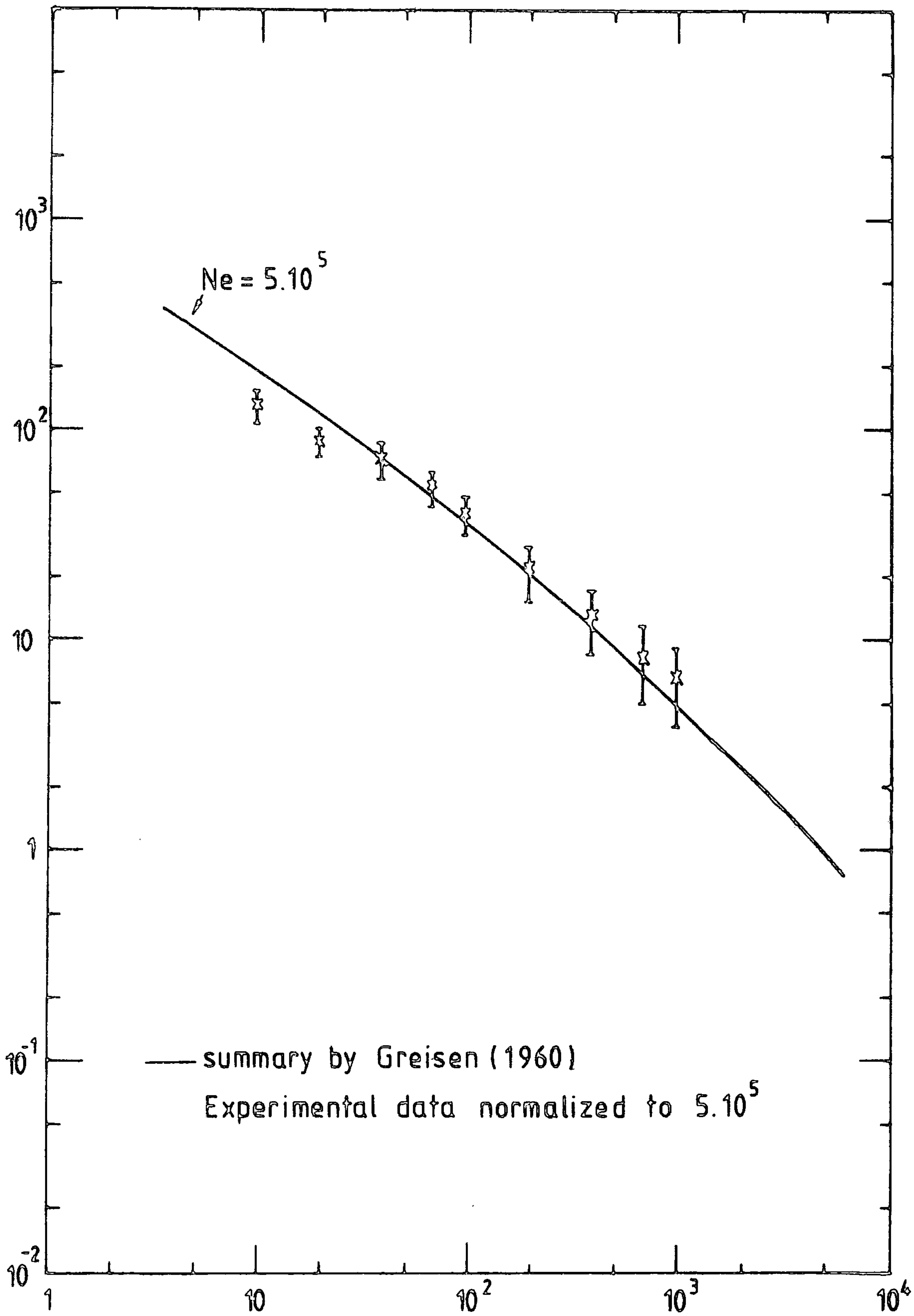

Figure 7.9 : The measured integral spectrum compared with the summary of Greisen (1960).

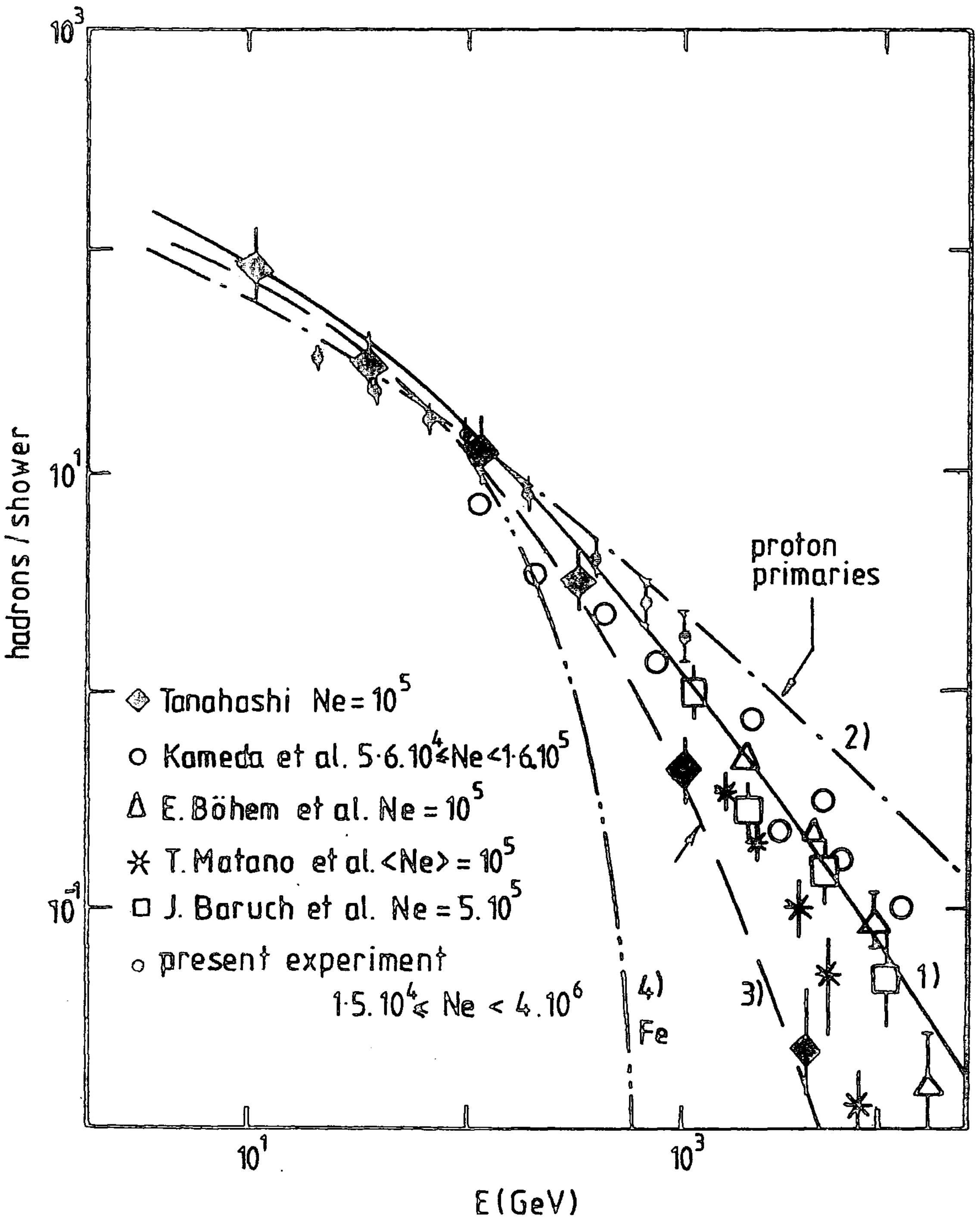

<u>Figure 7.1U</u> : Measured integral energy spectrum of hadrons compared with other measurements as well as theoretical predictions for primary energies $E_0 = 10^6$ GeV. Curves1, 2 and 3 refer to proton primaries and curve 4 to iron nuclei.

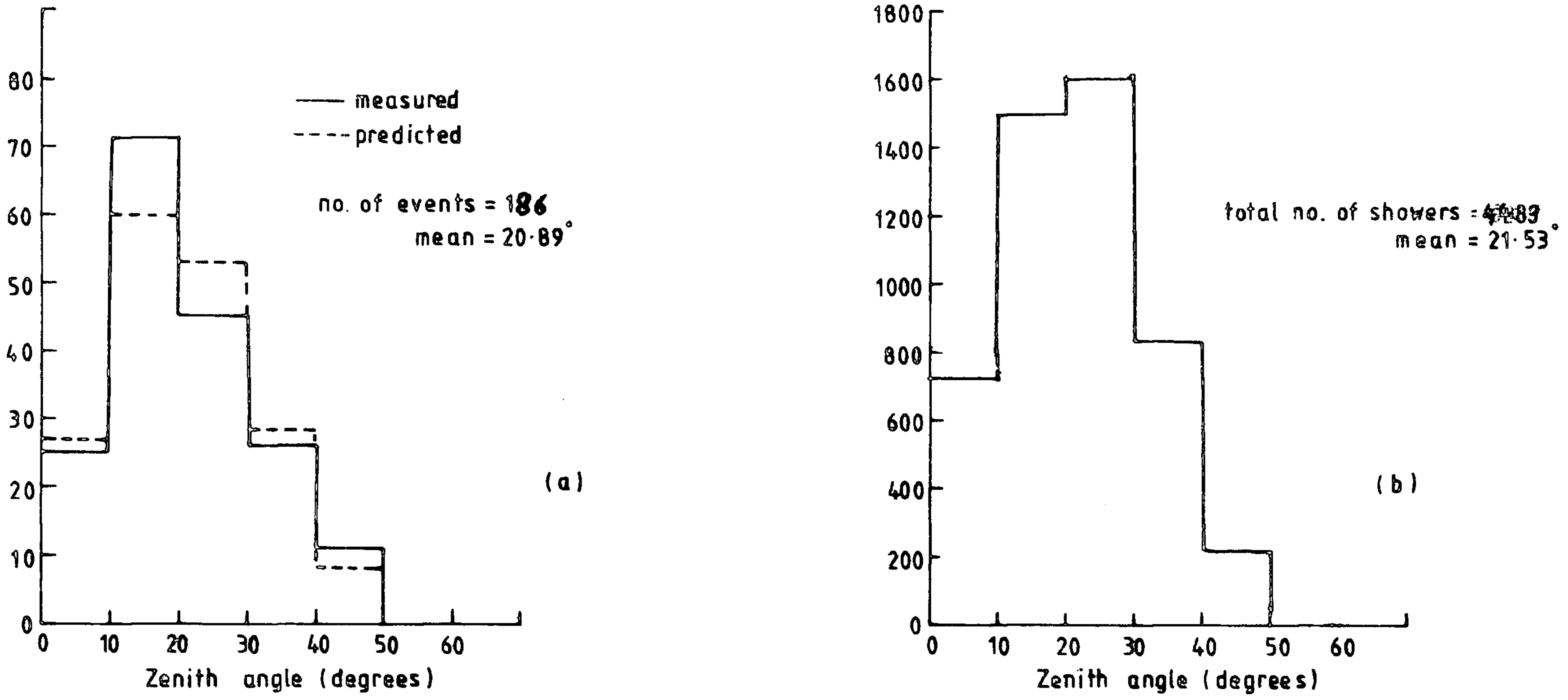

Figure 7.11 : Zenith angle distribution for hadrons observed in the flash tube chamber (a), and for all analyzed data (b). Dashed lines are a fit to the data according to $I(\theta) = I(o) \cos^n\theta$ where $n = 8.7 \pm 0.9$ and with the requirement $\theta < 50^o$ imposed.

vertical zenith angles $n = \frac{t}{\lambda_H}$, where t is the thickness of atmosphere (1030 gr cm^{-2}) and λ_H is the hadron attenuation length. After working out a value for n, it is possible to estimate λ_H. From the present measurement, $\lambda_H = \frac{1030}{n}$ gr cm^{-2}, is calculated to be 118.3 ± 11.1 for showers in the range of $1.5.10^4 - 4.10^6$. This value is inconsistent with $\lambda_H = 85$ gr cm^{-2} which was suggested by Kameda et al (1965).

7.5 THE RATIO OF CHARGED TO NEUTRAL HADRONS

The charge of the particles initiating a burst in the lead could not be determined since no flash tubes were located above the lead abosrber. However, for bursts occurring in the iron, charge identification was possible in the eight layers of flash tubes (Fla) situated directly above the iron absorber. The definition adopted for a burst produced by a charged particle was that it must have an observable track in (Fla) parallel to the burst direction and be coincident with the middle of the burst. A neutral particle burst was defined as one for which the above definition of a charged particle was not satisfied. Thus, only the bursts under the iron could be used to calculate the ratio of charged to neutral hadrons. Using the data in Table 6.1 the charge to neutral ratio of the hadrons with energy ≥ 13 GeV in the present experiment is calculated to be $\frac{c}{n} = 7.12$ (irrespective of shower size). To investigate the shower size dependence of the ratio the data has been divided into two ranges of shower size and $\frac{c}{n}$ has been found for each range. The ratio increases from 6.2 ± 1.1 for the showers in the range of $1.5.10^4-2.10^5$ particle, to 10.73 ± 1.4 for showers in the size range of $2.10^5- 4.10^6$. This result is in disagreement with the results of Kameda et al which did not show any size dependence for the charge to neutral ratio, and obtained a ratio of 4.5 ± .05 for showers in the range of $4.10^4 - 4.10^6$ particles. The discrepancy could be interpreted in this way: The neutral hadrons measured, may be an underestimation of the true number due to the losses caused by misidentification of a neutral burst being produced by a charged hadron. This arises when the density of penetrating charged particles become such that there is a significant probability that there will be an associated charged particle track in the flash tubes directly above the neutral burst and with approximately the same direction. When this happens, the burst will be wrongly identified as due to a charged particle. Figure 7.12 shows the variation of $\frac{c}{n}$ ($\geq$ 25 GeV) as a function of the primary EAS energy with the predictions of Gaisser et al (1976). The full line includes K_o, $\bar{K}_o$ and $n, \bar{n}$ while the dashed line includes only K_o, $\bar{K}_o$ and neglects $n, \bar{n}$ production. The mountain level results of Vatcha et al (1973), measured at 2200 m above sea level, are also shown. The present measurement is in reasonable agreement with Gaisser's calculations. In Figure 7.13 the experimental data on $\frac{c}{n}$ as a function of hadron threshold energy is shown and compared with expectation. Although the reasons why the discrepancy of the data exists are not answered yet, one of them may simply be the biasses introduced in the assignment of charge.

7.6 ESTIMATION OF THE RATIO OF PIONS TO NUCLEONS IN COSMIC RAYS AT SEA LEVEL

The measured ratio of charged to neutral hadrons can be used to estimate the ratio of pions to nucleons in EAS.

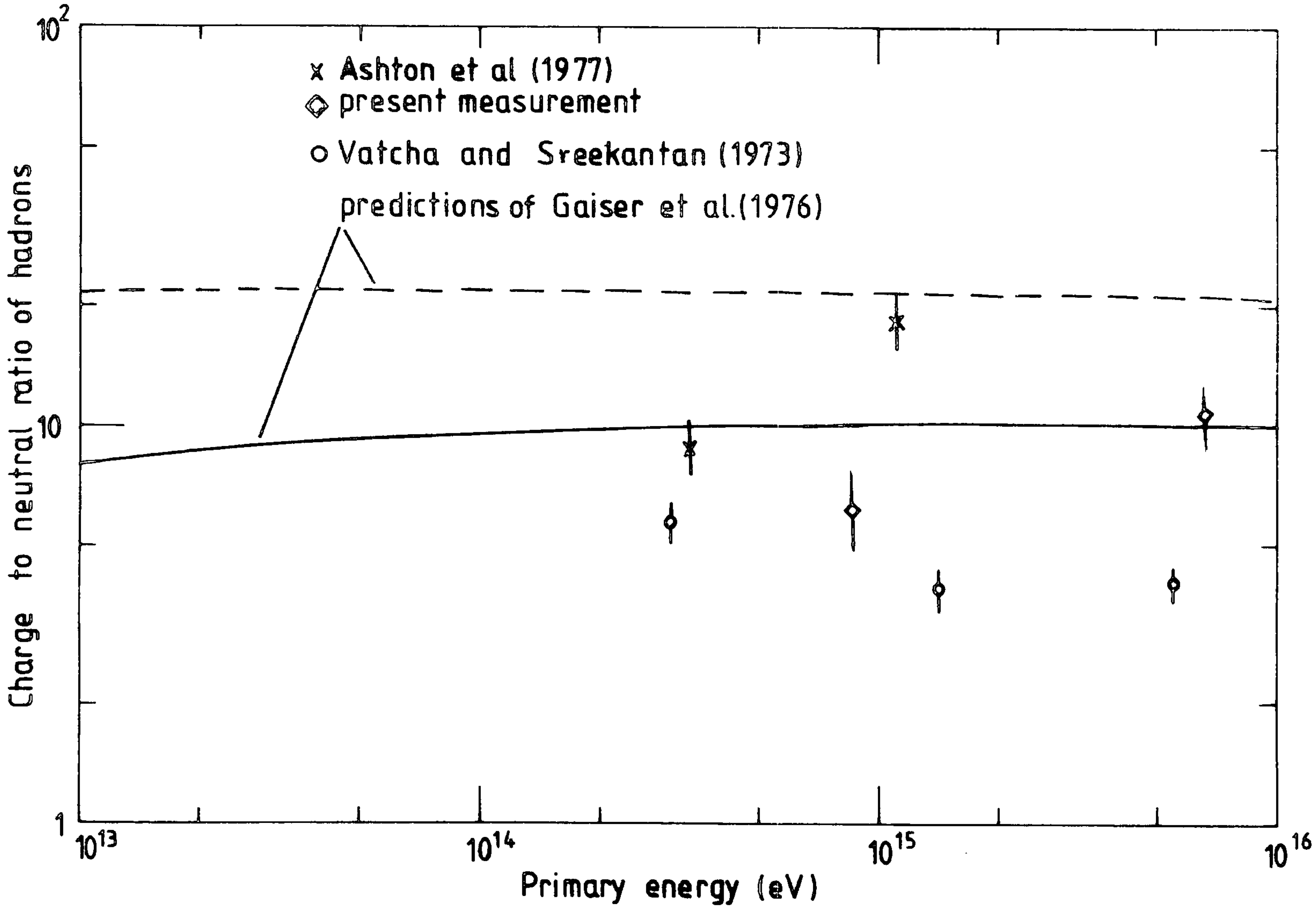

Figure 7.12 : Charge to neutral ratio of hadrons with energy $\geqslant 25$ GeV in EAS as a function of primary energy. Full line includes k_o, $\bar{k}_o$, n and $\bar{n}$. Broken line includes only k_o and $\bar{k}_o$. The experimental point from the present work is plotted at the average energy of the primary cosmic rays initiating the observed showers.

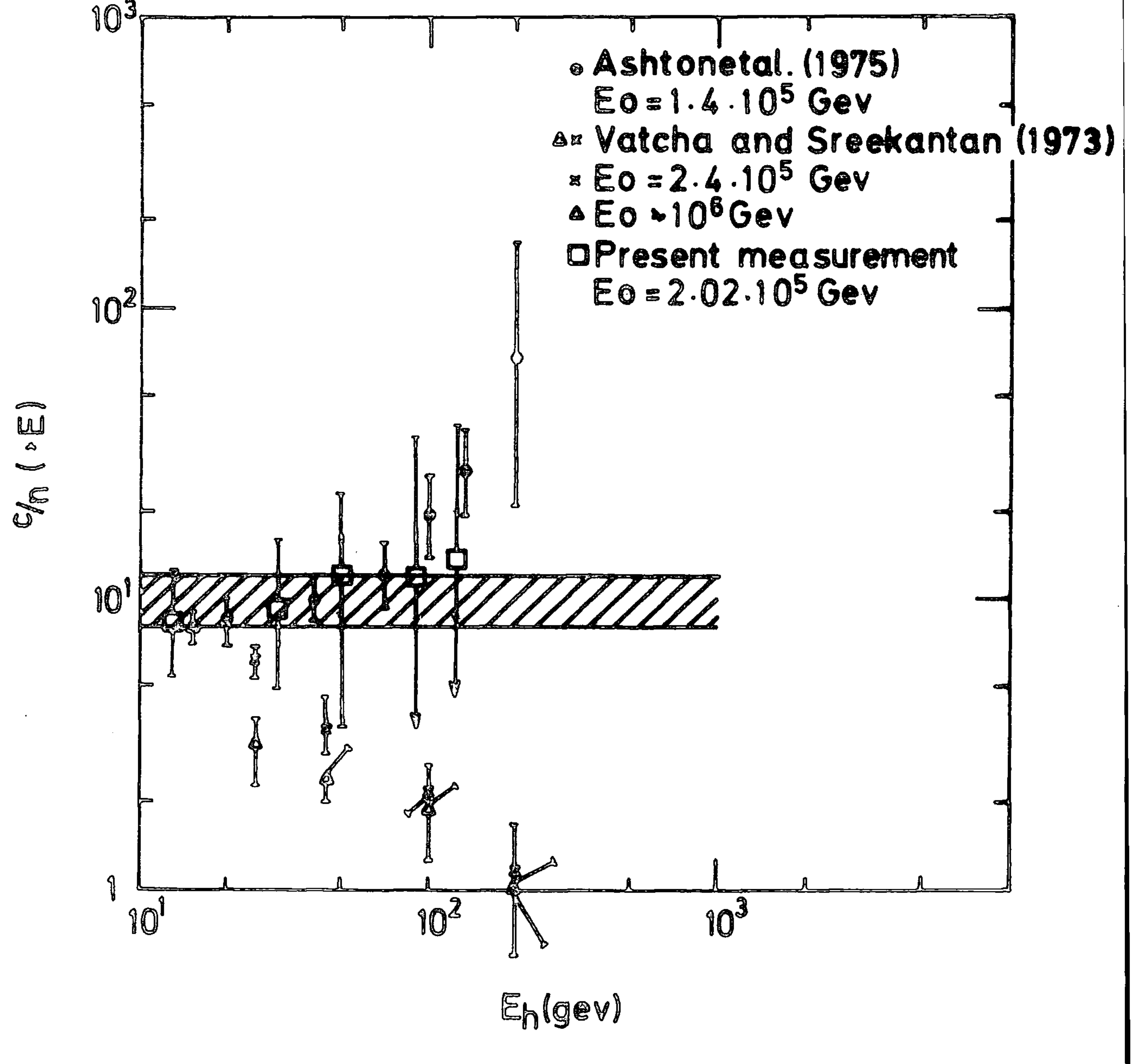

Figure 7.13 : Comparison of the calculated (dashed area) and measured values of c/n as a function of hadron threshold energy.

Assuming the charged bursts are produced either by pions or protons and the neutral bursts by neutrons and also assuming the number of protons equals the number of neutrons at sea level, one can write

$$\frac{c}{n} = \frac{N_\pi + N_p}{N_n} = \frac{N_\pi}{N_n} + \frac{N_p}{N_n} = 7.12$$

where N , N_p and N_n are the number of pions, protons and neutrons respectively. Assuming $N_p = N_n$ then

$$\frac{N_\pi}{N_n} = 6.12, \quad \text{therefore}$$

$$\frac{N_\pi}{N_n + N_p} = 3.1$$

To calculate $\frac{c}{n}$ only the bursts produced in iron are used and to obtain the actual ratio of pions to nucleons in EAS account should be taken for the fact that the hadrons that reach the iron target in the flash tube chamber, Figure 2.10, have already traversed 5'' of liquid scintillator and 15 cm of lead. Therefore, assuming $N_{o\pi}$ and $N_{o\,N}$ are the total number of pions and nucleons arriving at the top of the chamber then

$$\frac{\text{Number of pions interacting in iron}}{\text{Number of nucleons interacting in iron}} =$$

$$\frac{N_{o\pi}}{N_{oN}} \times \frac{\exp\left\{-\frac{Y_{sci}}{\lambda_{\pi,sci}}\right\}\exp\left\{-\frac{Y_{pb}}{\lambda_{\pi,pb}}\right\}\left[1-\exp\left\{-\frac{Y_{Fe}}{\lambda_{\pi,Fe}}\right\}\right]}{\exp\left\{-\frac{Y_{sci}}{\lambda_{N,sci}}\right\}\exp\left\{-\frac{Y_{pb}}{\lambda_{N,pb}}\right\}\left[1-\exp\left\{-\frac{Y_{Fe}}{\lambda_{N,Fe}}\right\}\right]} = 3.1$$

where Y_{sci}, Y_{pb} and Y_{Fe} are the thickness of scintillator, lead and iron and $\lambda_{\pi,sci}$, $\lambda_{\pi,pb}$ and $\lambda_{\pi,Fe}$ are mean free path of pions in the scintillator, lead and iron and $\lambda_{N,sci}$, $\lambda_{N,pb}$ and $\lambda_{N,Fe}$ are mean free path of nucleons in the scintillator, lead and iron respectively.

Using the constants shown in Table 7.2 the ratio of pions to nucleons in EAS is calculated to be

$$\frac{N_{o\pi}}{N_{o_N}} = 3.26$$

This value leads to the conclusion that the number of nucleons in cosmic rays is about 31% of that of charged pions and this is remarkably close to 30% suggested by Arakimori et al (1979).

Using the ratio of pions to nucleons the ratio of the number of pions interacting in lead to that of nucleons interacting in lead is calculated and consequently the percentage of bursts produced by pions and the percentage of bursts produced by nucleons are calculated to be 75.6% and 24.4% respectively.

7.7 RATIO OF BURSTS PRODUCED IN LEAD AND IRON ABSORBERS

The relative frequency of bursts produced in the lead and iron absorbers could lead us to an estimation of the contribution to the burst spectra by muon induced bursts, This ratio could be calculated from the following formula,

$$\frac{n(pb)}{n(Fe)} = \frac{1 - \exp\left\{-\frac{Y_{pb}}{\lambda_{pb}}\right\}}{1-\exp\left\{-\frac{Y_{Fe}}{\lambda_{Fe}}\right\}\exp\left\{-\frac{Y_{pb}}{\lambda_{pb}}\right\}}$$

where Y_{pb} and Y_{Fe} are the thickness of lead and iron absorbers (15 cm) and λ_{pb} and λ_{Fe} are interaction length of hadrons in lead and iron.

Material	Iron	Lead	Scintillator
Density	7.6 g cm^{-3}	11.34 g cm^{-3}	1.03 g cm^{-3}
Radiation length, X_0	14.1 g cm^{-2} $= 1.86$ cm	6.5 g cm^{-2} $= 0.58$ cm	42.5 g cm^{-2} $= 41.3$ cm
pion mean free path	21.6 cm $= 11.6\ X_0$	19.8 cm $= 34.5\ X_0$	110 cm $= 2.7\ X_0$
proton mean free path	18.5 cm $= 9.9\ X_0$	19.2 cm $= 33.1\ X_0$	92 cm $= 2.2\ X_0$
critical energy, E_c	21 MeV	7.6 MeV	70 MeV

TABLE 7.2 : Constants used in the calculation of the percentage number of bursts produced by pions and nucleons in EAS (Ashton et al, 1975).

Using the information of Table 7.2, this ratio is found to be 2.19 and 2.25 for nucleon and pion primaries respectively.

The ratio measured in this experiment is 1.59 ± .32 which is inconsistent with expectation. A value of 1.81 ± .14 was measured by Nasri (1977).

7.8 THE MEAN TRANSVERSE MOMENTUM OF HADRONS

7.8.1 A Brief Discussion about 'Scaling'

The scaling hypothesis was introduced by R.Feynman (1969) and has received a great deal of interest in cosmic ray studies.

The simplest feature of this model suggests that the total cross-section in high energy interactions tends to remain constant as primary energy increases.

$$\sigma_{total} \xleftrightarrow[E_0 \to \infty]{} \text{Const.}$$

The slow rising multiplicity, which has a logarithmic energy dependence is another feature of scaling which encounters serious difficulties in connection with air shower simulations and observations. In particular, this model cannot account for the large number of muons observed in air showers. Inadequacy of Feynman scaling in explaining the observed electron-muon ratio is neatly displayed in Figure 7.14 where,for comparison, the results of simulations based on the CKP model,and the experimental results of Moscow State University,is also shown. As is obvious from Figure 7.14, in the scaling model, the number of muons is far too low and in comparison to the observations of Moscow State University, it is as much as a factor of ten

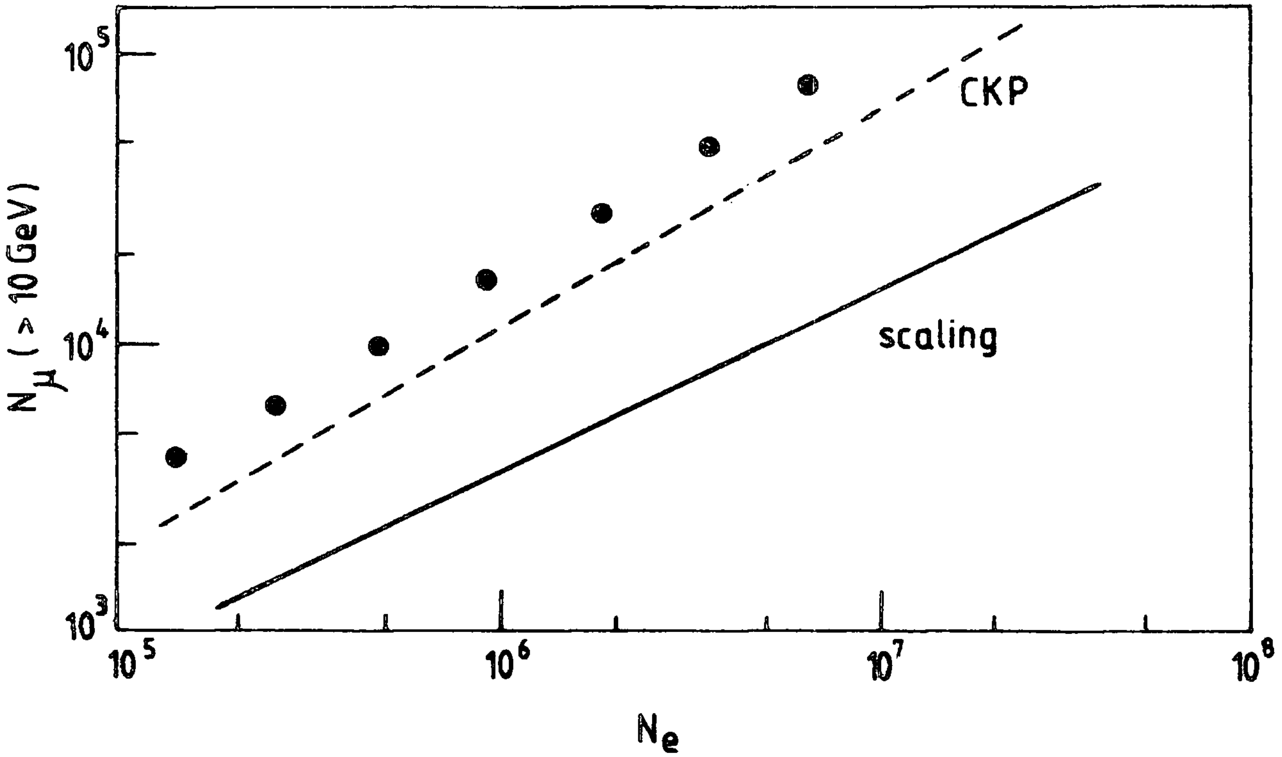

Figure 7.14 : Dependence of the number of muons to the number of electrons in a shower at fixed size. Experimental points are from the Moscow State University group and ----- CKP model, $N_\mu \sim Ne^{0.75}$. (After Capdevielle et al (1977).

or more down. Although there is some consistency between the results of observation and the scaling model at low energies (accelerator domain, below 5.10^{12} eV) many authors such as Wdowczyk and Wolfendale (1977), Gaisser et al (1978), Kalmykov and Khristiansen (1977), have shown that simulation results based on a scaling model is incompatible with observation and it would seem that the experimental data are in favour of slowly but continuously rising cross-sections over the entire energy range that has been investigated. One of the ways of testing the validity of scaling in cosmic rays is to study the transverse momentum which will be discussed in the next section.

7.8.2 Large Transverse Momentum

The occurrence of large transverse momenta was originally discovered by Japanese and Brazilian emulsion groups (1964). Subsequently, the search for large transverse momenta was extended to air shower investigations. After the discovery of the systematic rise of the tail of the transverse momentum distribution with energy at the CERN ISR, cosmic ray physicists intensified their efforts. There are several possibilities to look for large transverse momentum phenomena in air showers. One method is based on the lateral density distribution of the constituent particles in conjunction with simulation calculations, and another one consists of analysing multiple core events in air showers.

A hadron of energy E observed at sea level will on the average have made its last interaction at a height h km (corresponding to the interaction length of hadrons in air), above sea level. Assuming this hadron received transverse momentum P_T in the last interaction, then for the average case it will arrive at sea level at a distance r from the shower axis where with a good approximation one can write

$$\frac{r}{h} = \frac{P_T . C}{E} ,$$

$$E.r = h \, P_T C$$

In practice E and r can be measured and studying the average value of the distribution of the product will give information on the average value of $h \, P_T C$. Figure 7.15 shows a plot of E.r as a function of shower size where other experimental results are also shown. It is interesting to note that although the present measurement is below other measurements in general, the difference is not that significant.

Converting shower size N to an estimate of primary energy E_p using calculations of Kempa et al (1976), and also changing E.r to P_T assuming $h \simeq 0.8$ km, (corresponding to $\lambda = 9_0$ gr cm^{-2} which is the interaction length of a nucleon in the air) P_T can be plotted as a function of E_p. The final result is shown in Figure 7.16 where an attempt has also been made to summarize the available information on the variation of $< P_T >$ with incident hadron energy. Figure 7.17 shows the variation of the mean transverse momentum with incident hadron energy for the ranges $13 \geq E > 82$ Gev and $82 \geq E > 1500$ GeV. Although there is a difference in $< P_T >$ for the two ranges of hadron energy the shape of the curves for low and high energy hadrons in Figure 7.17 are similar.

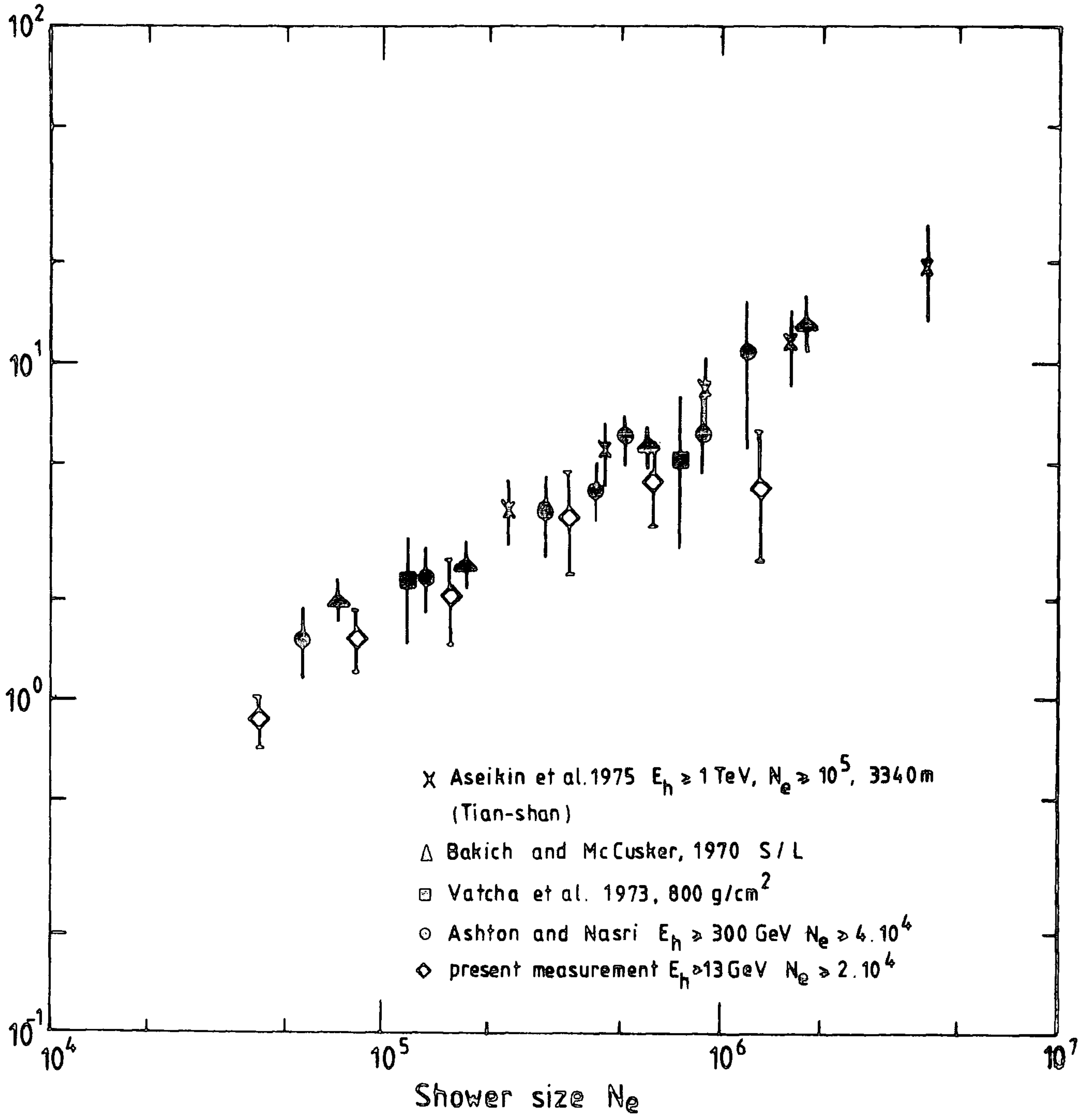

Figure 7.15 : Summary of measurements on the variation of $\langle E\, xr \rangle$ with shower size.

SOURCES OF POINTS IN FIGURE 7.16

The points 1, 2, 3, 4, 5, and 6 are the average of the following measurements :-

Point 1

Godksack, G., Riddiford, L., Tallini, B., French, B., Neal, W., Norbury, J., Skillicorn, I., Davies, W., Derrick, M., Mulvery, J., and Radojicic, D., Nuovo Cim., 23, 941 (1962).

Digi, A., Brandt, S., de Marco-Trabucco, A., Peyrou, Ch., Sosnowski, R. and Wroblewski, A., Nuovo Cim., 33, 1265 (1964).

Femino, S., Jannelli, S., and Mexxanares, F., Nuovo Cim., 31, 273 (1964).

Point 2

Fujioka, G., J. Phys. Soc., Japan, 16, 1107 (1961)

Brisbout, F., Cauld, C., Lehane, J., McCusker, C., Malos, J., Nishikawa, K. and Van Loon, L., Nucl. Phys., 26, 634 (1961).

Edwards, B., Losty, J., Perkins, D., Pinkau, K. and Reynolds, J., Phil. Mag. 3, 237 (1958).

Point 3

Edwards, B., Losty, J., Perkins, D., Pinkau, K. and Reynolds, J. Phil. Mag. 3, 237 (1958).

Minakawa, O. et al. Supp. Nuovo Cim., 11, 125 (1959).

Debenedetti, A., Garelli, C., Tallone, L. and Nigone, M., Nuovo Cim., 4, 1142 (1956).

Schein, M., Haskin, D., Lohrmann, E. and Teucher, M., Phys. Rev., 116, 1238 (1959).

Point 4

Edwards, B. et al, Phil. Mag., 3,237 (1958).

Malhotra, P. et al., Nuovo Cim., 40, A404 (1965).

Awunor-Renner, E. et al., Nuovo Cim., 17, 134 (1960).

Minakawa, O. et al., Suppl.Nuovo Cim., 11, 125 (1959).

Nishikawa, K., J. Phys. Soc., Japan, 14, 879 (1959).

Point 5

Ciok, P. et al., Nuovo Cim., 6, 1409 (1957).

Hasegawa, S., Nuovo Cim., 14, 909 (1959).

Kasuno, M., Nuovo Cim., 24, 1013 (1962).

Kasuno, M., Ph.D.Thesis, 1967 Dublin Institute for Advanced Studies.

Point 6

Adcock, C., Coats, R.B., Wolfendale, A.W., and Wdowczyk, J. J. Phys. A., 3, 697 (1970).

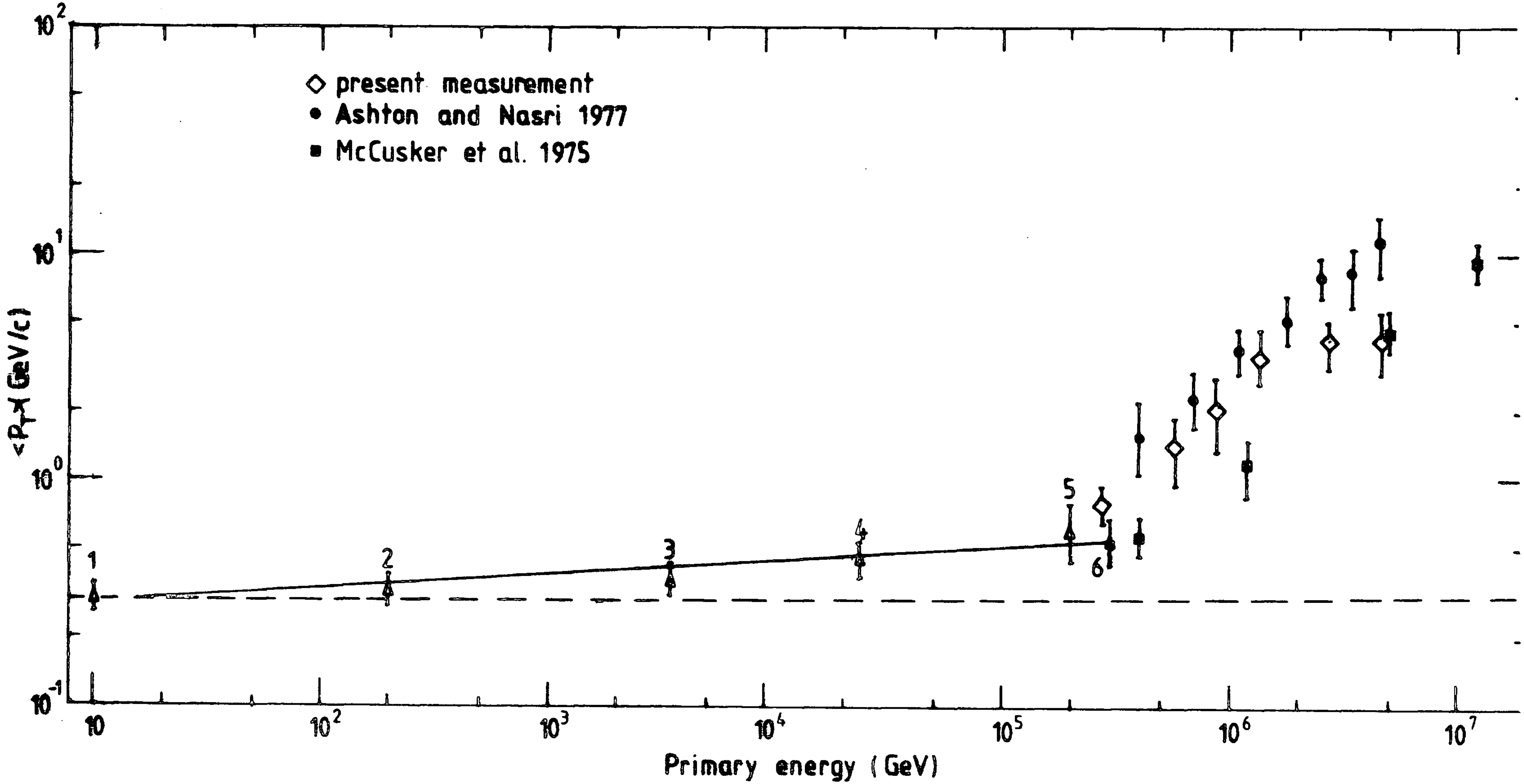

Figure 7.16 : Survey of measurements of the variation of $< P_T >$ with primary energy. The origin of the points 1,2,3,4, 5 and 6 are described in the text. The dashed line is as expected on the scaling model.

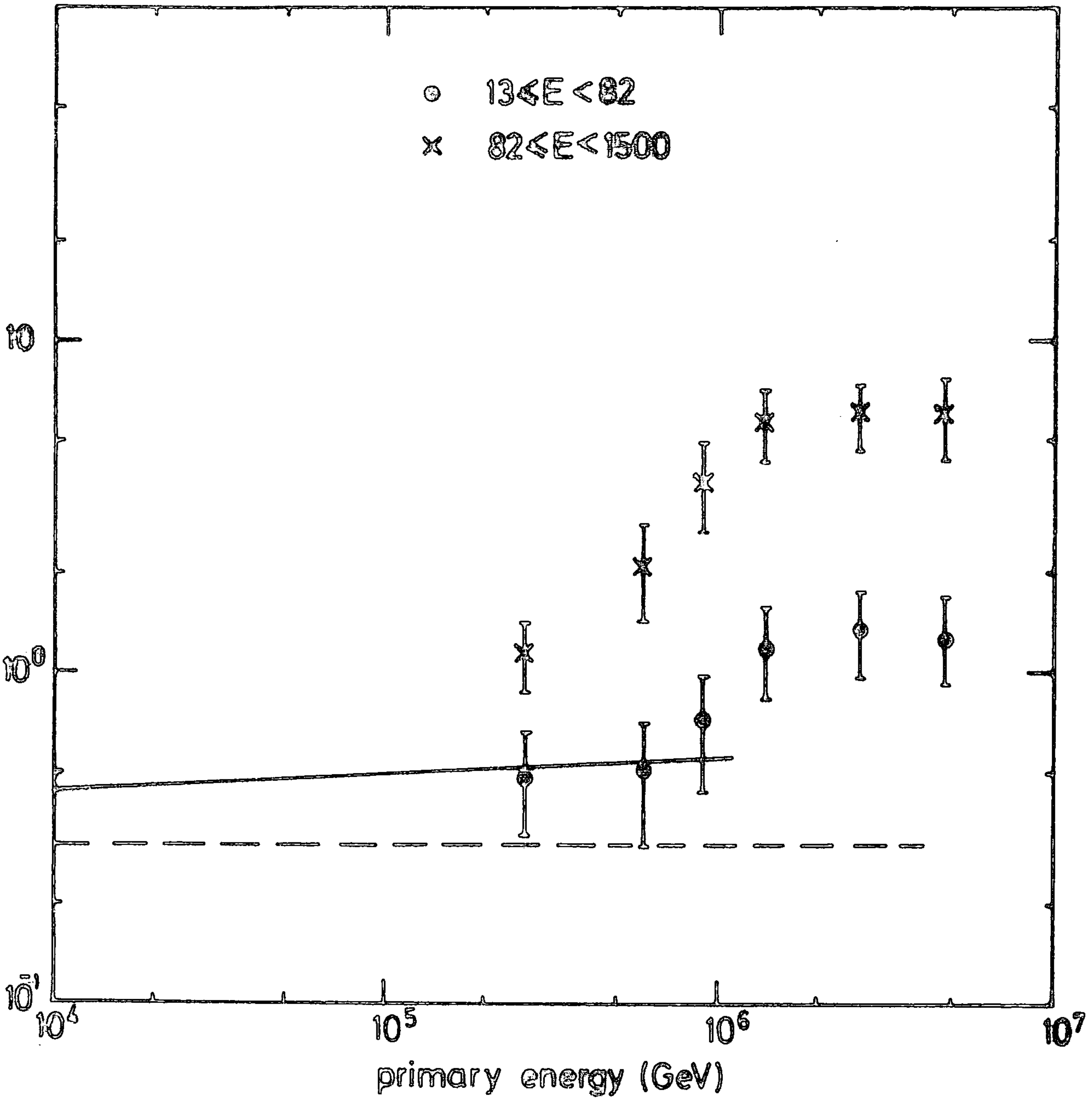

Figure 7.17 : Variation of $\langle P_T \rangle$ with primary energy for hadrons with energy $13 \leqslant E < 82$ GeV and $82 \leqslant E < 1500$ GeV. The expected lines (solid and dashed) are the same as in Figure 7.16.

Figure 7.18 shows the variation of E x r as a function of hadron energy while in Figure 7.19 the relation between E x r and shower size is displayed. On the basis of the present results shown in Figures 7.15 and 7.16, one can say that mean transverse momentum of hadrons increases slowly and steadily with increasing primary energy up to certain energy ($\sim$ 3.10^3 GeV). At around this point there is a sudden change of slope and mean transverse momentum increases drastically with increasing primary energy.

However, this is an anomalous effect and therefore requires careful consideration to see if any bias or error in measuring the different parameters involved may have caused it.

Looking at Figures 7.15 and 7.16 indicates that although previous measurements at Durham (Ashton et al,1977) had employed a hadron trigger, and the present work is based on an air shower trigger, there is reasonable agreement between the two methods and this automatically cancels out any possible bias due to triggering conditions.

The error in measuring hadron energy E and core distance r may have had an effect on the present result. The former is fully investigated in Appendix C and it is shown that the error in estimating hadron energy could not possibly have made such a difference to the results and the latter will be discussed in the following section.

7.9 EFFECT OF A CORE LOCATION ERROR ON THE MEASURED HADRON LATERAL STRUCTURE FUNCTION

To see the effect of a core location error on the present work the expected lateral distribution of hadrons is

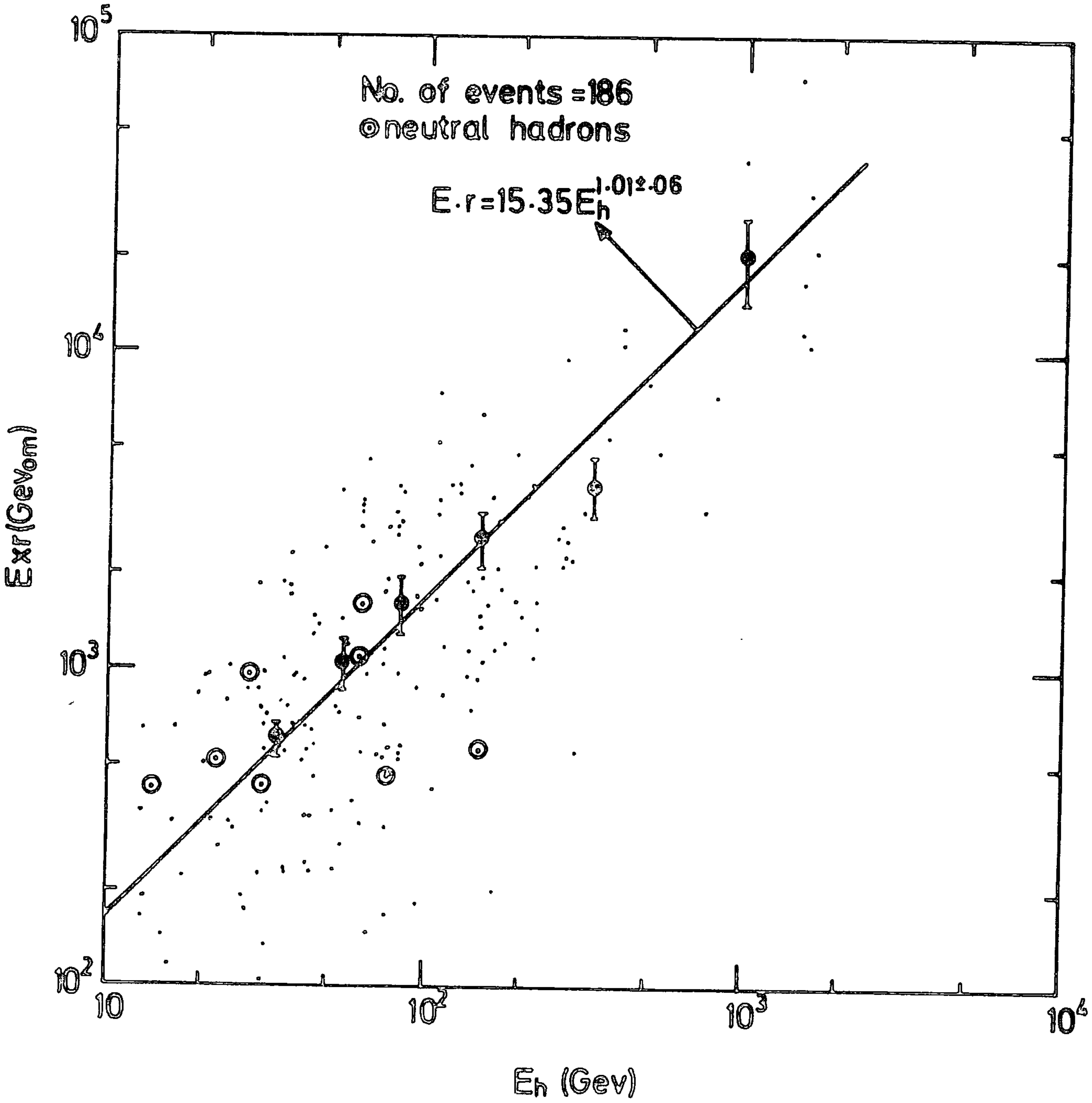

Figure 7.18 : Variation of Exr as a function of hadron energy. An analytical fit to the average behaviour is $E_r = 15.85\ E^{1.01} \pm 0.06$ GeV with E in GeV.

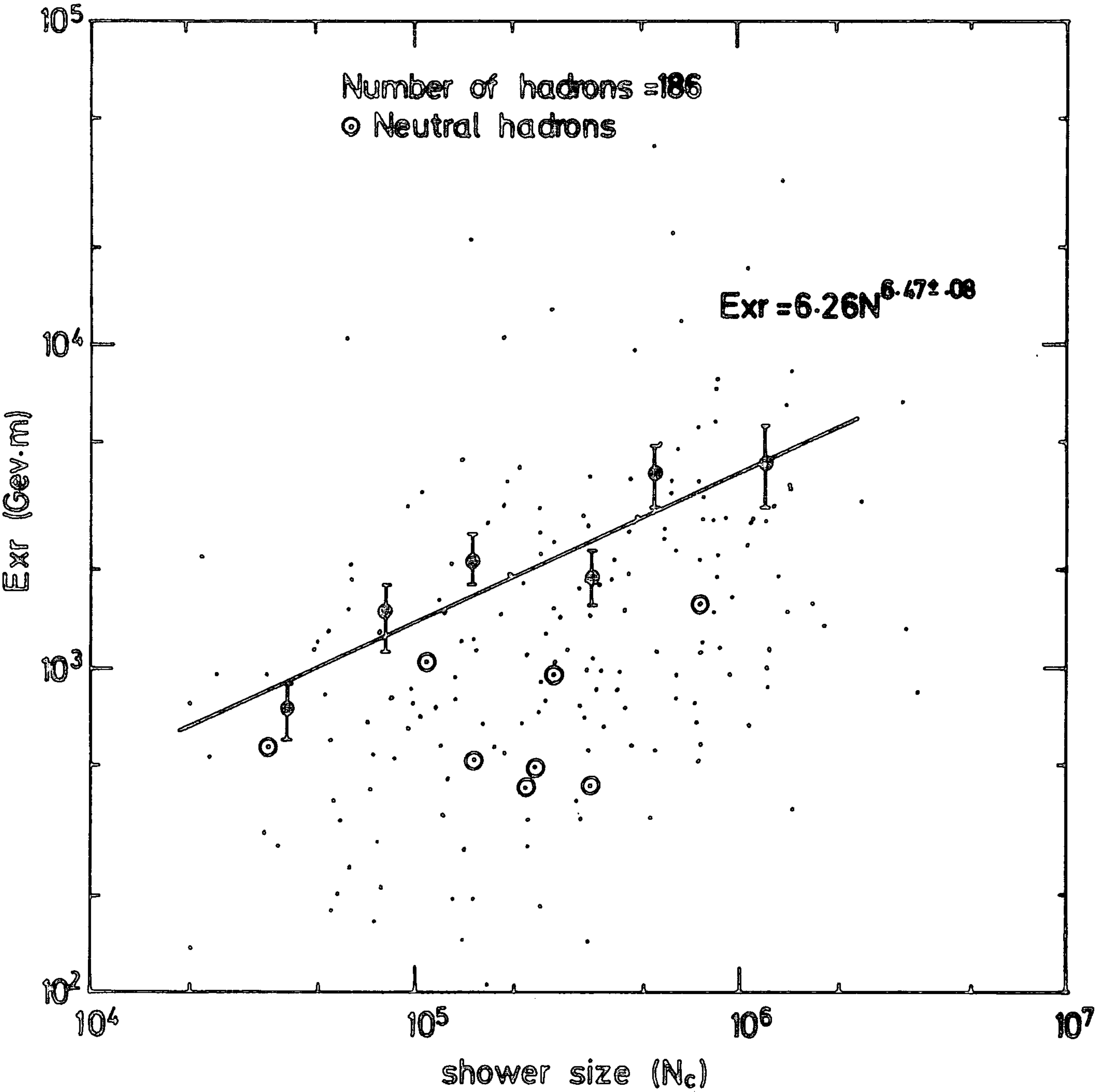

Figure 7.19 : The relation between E xr and shower size. An analytical fit to the average behaviour is $E_r = 6.26N^{0.47 \pm 0.08}$ GeVm with N in units of single particles.

calculated and is compared with the cases where the core location error is taken into account. To do this the following procedure is adopted.

For a normal expected case, it is assumed that hadrons are produced at a height h, ($h = 0.8$ km $= 90$ gr cm^{-2}), above sea level corresponding to one nucleon mean free path with the average transverse momentum $P_\perp = 0.33$ GeV/C for pions, (Predazzi, 1979), and $P_\perp = 0.58$ GeV/C for nucleons, (Hayakawa, 1969).

It is understood that the probability for a hadron of energy E falling at a distance r from the core of a shower is

$$P(r)dr = \frac{r}{r_0^2} e^{-\frac{r}{r_0}} dr \text{ where } r_0 = \frac{hP_0C}{E} \text{ with } P_0 = \frac{<P_\perp>}{2}$$

and the density of such hadrons is

$$\Delta(r) = \frac{P(r)dr}{2\pi r\ dr} = \frac{1}{2\pi r_0^2} e^{-\frac{r}{r_0}} \qquad (7.1)$$

where $r_0 = \frac{hP_0C}{E}$ with $P_0 = \frac{<P_\perp>}{2}$

Using equation 7.1, the probability of a hadron of energy E falling in the core distance range of ($r_1 \rightarrow r_2$) is calculated

$$P(r_1 \rightarrow r_2) = e^{-\frac{r_0}{r_0}} \left\{ 1 + \frac{r_1}{r_0} \right\} + e^{-\frac{r_2}{r_0}} \left\{ 1 + \frac{r_2}{r_0} \right\} \qquad (7.2)$$

Using equation 7.2, expected values are calculated and are shown in Figures 7.20a and 7.20b.

In Chapter 3, by means of Monte Carlo simulation, it was shown that the difference between the true core distances and the measured ones is a Gaussian distribution of standard deviation of $\sigma = 6.0$m. Bearing this in mind, and using statistical tables that give the area under the Gaussian probability curve, the dashed curves in Figure 7.20 are calculated. Comparison between the solid line and dashed line in Figure 7.20b indicates the effect of the core location error on the lateral distribution. Curves similar to those of Figures 7.20a and 7.20b were produced for the cases where $\sigma = 12.$m and also for different energy thresholds. Using the dashed distribution in Figure 7.20a and curves similar to that, the mean core distance $< r >$ is calculated and plotted against 2 r_0 in Figure 7.21,and Table 7.3 indicates the final results.

To see the effect of the core location error on transverse momentum, Figures 7.22, 7.23 and 7.24 display the variation of the average core distance as a function of the hadron energy for three different cases where it is assumed that all bursts are produced by nucleons, pions and a combination of the two, (24.4% nucleons, 75.6% pions), respectively. The expected curves with no core location error and also the cases where the core location error is taken into account are shown. It is clear from Figure 7.24, even if the error in core location is 12 metres, which is a 100% over-estimation, the difference between the present measurement and the expected calculation cannot be all due to measuring error. Hence it is claimed that the present measurement of transverse momentum is an anomalous result.

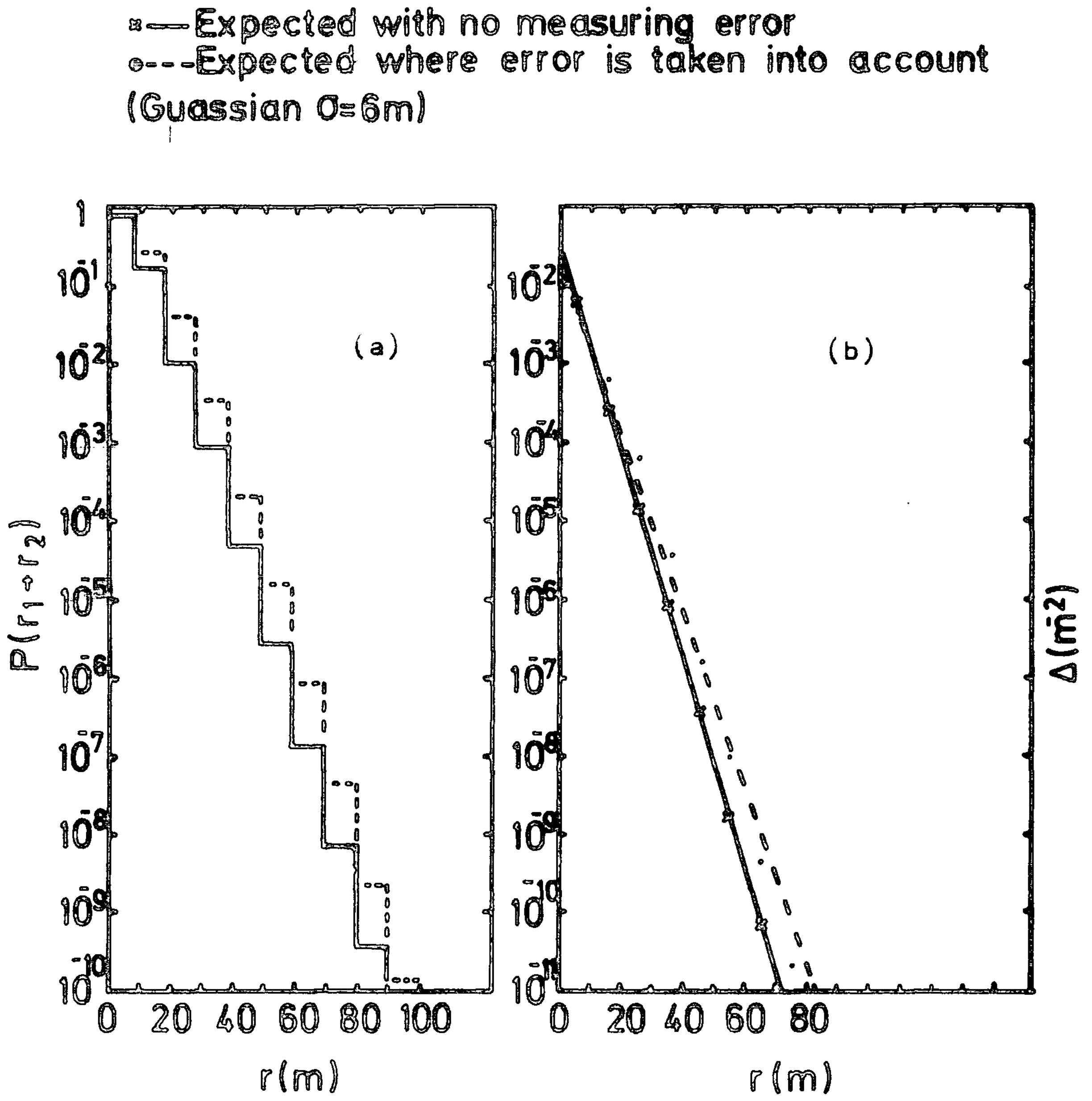

Figure 7.20 : (a) Probability that a hadron of energy E falls in the distance range indicated from the axis.

(b) Expected lateral distribution of hadrons calculated from (a).

In both (a) and (b) the solid lines assume no core location error and the dashed lines assume Gaussian core location errors of standard deviation 6.0m.

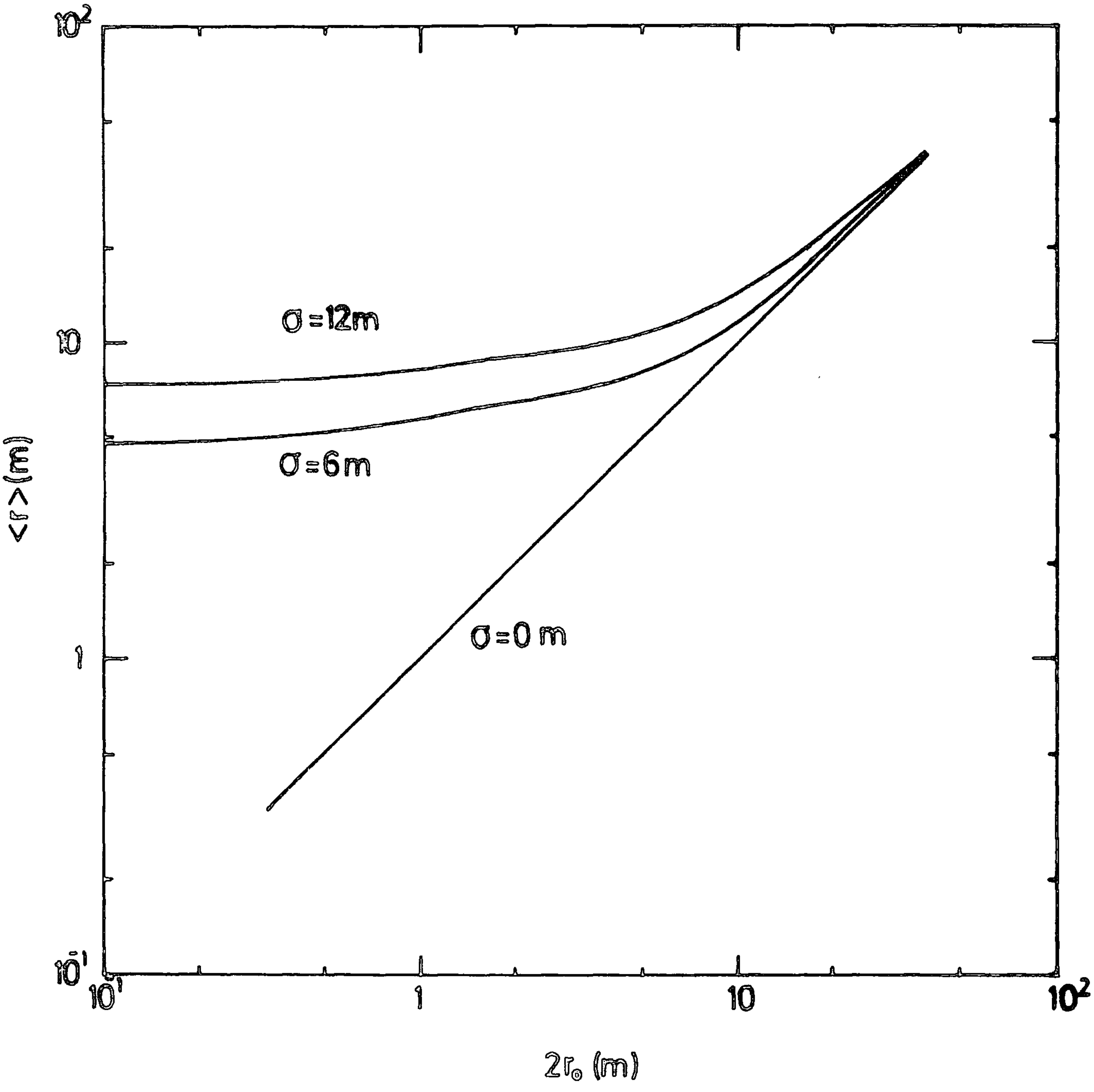

Figure 7.21 : Assuming the lateral distribution of hadrons is given by $\Delta(r) = Ae^{-r/r_0}$ then the average core distance $\langle r \rangle$ at which a hadron is observed is $2r_0$. $\langle r \rangle$ is plotted as a function of $2r_0$ for no core location error and Gaussian core location errors of standard deviation 6.0m and12.0m.

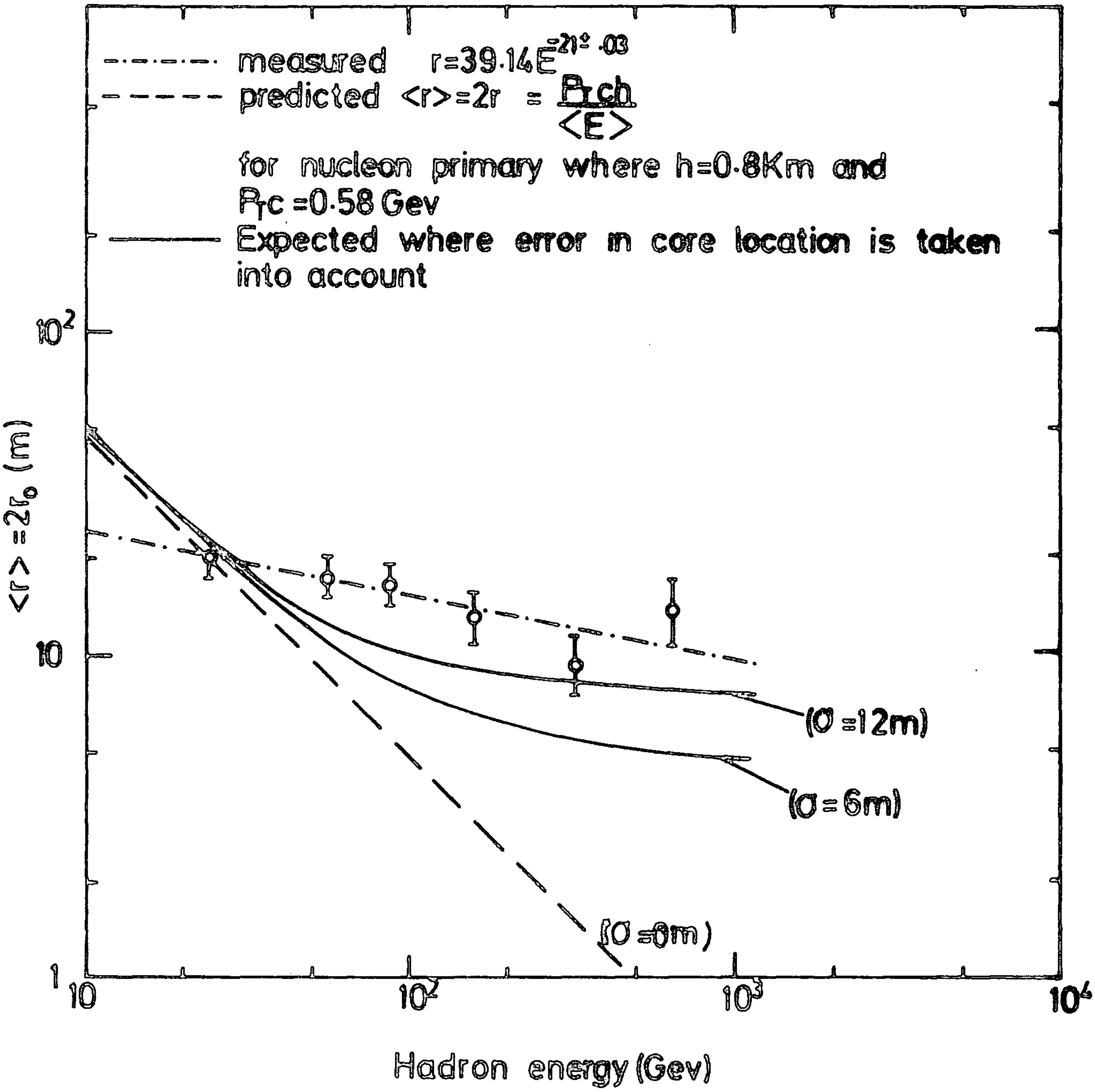

Figure 7.22 : Assuming all the detected hadrons are nucleons the measured variation of average core distance $\langle r \rangle$ at which hadrons of energy E are observed is compared with expectation. The expected curves with σ = 0, 6 and 12 m assume no core location error and core location errors of 6m and 12m respectively. An analytical fit to the measurements is $\langle r \rangle = 39.14\ E^{-0.21 \pm 0.03}$ m with E in GeV.

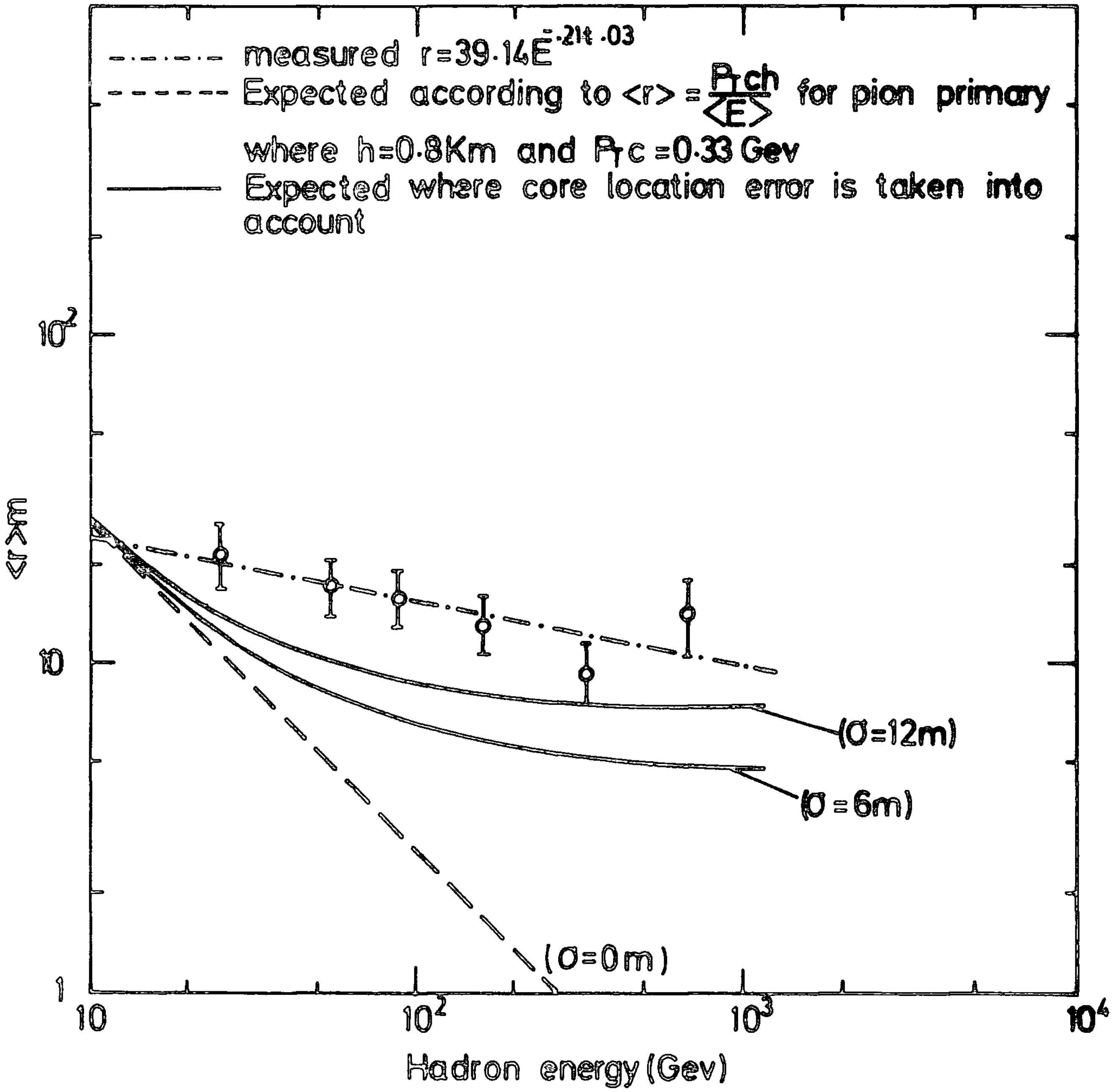

Figure 7.23 : The same as Figure 7.22 except all hadrons are assumed to be pions.

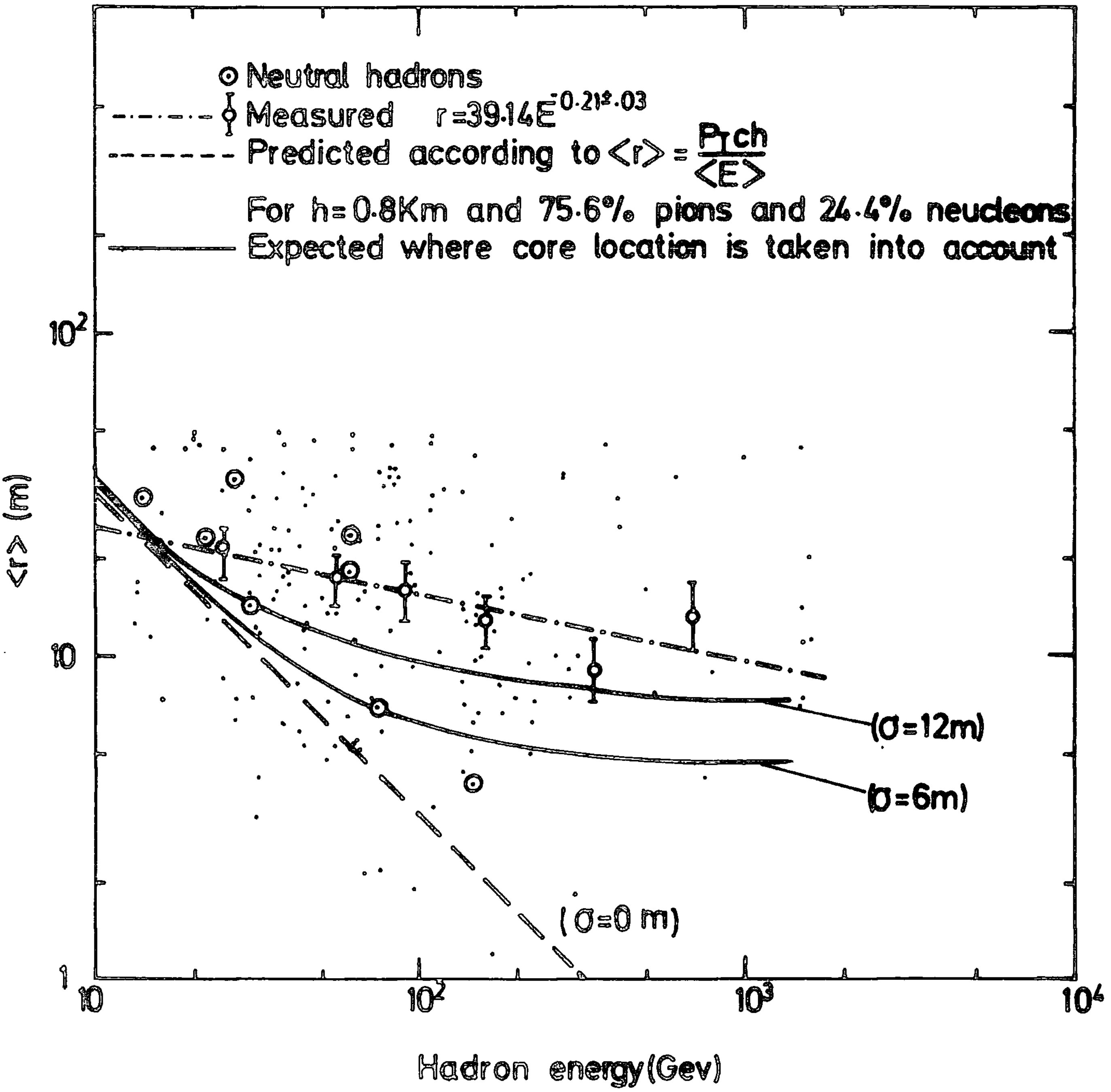

Figure 7.24 : Variation of the average core distance with hadron energy where for the expected lines it is assumed that the primaries are 24.4% nucleons and 75.6% pions.

Support for the present work comes from cosmic ray measurements. Figure 7.25 indicates that at energies around 10^5 Gev, a sharp rise of multiplicity (from 50 to somewhere around 500) is suggested to occur from cosmic ray data (Predazzi, 1979).

Figure 7.26 shows the variation of the average core distance with the minimum energy. To calculate E_{min}, burst size is converted to energy using the calculated minimum energy that can produce a given burst size (Appendix C).

Figure 7.27 shows the variation of the expected average core distance with hadron energy where the present measurement as well as the measurements from the summary of Greisen (1960) are also shown. It is believed that the average core distances given by Greisen are all far too small as they are well below expectation even when core location errors are discounted for energies $<$ 100 GeV.

7.10 SUMMARY AND CONCLUSION

The energy spectra of hadrons in EAS of size in the range of $1.5.10^4 - 4.10^6$ particles have been obtained by the technique of measuring burst widths below iron or lead absorbers. The results are in fairly good agreement with other measurements as well as models which consider a slowly but continuously rising cross-section.

The ratio of charged to neutral hadrons in EAS is measured and indicates an increase in value as energy increases and this is consistent with the calculations of Grieder (1971). Using this ratio, the pion to nucleon ratio in cosmic rays at sea level is calculated to be 3.26.

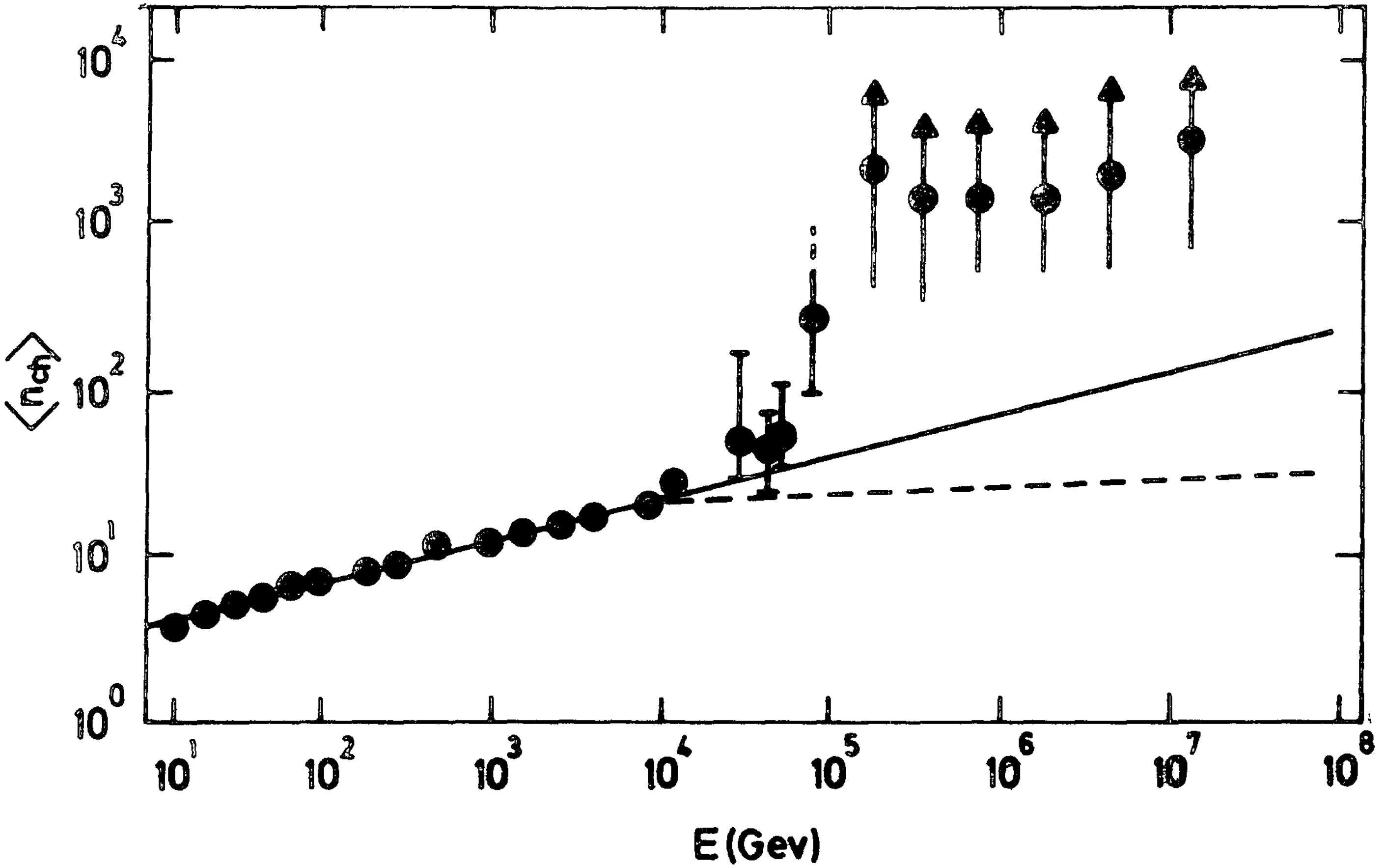

Figure 7.25 : Variation of multiplicity of secondaries with primary energy. A sharp change of multiplicity occurs at an energy around 10^5 GeV. (Predazi, 1979).

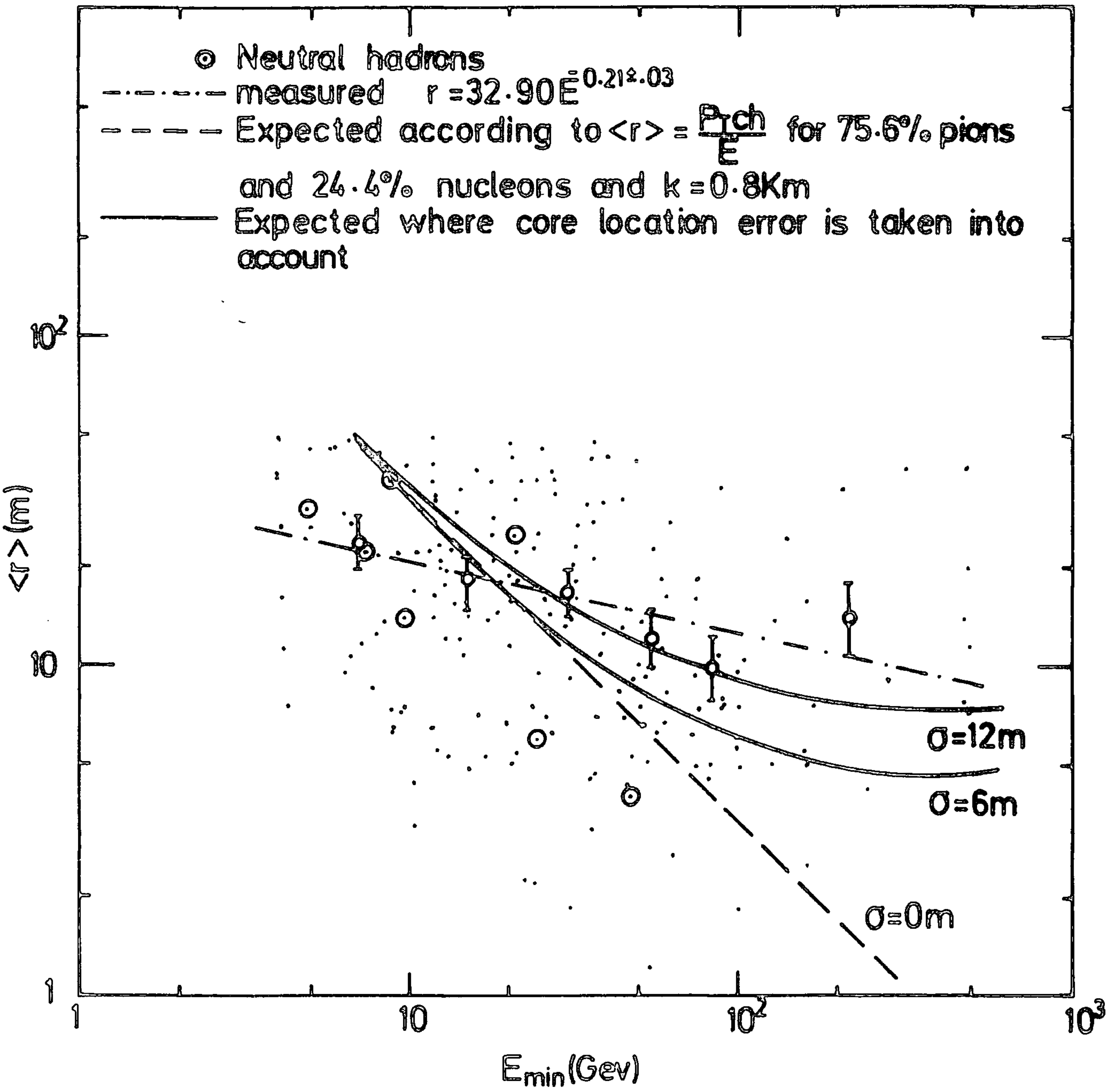

Figure 7.26 : Variation of the average core distance with absolute minimum hadron energy. Burst widths were converted to hadron energy using the absolute minimum energy to produce a given burst width rather than the average value.

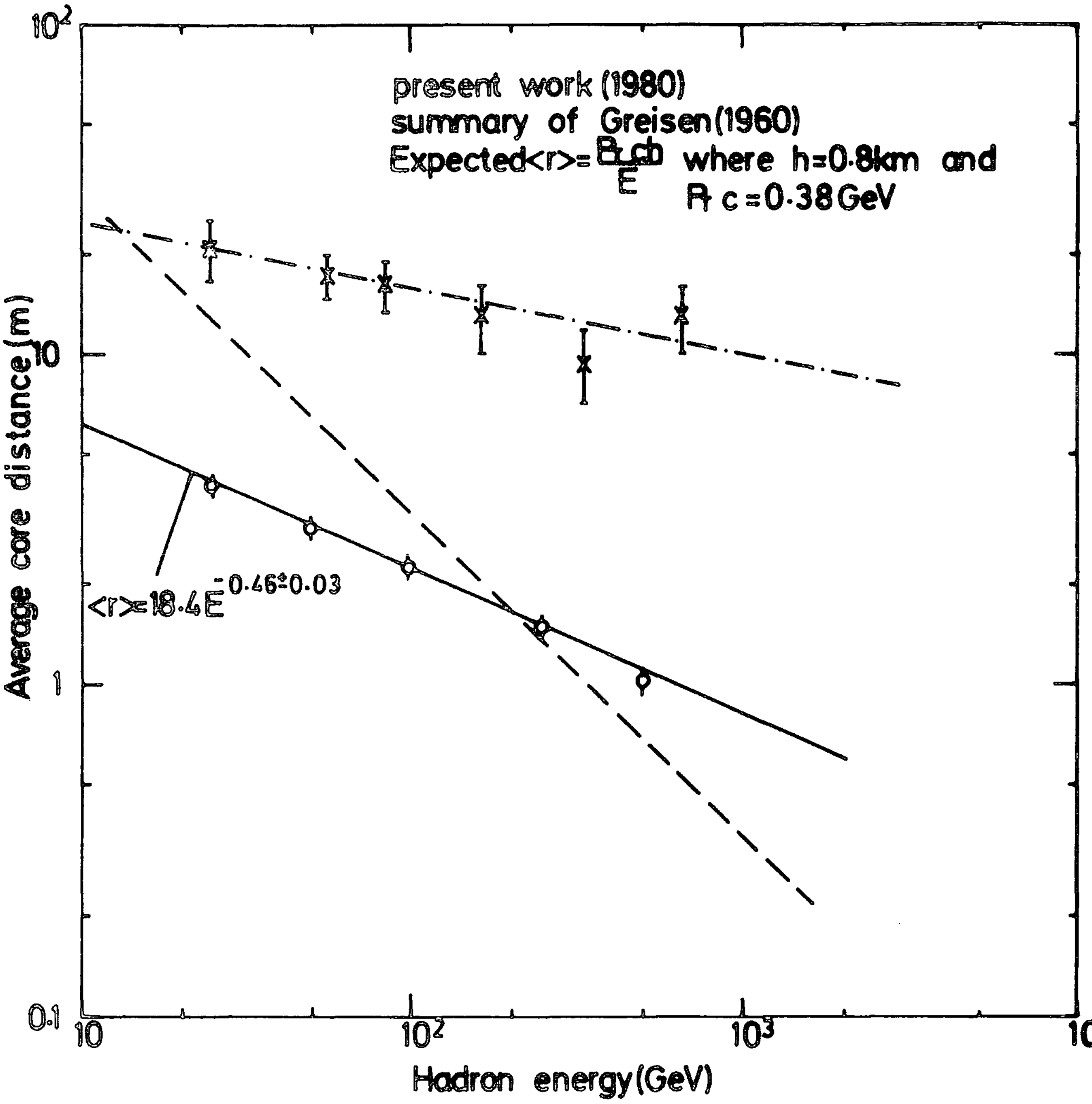

Figure 7.27 :Variation of the average core distance with hadron energy where both the present work and the measurements from the summary of Greisen (1960) are shown. The average core distances given by Greisen are all far too small as they are well below expectation even when core location errors are discounted for energies 100 GeV. An analytical fit to the Greisen summary is $\langle r \rangle = 18.4\ E^{-0.46 \pm 0.03}$ metres with E in GeV.

$$\Delta(r) = A\, e^{-\frac{r}{r_0}}$$

Expected $<r_0>$ with no measuring error	Expected $< r_0 >$ with error ($\sigma = 6.0$ m)	Expected $<r_0>$ with error ($\sigma = 12.0$ m)
0.5	2.80	4.18
1.0	3.10	4.60
2.0	3.88	5.38
5.0	6.53	8.0
10.0	11.07	12.0
20.0	20.9	21.6

TABLE 7.3 : The variation of r_0 in $\Delta(r) = A\, e^{-\frac{r}{r_0}}$ assuming no measuring error in determining core distance and errors of 6m and 12m respectively.

$$\Delta(r) = A e^{-\frac{r}{r_0}}$$

Expected $<r_0>$ with no measuring error	Expected $< r_0 >$ with error ($\sigma = 6.0$ m)	Expected $<r_0>$ with error ($\sigma = 12.0$ m)
0.5	2.80	4.18
1.0	3.10	4.60
2.0	3.88	5.38
5.0	6.53	8.0
10.0	11.07	12.0
20.0	20.9	21.6

TABLE 7.3 : The variation of r_0 in $\Delta(r) = A e^{-\frac{r}{r_0}}$ assuming no measuring error in determining core distance and errors of 6m and 12m respectively.

The transverse momentum phenomena for hadrons in EAS is looked at by means of looking at the $E.r$ distribution, and the present work shows a sudden rise in transverse momentum of secondary hadrons at energies around 3.10^5 GeV. However, part of this, but not all of it, could be due to the error in core location. The present result is in good agreement with other cosmic ray data.

APPENDIX A

DETERMINATION OF ERROR CURVES FOR INTERSECTING LOCI CURVES

In locating the core of a shower by the method of intersecting loci curves, Chapter 3 (Section 3.2) in two out of three possible cases it was required to draw the error curve for each locus to be able to locate the core. Here, the method of determination of the error curves are discussed.

The problem is to calculate the error on a ratio of two densities from any two detectors, in other words, if $y = \frac{a}{b}$ where a and b are densities at two detectors with areas A and B respectively, then we want to work out the error on y, σy.

If $a = \frac{N_1}{A}$ and $b = \frac{N_2}{B}$ where N_1 and N_2 are the number of particles at detectors with areas A and B then :

$$N_1 = a A \longrightarrow \sigma N_1 = \sigma A \quad a$$

$$N_2 = b B \longrightarrow \sigma N_2 = \sigma B \quad b$$

Now $$y = \frac{a}{b} \longrightarrow \ell n\ y = \ell n\ a - \ell n\ b$$

$$\frac{dy}{y} = \frac{da}{a} - \frac{db}{b}$$

Assuming that $dy = \sigma y$, $da = \sigma a$ and $db = \sigma b$ then :

$$\sigma y = y \left(\frac{\sigma a}{a} - \frac{\sigma b}{b} \right)$$ substituting for σa and σb

$$\sigma y = y \left(\frac{\sigma N_1}{aA} - \frac{\sigma N_2}{bB} \right) \qquad (A.1)$$

In Chapter 3, we have shown that the fluctuation distribution on sampling N particles follows a Poissonian distribution in shape, but with a standard deviation of $1.2\sqrt{N}$.

Therefore we can write $\sigma N = 1.2\sqrt{N}$. Substituting this in equation (A.1) gives

$$\sigma y = y\left(\frac{1.2\sqrt{N_1}}{aA} - \frac{1.2\sqrt{N_2}}{bB}\right)$$

$$\sigma y = y\left(\frac{1.2\sqrt{aA}}{aA} - \frac{1.2\sqrt{bB}}{bB}\right)$$

$$\sigma y = \frac{a}{b}\left(\frac{1.2}{\sqrt{aA}} - \frac{1.2}{\sqrt{bB}}\right)$$

Adding the errors in quadrature

$$\sigma y^2 = \left(\frac{1.2\ a}{b}\right)^2\left\{\left(\frac{1}{\sqrt{aA}}\right)^2 + \left(\frac{1}{\sqrt{bB}}\right)^2\right\}$$

$$\sigma y = \frac{1.2\ a}{b}\sqrt{\frac{1}{aA} + \frac{1}{bB}}$$

where a and b are the densities at any two detectors with areas A and B respectively and y = a/b.

APPENDIX B

DETERMINING THE ORTHUGONAL SHOWER AXIS DISTANCE FROM A SUBSIDIARY DETECTOR

Consider a central detector C placed at the origin of a right-hand set of cartesian coordinates and a single detector X placed at point (α, β, γ) as shown in Figure B.1. In small air shower arrays, such as the Durham E.A.S.Array, since the maximum distance between the detectors is about 100 m, then the shower front can be considered plane to a good approximation. Suppose a shower axis having zenith angle and azimuthal angle passes through detector X, then the shower front is defined by a plane containing XS which is normal to CS (Figure B.1). Assuming CS = ℓ and SX = R, for any position ofthe point S on the line CS one can write :

$$R = \left[(x_\ell - \alpha)^2 + (y_\ell - \beta)^2 + (z_\ell - \gamma)^2 \right]^{\frac{1}{2}} \qquad (B.1)$$

We know that : $x_\ell = \ell \sin\Theta \cos\phi$, $y_\ell = \ell \sin\Theta \sin\phi$ and $z_\ell = \ell \cos\Theta$. Substituting for x_ℓ, y_ℓ and z_ℓ in equation B.1 gives :

$$R = \left[(\ell \sin\Theta \cos\phi = \alpha)^2 + (\ell \sin\Theta \sin\phi - \beta)^2 + (\ell \cos\Theta - \gamma)^2 \right]^{\frac{1}{2}}$$

As ℓ varies in magnitude, XS will be orthogonal to CS

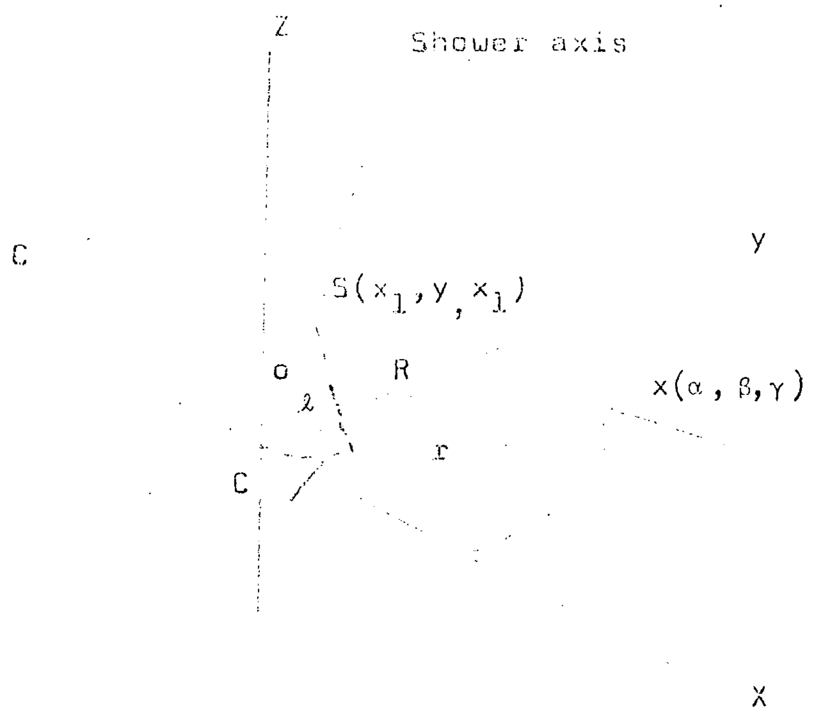

Figure B.1

Diagram showing a shower whose axis has zenith angle θ and azimuthal angle φ. The shower front is a plane containing XS which is normal to the shower axis direction CS.

CS = ℓ, SX = R and CX = r

when R is a minimum. Evaluating $\frac{dR}{d\ell}$ and equating to zero gives

$$\frac{dR}{dl} = \sin\theta\cos\phi\,(\ell\sin\theta\cos\phi - \alpha) + \sin\theta\sin\phi\,(\ell\sin\theta\sin\phi - \beta) + \cos\theta\,(\ell\cos\theta - \gamma) = 0$$

$$\ell(\sin^2\theta\cos^2\phi + \sin^2\theta\sin^2\phi + \cos^2\theta) - (\alpha\sin\theta\cos\phi + \beta\sin\theta\sin\phi + \gamma\cos\theta) = 0$$

$$\therefore\ \ell = \alpha\sin\theta\cos\phi + \beta\sin\theta\sin\phi + \gamma\cos\theta \qquad (B.2)$$

Substituting for ℓ in equation (B.1) gives

$$R = \left[(\alpha^2 + \beta^2 + \gamma^2) - (\alpha\sin\theta\cos\phi + \beta\sin\theta\sin\phi + \gamma\cos\theta)^2\right]^{\frac{1}{2}} \qquad (B.3)$$

Equation B.3 is useful in determining the orthogonal shower axis distance from a subsidiary detector (e.g. a muon hadron or electron density detector in an EAS array). Suppose a shower axis having zenith angle θ and azimuthal angle ϕ crosses the XY plane of the array coordinate system at the point $(x_1, y_1, 0)$ and that a subsidiary detector is located at the point (x_2, y_2, z_2). The orthogonal core distance R, from the subsidiary detector to the shower axis is given by

$$R^2 = \left\{ (x_2-x_1)^2 + (y_2-y_1)^2 + z_2^2 - \left[(x_2-x_1)\sin\theta\cos\phi + (y_2-y_1)\sin\theta\sin\phi + z_2\cos\theta \right]^2 \right\}$$

It is worth mentioning that using equation (B.2) the time difference t between an EAS shower front traversing a given detector and centre of the array (detector C) is given by

$$ct = \alpha \sin\theta \cos\phi + \beta \sin\theta \sin\phi + \gamma \cos\theta$$

where $c = 3.10^8$ m $\sec^{-1}$ is the velocity of light.

APPENDIX C

THEORY OF BURST PRODUCTION BY HADRONS IN THICK TARGETS

C.1 Probability that a Pion of Energy E produces a Burst of Size > N in 15 cm of Lead Absorber

Consider a hadron of energy E incident on 15 cm of thick lead absorber, (26.1 radiation lengths), interacting at a depth y_1. Assuming there is equipartition of energy among the produced particles and also equal energy for the two γ-rays from π^0 decay, then the number of shower electrons that emerge from the bottom ofthe absorber is easily calculated, (Ashton et al,(1977)). Figure C.1 shows the relation between the depth ofthe first interaction and the total number of particles emerging from the bottom of the absorber when pions of energy 10, 10^2, 10^3 and 10^4 GeV are incident on a 15 cm thick lead absorber (Saleh,(1975)). A quantity of interest is the probability that an incident pion of energy E produces a burst of size N particles, p(E,N). Using the fact that the probability that an incident pion makes its first interaction between y_1 and $y_1 + dy_1$ is

$$p(y_1)dy_1 = \frac{1}{\lambda} \exp\left(-\frac{y_1}{\lambda}\right) dy_1$$

where λ is mean path for a pion to undergo an inelastic interaction), then p(E,N) can be calculated directly by histogramming Figure C.1. The probability per unit N for 10, 10^2, 10^3 and 10^4 GeV pions incident on 15 cm of lead

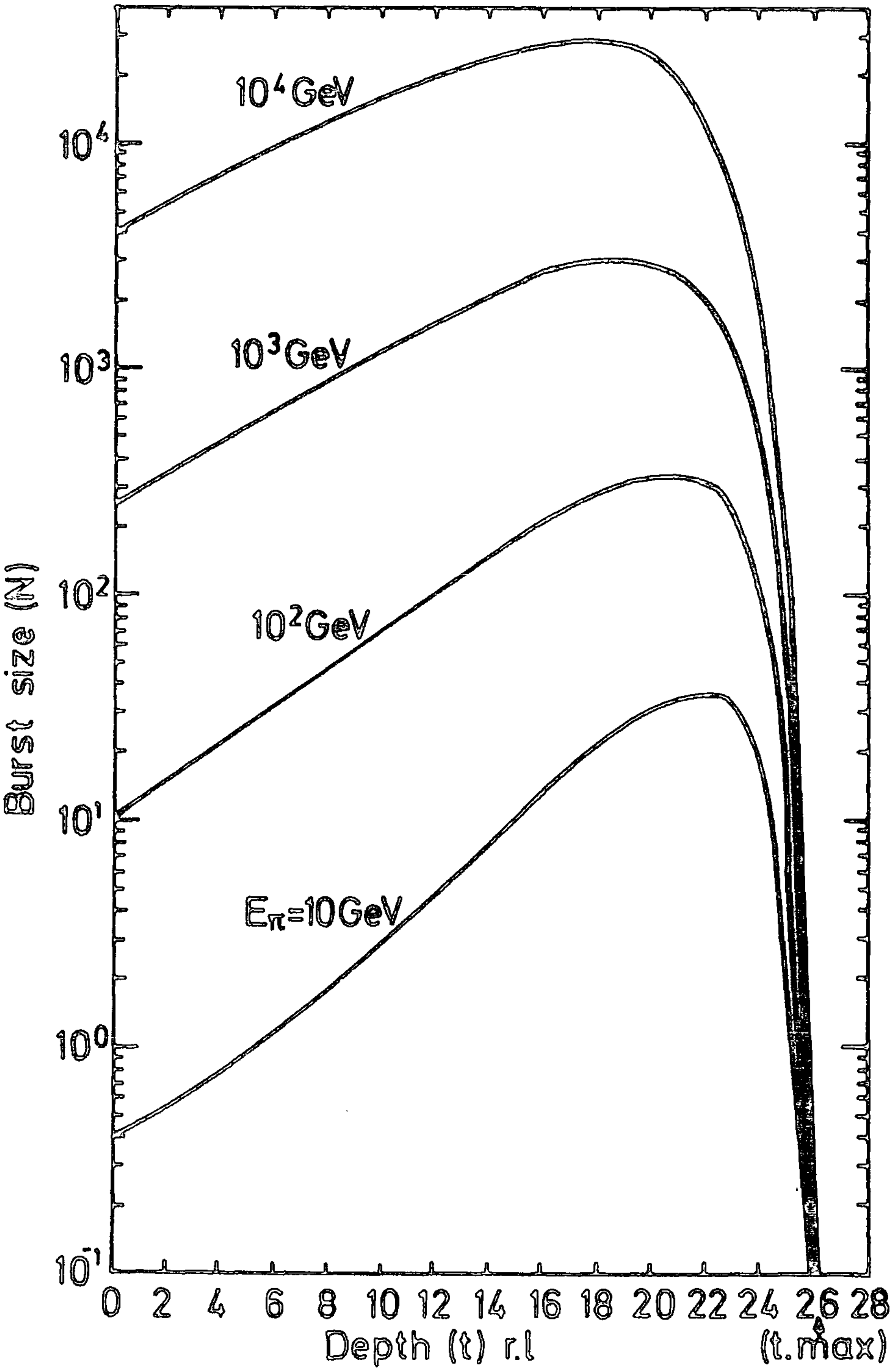

Figure C.1 : The relation between the depth of the first interaction for a pion with different primary energies (E_π) and the burst size (N) below 15 cms of lead, (Saleh (1975)).

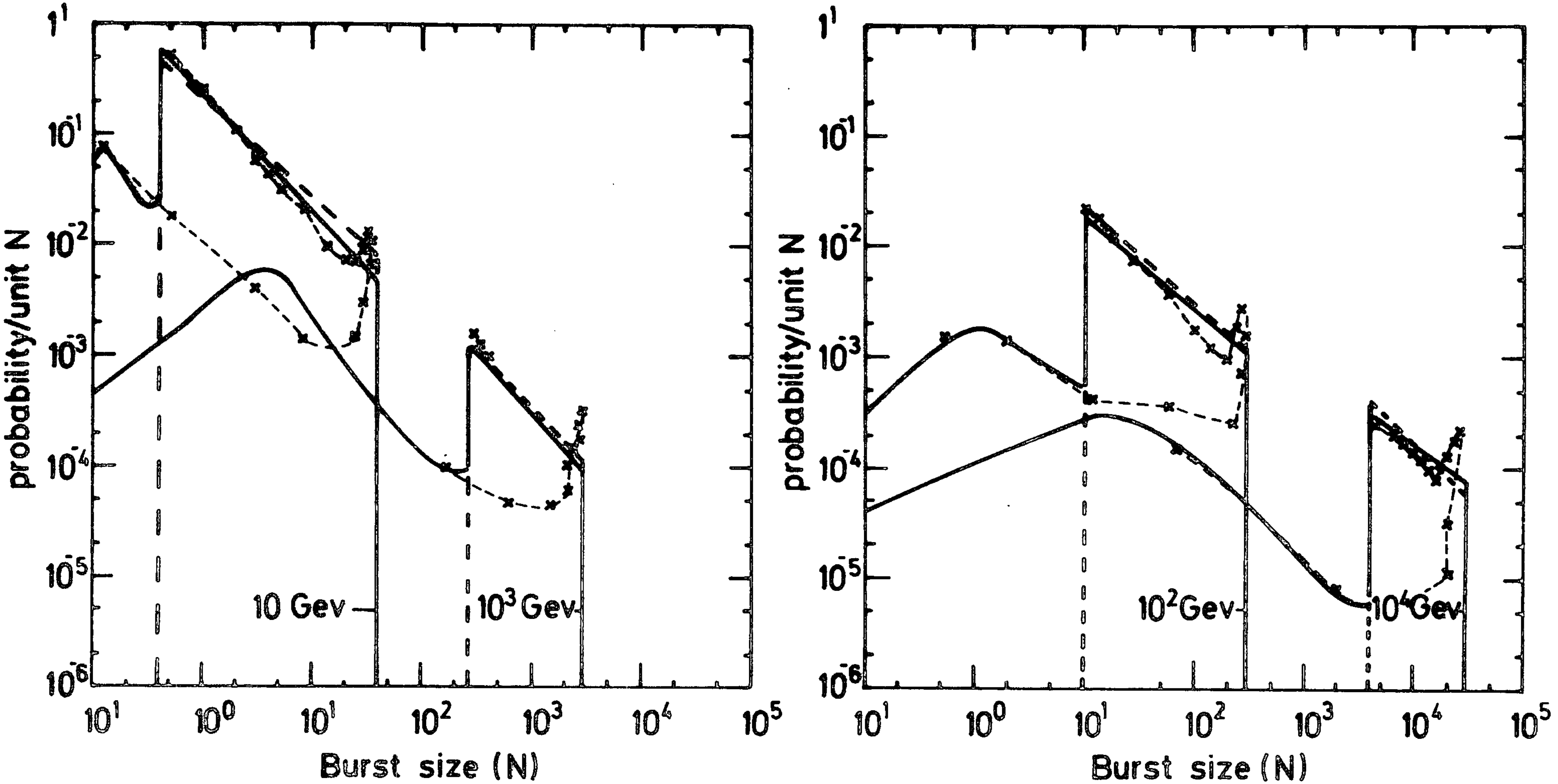

Figure C.2 : Probability that a pion of energy E produces a burst of size N/unit N. Dashed lines are adopted for the calculations.

absorber is shown in Figure C.2 and the results expressed in integral form $p(E, > N)$, are shown in Figure C.3.

In order to express the probability curves of Fig.C.2 analytically they are replaced by the dashed lines. This approximation neglects bursts of sizes $0-N_{min}$ and the probabilities of bursts in this size range for different pion energies are shown in Table C.1. It is seen that the approximation is good to an error of 1.7% at 10 Gev and 4.3% at 10^4 Gev.

Assuming $p(E,N) = AN^{-\alpha}$, Figure C.4a and Figure C.4b show the variation of α and A as a function of energy where a mean value of $\alpha = 0.90$ is adopted for future calculations. Thus the probability that a pion of energy E produces a burst of size N per unit number of particles can be expressed as

$$p(E,N) = B\,E^{-\beta}\,N^{-\alpha} \qquad (1)$$

where $\alpha = 0.9$ and $\beta = 0.073$ which is found by requiring $\int_{N_{min}}^{N_{max}} p(E,N)\,dN = 1.$

It is clear that due to the range of depth of interaction, an incident hadron of energy E can produce a range of burst sizes. Bearing this in mind and using Figure C.1 the relation between minimum and maximum produced burst sizes and pion energy as well as the relation betweenthe average burstsize produced and incident pion energy is shown in Figure C.5(a). To calculate $\bar{N}$, if $N(y_1)$ is the burst size produced by a pion that makes its first interaction at depth y_1 then we have

$$\bar{N} = \frac{\int_0^y p(y_1)\,N(y_1)\,dy_1}{\int_0^y p(y_1)\,dy_1}$$

Energy (GeV)	Minimum Burst Size (particles)	Maximum Burst Size (particles)	Percentage of pions interacting in lead so that burst size is $<N_{min}$
10	0.4	38.0	1.7%
10^2	10.1	320.0	2.5%
10^3	262.0	3,000	3.0%
10^4	4,000	30,000	4.3%

TABLE C.1 : Fraction of pions interacting in distance range in lead such that produced burst size is $< N_{min}$

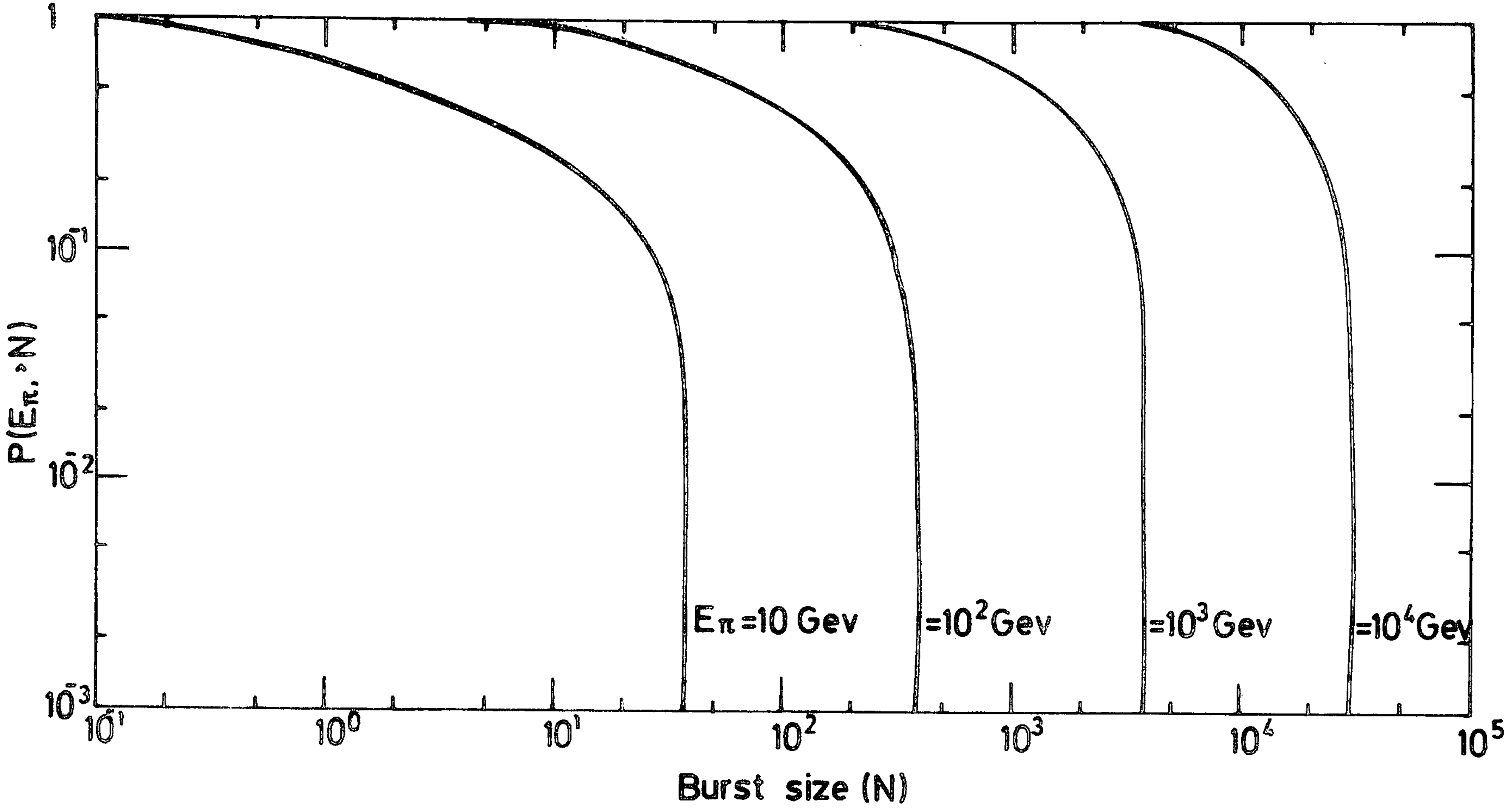

Figure C.3 : Probability that a pion of energy E produces a burst of > N

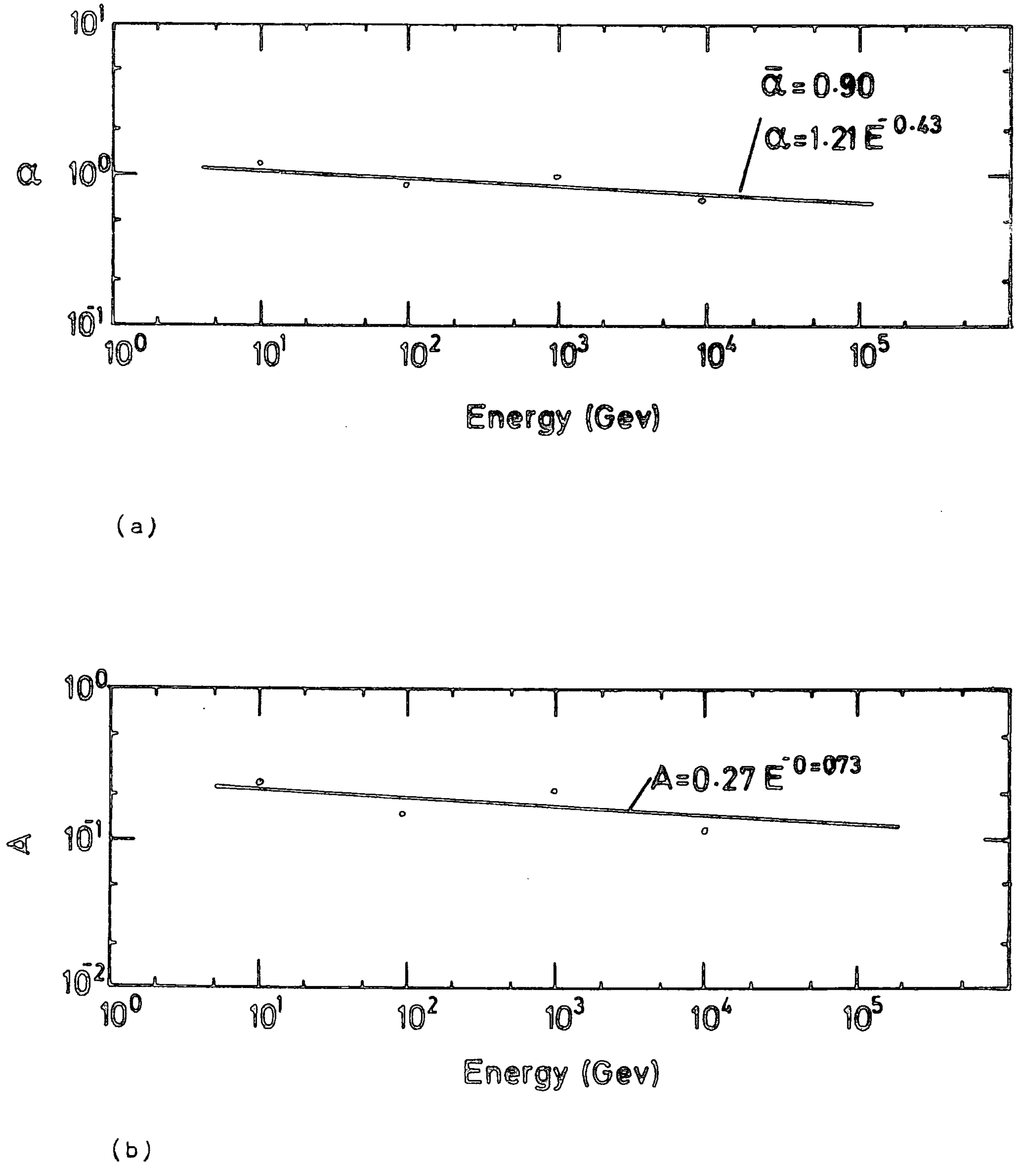

Figure C.4 : (a) Variation of α with energy assuming $P(E,N) = A\ N^{-\alpha}$

(b) Variation of A with pion energy assuming $P(E,N) = A\ N^{-\alpha}$

where $p(y_1) = \frac{1}{\lambda_1} e^{-\frac{y_1}{\lambda}}$. The relation $(\bar{N} - E_\pi)$ is used to convert measured burst size to incident hadron energy. Using Figure C.5 (a), the Maximum and minimum pion energy that can produce a burst of size N is evaluated and the relationis shown in Figure C.5(b).

C.2 The Energy Spread of Pions Producing a Given Burst Size (Burst Width).

Consider a pion spectrum of the form

$$n(E)dE = A E^{-\gamma} dE$$

The probability that a pion of energy E produces a burst of size N per unit number of particles is

$$p(E,N) = B E^{-\beta} N^{-\alpha}$$ where $B E^{-\beta}$ is a normalizing factor so that $\int_{N_{min}}^{N_{Max}} p(E,N) = 1$.

Now the distribution of pion energy that produces a burst of size N particles per unit number of particles is the product of p(E,N) and n(E)

$$p(E,N) \times n(E) = B E^{-\beta} N^{-\alpha} A E^{-\gamma} = A B E^{-(\gamma+\beta)} N^{-\alpha}$$

However, for a particular burst size, the probability that a burst of size N has been produced by a pion of energy E is functionally independent of burst size N and is

$$p(N,E) = K E^{-(\gamma+\beta)}$$ in the energy range of $(E_{min} - E_{Max})$

where K is a constant.

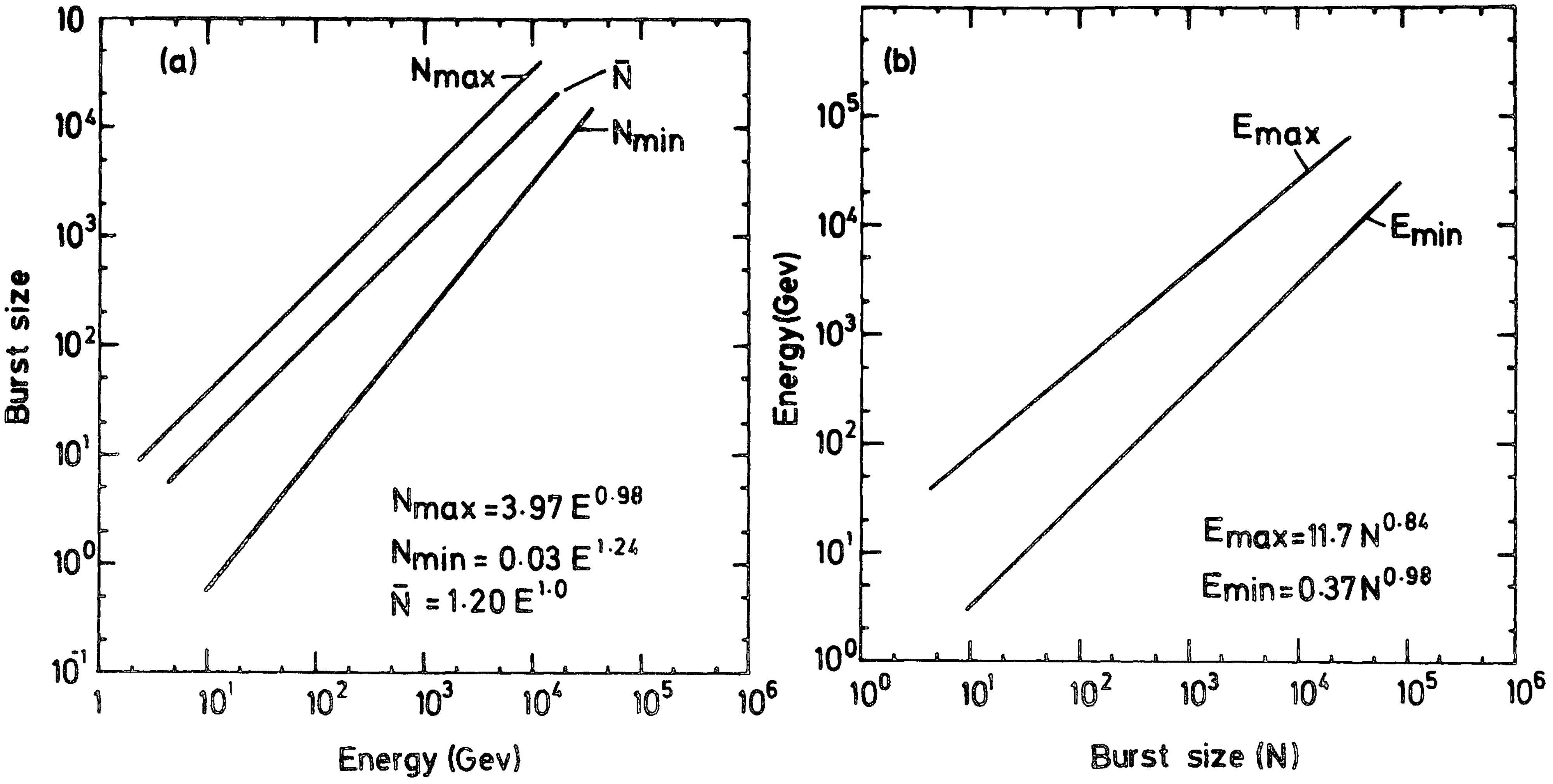

Figure C.5 : (a) Relation between pion energy and the minimum and maximum produced burst size. The relation between average burst size and incident energy is also shown.

(b) Variation of minimum and maximum energy that can produce a burst of size N.

Since $\int_{E_{min}}^{E_{Max}} p(E,N)\, dE = 1$ then :

$$\int_{E_{min}}^{E_{Max}} K\, E^{-(\gamma+\beta)} dE = 1 \quad \text{leads to :}$$

$$K = \frac{\gamma + \beta - 1}{E_{min}^{-(\gamma+\beta-1)} - E_{Max}^{-(\gamma+\beta-1)}}$$

therefore :

$$p(N,E) = \frac{\gamma + \beta - 1}{E_{min}^{-(\gamma+\beta-1)} - E_{Max}^{-(\gamma+\beta-1)}} E^{-(\gamma+\beta)} \text{GeV}^{-1} \qquad (2)$$

Now the probability that a burst of size N is produced by pions of energy > E is given by :

$$p(N,>E) = \int_{E_{min}}^{E_{Max}} p(N,E)\, dE$$

$$p(N,>E) = \frac{1}{E_{min}^{-(\gamma+\beta-1)} - E_{Max}^{-(\gamma+\beta-1)}} \left[\frac{1}{E^{\gamma+\beta-1}} - \frac{1}{E_{Max}^{\gamma+\beta-1}} \right]$$

This probability is evaluated for N = 50 and 200 particles and plotted in Figure C.6.

Using equation (2) the average energy of pions $\bar{E}_\pi$ producing bursts of a given size can be evaluated.

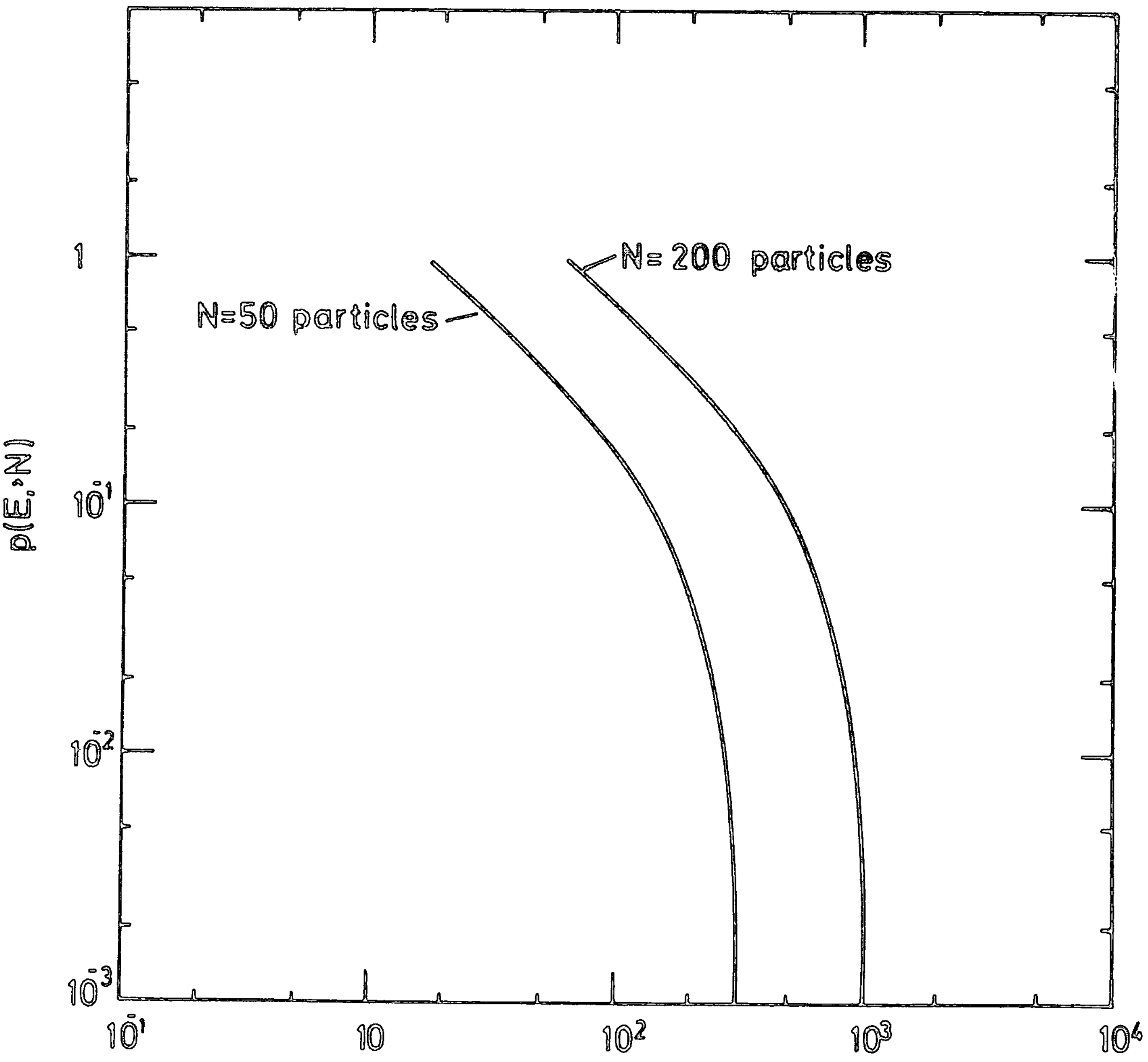

Figure C.6 : Probability that a burst of size 50 or 200 particles has been produced by a pion of energy > E.

$$\bar{E}_{\pi} = \frac{\int_{N_{min}}^{N_{Max}} p(N,E).E.dE}{\int_{N_{min}}^{N_{Max}} p(n,E)\ dE}$$

$$= \int_{N_{min}}^{N_{Max}} p(n,E)\ EdE \text{ as the denominator is unity}$$

$$= \frac{\gamma+\beta-1}{E_{min}^{-(\gamma+\beta-1)} - E_{Max}^{-(\gamma+\beta-1)}} \int_{E_{min}}^{E_{Max}} E^{-(\gamma+\beta)+1} dE$$

$$= \frac{\gamma+\beta-1}{E_{min}^{-(\gamma+\beta-1)} - E_{Max}^{-(\gamma+\beta-1)}} . \frac{1}{\gamma+\beta-2} . \left[\frac{1}{E_{min}^{\gamma+\beta-2}} - \frac{1}{E_{Max}^{\gamma+\beta-2}} \right]$$

where E_{min} and E_{Max} are the minimum and maximum pion energies that can produce bursts of a given size. The variation of $\bar{E}_{\pi}$ with burst size is shown in Figure C.7 .

Table C.2 shows important energies relevant to the interpretation of observed burst sizes of 50 and 200 particles emerging from a 15 cm thick lead target when a pion energy spectrum of the form $N(E, dE) = A\ E^{-1.73}\ dE$ is incident on the target as occurs in E.A.S.

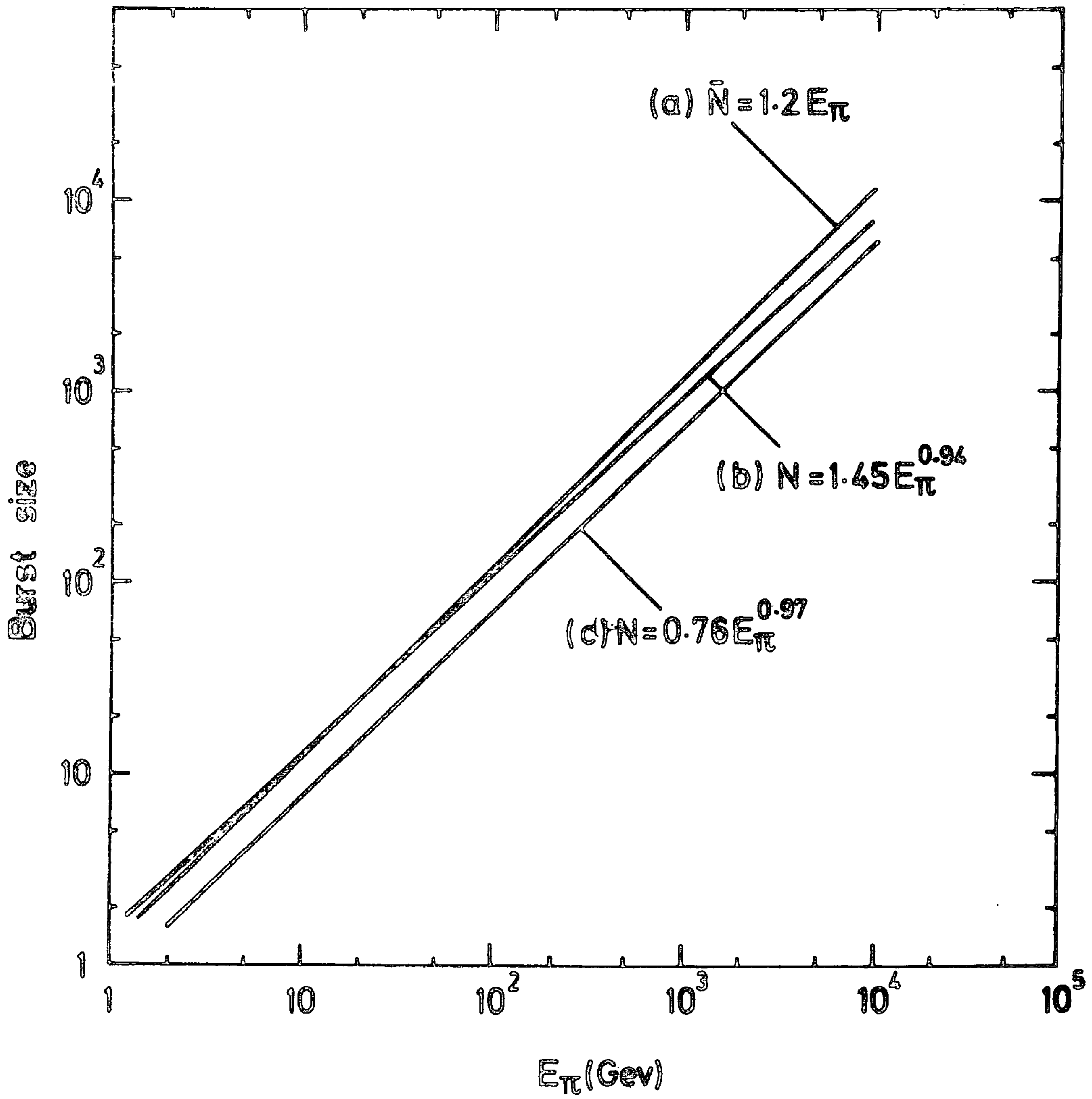

Figure C.7 : (a) Average burst size produced by pions of a given energy.

(b) Average pion energy producing bursts of a given size for a pion differential spectrum of the form $AE^{-1.73}$

(c) Average pion energy producing bursts of a given size for a pion differential spectrum of the form $AE^{-2.8}$

Burst Size	50 Particles	200 Particles
Burst Width	14 cm.	38.5 cm.
Pion energy determined from average burst size energy calculation	60 GeV	240 GeV
Minimum pion energy	17.1 GeV	66.5 GeV
Maximum pion energy	314.6 GeV	1008.4 GeV
Most probable pion energy	17.1 GeV	66.5 GeV
Median pion energy (50% probability)	36.0 GeV	130 GeV
Average pion energy producing the stated burst size for a differential pion spectrum of the form $E^{-1.73}$	59.9	216.1
Average pion energy producing the stated burst size for a differential pion spectrum of the form $E^{-2.8}$	34.0	130.4

TABLE C.2 : Important energies relevant to the assignment of an energy to a measured burst size of 50 and 200 particles emerging from a 15 cm thick lead absorber.

C.3 Comparison Between an Incident Pion Spectrum and the Measured Burst Spectrum

In Chapter 7 it is shown that the pion spectrum in E.A.S. has the form of $A\ E^{-1.73}\ dE$ (curve a, Figure C.7). Consider the spectrum $n(E)dE = A\ E^{-\gamma}\ dE$ incident on the top of a 15 cm thick lead target. If

$p(N,E)\ dN = B\ E^{-\beta}\ N^{-\gamma}\ dN$ (equation 1) is the probability that an incident pion produces a burst of size N, then the measured burst spectrum will be of the form

$$n(N)dN = (1-e^{-15/\lambda}) \int_{E_{min}}^{E_{Max}} n(E)\ dE\ p(E,N)\ dN$$

where E_{min} and E_{Max} are the minimum and maximum pion energies that can produce a burst of size N and have the form of $E_{min} = C\ N^{\sigma}$ and $E_{Max} = D\ N^{\varepsilon}$ (Figure C.5). $\lambda = 19.8$ cm is the interaction length of pions in lead.

Substituting for n(E) dE and p(E,N) dN then

$$n(N)\ dN = .53 \int_{E_{min}}^{E_{Max}} n(E)d\ E\ p(E,N)\ dN$$

$$= .53 \int_{E_{min}}^{E_{Max}} A\ B\ E^{-\beta}\ N^{-\alpha}\ dN\ dE$$

$$= .53\ A\ B\ N^{-\alpha}\ dN\ \frac{1}{\gamma+\beta-1} \left[\begin{array}{ll} C^{-(\gamma+\beta)\ +\ 1} & N^{-\delta(\gamma+\beta)\ +\ \delta} \\ & D^{-(\gamma+\beta)\ +\ 1}\ \ N^{-\varepsilon(\gamma+\beta)\ +\varepsilon} \end{array} \right] \quad (3)$$

Substituting for $C, D, \alpha, \beta, \gamma, \epsilon$ and δ, (from Figure C.4), for a particular burst size N the second term in brackets is much smaller than the first term and to a good approximation it can be neglected. Therefore, equation (2) can be written as :

$$n(N)\ dN = \frac{.53\ A\ B\ C^{-(\gamma+\beta)+1}}{\gamma+\beta-1}\ N^{-\alpha-(\gamma+\beta)+\delta}$$

This equation has been evaluated numerically and the result is shown as curve (b) in Figure C.8. An estimate of the incident pion spectrum is made from this burst spectrum using the relation between pion energy and the average burst size ($\bar{N} = 1.2\ E$, Figure C.5a) and the result is curve (c) of Figure C.8, account being taken of the probability that the pion does not interact in the lead. Comparing curves (a) and (c) in Figure C.8, indicates that the measured pion spectrum (c) has approximately the same slope as the incident pion spectrum initially assumed, (a), but its absolute intensity must, on the average, be decreased by a factor of 1.4 to obtain agreement with the initially assumed spectrum.

A similar calculation for a pion spectrum of the form $n(E)\ dE = A\ E^{-2.8}\ dE$, corresponding to the incoherent pion component of cosmic rays at sea level, has also been carried out. In this case, using the relation between the average burst size and pion energy to convert a measured burst spectrum to an energy spectrum produced an energy spectrum of the form $E^{-2.74}$ and the absolute intensities must be reduced by a factor of 1.6 at 10 GeV and 2.0 at 1,000 GeV as shown in Figure C.9 to recover the initially assumed incident pion spectrum.

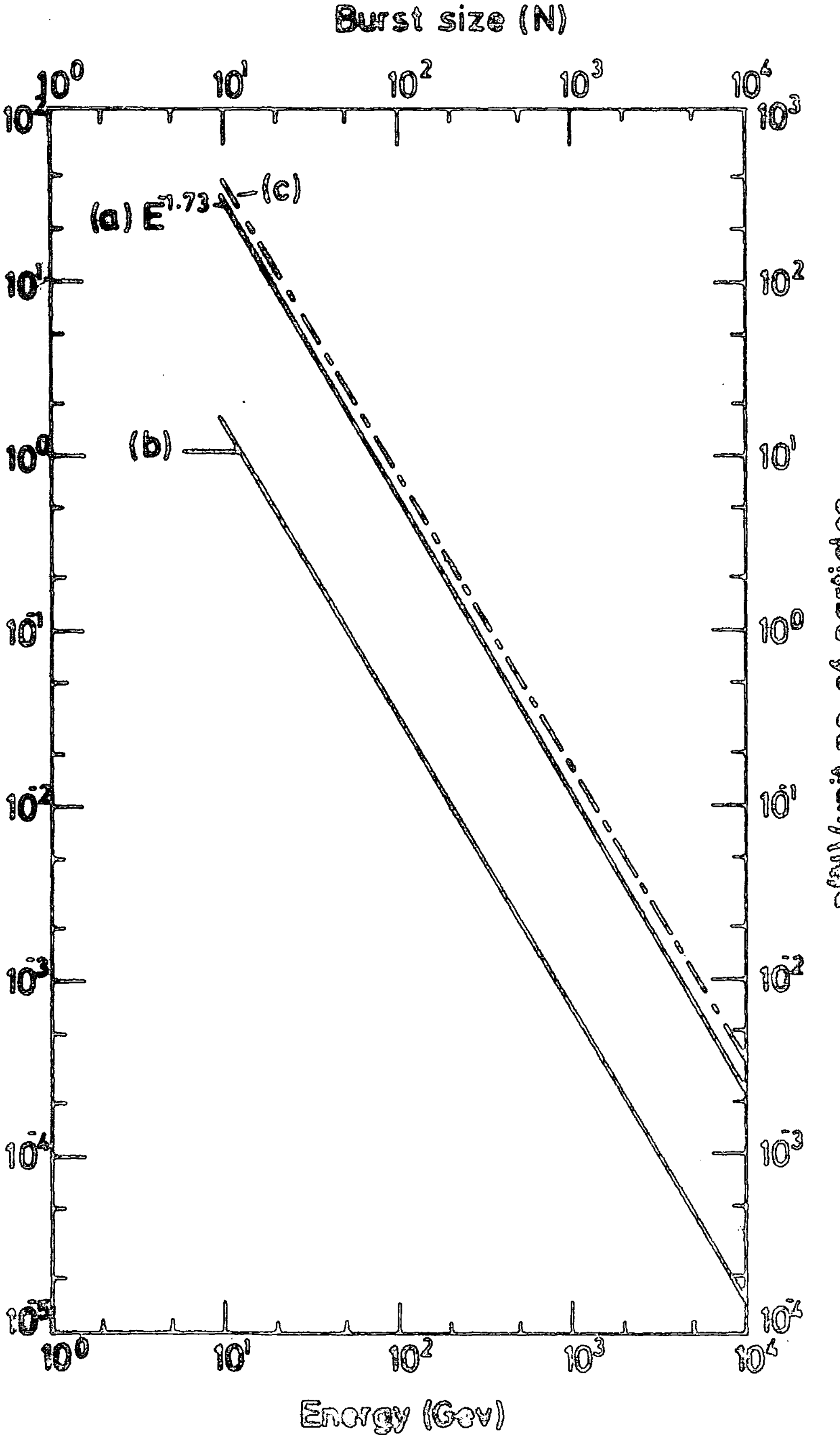

Figure C.8 : Comparison between an assumed differential pion spectrum of the form $AE^{-1.73}$ (a), and the resulting burst spectrum (b). Curve (c) is the estimate of the incident pion spectrum using the relation between average burst size and incident pion spectrum.

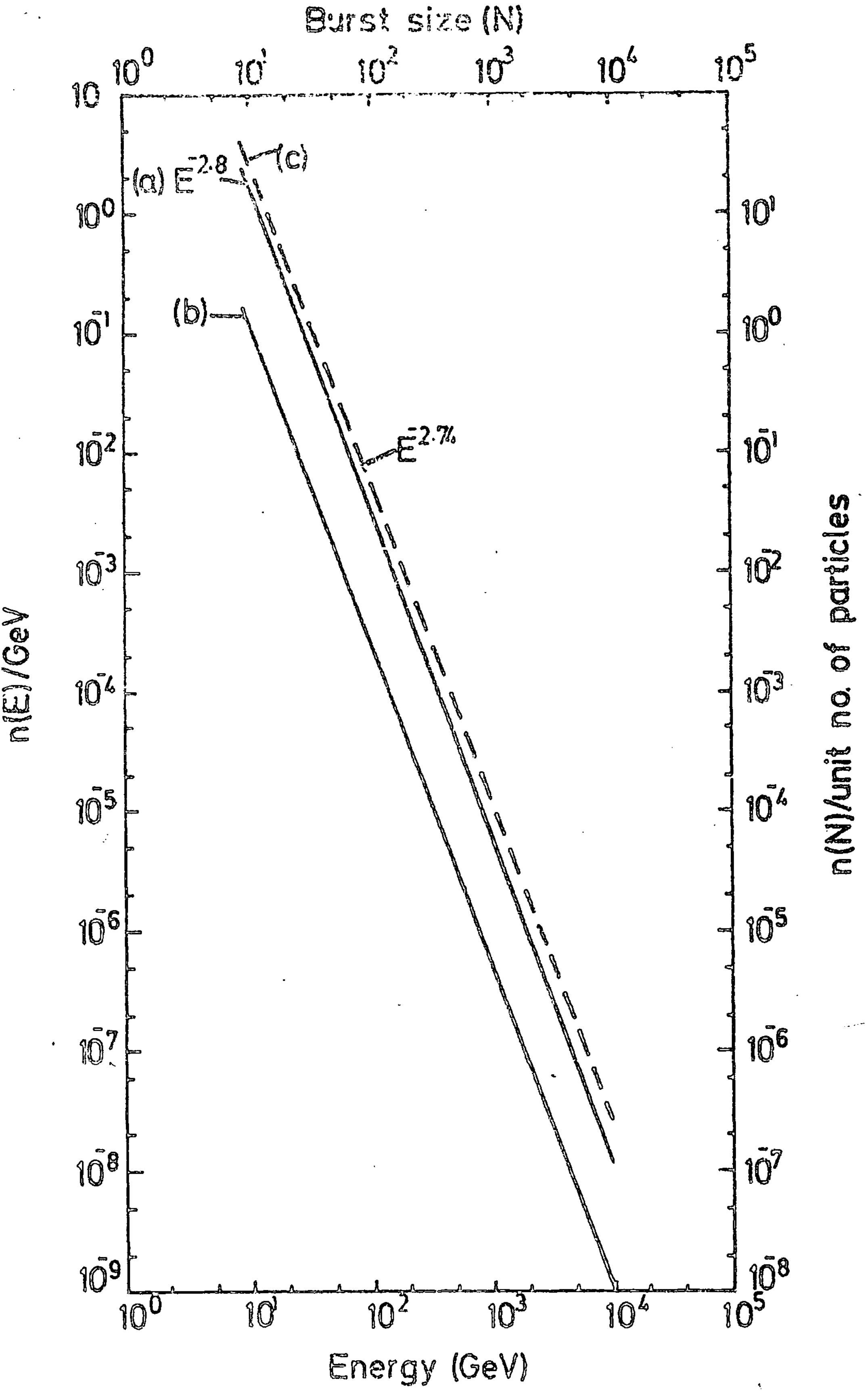

Figure C.9 : Comparison between an assumed differential pion spectrum of the form $E^{-2.8}$ curve (a) and the resulting burst spectrum (b). Curve (c) is the estimate of the incident pion spectrum using the relation between average burst size and incident pion energy.

C.4 Conclusion

The differential energy spectrum of incoherent hadrons in cosmic rays at sea level can be expressed by a power law of the form $n(E)\,dE = A\,E^{-2.8}\,dE$ over the range $10\text{-}10^{3}$ GeV while the energy spectrum of coherent hadrons in an extensive air shower of a given size has a flatter spectrum of the form $n(E)\,dE = A\,E^{-1.73}\,dE$.

The simplest experimental approach to extend measurements of both these spectra to higher energies and shower sizes is to measure the burst spectrum produced by hadrons in a thick target. It is shown in the present work that for a power law spectrum of pions incident on a 15 cm thick lead target that the resulting burst spectrum has almost the same slope as the incident pion spectrum, in spite of the fact that pions of a given energy produce burst with a large variation in size. So, if the calculated relationship between average burst size and incident pion energy is used to convert measured burst spectrum to the incident pion spectrum then the absolute intensity is found to be overestimated by a factor which is given in the text and depends on the exponent of the pion power law spectrum. The distribution of pion energy producing a burst of a given size has also been evaluated as well as the mean pion energy that produces a burst of a given size, the result depends on the shape of the incident pion spectrum. It is found that if the pion energy producing a burst of a given size is estimated, using the relation between mean burst size and pion energy then the resulting energy is remarkably close to the more accurate value determined from the relation between the average pion energy producing bursts of a given size as shown in Table C.2 and Figure C.7, even though the latter value depends on the exponent of the incident pion spectrum.

APPENDIX D

EXAMPLES OF RELEVANT AND INTERESTING EVENTS OBSERVED IN THE FLASH TUBE CHAMBER

Plate 1.

Event M22 - 1162693

A burst produced in the lead and penetrating the iron.

Burst width under lead = 20 flash tube diamet
(units of 1.81 cm)

Hadron energy E = 191 GeV

Burst size N = 250 particles

Shower parameters

r_H = 26.0 m

N_e = $5.6.10^5$

θ = 12.1^o

ϕ = 229^o

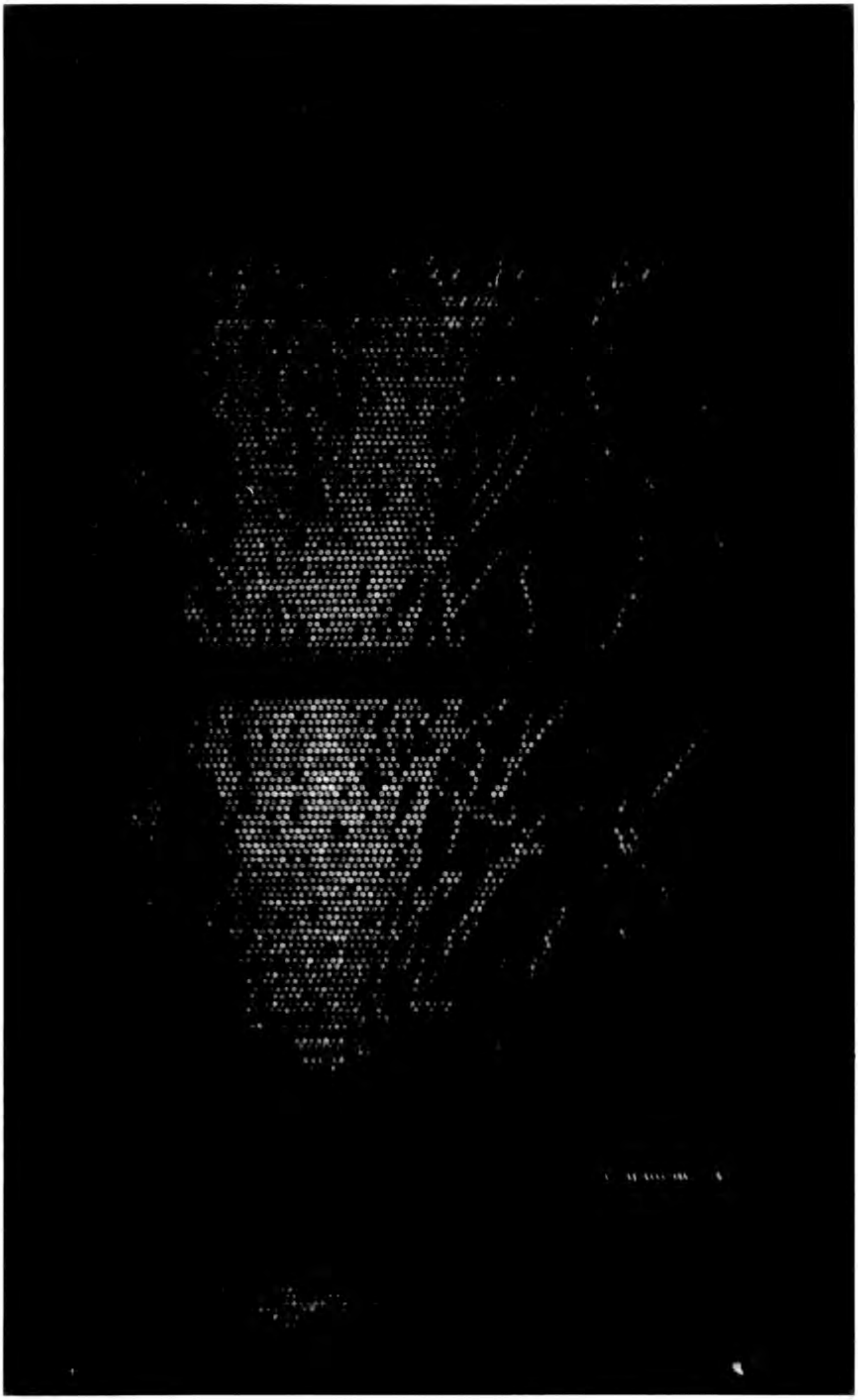

Plate 2.

Event M13 - 1161563

A charged particle burst produced in the iron

Burst width under iron = 19 flash tube diamet
(units of 1.81 cm)

Hadron energy E = 224 GeV

Burst size N = 309 particles

Shower parameters

$r_H = 6.1\text{m}$

$N_e = 5.46.10^4$

$\theta = 26.2^o$

$\phi = 282$

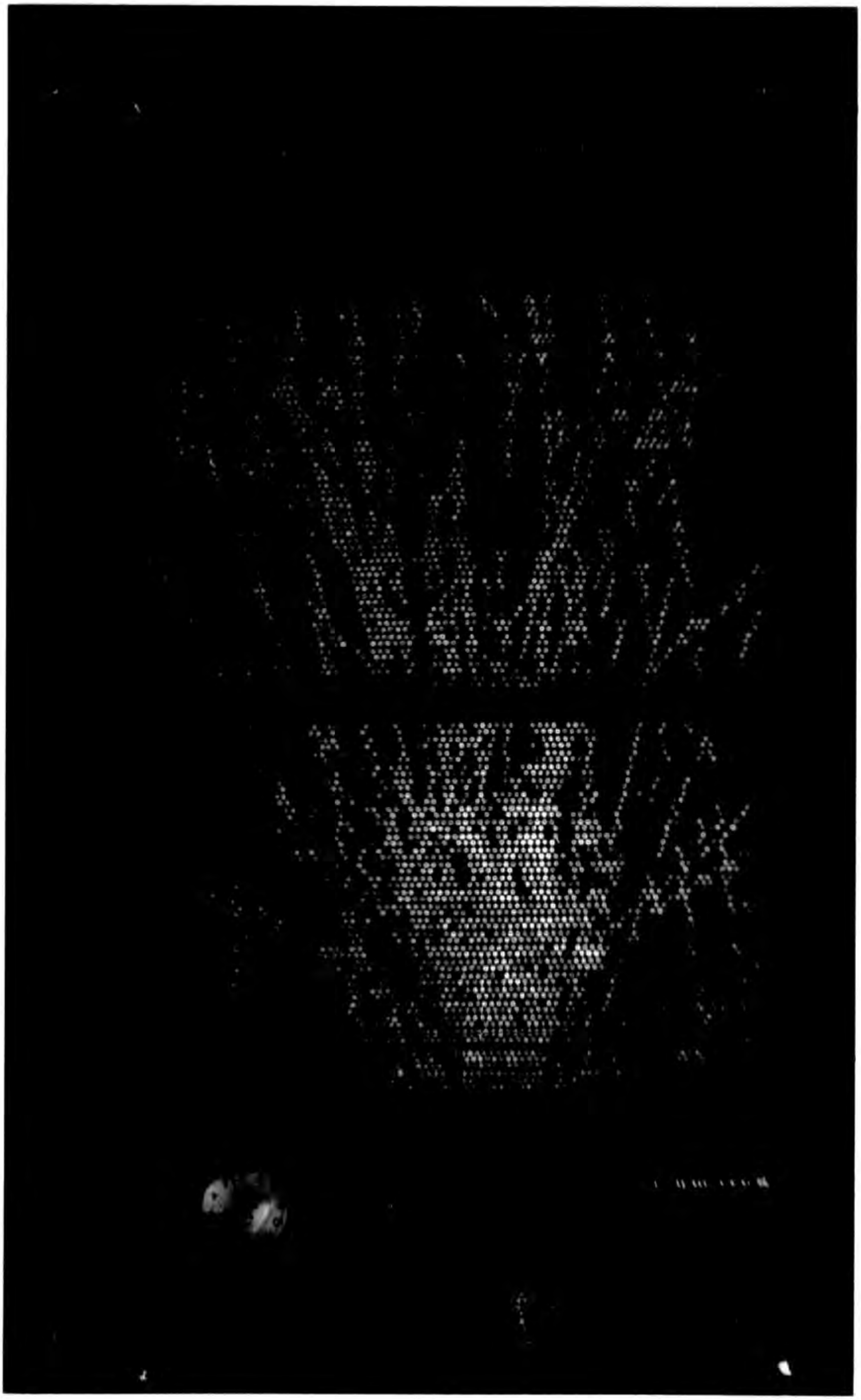

Plate 3.

Event M61 - 1176885

A burst produced in the lead but most of it absorbed in the iron.

Burst width under lead = 16 flash tube diame
(units of 1.81 cm)

Hadron energy E = 150 Gev

Burst size N = 177 particles

Shower parameters

r_H = 41.6m

N_e = $1.15.10^5$

θ = 15.9^o

ϕ = 18.0^o

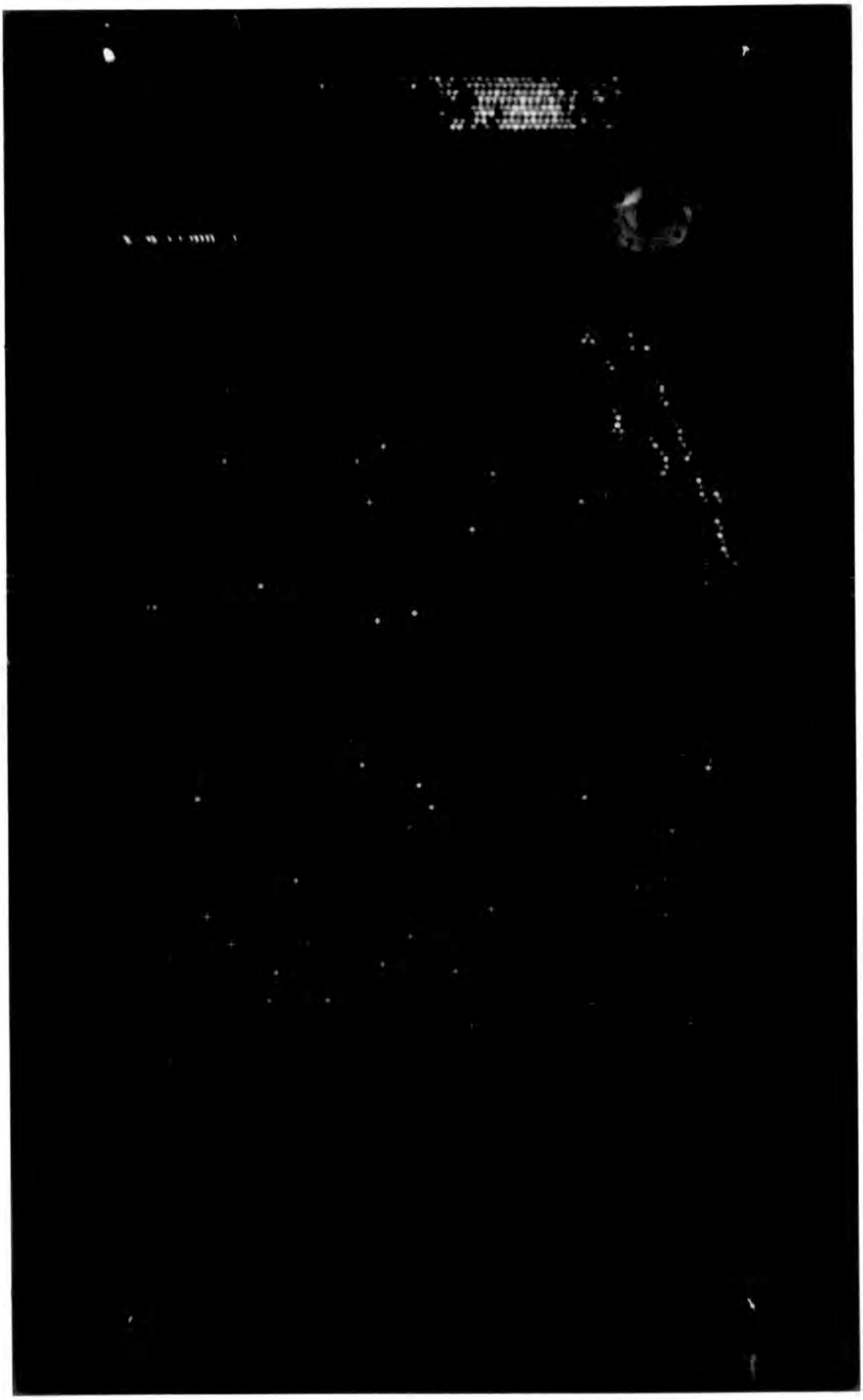

Plate 4.

Event M56 - 1173702

An example of a burst produced in the iron target by a neutral particle.

Burst width under iron = 12 flash tube diamet
(units of 1.81 cm)

Energy E = 79 GeV

Burst size N = 124 particles

Shower parameters

r_H = 6.2m

N_e = $2.32.10^5$

θ = 10.4^o

ϕ = 191^o

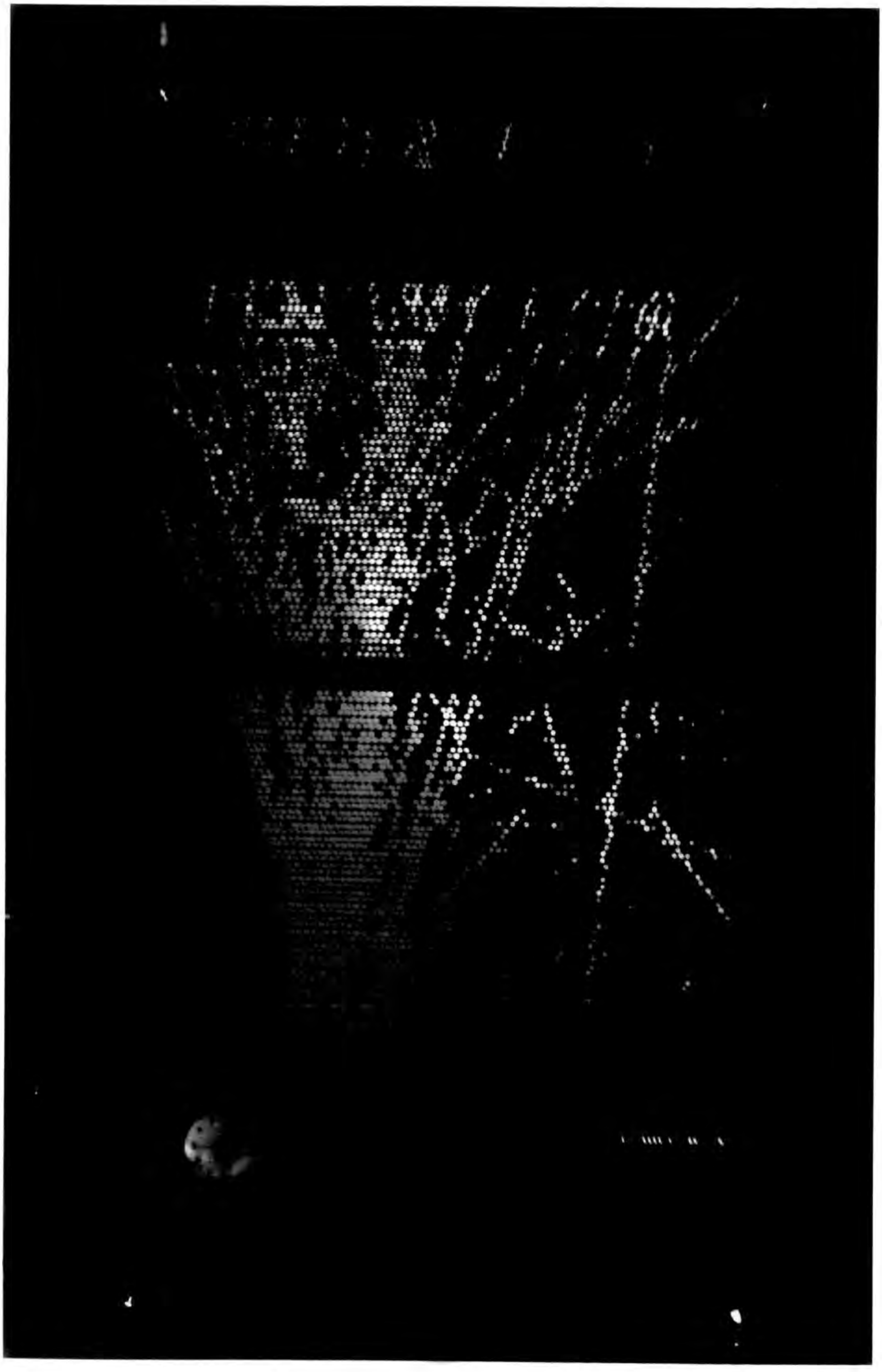

Plate 5.

Event M64 - 1179680

An example of a shower of muons traversing the flash tube chamber (18 muons)

Shower parameters

$r_H = 34.8$m

$N_e = 2.82.10^6$

$\theta = 32.5^o$

$\phi = 36.8^o$

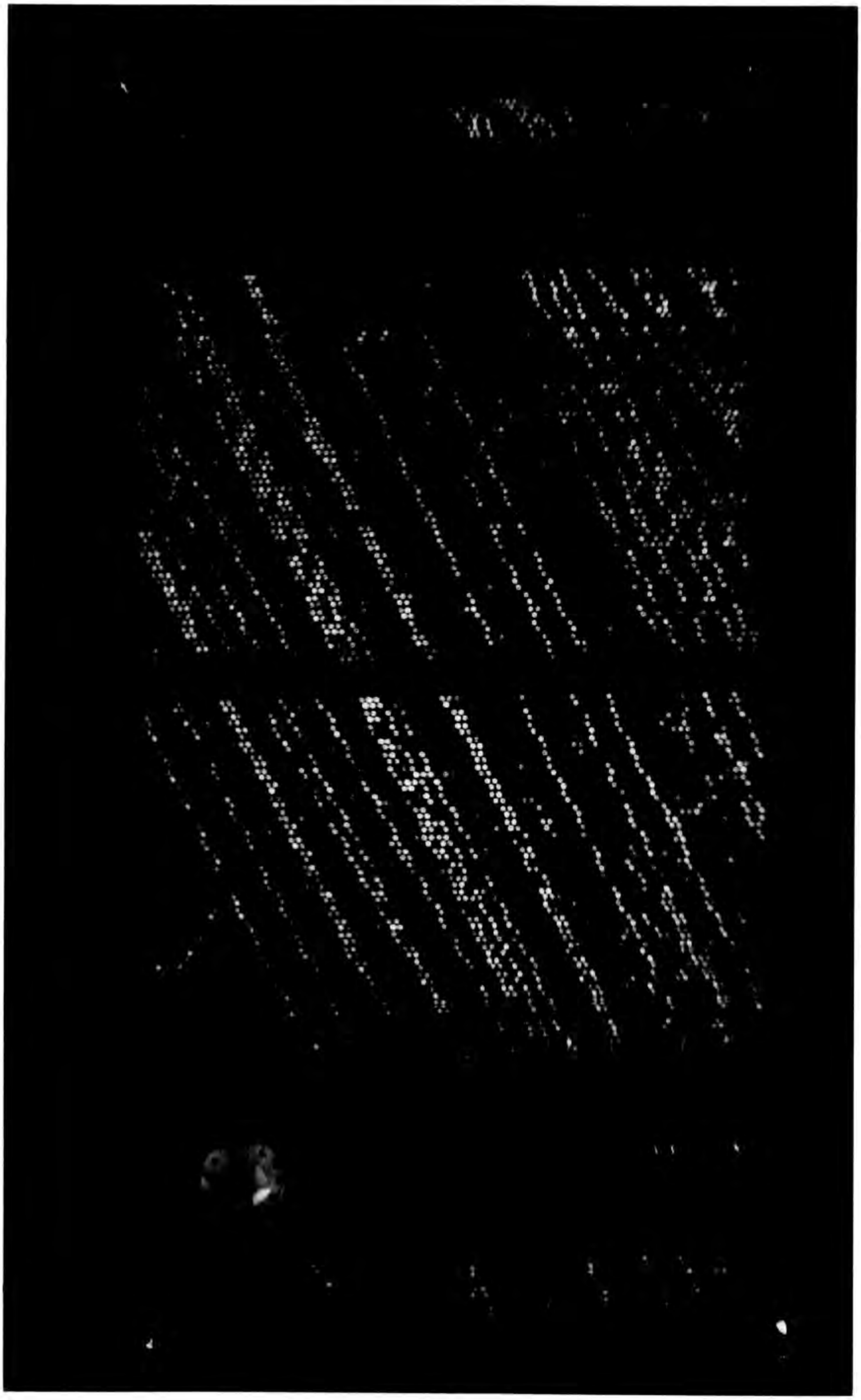

Plate 6.

Event M13 - 1161528

An example of a burst produced when a charged particle interacts in the glass of a flash tube.

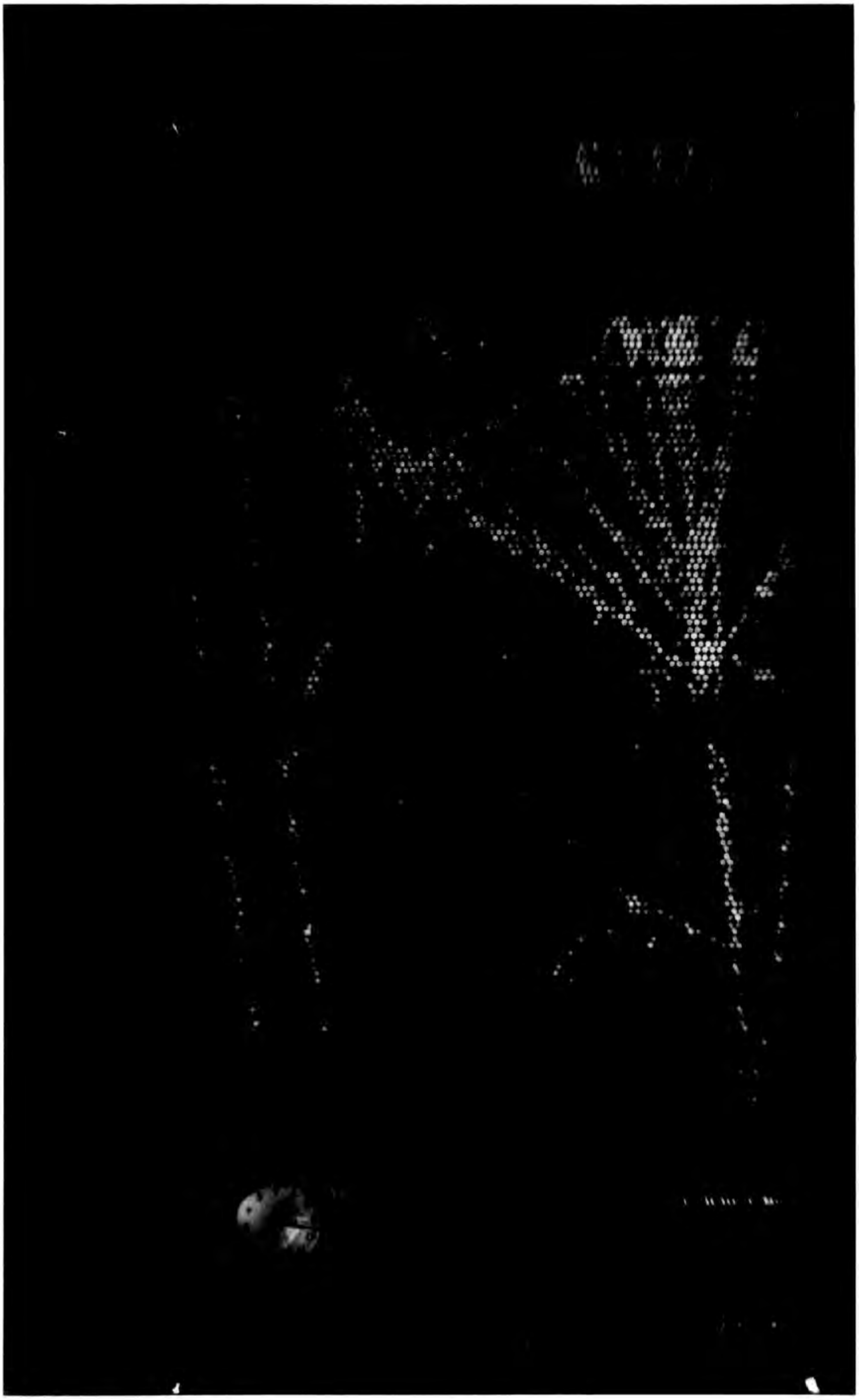

Plate 7.

Event M61 - 1176757

An example of a burst produced when a neutral particle interacts in the glass of a flash tube.

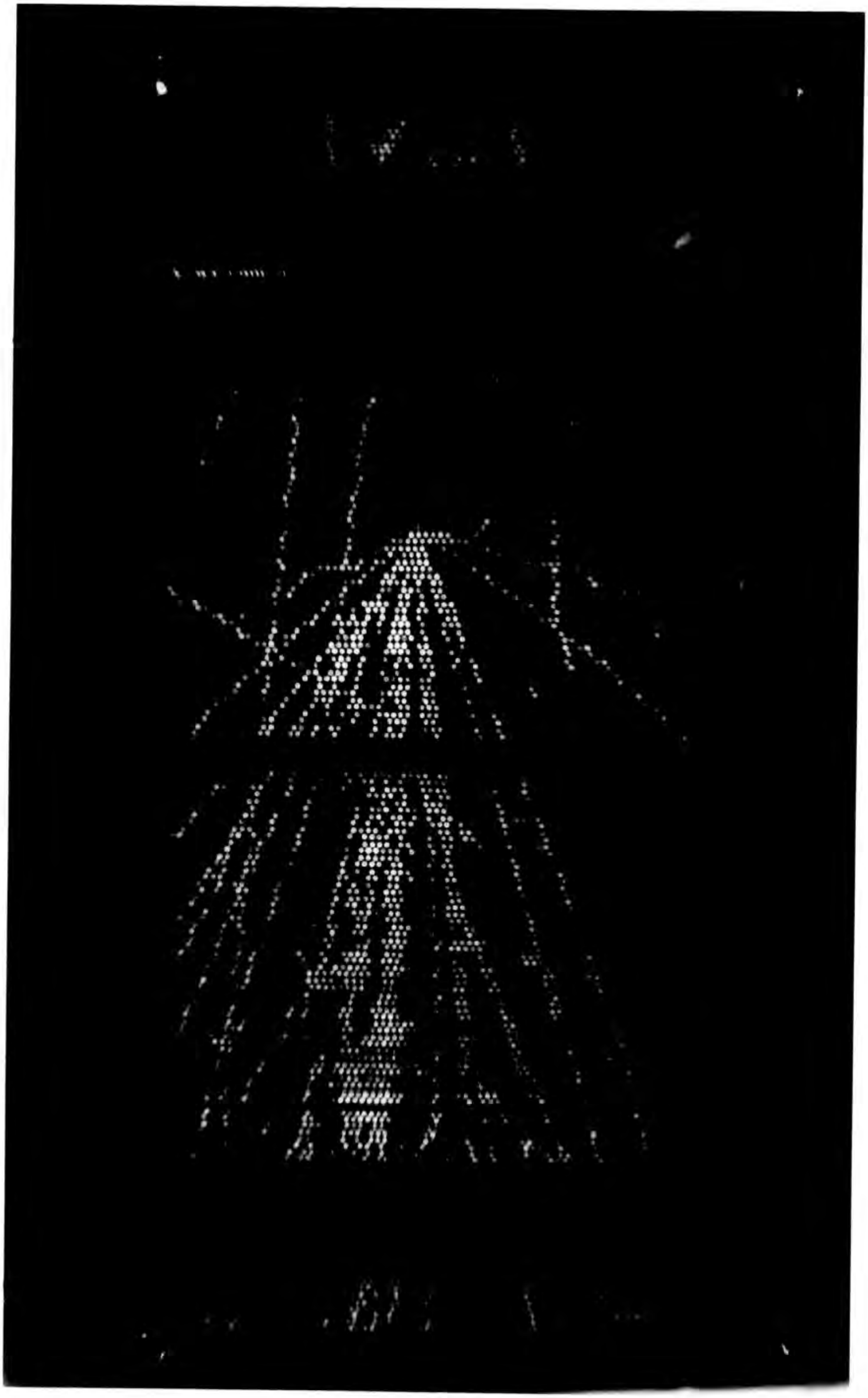

APPENDIX E

TABLE OF PROPERTIES OF HADRONS OBSERVED IN THE PRESENT EXPERIMENT

In the course of present experiments, 186 hadrons were deteced. The following is a table of properties of these hadrons and accompanied air showers. The keys to the table are :

$\frac{i}{0}$ - indicates whether the hadron was observed in a shower producing an inner ring trigger (i) or an outer ring trigger (0).

N_e - shower size.

r_H - orthogonal core distance from the flash tube chamber.

θ - zenith angle.

ϕ - azimuthal angle

$\frac{P_b}{F_e}$ - indicates whether the hadron interacted in the lead or the iron.

$\frac{c}{n}$ - indicates whether the hadron is charged or neutral.

E - hadron energy

S - age parameter

r - core distance from the flash tube chamber in the xy plane.

No	N_e	r_H(m)	θ^{o}	ϕ^{o}	Pb/Fe	C/π	E(GeV)	Exr	S	r
1	4.32.10^{5}	28.7	16.3	337	Fe	C	30	861	1.35	24.9
2	2. 4.10^{6}	49.1	27.9	276	Fe	C	62	3044	1.44	40.3
3	6. 2.10^{5}	17.1	27.2	354	Fe	?	66	1128	1.27	13.7
4	5. 4.10^{4}	6.1	26.6	282	Fe	C	224	1366	1.80	5.8
5	1.94.10^{5}	25.5	36.7	171	Pb	?	76	1938	1.77	19.4
6	1.79.10^{5}	12.0	13.8	198	Fe	C	44	528	1.19	10.3
7	1.53.10^{6}	22.0	19.9	200	Pb	?	167	3674	1.07	17.9
8	1.05.10^{6}	11.3	19.4	331	Pb	?	∿ 1500	∿16950	1.64	9.1
9	2. 4.10^{5}	1.9	26.2	324	Pb	?	96	182	1.14	1.6
10	2. 1.10^{5}	10.3	31.7	348	Fe	?	45	463	1.0	7.7
11	1.37.10^{6}	20.0	4.92	296	Pb	?	∿ 1600	32000	0.93	18.6
12	2.51.10^{6}	16.0	22.2	311	Pb	?	500	8000	1.36	13.4
13	7. 8.10^{5}	37.0	23.9	55.2	Pb	?	76	2812	1.40	31.5
14	5. 5.10^{5}	5.0	11.3	16.6	Pb	?	220	1100	1.10	4.6

No	N_e	r_H (m)	θ^o	ϕ^o	Pb/Fe	C/π	E (GeV)	Exr	S	r
15	$3.\ 2.10^{6}$	29.5	11.5	231	Fe	C	44	1290	1.19	26.4
16	$1.83.10^{5}$	10.0	23.4	198	Fe	C	305	3050	1.06	8.0
17	$6.16.10^{5}$	46.0	20.7	296	Pb	?	82	3772	1.29	41.2
18	$7.98.10^{5}$	8.4	15.1	204	Pb	?	138	1159	1.80	7.5
19	$5.64.10^{5}$	26.0	12.1	229	Pb	?	191	4966	1.05	25.1
20	$1.39.10^{5}$	2.2	44.6	174	Pb	?	69	151	1.49	1.8
21	$1.38.10^{5}$	17	31.8	275	Fe	?	13.5	195	1.25	13.0
22	$4.1.10^{5}$	45.0	8.5	218	Pb	?	≥ 1500	67500	1.43	41.5
23	$7.\ 6.10^{5}$	36.0	16.8	18.1	Pb	?	55	1980	1.24	34.3
24	$2.\ 4.10^{5}$	36.8	17.8	162	Pb	?	85	3068	1.48	33.2
25	$7.\ 4.10^{5}$	25.1	20.2	158	Fe	n	62	1556	1.30	21.4
26	$8.\ 4.10^{5}$	46.0	27.3	359	Pb	?	110	5060	1.38	40.0
27	$5.\ 4.10^{5}$	41	34.1	85.8	Pb	?	1000	41000	1.22	38.0
28	$3.\ 8.10^{5}$	15.7	18.5	218	Fe	C	13.0	204	1.31	13.1

No	N_e	r_H (m)	θ^o	ϕ^o	Pb/Fe	C/π	E(GeV)	Exr	S	r
29	$4.\ 9.10^5$	35	16.2	20.6	Pb	?	277	9695	1.80	32.9
30	$4.\ 9.10^5$	35	16.2	20.6	Pb	?	83	2905	1.80	32.9
31	$5.23.10^5$	5.2	9.04	330	Fe	C	64	332	0.97	5.0
32	$4.62.10^5$	25.3	22.5	236	Fe	C	36	910	1.15	22.8
33	$7.69.10^5$	30.4	34.0	2945	Fe	?	36.0	1094	1.46	28.0
34	$1.30.10^6$	50.0	9.0	89.7	Fe	?	37	1872	1.39	48.1
35	$5.\ 8.10^5$	26.3	5.6	297.5	Fe	C	94	2472	0.68	26.1
36	$6.71.10^5$	7.55	13.2	281.5	Pb	?	>1500	11325	1.26	7.0
37	$1.45.10^5$	32.1	22.7	352.7	Pb	?	138	4429	1.16	29.2
38	$7.31.10^5$	5.06	13.0	169.9	Pb	?	145	733	0.93	4.6
39	$1.02.10^6$	15.7	18.9	90.3	Fe	C	150	2355	1.31	15.1
40	$1.02.10^6$	15.7	18.9	90.3	Pb	?	42	659	1.31	15.1
41	$4.52.10^5$	9.01	30.0	193	Pb	?	290	2612	1.18	6.8
42	$3.\ 2.10^5$	21.2	25.1	182.1	Fe	?	37	784	1.03	19.0

No	N_e	r_H(m)	θ°	ϕ°	Pb/Fe	C/π	E(GeV)	Exr	S	r
43	$7.8 \cdot 10^5$	12.4	15.1	141	Fe	C	41	508	.70	10.1
44	$6.3 \cdot 10^5$	7.54	17.1	241	Pb	?	295	2212	1.04	6.0
45	$4.3 \cdot 10^5$	24.6	11.9	162	Pb	?	39	955	1.22	22.9
46	$8.1 \cdot 10^5$	45.8	14.8	18.8	Fe	C	62	2839	1.07	43.0
47	$4.1 \cdot 10^5$	47.5	14.2	54.4	Pb	?	38	1805	1.17	42.2
48	$1.2 \cdot 10^6$	46.8	8.60	47.8	Fe	C	21	982	1.27	45.8
49	$3.3 \cdot 10^4$	8.47	42.4	296	Pb	?	198	1665	1.11	5.9
50	$1.6 \cdot 10^5$	8.82	28.1	190	Fe	?	63	554	1.09	6.8
51	$5 \cdot 10^4$	6.70	17.8	285	Pb	?	180	1206	1.7	6.1
52	$2.4 \cdot 10^5$	13.1	21.0	62.5	Fe	C	55	720	.69	12.3
53	$1.22 \cdot 10^5$	5.45	31.2	246.0	Fe	C	64	348	1.01	3.8
54	$9 \cdot 10^5$	16.2	23.5	128	Fe	C	178	2883	0.92	13.5
55	$5.08 \cdot 10^4$	8.1	20.9	57.6	Pb	?	42	340	1.10	6.3
56	$6.25 \cdot 10^4$	16.3	10.9	49.1	Pb	?	96	1564	1.51	14.4

No	N_e	r_H(m)	θ^o	ϕ^o	Pb/Fe	C/π	E(GeV)	Exr	S	r
57	$3.47.10^5$	11.3	12.9	222	Pb	?	14.7	143	1.05	9.8
58	$3.47.10^5$	11.3	12.9	222	Fe	C	62	700	1.05	9.8
59	$7.\ 3.10^4$	7.0	29.7	125	Fe	C	75	525	1.29	5.5
60	$1.23.10^5$	33	12.4	86.2	Fe	C	144	1452	1.01	30.7
61	$8.42.10^4$	14	30.5	74.0	Fe	C	135	1890	0.85	11.3
62	$9.47.10^4$	4.2	32.0	22	Pb	?	760	3192	1.08	3.3
63	$3.44.10^4$	4	16.6	251	Pb	?	76.0	304	0.95	3.6
64	$3.\ 4.10^4$	4	16.6	251	Fe	n	145	580	0.95	3.6
65	$5.44.10^4$	6.5	10.8	204	Pb	?	27	175	0.96	5.9
66	$5.44.10^4$	6.5	10.8	204	Pb	?	60	390	0.96	5.9
67	$1.03.10^5$	22	21.0	117	Pb	?	32	704	1.62	19.7
68	$5.09.10^4$	7	32.1	71.5	Fe	C	115	805	0.96	5.4
69	$1.58.10^5$	23	30	291	Fe	n	22	506	0.90	20.7
70	$6.05.10^4$	7	10.9	225	Pb	?	>1500	10500	1.06	6.3

No	N_e	r_H(m)	θ°	φ°	Pb/Fe	C/π	E(GeV)	Exr	S	r
71	$1.36.10^5$	22	26.7	67.2	Fe	C	36	792	0.69	18.9
72	$9.41.10^4$	22	13.2	190	Pb	?	42	924	0.92	20.4
73	$8.69.10^5$	9	13.8	159	Pb	?	800	7200	1.03	7.7
74	$6.33.10^4$	12	19	348	Pb	?	170	2040	0.93	10.8
75	$2.97.10^5$	16	17.4	80	Pb	?	69	1104	1.13	14.6
76	$3.72.10^4$	5.2	6.2	336	Pb	?	55	286	1.20	4.8
77	$1.56.10^6$	7.1	29.3	176	Fe	?	51	362	1.33	6.0
78	$3.\ 1.10^5$	12.0	16.6	254	Pb	?	32	384	0.71	10.5
79	$2.\ 4.10^5$	10.0	13.5	42.9	Pb	?	260	2600	1.10	8.9
80	$4.98.10^4$	10.2	21.2	168	Fe	?	115	1173	1.54	8.3
81	$1.52.10^5$	22.0	47.7	257	Pb	?	55	1210	1.11	17.9
82	$3.53.10^5$	6.1	18.9	3.1	Pb	?	167	1018	.96	5.5
83	$1.85.10^5$	7.2	9.18	326	Pb	?	77	554	1.07	6.6
84	$2.28.10^4$	8	19.4	113	Pb	?	277	2216	1.80	6.90

No	N_e	r_H (m)	θ^o	ϕ^o	Pb/Fe	C/π	E(GeV)	Exr	S	r
85	$5.43.10^5$	15	17.4	179	Fe	?	36	540	1.0	13.3
86	$1.49.10^5$	14.0	21	200	Pb	?	>1500	21000	1.10	11.1
87	$7.32.10^4$	4.9	33	170	Fe	?	51	229	1.05	3.1
88	$6.11.10^5$	32.2	35.2	13.8	Pb	?	110	3542	1.01	29.0
89	$3.37.10^5$	10.3	23.9	272	Pb	?	260	2678	0.97	8.8
90	$8.21.10^4$	18.0	32.4	324	Pb	?	220	3960	1.35	15.8
91	$8.21.10^5$	40.1	13.8	68.8	Fe	C	30	1230	0.95	38.6
92	$7.37.10^4$	9.3	36.0	357	Fe	?	76	684	1.53	7.1
93	$1.55.10^5$	15.0	13.6	181	Pb	?	76	1140	1.33	14.0
94	$1. 4.10^5$	18.0	31.0	72.6	Fe	?	94	1692	1.42	15.7
95	$6.08.10^4$	5.9	8.5	215	Pb	?	42	247	0.93	5.5
96	$2.32.10^5$	6.0	1.41	119	Fe	π	77	462	1.08	5.5
97	$8.52.10^5$	22.0	20.5	25.5	Pb	?	96	2112	1.52	20.3
98	$9.49.10^5$	10	3.78	178	Pb	?	154	1540	1.06	8.9

No	N_e	r_H(m)	θ^o	ϕ^o	Pb/Fe	C/π	E(GeV)	Exr	S	r
99	7. 1.10^5	26.0	11	353	Pb	?	55	1430	0.65	24.0
100	3. 6.10^5	23	18.3	77.5	Fe	?	75	1725	1.25	21.4
101	7. 9.10^4	9.2	11	244	Fe	C	150	1380	1.19	9.0
102	5.82.10^5	35	20.2	342	Pb	?	69	2415	1.18	32.8
103	1.95.10^5	28.1	17.1	178	Pb	?	110	3091	1.09	26.0
104	4.02.10^5	8.0	8.6	346	Pb	?	277	2216	0.80	7.3
105	3. 5.10^4	15.0	42.4	296	Fe	C	81	975	1.51	11.9
106	2. 10^4	4.2	14.2	95.6	Pb	?	32	134	1.80	3.5
107	5.68.10^4	1.2	28.1	109	Pb	?	167	200	1.12	1.0
108	7.43.10^4	2.2	14.2	61.4	Pb	?	76	167	0.96	2.1
109	3.24.10^4	4.3	32.2	71.3	Pb	?	138	593	1.41	3.7
110	2.31.10^4	6.4	30.2	128	Pb	?	82	524	1.10	5.1
111	8.21.10^4	7.4	36.1	82.6	Pb	?	70	518	1.09	6.0
112	2.02.10^5	7.7	27.9	25.4	Pb	?	530	4081	0.84	6.3

No	N_e	r_H(m)	θ^o	ϕ^o	Pb/Fe	C/π	E(GeV)	Exr	S	r
113	$1.14.10^5$	6.7	7.70	352	Fe	C	150	1005	1.05	6.1
114	$1.14.10^5$	6.7	7.70	352	Fe	?	83	556	1.05	6.1
115	$3.\ 5.10^4$	15.9	25.2	12.8	Fe	C	36	572	1.33	14.4
116	$1.\ 5.10^5$	7.5	18.9	3.6	Fe	C	30	225	1.30	7.0
117	$9.\ 6.10^4$	20.9	12.5	151	Fe	C	31	647	1.0	19.3
118	$2.07.10^5$	23.5	23.8	354	Fe	C	22	517	0.95	20.8
119	$2.59.10^5$	20.7	8	96	Pb	?	110	2277	0.97	19.5
120	$7.34.10^5$	17.5	14.3	6.36	Pb	?	32	560	1.16	16.0
121	$1.15.10^5$	41.6	15.9	18	Pb	?	150	6240	1.14	38.9
122	$1.37.10^5$	15.1	8.9	186	Fe	?	150	2265	1.43	14.0
123	$1.65.10^5$	6.1	15.2	212	Pb	?	38	231	1.09	5.7
124	2.10^4	7.0	20	216	Pb	?	138	966	1.80	6.0
125	$2.21.10^5$	14.2	25.5	7.8	Fe	n	30	426	1.0	12.8
126	2.64.18	36.0	10.2	71.5	Pb	?	38	1368	1.43	34.8

No	N_e	r_H(m)	θ^o	ϕ^o	Pb/Fe	C/n	E(GeV)	Exr	S	r
127	$9.92.10^{4}$	9.1	16.2	109	Pb	?	96	873	.82	
128	$1.59.10^{5}$	7.4	23.1	347	Pb	?	27	199	1.09	
129	$6.75.10^{4}$	9.4	42.4	268	Pb	?	220	2068	1.0	
130	$2.\ 7.10^{5}$	5.3	8.09	157	Fe	C	44	233	1,23	
131	$5.64.10^{4}$	7.3	20.7	240	Fe	C	224	1635	1.09	
132	$1.45.10^{5}$	13.5	15.2	347	Pb	?	150	2025	1.38	
		EVENTS	FROM	RUN	(M)					
133	$3.\ 7.10^{5}$	35.1	26.7	88.9	Fe	n	27	947	0.73	32.0
134	$8.\ 2.10^{5}$	48.4	20.8	339	Pb	?	110	5324	1.24	45.7
135	$1.\ 6.10^{6}$	43.7	30.4	344	Fe	C	25	1092	1.22	39.2
136	$2.\ 2.10^{5}$	12.3	8.7	58.8	Fe	C	26	319	1.23	10.6
137	$3.\ 7.10^{6}$	13.8	13.3	28.1	Pb	?	53	731	1.80	12.2
138	$4.\ 8.10^{5}$	7.4	24.4	349	Pb	?	16	118	1.23	6.0
139	$1.\ 3.10^{5}$	6.25	36.9	15.9	Pb	?	146	912	1.24	5.0

No	N_e	r_H(m)	θ^o	ϕ^o	Pb/Fe	C/π	E(GeV)	Exr	S	r
140	$1.\ 7.10^{5}$	3.2	19	36.4	Fe	C	31	99	1.35	2.7
141	$9.\ 2.10^{5}$	11.7	7.4	53.7	Fe	C	23	269	.74	10.6
142	$3.\ 1.10^{6}$	44.8	10.1	267	Pb	?	15	672	1.19	42.8
143	$7.\ 2.10^{5}$	12.5	9.6	291	Pb	?	31	387	1.16	11.6
144	$2.\ 4.10^{5}$	31.8	43.7	52.9	Fe	?	25	795	1.13	27.1
145	$8.\ 8.10^{5}$	47.0	13.2	262	Fe	C	20	940	1.32	45.1
146	$4.\ 5.10^{5}$	14.2	18.9	120	Pb	?	45	639	1.24	12.2
147	10^{5}	24.7	17	311	Pb	?	30	741	1.51	23.0
148	$1.\ 8.10^{5}$	31.7	4.8	19	Fe	C	46	1458	1.50	30.6
149	$7.\ 2.10^{5}$	12.8	16.1	70.6	Fe	C	13	166	1.21	11.5
150	$7.\ 2.10^{5}$	12.8	16.1	70.6	Fe	?	45	576	1.21	11.5
151	$1.86.10^{6}$	27.1	9.4	162	Fe	C	16	434	0.88	25.9
152	$2.\ 8.10^{5}$	14.2	36	90	Pb	?	74	1050	1.20	11.8
153	$2.\ 7.10^{5}$	30.2	43.7	27.1	Pb	?	405	12231	1.27	26.6

No	N_e	r_H(m)	θ^o	ϕ^o	Pb/Fe	C/π	E (GeV)	Exr	S	r
154	1. 2.10^5	15.3	24	38	Pb	?	97	1652	1.55	12.9
155	3. 1.10^5	15.4	21.9	39.6	Pb	?	21	323	1.03	12.7
156	1.72.10^6	7.4	3.7	249	Pb	?	200	1480	1.18	7.1
157	2. 7.10^5	16.8	20.7	205	Fe	C	40	672	0.91	14.7
158	8. 3.10^5	17.8	10.9	203	Pb	?	39	694	0.79	16.3
159	2. 2.10^5	8.8	12	210	Fe	?	25	220	1.61	8.1
160	4. 8.10^5	32.7	36	162	Pb	?	120	3924	1.42	30.1
161	3. 4.10^5	48.2	19.1	21.3	Fe	C	20	964	1.08	46.3
162	1. 1.10^6	45.9	12.3	313	Pb	?	48	2203	1.13	44.0
163	1. 1.10^5	17.9	4.8	278	Fe	n	61	1091	1.35	17.0
164	2.10^5	12.8	18.2	284	Pb	?	146	1792	1.70	10.9
165	2.10^5	12.8	18.2	284	Fe	C	150	1920	1.70	10.9
166	1.23.10^6	31.0	16	327	Fe	?	31	961	1.19	21.0
167	6. 3.10^5	273	7.9	238	Fe	?	13.8	376	1.7	25.8

No	N_e	r_H(m)	θ^o	ϕ^o	Pb/Fe	C/π	E(GeV)	Exr	S	r
168	$1.\ 2.10^6$	35.4	21.3	325	Pb	?	81	2867	0.97	33.1
169	$1.\ 2.10^6$	45.9	11	4.15	Pb	?	18	826	0.83	34.1
170	$1.95.10^5$	26.3	34.2	162	Fe	C	408	10730	1.27	21.7
171	$1.\ 2.10^6$	38.2	37.4	187	Pb	?	80	3056	0.64	34.2
172	6.10^5	36.2	33	136	Fe	?	610	22082	1.07	33.0
173	$7.\ 4.10^5$	14.1	40.5	314	Pb	?	380	5358	1.0	10.1
174	$1.\ 2.10^5$	1.82	47.0	265	Fe	C	300	546	1.47	1.10
175	$3.55.10^5$	30.3	23.9	100	Fe	n	14	424	1.13	27.7
176	$1.\ 6.10^5$	36.1	17	191	Fe	C	81	2924	1.8	34.3
177	$3.\ 8.10^5$	12	29.2	313	Fe	C	81	972	1.36	10.0
178	$6.\ 5.10^5$	6.6	47.1	297	Fe	C	81	534	1.0	5.1
179	$1.\ 4.10^6$	9.7	24.7	43.1	Pb	?	150	1455	1.80	8.4
180	$3.\ 3.10^5$	25.0	49.3	166	Pb	?	54	1350	1.10	20.8
181	10^5	17.4	21.7	74	Fe	?	210	3654	1.8	15.3

No	N_e	r_H(m)	θ°	φ°	Pb/Fe	C/π	E(GeV)	Exr	S	r
182	4. 6.10^{5}	23.3	28.7	181	Fe	?	65	1514	1.33	20.6
183	3. 0.10^{5}	27.1	9.13	3.7	Fe	C	13	298	1.05	25.0
184	2. 8.10^{5}	24.2	35	219	Fe	?	59	1476	1.32	22.2
185	1. 2.10^{5}	15.3	14.4	68.8	Pb	?	180	2754	1.15	13.8
186	1. 8.10^{5}	3.4	11	351	Fe	C	110	374	1.02	3.0

APPENDIX F

AN EXPRESSION FOR (E,r,N) WHEN CORE LOCATION ERRORS ARE TAKEN INTO ACCOUNT

F.1 EFFECT OF RANDOM ERRORS IN MEASURING CORE DISTANCE ON A LATERAL DENSITY DISTRIBUTION OF THE FORM $\Delta(r) = A\, e^{-r/r_o}$

If N events with a true lateral density distribution of the form $\Delta(r) = A\, e^{-r/r_o}$ are measured with zero measuring error then the number expected at core distance between r and r + dr is

$$n(r)dr = N\ \Delta(r)\ 2\pi r dr = N\ A\ e^{-r/r_o}\ 2\pi r dr$$

$$n(r)dr = N.A.2\pi r\ e^{-r/r_o}\ dr \qquad (F.1)$$

If the error in measuring r is Gaussian with a standard deviation σ then the expected measured distribution is

$$n(r')dr' = \int_{r=0}^{r=\infty} N.A.2\pi r\ e^{-r/r_o}\ dr.\ \frac{1}{\sqrt{2\pi}\sigma}\ e^{-\frac{(r'-r)^2}{2\sigma^2}}\ dr' \qquad (F.2)$$

where events appearing between $-r'$ to $-(r'+dr')$ due to core location errors are counted between r' and $r'+dr'$ which is what happens in practice.

Equation F.2 has been evaluated numerically and dividing $n(r')dr'$ by $N2\pi r'dr'$, the expected form of the lateral distribution

$\Delta(r')$ is found. Fitting an equation of the form $\Delta(r') = A\, e^{-\frac{r'}{r'_0}}$ to the $\Delta(r')$ distribution and requring conservation of the number of events gives

$$\int_{r=0}^{\infty} A\, e^{-\frac{r}{r_0}}\, 2\pi r\, dr = \int_{r'=0}^{\infty} A'\, e^{-\frac{r'}{r'_0}}\, 2\pi r'\, dr'$$

$$A\, r_0^2 = A'\, {r'_0}^2$$

$$\frac{A'}{A} = \left(\frac{r_0}{r'_0}\right)^2$$

Table F.1 lists the results of numerical calculations which are displayed in Figures F.1 and F.2.

F.2 AN ACCURATE EXPRESSION FOR $\Delta(E,r,N)$ ASSUMING A CORE LOCATION ERROR OF STANDARD DEVIATION 6.0 AND 12.0m

In the analysis of the data presented in Chapter 6 (Figures 6.7 and 6.8) it was assumed that there was no core location error in interpreting the measured lateral distribution of hadrons as a function of shower size and energy. The results presented in the previous section can be used to assess the error involved in making this assumption and the results are summarized in Table F.2.

Using the results shown in Table F.2, (E,r,N) has been evaluated for $\sigma = 6$m and $\sigma = 12$ m in the same way discussed in Chapter 6. The final result is shown in Table F.3.

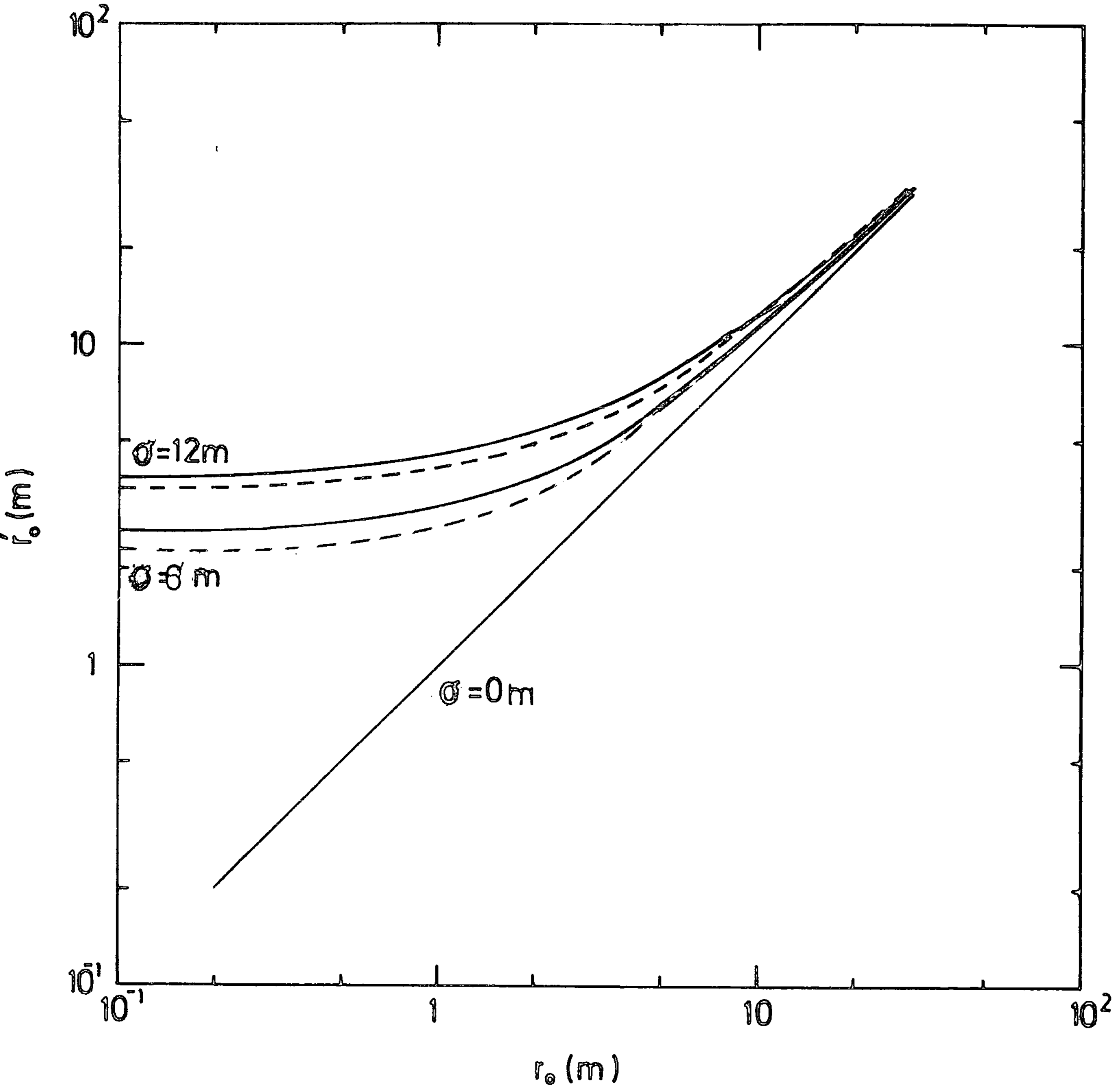

Figure F.1 : ___ $r_0' = \frac{\langle r \rangle}{2}$ calculated from Figure 7.21
--- r_0' calculated by fitting $\Delta(r') = A'e^{-\frac{r}{r_0'}}$, for r' in the range of 0-50m, to the result of folding Gaussian errors of standard deviation σ into $\Delta(r) = A\,e^{-\frac{r}{r_0}}$ for all r_0

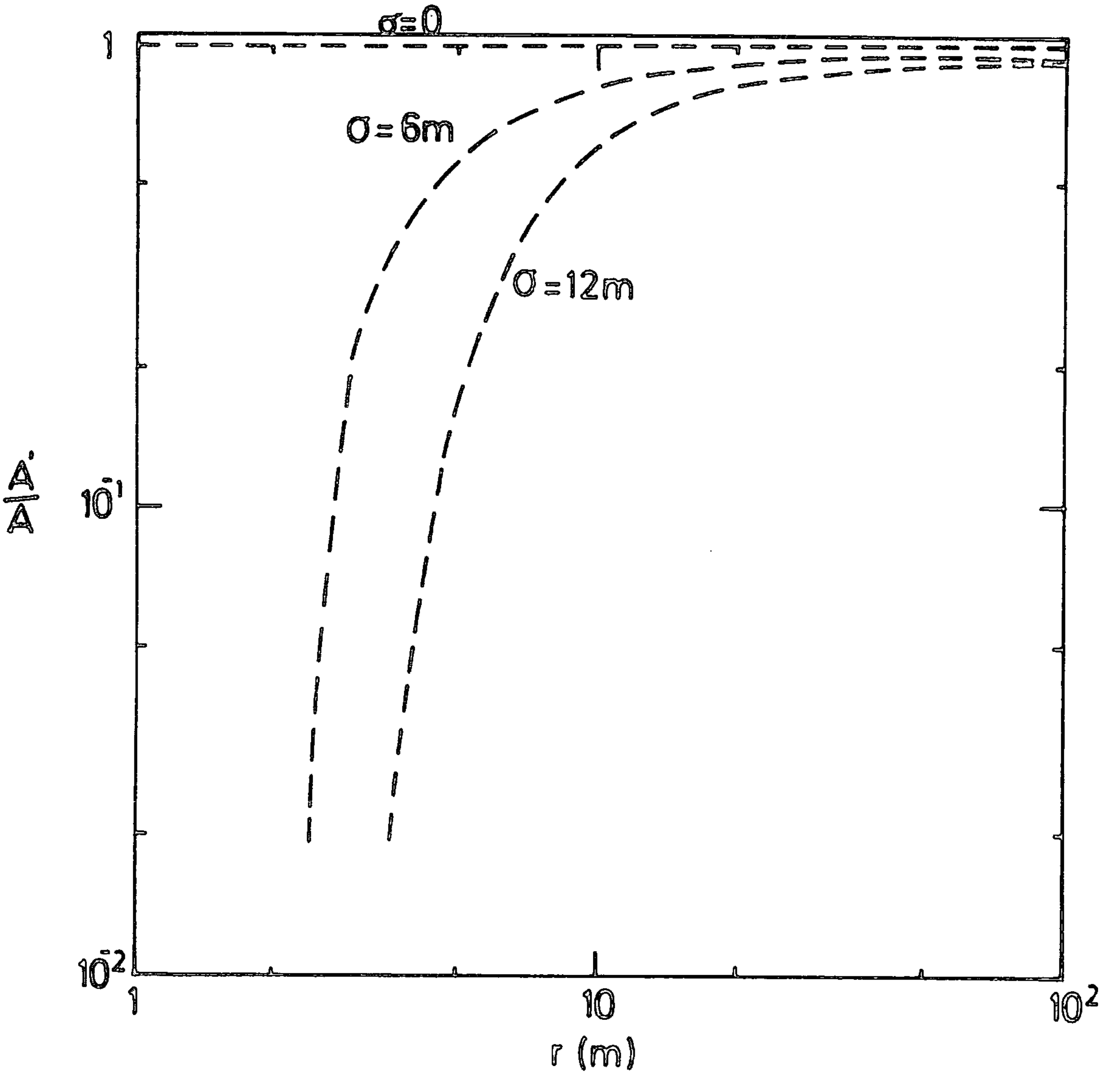

Figure F.2 : Variation of $\frac{A'}{A} = \left(\frac{r_o}{r'_o}\right)^2$ with r_o where error core location is taken into account. r'_o is taken from the dashed curves of Figure F1 .

r_o (m)	r'_o (m)		$\frac{A'}{A} = \left\{ \frac{r_o}{r'_o} \right\}^2$	
	σ = 6.0m	σ =12m	σ=6m	σ = 12m
0.1	2.4	3.5	$1.7.10^{-3}$	$8.1.10^{-4}$
0.5	2.4	3.8	.04	.02
2.0	3.4	4.8	.35	.17
8.0	9.2	10.5	0.76	0.58
20.0	21.1	21.9	0.90	0.83

TABLE F.1 : The variation of A and r_o in $\Delta(r) = A\,e^{-\frac{r}{r_o}}$ assuming no measuring error in determining the core distance and Gaussian errors of standard deviation 6.0m and 12.0m.

Range of N	$\bar{N}$	$\sigma = 0$	$\sigma = 6m$	$\sigma = 12m$
$1.5.10^4 < N < 2.3.10^5$	$1.03.10^5$	$\Delta(r) = .202e^{-(.085 \pm .009)r}$	$\Delta(r) = .17e^{-(.079 \pm .009)r}$	$\Delta(r) = .144e^{-(.072 \pm .009)r}$
$2.3.10^5 < N < 4.10^6$	$6.02.10^5$	$\Delta(r) = .131e^{-(.142 \pm .01)r}$	$\Delta(r) = .098e^{-(.12 \pm .01)r}$	$\Delta(r) = .083e^{-(.11 \pm .01)r}$

Range of E (GeV)	$\bar{E}$ (GeV)	$\sigma = 0$	$\sigma = 6m$	$\sigma = 12m$
$13 \leq E < 82$	44.3	$\Delta(r) = .12e^{-(.09 \pm .03)r}$	$\Delta(r) = .10e^{-(.082 \pm .03)r}$	$\Delta(r) = .087e^{-(.077 \pm .03)r}$
$82 \leq E < 1500$	289.9	$\Delta(r) = .14e^{-(.13 \pm .03)r}$	$\Delta(r) = .11e^{-(.11 \pm .03)r}$	$\Delta(r) = .094e^{-(.10 \pm .03)r}$

<u>TABLE F.2</u> : Interpretation of the lateral distribution of hadrons as a function of shower size and energy

	$\Delta(E,r,N)$
$\sigma = 0$	$7.5.10^{-5}\ E^{-1.35 \pm .04}\ N^{0.24 \pm .05}\ \exp\left\{-\frac{r}{r_o}\right\}\ m^{-2}\ GeV^{-1}$ where $r_o = 5.67\ N^{.29}\ E^{-0.19}\,m$
$\sigma = 6m$	$1.95.10^{-5}\ E^{-1.41 \pm 0.04}\ N^{0.32 \pm .05}\ \exp\left\{-\frac{r}{r_o}\right\}\ m^{-2}\ GeV^{-1}$ where $r_o = 11.09\ N^{0.25}\ E^{-.16}\ m$
$\sigma = 12m$	$1.56.10^{-5}\ E^{-1.39 \pm .04}\ N^{0.32 \pm .05}\ \exp\left\{-\frac{r}{r_o}\right\}\ m^{-2}\ GeV^{-1}$ where $r_o = 12.38\ N^{.25}\ E^{-.17}\ m$

TABLE F.3 : Analytic expressions for the density of hadrons of energy E at core distance r in a shower of size N assuming no measuring error and Gaussian errors of standard deviation 6m and 12m in core location. All energies are in GeV and all shower sizes N are in units of single particles.

REFERENCES

P.I.C.C.R. - PROCEEDINGS OF THE INTERNATIONAL CONFERENCE ON COSMIC RAYS.

1. Abrosimov, A.T., et al., (1960), Sov.Phys.JETP,38,200.
2. Adcock, C., Wolfendale, A.W., and Wdowczyk, J.,(1969) J. Phys., A,2,2,574.
3. Adcock, C., et al.,(1971), J.Phys.A, 4, 276.
4. Antonov, R.A., Ivanenko, I.P., Samosodv, B.E., Tulinova, Z.I., (1971), P.I.C.C.R.(Hobart), 6, 2194.
5. Asakimori, K., et al.,(1979), P.I.C.C.R.(Kyoto),13 229.
6. Aseikin, V.S., et al.,(1971), P.I.C.C.R.(Hobart), 6, 2152.
7. Aseikin, V.S., et al.,(1975a),P.I.C.C.R.(Munich), 8, 2960.
8. Aseikin, V.S., et al.,(1975b),P.I.C.C.R.(Munich), 7, 2462.
9. Ashton, F., and Parvaresh, A.,(1975),P.I.C.C.R. (Munich),8, 2719.
10. Ashton, F., Parvaresh, A., and Saleh, A.J., (1975), P.I.C.C.R.(Munich), 8, 2831.
11. Ashton, F., Cooper, D.A., Nasri, A., Parvaresh, A., and Saleh, A.J., (1975), P.I.C.C.R.(Munich),8, 2980.
12. Ashton, F., Fatemi, C., Nejabat, H., Nasri, A., Rada, W.S., Shaat, E., Smith, A.C., Stewart, T.R., Thompson, M.G., Treasure, M.W., and Ward, I.A.,(1977) P.I.C.C.R. (Plovdiv), 11, 400.

13. Bagge, F.R., Samorski, M., Stamm, W., (1977), P.I.C.C.R. (Plovdiv), 12, 24.

14. Bakich, A.M., McCusker, C.B.A., Nelson, D., Peak, L.S., Rathgeber, M.H., and Winn, M.M., (1970) Acta Phys. Acad. Sci. Hung., 29, Suppl, 3, 501.

15. Baruch, J.E.F., Brooke, G., Kellermann, E.W., and Rezazadeh, A., P.I.C.C.R.(Munich), 8, 2949.

16. Bassi, P., Clark, G., and Rossi, B., (1953), Phys.Rev., 92, 441.

17. Bennett, S., Delvaille, J., Greisen, K., and Kendziorski, F., (1962), J.Phys.Soc.Japan, Suppl.A-III, 17, 196.

18. Bohm, E., Fritze, R., Kassner, F., Roose, U., Samorski, M., Staubert, R., and Trumper, J.,(1969), Can.J.Phys., 46, S5.

19. Bonezak, B., et al., (1968), Can.J.Phys., 46, S102.

20. Capdevielle, J.N., Procuteur, J., and Bourdeau, M.F., (1977), Lett.Al Nuovo Cim. Vol.18, No.15.

21. Catz, ph. , et al., (1975), P.I.C.C.R.(Munich), 12, 4329.

22. Chatterjee, B.K., Murthig, G.T., Naranan, S., Sreckantan, B.V., Srinivasa, M.V., Tonwar, S.C., and Vatcha, R. H., (1968), Can.J.Phys., 46, S 136.

23. Cocconi, G., Koester, L.J., and Perkins, D.H., (1961), Lawrence Radiation Lab.,High Energy Physics Study Seminars, No.28 2.

24. Cooper, D.A., (1974), Ph.D.Thesis, University of Durham.

25. Crouch, P.C., Kuhlmann, J.D., Clay, R.W., Gregory, A.G.T., Patterson, J.R., and Thornton, G.J., (1977), P.I.C.C.R. (Plovdiv), 12, 166.

26. De Beer, J.F., et al., (1966), Proc.Phys.,Soc., 89, 567.

27. Dixon, H.E., Machin, A.C., Pickersgill, D.R., Smith, G.J., and Turver, K.E., (1973), P.I.C.C.R. (Denver), 4, 2556.

28. Dovzhenko, O.J., Zatsepin, G.T., Murzina, E.A., Nikolsky, S.I., and Yakorlev., V.I., (1959), P.I.C.C.R, (Moscow), 2, 144.

29. Earnshaw, J.C., et al., (1967), Proc.Phys.Soc.,90, 91.

30. Egorov, T.A., Efemov, N.N., Kolosov, V.A., Krasilnikov., D.D., Kuzmin, A.I., Kulakovskaya, V.P., Maksimov., S.V., Orlov, V.A., Sizov., V.V., Skripin,G.V., Sleplsov., I.E., Shamsutdinov., F.K., Vernov, S.N., Khristiansen, G.B., (1971), P.I.C.C.R.(Hobart), 6,2059.

31. Evans, A.,(1970), Ph.D.Thesis, University of Leeds.

32. Fermi, E., (1949), Phys.Rev., 75, 1169.

33. Feynman, R.P., (1969), Phys.Rev.Lett. 23 , 1415.

34. Fritze, R., Samorski, M., Staubert, R., Trumper, J., Aschenbach, B.A., and Bohm, F., Acta.Phys.Acad.Sci.,(1970), Hung., 29, Suppl.3, 439.

35. Gaisser, T.K., and Rudolf, P., (1976), J.Phys.G,2,781.

36. Gaisser, T.K., Protheroe, R.J., Turver, K.E., and McComb, T. J. L., (1978), Rev.Mod.Phys.Vol.50, No.4.

37. Galbraith, W., (1958), 'Extensive Air Showers' published by Butterworths.

38. Greisen, K., (1960), Ann.Rev.Nuc.Sci., 10, 63.

39. Greisen, K., (1956), Progress in Cosmic Ray Physics, 3, 1, Edited by J.G.Wilson, published by North Holland.

40. Grieder, P.K.F., (1972), Nuovo, Cim., 7A, 867.

41. Grieder, P.K.F., (1973), P.I.C.C.R.(Denver), 4, 2467.

42. Grieder, P.K.F., (1975), P.I.C.C.R.(Munich), 8, 2895.

43. Grieder, P.K.F., (1977), Revista del Nuovo, Cim., 7, 1-79.

44. Hansen, S., (1975), Ph.D.Thesis, University of Durham.

45. Hayakawa, S., (1969), 'Cosmic Ray Physics', published by Wiley.

46. Hess, V.F., (1912), Phys. Zeitschr, 13, 1084.

47. Hillas, A.M. (1970a), Acta.Phys, Hung., 29 Suppl., 3, 539.

48. Hillas, A.M., (1970b), Acta.Phys., Hung., 29, Suppl. 3, 355.

49. Hillas, A.M., (1972), 'Cosmic Rays', Pergamon Press.

50. Hillas, A.M., (1975), Phys.Rep, (Phys.Lett.C), 20 C, 61.

51. James, F., and Roos, M., (1975), Computer Physics Communication, 10, 343.

52. Kameda, T., Maeda, T., Oda, H., and Sugihara, T., (1965), P.I.C.C.R.(London), 2, 681.

53. Kempa, J., (1976), Nuovo Cim., 31A, 568.

54. Kerschenolz, I.M., Krasilnikov, D.D., Kuzmin, A.I., Orlov., V.I., Steptsov., I.Y., Yegotov, T.A., (1973), P.I.C.C.R.(Hobart), 4, 2507.

55. Khristiansen, G.B., Vedoneev, O.V., Kulikov., G.V., Nazarov., V.I., and Solovjeva, V.I., (1971), P.I.C.C.R.(Hobart), 6, 2097.

56. Khristiansen, G.B., Kulikov, G.V., Sirodjev, N., and Solov'eva, V.I., (1975), P.I.C.C.R.(Munich), 8, 2801.

57. Linsley, J., and Scarsi, L., (1962), Phys.Rev., 128, 2384.

58. Linsley, P., (1963), P.I.C.C.R.(Jaipur),4, 77.

59. Lloyd, J.L., (1960), Proc.Phys.Soc., 75, 387.

60. Matano, T., Machida, M., Otha., K., and Tanahashi, G., (1970), Acta. Phys. Acad.Sci.Hung., 29, Suppl.3, 451.

61. McCusker, C.B.A., Peak, L.S., and Rathgeber, M.H., (1969), Phys.Rev., 177, 1902.

62. McCusker, C.B.A., (1975), Phys.Rep., 20C, 229.

63. Meyer, P., Ramaty, R., and Webber, W.R.,(1974), Phys. Today, 27, 23.

64. Miyake, S., Hinotani, K., Ito, N., Kino, S., Sakuyama, H., Kawahami, S., and Hayashida, N., (1970), Acta.Phys.Acad.Sci.Hung., 29, Suppl. 3, 461.

65. Morison, P., Ulbert, S., and Rossi, B.,(1954), Phys. Rev., 94, 440.

66. Nasri, A., (1977), Ph.D.Thesis, University of Durham.

67. Nishimura, J., and Kamata, K., (1952), Prog.Theo.Phys. 1, 185.

68. Norman, R.J., (1955), Aus.J.Phys., 8, 419.

69. Norman, R.J., (1956), Proc.Phys.Soc., 69A, 804.

70. Ouldridge, M., and Hillas, A.M., (1978),J.Phys.G., Nucl.Phys. Vol.4, No. 2. p. 28.

71. Predazzi, E., (1979), Nuovo.Cim., 2, 1-43.

72. Porter, N.A., et al., (1975), Phil.Mag.2, 900.

73. Rada, W.S., Bhaat, L., Smith, A.C., Stewart, T.R., Thompson, M.G., and Treasure, M.W., (1977), Nuc.Inst. and Meth., 145, 283.

74. Rossi, B., (1932), Phys. Z, 33, 304.

75. Rossi, B., (1952), 'High Energy Particles', Prentice Hall.

76. Rossi, B., (1960), P.I.C.C.R. (Moscow), 2, 18.

77. Saleh, A.J., (1975), Ph.D.Thesis, University of Durham.

78. Shibita, T., (1975), P.I.C.C.R. (Munich), 8, 2910.

79. Smith, A.C., (1976), Ph.D.Thesis, University of Durham.

80. Smith, A.C., and Thompson, M.G., (1977), Nucl.Inst.and Meth., 145, 289.

81. Tanahashi, G., (1965), J.Phys.Soc.Japan, 20, 883.

82. Tanahashi, G., and Miura, Y., (1975), P.I.C.C.R. (Munich), 8, 2866.

83. Teller, E., (1948), Phys.Rev., 76, 1735.

84. Turver, K.E., (1973), 'Cosmic Rays at Ground Level', Edited by A. W. Wolfendale, published by The Institute of Physics, London.

85. Van Staa, R., Aschenbach, B., Bohm, E., and Cachon,A., (1974), J.Phys.A, 7, 135.

86. Vatcha, R.H., and Sreckantan, B.V., (1973), P.I.C.C.R. (Denver), 4, 2625.

87. Vatcha, R.H., and Sreckantan, B.V., (1973), J.Phys.A 6, 1050, 1067 and 1078.

88. Vernov, S.N., Goryunov, N. N., Dmitriyev, V.A., Kulikov., G.V., Nechin, Yu.A., and Khristiansen, G.B., (1960), P.I.C.C.R.(Moscow), 2, 12963.

89. Vernov, S.N., Khristiansen, G.B., Vedenev, O.V., Kalmikov, N.N., Kulikov, G.V., Mandritskaya, K.V., and Soloveva, V.I. Acta.Phys.Acad.Sci.Hung.(1970), Suppl.3, 429.

90. Wdowczyk, J., (1973), 'Cosmic Rays at Ground Level', Edited by A.W.Wolfendale, published by The Institute of Physics, London.

91. Wdowczyk, J., and Wolfendale, A.W., (1973), J.Phys.A. 6, 1594.

92. Wdowczyk, J., and Wolfendale, A.W., (1973), P.I.C.C.R. (Denver), 3, 1781.

93. williams, R.W., (1948), Phys.Rev., 74, 1689.

94. Wolfendale, A.W., (1973), 'Cosmic Rays at Ground Level', Edited by A.W.Wolfendale, published by The Institute of Physics, London.

95. Yock, P.C.M., (1975), Nuc.Phys.886, 216.